Prospects of Drell-Yan Physics with the HERA–B Detector

Diplomarbeit
im Studiengang Physik

am Lehrstuhl für
Experimentelle Physik V
des Fachbereiches Physik der
Universität Dortmund

vorgelegt von
Ulrich Husemann

März 2001

It takes a man to suffer ignorance and smile
Be yourself no matter what they say
Sting, Englishman In New York

Abstract

In this Diploma thesis, data from the 2000 data-taking period of the HERA–B experiment at the HERA storage ring at DESY, Hamburg, are analyzed, and the prospects of HERA–B in the field of Drell-Yan physics are evaluated.

An analysis of the properties of the J/ψ meson and a comparison with Monte Carlo simulations are performed. After applying all cuts, the complete di-muon triggered data sample of the 2000 run contains approximately 2,700 J/ψ mesons. The measured position and width of the J/ψ signal are $(3081 \pm 1)\,\mathrm{MeV}/c^2$ and $(51 \pm 1)\,\mathrm{MeV}/c^2$ respectively.

Measuring the angular distributions of leptons from Drell-Yan processes allows testing of the Lam-Tung relation, a prediction of perturbative QCD. Based on the data of the 2000 run and on additional Monte Carlo simulations, the feasibility of a measurement of Drell-Yan processes with the HERA–B detector is evaluated. Rate expectations for signal and background events are formulated. In addition, preliminary tools for the analysis of angular distributions in the Drell-Yan process are developed and tested.

For invariant masses larger than $4\,\mathrm{GeV}/c^2$, approximately 8,000 fully reconstructed Drell-Yan events are expected in the HERA–B detector in the 2001/2002 run. Due to the small statistics the expectations for the background rate are only poorly known. Hence, with the HERA–B data of 2001/2002, a test of the Lam-Tung relation will be difficult without major improvements of the detector and trigger performance and of the rejection of background events.

Zusammenfassung

Diese Diplomarbeit beinhaltet eine Analyse von Daten, die während der Datennahmeperiode des Jahres 2000 mit dem HERA–B-Detektor am HERA-Speicherring des Deutschen Elektronen-Synchrotrons (DESY) in Hamburg aufgezeichnet wurden. Darüber hinaus werden die Perspektiven des HERA–B-Experiments auf dem Gebiet der Drell-Yan-Physik untersucht.

Anhand der Daten werden die Eigenschaften des J/ψ-Mesons bestimmt und mit Simulationsrechnungen verglichen. Nach allen Schnitten umfasst der Datensatz der mit einem Myonpaar-Trigger aufgenommenen Daten des Jahres 2000 etwa 2.700 J/ψ-Mesonen. Die J/ψ-Resonanz liegt bei einer Masse von $(3081 \pm 1)\,\mathrm{MeV}/c^2$ und besitzt eine Breite von $(51 \pm 1)\,\mathrm{MeV}/c^2$.

Eine Analyse der Winkelverteilungen der Leptonen aus Drell-Yan-Prozessen erlaubt eine Überprüfung der Lam-Tung-Relation, einer Vorhersage der perturbativen QCD. Auf Basis der Daten aus dem Jahr 2000 und weiterer Monte-Carlo-Simulationsrechnungen wird die Machbarkeit einer Vermessung von Drell-Yan-Prozessen mit dem HERA–B-Detektor geprüft. Dazu werden die erwarteten Ereignis- und Untergrundraten für Drell-Yan-Prozesse bestimmt. Gleichzeitig werden erste Werkzeuge für eine Analyse der Winkelverteilungen im Drell-Yan-Prozess entwickelt und getestet.

In der Datennahmeperiode 2001/2002 werden im HERA–B-Detektor etwa 8.000 Drell-Yan-Ereignisse mit invarianten Massen von mehr als $4\,\mathrm{GeV}/c^2$ erwartet. Aufgrund der geringen Statistik ist die erwartete Untergrundrate derzeit nur sehr ungenau bestimmt. Somit ist ohne eine wesentliche Verbesserung des HERA–B-Detektor- und -Triggersystems, sowie der Unterdrückung von Untergrund, eine Überprüfung der Lam-Tung-Relation auf Basis der Daten, die in den Jahren 2001/2002 genommen werden sollen, schwierig.

Contents

1 Scope of this thesis **1**
1.1 Introduction . . . 1
1.2 Drell-Yan physics . . . 3
1.3 Thesis guide . . . 3

2 The HERA – B experiment **5**
2.1 The HERA storage ring . . . 5
2.2 Physics goals . . . 6
2.2.1 B physics and *CP* violation . . . 6
2.2.2 QCD and heavy flavor physics . . . 9
2.3 The HERA – B detector . . . 10
2.3.1 The subdetectors . . . 10
2.3.2 The trigger system . . . 15
2.3.3 The data acquisition system . . . 19

3 The Drell-Yan process **21**
3.1 Basic theory . . . 21
3.1.1 Naïve quark-parton model . . . 21
3.1.2 Perturbative QCD . . . 23
3.1.3 Angular distributions and the Lam-Tung relation . . . 24
3.2 Violation of the Lam-Tung relation . . . 25
3.2.1 Experimental results . . . 25
3.2.2 Theoretical models . . . 29
3.2.3 Concluding remarks . . . 33

4 The HERA – B di-muon trigger in the 2000 data-taking period **35**
4.1 Status of the trigger commissioning in spring 2000 . . . 35
4.1.1 The pretrigger–SLT di-electron trigger . . . 35
4.1.2 Trigger based on the muon pretrigger emulation . . . 36
4.1.3 Commissioning of the muon pretrigger . . . 37
4.2 The First Level Trigger emulation . . . 38
4.2.1 Utilization of the muon pretrigger . . . 39
4.2.2 The “transparent” First Level Trigger . . . 39
4.2.3 Tracking in the muon system . . . 40
4.2.4 Tracking in the Second Level Trigger . . . 43
4.3 Analysis strategies . . . 44
4.3.1 Matching of track segments . . . 44
4.3.2 Second-Level-Trigger-based tracking . . . 51
4.3.3 The “standard” procedure . . . 53
4.3.4 Summary . . . 58

5 Analysis of the di-muon triggered data in the 2000 data-taking period 59
5.1 Analysis chain . . . 59
5.1.1 Preselection of tracks and vertices . . . 59
5.1.2 The final analysis . . . 62
5.1.3 Relation to the SLT information . . . 67
5.1.4 Comparison with Monte Carlo simulations . . . 69
5.2 Discussion of the results . . . 70
5.2.1 Track and vertex multiplicities . . . 70
5.2.2 Effects of the cuts . . . 71
5.2.3 Properties of the invariant mass spectrum . . . 72
5.2.4 Background in the invariant mass spectrum . . . 74
5.2.5 Systematic effects . . . 77
5.2.6 Concluding remarks . . . 79

6 Prospects of HERA – B in the field of Drell-Yan physics 81
6.1 Acceptance studies . . . 81
6.1.1 The Drell-Yan process in the HERA – B event generators . . . 82
6.1.2 Definition of the acceptance requirements . . . 83
6.1.3 The acceptance as a function of the kinematic variables . . . 84
6.1.4 Acceptance corrections . . . 87
6.2 Experimental observables . . . 92
6.2.1 Fits to the angular distributions . . . 92
6.2.2 The method of moments . . . 93
6.3 Expectations for HERA – B . . . 96
6.3.1 The December 2000 estimate for J/ψ and Drell-Yan rates . . . 96
6.3.2 The March 2001 estimate . . . 98
6.3.3 Discussion of the prospects of HERA – B in the field of Drell-Yan physics . . . 107

7 Summary 111

A Kinematics of the Drell-Yan process 113
A.1 General fixed-target kinematics . . . 113
A.2 Angular distributions . . . 114

B Track parameters 117
B.1 The basic track parameters . . . 117
B.2 The position of closest approach . . . 117
B.3 The χ^2 of tracks and vertices . . . 118

C Monte Carlo simulations in HERA – B 121
C.1 Event generators . . . 121
C.2 Detector simulation . . . 122
C.3 Trigger simulation . . . 122

D List of di-muon triggered runs in the 2000 data-taking 125

List of Acronyms 131

Bibliography 133

Danksagung 143

List of Figures

2.1 The HERA storage ring 6
2.2 The unitarity triangle 8
2.3 Schematic views of the HERA–B detector 11
2.4 Sketch of the HERA–B muon detector 14
2.5 Functional principle of the muon pretrigger system 16
2.6 Schematic overview of the FLT 18

3.1 Feynman diagram of the lowest order Drell-Yan process 22
3.2 Leading and next-to-leading order QCD corrections to the Drell-Yan process 23
3.3 Results of the E615 experiment 26
3.4 Results of the NA10 experiment 27
3.5 $\cos\theta$ distribution of Drell-Yan muon pairs in the E866 experiment . . . 28
3.6 $\cos\theta$ distribution of high-mass Drell-Yan muon pairs in the E772 experiment 29
3.7 Feynman diagram of a "higher-twist" contribution to pion-nucleon scattering 30
3.8 Higher-twist model: Fits to the E615 data 31
3.9 Color domain model: Fit to the 194 GeV/c π^- data of NA10 32
3.10 Intrinsic transverse momentum-dependent parton distribution functions: Fit to the 194 GeV/c π^- data of NA10 33
3.11 Coherent states model: Fit to the 194 GeV/c π^- data of NA10 34

4.1 Coincidence logic of the muon pretrigger emulation 36
4.2 Coverage of the muon pad system by the muon pretrigger 38
4.3 Default "transparent" FLT setup for the di-muon trigger 40
4.4 Illustration of the FLTm algorithm 42
4.5 Illustration of the track parameter matching procedure 45
4.6 VDS-RICH matching in a Monte Carlo simulation 47
4.7 Deflection of a charged particle in a magnetic field 48
4.8 Fits to the momentum dependence of the deflection angle 49
4.9 First observation of a J/ψ signal with the matching algorithm 50
4.10 Sketch of the SLT event structure 52
4.11 Illustration of the ARTE event record 54

5.1 Structure of the ROOT event class 60
5.2 The invariant mass of muon pairs as a function of the number of RICH photons 64
5.3 Dependence of the signal and background efficiency on the muon likelihood 65
5.4 Distribution of the distance between a vertex and the closest target wire 66
5.5 Position of the reconstructed J/ψ vertices after cuts in Run 16784 67
5.6 The J/ψ signal in the 2000 data after the final analysis 68

5.7 Influence of the selection cuts on the J/ψ signal and the background . . 72
5.8 Influence of the selection cuts on the J/ψ signal efficiency in data and Monte Carlo simulations 73
5.9 Invariant mass spectrum obtained from the SLT trigger information . . 74
5.10 Invariant mass spectrum obtained from a Monte Carlo simulation 75
5.11 Invariant mass spectrum after the subtraction of combinatorial background 78

6.1 Angular distributions of Drell-Yan muons at the generator level 82
6.2 Geometrical acceptance for Drell-Yan events 86
6.3 Illustration of the response matrix for the angular variables $\cos\theta_{\mathrm{CS}}$ and ϕ_{CS} 88
6.4 Correction factors for the geometrical acceptance 90
6.5 Application of the acceptance correction to Monte Carlo simulations and data 91
6.6 Estimate of the systematic error of the correction factor method. 92
6.7 Distribution of the angular components of the Drell-Yan cross section . 95
6.8 Invariant mass spectrum of December 2000 98
6.9 Comparison of the reconstructed muon p_{T} distributions for Drell-Yan and J/ψ events from a Monte Carlo simulation 102
6.10 Differential Drell-Yan cross sections from the E772 experiment 104
6.11 Invariant mass spectra for different muon likelihood cuts 108

A.1 Reference frames for angular distributions of lepton pairs 115

C.1 The data path in real data and Monte Carlo simulations 123
C.2 Data flow in the simulation of the SLT 124

List of Tables

1.1 The fundamental fermions 1
1.2 The fundamental gauge bosons 2

4.1 Two-track efficiency of the muon pretrigger and the FLTm algorithm . . 41
4.2 SLT two-track efficiencies 43

5.1 Total statistics of the reprocessed di-muon triggered runs 2000 67
5.2 Effects of the SLT seed for RANGER 68
5.3 Average numbers of tracks per event 70
5.4 Average numbers of preselected vertices per event 71
5.5 Efficiency of the cuts on the numbers of signal and background events . 71
5.6 Comparison of the J/ψ peak from the SLT-based and the "standard" analysis 73
5.7 Properties of the J/ψ signal in Monte Carlo simulations and in data . . 75
5.8 Properties of muons, charged pions, and charged kaons 76
5.9 Systematic effects of the bin size in the invariant mass spectrum 78
5.10 Systematic effects on the position of the J/ψ peak in the invariant mass spectrum 79

6.1 Definition of the acceptance requirements for Drell-Yan muon pairs . . . 84
6.2 Correlations between the kinematic variables 85
6.3 Results of a direct fit to the generated angular distribution of 100,000 Drell-Yan muon pairs 93
6.4 Test of the Lam-Tung relation with the method of moments 96
6.5 Two-track efficiencies of the SLT algorithms from Monte Carlo simulations with an ideal detector 100
6.6 Comparison of the J/ψ rate estimates of December 2000 and March 2001 101
6.7 Comparison of the geometrical acceptances for Drell-Yan and J/ψ events 103
6.8 Integrated cross sections for the Drell-Yan process from E772 105
6.9 Expectations for the number of Drell-Yan events in 2001/2002 106
6.10 Number of events in the sidebands of the J/ψ peak 108

D.1 List of di-muon triggered runs in the 2000 data-taking 125

Chapter 1

Scope of this thesis

1.1 Introduction

Mankind has been investigating the structure of matter on the "fundamental" level for a long time. The meaning of "fundamental" was subject to various changes connected with new theoretical and experimental insights to nature.

Based on two of the most successful theories that physics of the twentieth century gave birth to, i.e. quantum mechanics [Pla00, Sch26, Hei26] and special relativity [Ein05], the Standard Model of elementary particle physics was built, the most successful theory on the current fundamental level.

According to this theory, all matter and all interactions between the constituents of matter – except gravity, see below – can be described by two kinds of fundamental quantum objects: fermions and bosons. The fermions can be divided into quarks and leptons, each arranged in three generations with similar properties, as shown in Table 1.1. For each fermion there is an antiparticle, bearing the same quantum numbers as the particle except for opposite charge-like quantum numbers.

Table 1.1: *The fundamental fermions: quarks (left) and leptons (right). In brackets the usual symbols for the fermions. The fermions are arranged in three generations, and for each fermion there is an antiparticle.*

Generation	Quarks	Leptons
1	up quark (u) down quark (d)	electron neutrino (ν_e) electron (e)
2	charm quark (c) strange quark (s)	muon neutrino (ν_μ) muon (μ)
3	top quark (t) bottom quark (b)	tau neutrino (ν_τ) tau (τ)

The interactions between the fermions are described in the formalism of a quantum field theory, where interactions are mediated by fundamental bosons, the gauge bosons. A list of the gauge bosons and their underlying dynamical theories is shown in Table 1.2.

The leading idea of a quantum field theory is that the invariance of a theory under a local symmetry in nature determines the structure of interactions between the quantum objects described by the theory. The Standard Model consists of two quantum field theories:

Table 1.2: *The fundamental gauge bosons and their corresponding underlying dynamical theories*

Boson	Dynamical theory	
photon (γ) $W^{\pm}$, Z^0	quantum electrodynamics (QED) quantum flavor dynamics (QFD)	} electroweak theory
8 gluons	quantum chromodynamics (QCD)	

1. Quantum electrodynamics (QED) [Fey49, Sch48, Tom46] describes the interactions between charged fermions via the exchange of photons. Quantum flavor dynamics (QFD) deals with the so-called weak interactions that change the flavor of the fermions, e.g. in radioactive decays. QED and QFD have been merged to form the electroweak theory [Gla61, Sal68, Wei67, tHo72] which describes the transitions between different types of left-handed quarks and leptons. The gauge bosons that mediate electroweak interactions include the photon, the Z^0 boson, and the $W^{\pm}$ bosons.

2. Strong forces between the quarks, which carry an internal degree of freedom called color, are described by quantum chromodynamics (QCD). The gauge bosons of QCD are eight bi-colored gluons.

Altogether these theories form the Standard Model of elementary particle physics. The predictions of this models have been tested in various complementary experiments, and the agreement between experimental data and the Standard Model predictions is impressive [Gur00].

However, there are still a lot of open questions connected with the Standard Model, leading to the conclusion that the Standard Model cannot be nature's final answer. While the microscopic world is described very well by the Standard Model, attempts to merge gravitation, the force that rules the macrocosm, into this set of theories have failed so far. On the other hand, a unification of gravitation and quantum mechanics is needed to describe the behavior of objects like black holes in the energy regime where the gravitational and quantum mechanical forces become equally large, the Planck energy.

Another problem concerns the masses of the elementary particles. In the Standard Model, the masses of the fermions are free parameters and thus not predicted by the theory. However, the mechanism of the generation of masses is described by the Standard Model. The particles acquire mass by the interaction with the Higgs field. The corresponding field particle, the Higgs bosons, is the only particle in the Standard Model which has not yet been observed experimentally. However, some evidence for the discovery of the Higgs bosons was reported recently [Igo00].

A third battery of questions arises from the development of the universe from a symmetric situation, the Big Bang, to its present state with a large asymmetry between the amount of matter and antimatter in the universe. Sakharov pointed out that three conditions had to be fulfilled to explain the content of matter and antimatter of the universe as it is now [Sak67]:

1. thermal non-equilibrium at the beginning of the universe,

2. processes that violate the conservation of the baryon number,

3. violation of the C and the CP symmetries.

The first condition is fulfilled by the Big Bang, while the explanations for the second and third conditions are not yet satisfactory. Therefore, the mechanism of *CP* violation is one of the big open questions in particle physics today.

1.2 Drell-Yan physics

Despite the great success of the Standard Model there are still some puzzles connected with QCD. Due to the asymptotically free structure of QCD [Gro73, Pol73], the non-perturbative part of the theory is only partially under control. The Drell-Yan process represents a good testing ground for some of these non-perturbative aspects of QCD.

The ideas of the parton model [Fey69] were developed for deep-inelastic scattering. In this model, the phenomenology of proton-lepton scattering is described by interactions between the lepton and members of a substructure of the proton, the partons. Drell and Yan also applied these ideas to processes in hadron-hadron collisions [Dre70]. The main process is the production of a lepton pair by quark-antiquark annihilation – the so-called Drell-Yan process. To lowest order in perturbation theory the process takes place via the exchange of a virtual photon. As will be discussed in Chapter 3, the partonic structure of the proton can be probed with this process. A good knowledge of the proton structure is especially important because it serves as essential input to almost all analyses which are planned at present and future hadron colliders such as Tevatron II at FNAL and the Large Hadron Collider (LHC) at CERN. This can be exemplified by the future search for the Higgs boson. The most important channel for the discovery of the Higgs boson at the LHC will be gluon-gluon fusion ($gg \rightarrow H$) [Dit00]. A precise knowledge of the gluonic structure of the proton for momentum fractions in the range from 0.006 to 0.06 is needed to perform this measurement.

The Drell-Yan process can provide information about the gluonic structure of the proton in a kinematic regime where the transverse momentum of the virtual photon is larger than half the invariant mass of the outgoing lepton pair. In this region the dominant contribution to the Drell-Yan cross section is QCD Compton scattering [Ber98].

Non-perturbative aspects of QCD can be tested by measuring the angular distribution of the leptons in the final state. The Lam-Tung relation [Lam78, Lam80] is a prediction of the parton model that describes a connection between the individual contributions to the angular distribution of the Drell-Yan cross section. Experiments show that the Lam-Tung relation is clearly violated in pion-nucleon scattering [Gua88, Con89]. This topic will be discussed in greater detail in Chapter 3.

1.3 Thesis guide

The HERA – B experiment has been designed to measure *CP* violation in the B meson system. For the HERA – B collaboration the year 2000 was marked by the commissioning of the detector and the trigger system. A trigger is a hardware or software device to perform a fast preselection of events to be recorded which are potentially interesting for further analyses. This is needed in experiments where the primary interaction rate is large, in order to reduce the amount of data taken to a size that can be handled by the data acquisition and storage systems.

The commissioning phase included data-taking with mostly completed detector and trigger systems. These endeavors are essential to understand the details of the response of the HERA – B detector and to commence with the physics program.

A good "benchmark" process for the detector performance is the direct production of J/ψ mesons with a subsequent decay into a lepton pair. A clear peak in the invariant mass spectrum of oppositely charged lepton pairs is expected around the mass of the J/ψ. Therefore, a provisional trigger system for lepton pairs was developed. Starting in 1998, a di-electron trigger was set up, in June 2000 a di-muon trigger followed [HB00a]. A sample of about 3,000 J/ψ mesons was collected with the latter.

The first attempts to reconstruct a J/ψ signal in the di-muon channel started with studies of the matching of track parameters in different subdetectors [Eig99]. The data for this analysis was taken with a pure software di-muon trigger. After the commissioning of the muon pretrigger, the output of this trigger system could be used to preselect muon candidates such that the data could be recorded with higher statistics compared to the pure software trigger. The Second Level Trigger (SLT) code, a part of the default HERA–B software trigger algorithm, was used together with the muon pretrigger. This combination of a hardware and a software trigger was established as the standard di-muon trigger in the data-taking period of the year 2000.

It became clear in spring 2000 that the primary physics goal of the HERA–B experiment, the measurement of *CP* violation in the B meson system, could not be reached in the near future (2001/2002). However, new physics topics worthwhile to study during this period have been identified [HB00b]. Data taken with an improved di-muon trigger can not only be used to study the physics of J/ψ mesons. The continuous spectrum of lepton pairs that pass this trigger also contains Drell-Yan events, allowing for measurements of the violation of the Lam-Tung relation and of the gluonic structure of the proton.

This thesis describes the development of the search for J/ψ mesons in di-muon triggered data in the year 2000. The expertise gained in these analyses serves as a starting-point to evaluate the prospects of HERA–B for the years 2001/2002 in the field of Drell-Yan physics, especially in the measurement of the violation of the Lam-Tung relation. Thus the following structure of this thesis:

- In Chapter 2, the challenges of the HERA–B experiment and the designs of the detector and trigger system to meet these challenges are described.
- The basic theory of the Drell-Yan process – as far as it is relevant to this thesis – is introduced in Chapter 3. In addition, important theoretical and experimental results connected with the violation of the Lam-Tung relation are reviewed.
- In Chapter 4, the J/ψ trigger that was developed for HERA–B's data-taking in 2000 is described.
- The analysis chain that was developed for J/ψ searches during the 2000 data-taking is described in detail in Chapter 5.
- The prospects of HERA–B in the field of Drell-Yan physics, especially regarding the violation of the Lam-Tung relation, are evaluated in Chapter 6. The study is based on the data and analysis experience gained in the year 2000.

Chapter 2

The HERA – B experiment

In this chapter, some general remarks about the HERA – B experiment will be made. Beginning from a description of the HERA storage ring, the border conditions and challenges for the HERA – B experiment will be discussed. The physics goals will be briefly reviewed, starting from the primary goals for which HERA – B was originally planned to the physics program for 2001/2002. The chapter will close with a brief description of the HERA – B detector components and trigger system.

2.1 The HERA storage ring

The HERA – B experiment is one of the four experiments situated at the HERA storage ring at DESY, Hamburg, Germany. HERA accelerates protons and stores them at an energy of 920 GeV. In a second ring, electrons or positrons[1] are accelerated to an energy of 27.5 GeV and stored. At two interaction points the proton and the electron beams collide. Here the H1 [Abt97] and the ZEUS [Hol93] experiments, designed to study the proton structure in deep-inelastic electron-proton scattering, are placed. The HERMES experiment [Dür96] examines the spin structure of nucleons. For this experiment, the electrons are longitudinally polarized and directed onto a polarizable gas target. An overview of the DESY accelerator complex and the HERA storage ring can be found in Fig. 2.1.

Since only protons are used by the HERA – B experiment, the acceleration of the electrons will not be discussed here. The acceleration of the protons is done in four steps. First negatively charged hydrogen ions are accelerated to 50 MeV in the linear accelerator LINAC III. After the electrons are stripped off the protons, the latter are injected in the accelerator DESY III where they are accelerated to 7.5 GeV. After that, the protons are transferred to the PETRA ring to be accelerated to 40 GeV. Finally, the HERA ring is filled.

The protons are injected in the proton ring in bunches. With a circumference of 6335.8 m, the ring provides space for up to 220 such bunches. This results in a time interval between bunch crossings of 96 ns at the interaction points. Typically, 180 of the bunches are injected.

[1] In the following, the term "electron" will be used both for electrons and positrons.

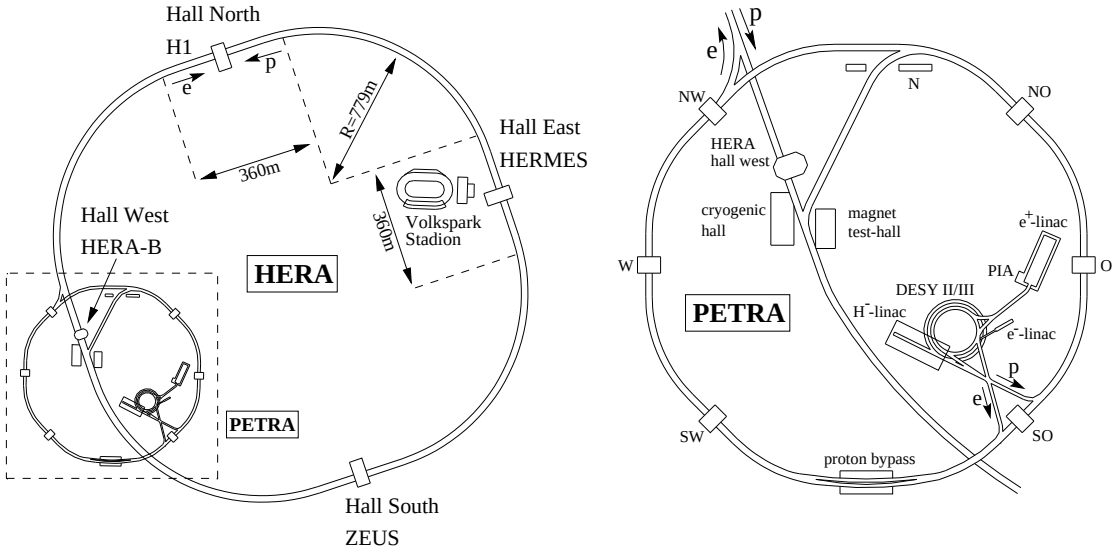

Figure 2.1: *The HERA storage ring [DES00]. The HERA ring with the four experimental areas and the experiments situated at them is shown on the left side. On the right side a magnified view of the DESY accelerator complex (dashed box in the left picture) is shown.*

2.2 Physics goals

In 1992 HERA – B was proposed as an experiment to study *CP* violation in the B meson system [Alb92]. Protons in the halo of the HERA beam should interact with an internal wire target to produce B mesons. At a center-of-mass energy of 41.6 GeV, well above the $b\overline{b}$ threshold of about 10.5 GeV, and assuming a $b\overline{b}$ production cross section of 12 nb per nucleon and an interaction rate of 40 MHz, B mesons are produced at a rate of approximately 20 Hz. Therefore, the whole field of B physics, provided with a rich phenomenology, is accessible to HERA – B. However, B physics at hadron machines implies a lot of experimental and technological challenges, as will be described in Section 2.3.

These challenges turned out to be so difficult to meet, that the HERA – B detector and trigger system do not yet work at their design performance. Thus, the physics topics that will be tackled by HERA – B in the future have to be divided into the final physics goals in the field of B physics and realistic goals for the immediate future. A detailed discussion of both topics can be found in [HB00a]. Here some of the most important topics will be briefly described.

2.2.1 B physics and *CP* violation

The original goal of HERA – B was a major contribution to the field of B physics. It seems unlikely that this goal will be reached in the near future. However, it is possible that HERA – B will tackle B physics topics in the coming years. Since the HERA – B detector and trigger have been designed for B physics, some aspects of this field will be sketched in the following.

CP violation in $B^0/\overline{B^0} \to J/\psi\, K^0_S$ decays

In the Standard Model, the only source of *CP* violation is the mixing of the quarks in electroweak interactions. Overviews of this mechanism can be found e.g. in [Nac86] or [Man00]. The quark mixing is commonly described by the Cabibbo-Kobayashi-Maskawa (CKM) matrix [Cab63, Kob73]. The states of the "down-type" quarks d′, s′, b′ that take part in the electroweak interaction are a mixture of the mass eigenstates d, s, b:

$$\begin{pmatrix} d' \\ s' \\ b' \end{pmatrix} = \mathbf{V}_{\mathrm{CKM}} \begin{pmatrix} d \\ s \\ b \end{pmatrix} \qquad \text{with } \mathbf{V}_{\mathrm{CKM}} = \begin{pmatrix} V_{ud} & V_{us} & V_{ub} \\ V_{cd} & V_{cs} & V_{cb} \\ V_{td} & V_{ts} & V_{tb} \end{pmatrix}. \tag{2.1}$$

The transition probability from quark i to quark j is proportional to the square modulus of the matrix element V_{ij}. The CKM matrix contains three real parameters and one complex phase, which is the condition precedent to *CP* violation. The matrix elements V_{ij} can be expanded in the parameter $V_{us} \equiv \lambda \equiv \sin\theta_C \approx 0.22$, the Cabibbo angle [Wol83]. The other three parameters are fixed by choosing $V_{cb} \equiv \lambda^2 A$ and $V_{ub} \equiv \lambda^3 A(\varrho - i\eta)$. Up to $\mathcal{O}(\lambda^4)$ this expansion yields:

$$\mathbf{V}_{\mathrm{CKM}} = \begin{pmatrix} 1-\lambda^2/2 & \lambda & \lambda^3 A(\varrho - i\eta) \\ -\lambda & 1-\lambda^2/2 & \lambda^2 A \\ \lambda^3 A(1-\varrho-i\eta) & -\lambda^2 A & 1 \end{pmatrix}. \tag{2.2}$$

The advantage of this representation of the CKM matrix is that the expansion in the small parameter λ^2 reveals the relative strengths of the couplings between the quarks. Since $\mathbf{V}_{\mathrm{CKM}}$ is unitary, several relations between the matrix elements can be derived, the most important for *CP* violation in the B meson system being the product of the first column with the complex conjugate of the third column:

$$V_{ud}V_{ub}^* + V_{cd}V_{cb}^* + V_{td}V_{tb}^* = 0. \tag{2.3}$$

Neglecting terms of $\mathcal{O}(\lambda^5)$, the insertion of Equation (2.2) into (2.3) yields:

$$\lambda^3 A\left[(\varrho + i\eta) - 1 + (1 - \varrho - i\eta)\right] = 0. \tag{2.4}$$

Relations of this type can be visualized as triangles in the complex plane, the so-called unitarity triangles. The triangle that corresponds to Equation (2.4) can be found in Fig. 2.2. The area of all unitarity triangles has the same size, and it is a measure of the amount of *CP* violation [Jar88]. However, most of the triangles are far from equilateral. The triangle formed by the relation (2.3) is chosen because all contributions are of the same order of magnitude $\mathcal{O}(\lambda^3)$.

The preferred channel for studying *CP* violation in the B meson system is the "gold-plated" decay $B^0/\overline{B^0} \to J/\psi\, K^0_S$. Here a B^0 meson and its antiparticle, the $\overline{B^0}$ meson, decay into the same *CP* eigenstate. From a measurement of the asymmetry A_{CP} of the decay rates Γ

$$A_{CP}(t) \equiv \frac{\Gamma(B^0(t) \to J/\psi\, K^0_S) - \Gamma(\overline{B^0}(t) \to J/\psi\, K^0_S)}{\Gamma(B^0(t) \to J/\psi\, K^0_S) + \Gamma(\overline{B^0}(t) \to J/\psi\, K^0_S)} \sim \sin(2\beta)\, \sin(\Delta m_d t) \tag{2.5}$$

the angle β of the unitarity triangle can be extracted [Bur97]. The name "gold-plated decay" stems from the fact that the angle β of the unitarity triangle can be extracted from a measurement of the *CP* asymmetry in this decay without hadronic uncertainties. Δm_d is the mass difference between the B^0_d and the $\overline{B^0_d}$ mesons and has the meaning of an oscillation frequency in $B^0_d - \overline{B^0_d}$ mixing. The mixing of the B^0_d and the $\overline{B^0_d}$ mesons has been discovered by the ARGUS experiment in 1987 [Alb87].

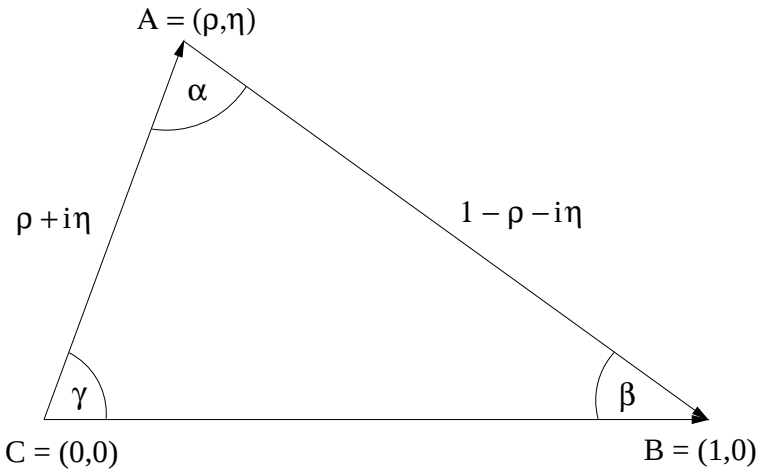

Figure 2.2: *The unitarity triangle. Equation 2.3 is commonly rescaled by* $V_{cd}V_{cb}^{*} = -\lambda^3 A$ *(after [Bur97]).*

The B_s^0 system

The B_s^0 system is not accessible to the B factories at e^+e^-colliders that are running on the $\Upsilon(4S)$ resonance because the available center-of-mass energy in these experiments is not sufficient to produce B_s^0 mesons. The B_s^0 system encompasses a wide variety of physics topics, which supplement measurements in the B_d^0 system or are sensitive to processes that are not accessible in the B_d^0 system. For recent overviews see [Har98, Bal00b, HB00a].

The decay $B_s^0 / \overline{B_s^0} \to J/\psi\,\Phi$, the process corresponding to the gold-plated decay in the B_s^0 sector, is also a candidate for measuring *CP* violation. From a measurement of these decays, the parameter η, i.e. the height of the unitarity triangle, can be extracted [Bur97].

Contrary to the B_d^0 sector, mixing in the B_s^0 sector has not yet been measured. Besides being an important discovery in itself this process would provide a measurement of the length of the side $\overline{AB}$ of the unitarity triangle [Bur97]. However, the mixing parameter $x_s \equiv \Delta m_s/\Gamma_s$ in the B_s^0 sector, Γ_s being the mean decay rate of the B_s^0 and the $\overline{B_s^0}$ mesons, is expected to be large in the Standard Model. While the value for B_d^0 mixing is measured as $x_d = 0.730 \pm 0.029$ [Gro00], the Standard Model expectation for x_s is $\mathcal{O}(20)$. In order to resolve these rapid oscillations, excellent tracking and vertex resolution are needed.

Rare decays

Rare B decays include decays containing two types of transitions on the quark level: $b \to u$ transitions which are Cabibbo-suppressed and $b \to d$, s transitions which are flavor changing neutral currents (FCNC) and thus forbidden at tree level in the Standard Model. Rare B decays are an important testing ground of the Standard Model because they allow probing of the detailed structure of the Standard Model beyond tree level. Furthermore, they offer an important strategy in the search for new physics since they probe the indirect effects of new particles and interactions at mass scales not reachable for existing accelerators in higher-order processes [Har98].

Experimentally, these decays are extremely difficult to detect, since they suffer from large backgrounds. Background rejection demands a highly efficient trigger sys-

tem and sophisticated tracking and vertexing. Several studies of rare decays can be found in [HB00a]. See [Kla00] for a recent Monte Carlo study of the rare FCNC decay $B^0 \to K^{*0}\,\mu^+\mu^-$ in HERA–B.

2.2.2 QCD and heavy flavor physics

Problems related to the very advanced technology of the HERA–B detector and trigger have led to delays in the time schedule of the HERA–B experiment. Hence HERA–B's short-term physics goals, i.e. plans for data-taking in the years 2001 and 2002, concentrate on topics that are already accessible with merely some improvements of the detector and trigger as used in the 2000 run. Nevertheless, these topics bear interesting physics. This section can only give a brief overview; details are discussed in [HB00b, HB00a].

$b\overline{b}$ production cross section

Heavy flavor production has been studied extensively in fixed-target experiments [Kap94, Ale97]. The results are in qualitative agreement with predictions from perturbative QCD at next-to-leading order, so that heavy flavor production can be seen as a predominantly hard scattering process. However, both theoretical and experimental errors are large, and several deviations from perturbative QCD have been observed, so that an influence of non-perturbative phenomena is expected.

In HERA–B the $b\overline{b}$ production cross section can be measured in inclusive B decays, such as $b\overline{b} \to J/\psi\, X \to \ell^+\ell^- X$ or $b\overline{b} \to \ell^+\ell^- X$. Due to the good vertex resolution of the HERA–B detector, the channel $b\overline{b} \to \ell^+\ell^- D X$ is also accessible.

Charmonium physics

In the field of heavy quarkonium production, the production and decay angular distribution and the A dependence are of particular interest. Here A is the atomic number of the target nucleus.

There are currently two models for the production mechanism of heavy quarkonia $q\overline{q}$ (q = c, b): In the color singlet model, the $q\overline{q}$ pair forms a color singlet directly, and in the color octet model, the $q\overline{q}$ pair can neutralize its color via the emission of soft gluons before the quarkonium state is formed. Measurements of the production cross section and the angular distribution of the decay products are essential in that they can test these models or future theories of quarkonium production.

The production cross section of J/ψ mesons is sensitive to nuclear effects. A suppression of the production of J/ψ mesons has been observed in Pb-Pb collisions in the NA50 experiment [Abr99]. The suppression that results from nuclear effects has to be distinguished from the suppression by the formation of a quark-gluon plasma. HERA–B's ability to reconstruct most of the particles in an event allows a direct comparison with the measurements of NA50 and other fixed-target experiments and can help to understand the suppression mechanism.

Drell-Yan physics

The prospects for Drell-Yan physics in HERA–B form one of the main topics of this thesis and are discussed in detail in Chapter 6.

Open charm production

Charmed mesons are produced abundantly in HERA – B and can be triggered, e.g. with a single muon trigger as demonstrated in the 2000 run. Several interesting questions arise in the field of charm physics:

$D^0 - \overline{D^0}$ mixing is expected to be small in the Standard Model, and the observation of a lifetime difference between the D^0 and the $\overline{D^0}$ meson would be a clear sign for new physics. Recent results for lifetime differences in the neutral D meson system from CLEO and FOCUS do not agree very well [Ber00]. Due to an improved proper time resolution as compared to FOCUS, HERA – B is in the position to contribute to this field.

The rare decay $D^0 \to \mu^+\mu^-$ has a negligibly small Standard Model branching fraction of $\mathcal{O}(10^{-19})$ but a very clean experimental signature. Therefore it is a good candidate for the search for new physics.

Direct photon production

The dominant contribution to hard quark-gluon scattering at high p_T values comes from the QCD Compton subprocess $qg \to q\gamma$. This fact allows the extraction of the gluon structure function of the nucleon from a measurement of high-p_T photons with transverse momenta of $p_T > 3 - 4\,\mathrm{GeV}/c$. The main physics background for this decay is formed by high-p_T photons from π^0 and η decays, which are expected to be strongly suppressed for transverse momenta in the regime mentioned above [Zoc01].

2.3 The HERA – B detector

The HERA – B detector is designed as a fixed-target forward spectrometer. A schematic view of the detector can be found in Fig. 2.3. The following coordinates will be used throughout this thesis: The direction of the proton beam defines the z direction. The vertical axis is called the y axis, and the horizontal axis perpendicular to the beam is the x axis.

The detector has an aperture of 10–220 mrad in the laboratory frame, corresponding to the coverage of the central rapidity region $-1.5 < y < 1.5$ in the proton-nucleon center-of-mass frame, This large acceptance is needed to cover the high transverse momenta found in B physics, and is also very advantageous for other analyses.

2.3.1 The subdetectors

In HERA – B particles are produced via interactions of protons with a wire target. The subdetectors can be divided into tracking and particle identification devices. Primary and secondary vertices can be found with the vertex detector system (VDS). The main tracker, consisting of an inner part (Inner Tracker, ITR) and an outer part (Outer Tracker, OTR), serves to follow tracks through a spectrometer magnet and to determine the track parameters. The high-p_T chambers – left out in Fig. 2.3 – are used in the trigger. The ring-imaging Čerenkov hodoscope (RICH) is used for particle identification. In the electromagnetic calorimeter (ECAL), the energy of electrons and photons is measured. The transition radiation detector (TRD) supplements the electron/hadron separation of the ECAL in the region close to the HERA proton beam pipe. Using the muon detector, muon candidates can be identified and their track parameters can be estimated. In the following, the subdetectors of the HERA – B experiment will be explained in greater detail.

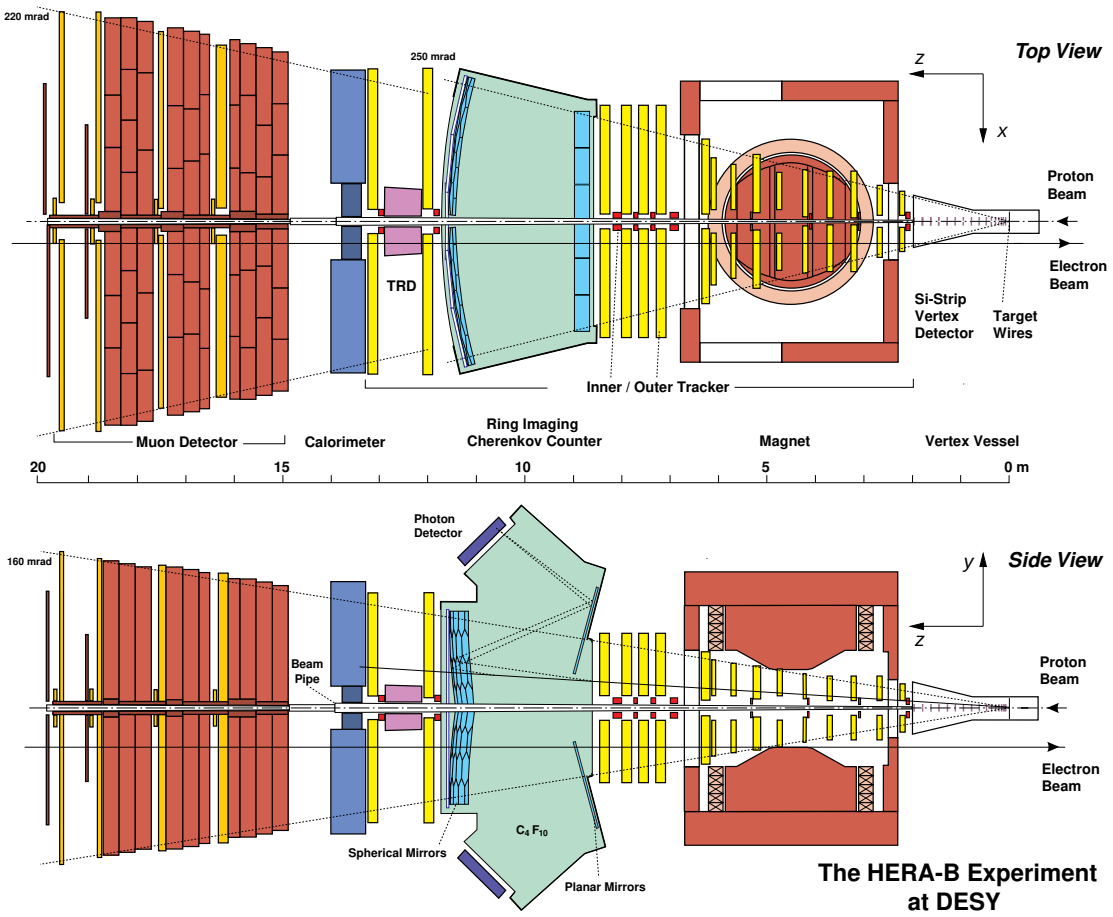

Figure 2.3: *Schematic views of the HERA – B detector [Pyr98]: top view (above) and side view (below). The individual subdetectors are explained in the text.*

Target

The HERA – B target is a multi-wire fixed target designed to produce the required large number of B mesons in proton-nucleon interactions [Has95]. It consists of two stations – Station I and Station II – containing four wires each. The wires are arranged around the HERA proton beam. Each wire can be moved independently transversal to the proton beam to adjust the number of interactions per bunch-crossing that take place on the wire [Spr00]. While Station I consists of four titanium wires, Station II also contains aluminum, carbon, and tungsten wires. This wide spread of materials allows the study of nuclear dependences, for example in quarkonium production.

Vertex detector

The vertex detector system, situated between the target and the magnet, consists of 64 double-sided silicon micro-strip detector modules with a pitch of about 50 μm, arranged in eight superlayers [Bau00]. The VDS modules are mounted in so-called roman pots in a vacuum vessel. They can be moved as close as 10 mm from the proton beam. This results in an acceptance region that corresponds to polar angles of 10–250 mrad.

The VDS provides fine-granularity tracking information close to the point of the primary interaction, which is used in the higher trigger levels and in offline analyses. To be

able to separate secondary vertices, e.g. of B meson decays, from primary vertices on the target wires, the VDS provides a secondary vertex resolution of $\mathcal{O}(70\,\mu\text{m})$ perpendicular to the beam and of $\mathcal{O}(700\,\mu\text{m})$ in beam direction [HB00a].

Magnet

The HERA – B magnet is a dipole magnet with a field integral of up to 2.2 Tm perpendicular to the HERA proton beam. Charged particles are deflected in the xy plane by the magnetic field. This allows a momentum determination of the particles in the tracking detectors.

Inner Tracker

The Inner Tracker system covers the inner, high-occupancy part of the detector, 6–30 cm away from the proton beam pipe, corresponding to a polar angle of 10–100 mrad. It is constructed as 10 superlayers of four micro-strip gaseous chamber detectors with gas electron multiplier foils (MSGC-GEM) each. In an MSGC-GEM, a two-step amplification of the primary ionization deposited by a charged particle is performed [Zeu00]. The GEM foils had to be introduced as a second amplification step because the gas amplification in one step causes sparks and short circuits between the mirco-strips and destroys the ITR modules. This fact may serve as an example of the technological challenges HERA – B had to face.

The micro-strips, having a pitch of 300 μm, are arranged as three stereo layers (0°, ±5°). This results in a spatial resolution of better than 100 μm in the x direction and of 1 mm in y. The superlayers are positioned in and after the magnet and are used in the offline analysis as well as partially in the trigger.

Outer Tracker

The tracking in the outer acceptance region of the HERA – B detector, up to 250 mrad, is performed by the Outer Tracker [Ste00]. The OTR consists of 13 superlayers of honeycomb drift chambers, seven layers in the magnet, four layers in the region between the magnet and the RICH, and two layers between the RICH and the ECAL. As in the ITR, each superlayer is composed of three stereo layers with orientations of 0° and ±5° with respect to the y axis.

The honeycomb cells have diameters of 5 mm in the inner and 10 mm in the outer region of the OTR. Apart from the hit information used in the FLT, the OTR also provides the drift time, i.e. the time needed by the avalanche of ionization electrons in the chamber to reach the anode wires. Including the drift time information the measured hit resolution was about 350 μm perpendicular to the wire in the 5 mm cells [HB00a]. In the superlayers used for the first trigger level, each stereo layer is built as a double layer to provide a good hit efficiency for the trigger.

High-p_{T} chambers

The high-p_{T} chambers are designed as gas pixel cells in the inner part and as straw tube chambers with cathode pad readout in the outer part [Bal00a]. They are situated in the HERA – B magnet. The high-p_{T} chambers are only used in the trigger.

The inner part covers the acceptance region of 10–58 mrad in the x and of 10–44 mrad in the y direction. The outer chambers cover the ranges of 38–250 mrad in x

and of 44–133 mrad in y. The trigger resolution is determined by the cell and cathode pad sizes. The cells in the inner part have a size of $4 \times 8\,\mathrm{mm}^2$, $6 \times 8\,\mathrm{mm}^2$, and $8 \times 8\,\mathrm{mm}^2$. The size of the cathode pads varies from $15 \times 15\,\mathrm{mm}^2$ to $30 \times 120\,\mathrm{mm}^2$.

Ring-imaging Čerenkov hodoscope

In the ring-imaging Čerenkov hodoscope, the Čerenkov effect is used for particle identification. A proper identification of the most abundant particles in an event is needed for many studies in the field of B physics.

In the RICH the Čerenkov photons form rings, which are projected via a system of mirrors to a plane of photomultiplier tubes that detect the photons. In HERA – B the radiator medium is perfluorobutane gas (C_4F_{10}), leading to a Čerenkov angle of 51.5 mrad for particles with the velocity $\beta \equiv v/c = 1$. Due to their different masses, particles of different types with the same momentum produce rings with different opening angles. This effect can be used for particle identification, mainly for the separation of pions from kaons in the momentum range from approximately $12\,\mathrm{GeV}/c$ to $50\,\mathrm{GeV}/c$.

Furthermore, the slope of particle trajectories in the RICH can be determined by the shape of the associated photon rings. These information supports the tracking in the genuine tracking devices. The single photon resolution of the HERA – B RICH has been measured to be 0.7–1.0 mrad [Ari00].

Electromagnetic calorimeter

The electromagnetic calorimeter provides energy and position measurements of electrons and photons. Fast information on pairs of electrons and positrons and on high-p_T photons is of interest for diverse physics channels, e.g. for decays of J/ψ mesons into an electron and a positron. In addition, the ECAL serves as a particle identification device, since it provides good hadron/electron separation. Information from the ECAL is also used as one of the starting-points for the HERA – B trigger.

The ECAL is designed as a sampling calorimeter, consisting of alternating layers of scintillator and converter materials. It is divided into an inner, a middle and an outer part with different granularities and detector materials. In the inner part (about 23 radiation lengths containment) a W-Ni-Fe metal alloy with a Molière radius[2] of 1.3 cm serves as the converter. The middle and outer parts (approximately 21 radiation lengths containment) are filled with a Pb converter (Molière radius 3.5 cm) [Zoc00].

Transition radiation detector

In HERA – B the transition radiation detector, in addition to the inner part of the ECAL, where occupancies are high, has to provide good electron identification and hadron rejection. Due to its multilayer structure the TRD is also a good pattern recognition and tracking device. While in the RICH particles of different velocities β can be separated, the TRD uses the energy-mass relation $\gamma \equiv 1/\sqrt{1-\beta^2} = E/mc^2$ to identify particles.

The TRD consists of two superlayers with straw tube detector planes tilted by $\pm 30^\circ$ relative to the x axis. Each superlayer contains 16 planes of alternate straw tubes and radiator material. The straw tubes have a diameter of 6 mm, and the radiator consists of polypropylene fibres with a diameter of $20\,\mu$m [Sav98]. The acceptance of the TRD covers a range of 18–100 mrad.

[2] The Molière radius R_M is an approximate measure of the lateral spread of the energy deposition of an electromagnetic cascade. About 90% of the energy is deposited in a cylinder with the radius R_M.

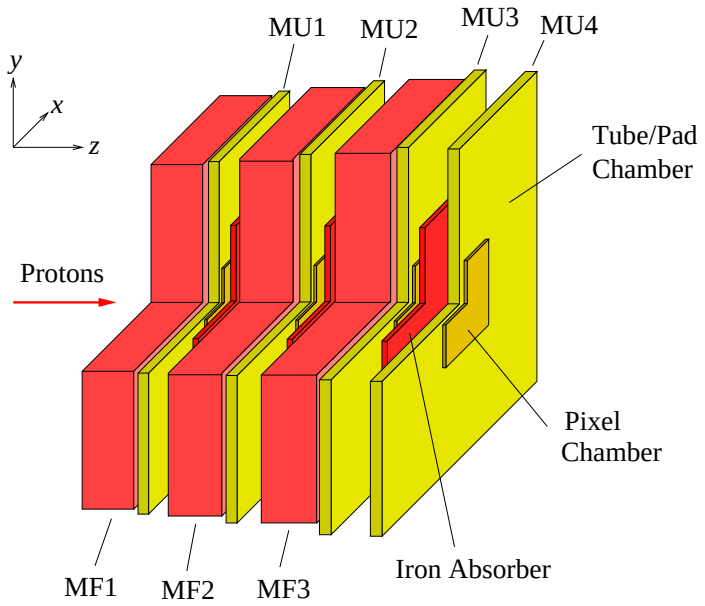

Figure 2.4: *Sketch of the HERA – B muon detector. Shown are the four detector layers MU1–MU4, each consisting of an inner part with gas pixel chambers and an outer part with drift chambers, and the three absorber layers MF1–MF3. The upper right quadrant of the detector in beam direction is omitted for the sake of a better view of the inner part of the detector.*

Muon detector

The muon detector is the part of the detector which is furthermost from the target. The energy loss of muons in matter is very small, so that muons penetrate even through thick absorber walls while most of the hadrons are absorbed. Therefore the muon detector provides identification of muons in a relatively clean environment.

The muon detector consists of four superlayers (MU1–MU4), each divided into an inner and an outer part. Before MU1 and between MU1 and MU2 as well as MU2 and MU3 a muon filter of iron and armored concrete is placed (MF1–MF3). Between MU3 and MU4 there is only very little absorber material. Therefore the effects of absorption and multiple scattering are small, and coincidences of hits in these superlayers can be used by the muon pretrigger. A sketch of the HERA – B muon detector is shown in Fig. 2.4.

The outer part covers a polar angle up to 220 mrad in the x direction and 160 mrad in the y direction. In MU1 and MU2, the outer part consists of three stereo layers ($0°$, $\pm 20°$) of proportional wire chambers with a drift cell profile of $14 \times 12\,\mathrm{mm}^2$. The outer parts of the superlayers MU3 and MU4 are built of a single drift chamber layer ($0°$) with cathode pad readout. These pads, having a size of approximately $12 \times 10\,\mathrm{cm}^2$, are used in the muon pretrigger.

The inner part of all four superlayers covers the high-occupancy region from 9 mrad around the proton beam pipe and has a size of $80 \times 60\,\mathrm{cm}^2$, overlapping with the outer part. It is formed by gas pixel chambers with a cell size of $9 \times 9\,\mathrm{mm}^2$ in MU1–MU3 and $9.4 \times 9.4\,\mathrm{mm}^2$ in MU4 [Tit00].

2.3.2 The trigger system

With current technology it is impossible to record every single event in the HERA – B detector. More than 600,000 detector channels would have to be read out every bunch-crossing, resulting in a data rate of about 5 TBit/s. Therefore, to extract the small fraction of events of interest out of the vast amount of background events, a fast, highly selective and efficient trigger system is needed.

In HERA – B the trigger is implemented as a flexible multi-level system. The complete detector information of 128 bunch-crossings is stored in a pipeline, so that a first trigger decision has to come within approximately 12 μs. Three pretrigger systems, implemented as custom-built complex electronic devices, provide fast decisions based on a small fraction of the subdetector information. In a message-driven system, search regions for the First Level Trigger (FLT), "Regions of Interest" (RoIs), are defined. The FLT, a network of likewise custom-built electronic devices, performs a track search starting from the RoIs passed by the pretriggers and using information from additional parts of the detector. Pretriggers and the FLT are designed to reduce the event rate by a factor of 200.

Accepted events are read from the pipeline and passed to the Second and Third Level Triggers (SLT, TLT). The input rate of the SLT is limited to about 50 kHz. These trigger levels are implemented in software, i.e. calculations are performed on a farm of standard PCs. With extra information from the VDS, tracking through the magnet and a vertex fit become possible. For certain classes of events, the TLT is used to refine the trigger decision of the SLT. Reduced to a rate of approximately 50 Hz, the data is fed into the Fourth Level Trigger (4LT). The 4LT, also a pure software trigger implemented as a PC farm, uses the information of all readout channels to perform a complete online event reconstruction. Data from events that pass all these steps are archived. In the following some important details of the four trigger levels are presented.

The pretriggers

In HERA – B three pretriggers provide fast information on track candidates as seeds for the FLT.

- The ECAL pretrigger performs a search for 3×3 matrices of cells in the ECAL having a local maximum of energy deposited [Loh94]. In addition, programmable threshold conditions are checked, i.e. the energy sum in the matrix and the energy in the middle cell, both with a position-dependent energy threshold. Furthermore, a recovery of the energy loss due to bremsstrahlung can be performed. This information is translated into messages containing an RoI for the FLT.

  The algorithm described above can be used for two kinds of triggers: a lepton pair trigger for electron/positron pairs, e.g. from J/ψ decays, and a trigger for single high-p_{T} photons or electrons.

- The high-p_{T} pretrigger searches for coincidences of hits in projective segments of three high-p_{T} chamber superlayers. A coincidence logic estimates the track parameters from the arrangement of hits in the three layers. Such a trigger is sensitive to high-p_{T} particles, which are produced for example in hadronic B decays like $\mathrm{B}^0 \to \pi^+\pi^-$.

- The muon pretrigger searches for coincidences of hits in projective segments of MU3 and MU4. The functional principle of the muon pretrigger is depicted in

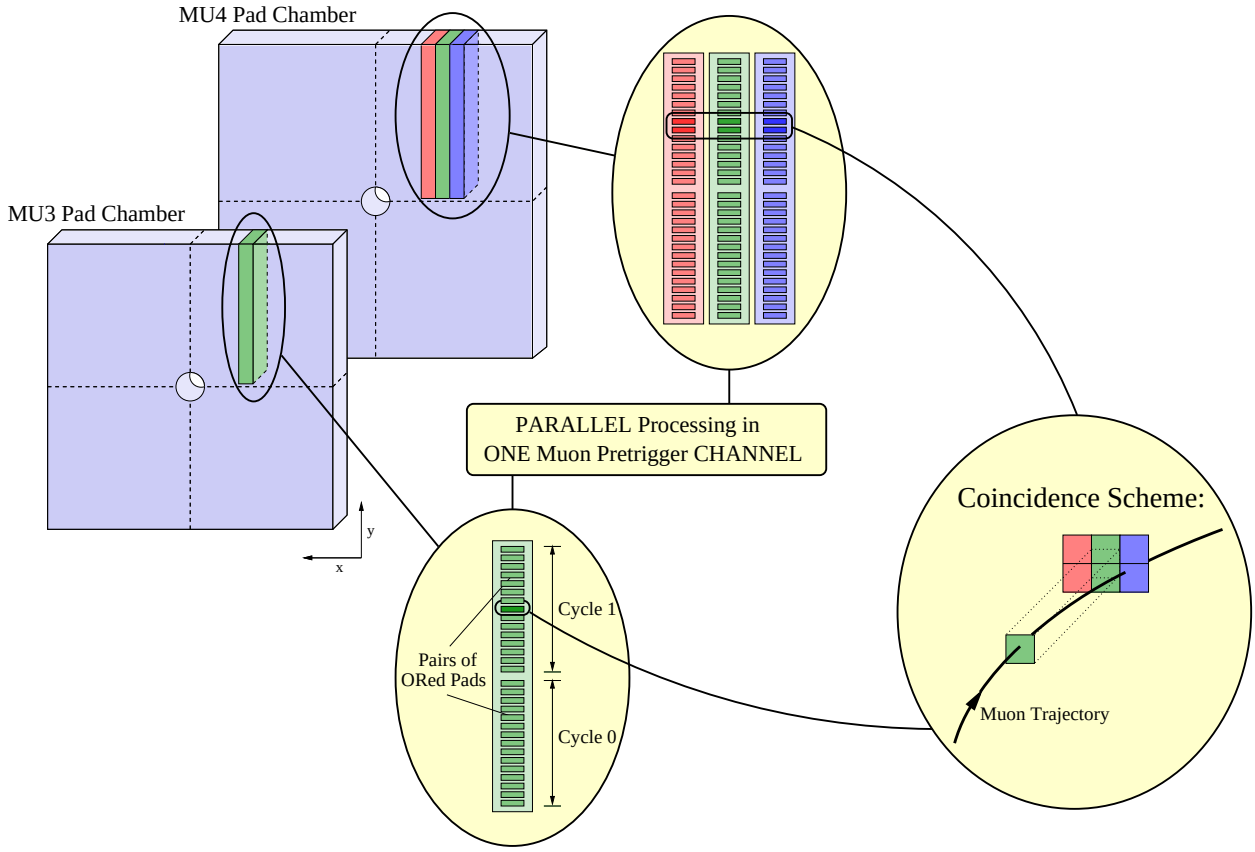

Figure 2.5: *Functional principle of the muon pretrigger system. One column of pads in MU3 is processed with three columns in MU4 in parallel. A coincidence message is generated if at least one of the six pads in MU4 that are placed behind a fired MU3 pad is hit in the same bunch-crossing, indicating a candidate for a muon trajectory ("one-to-six coincidence"). In the pixel system a one-to-four coincidence is required.*

Fig. 2.5. The coincidence condition is fulfilled in the outer part, if there are simultaneous hits in one cathode pad in MU3 and in at least one out of six projective cathode pads in MU4. In the inner part an array of 6×4 pixel cells is combined to form "pseudo-pads" which are used analogous to the cathode pads in the outer part. A coincidence in the inner part is formed by one MU3 pseudo-pad in combination with four MU4 pseudo-pads.

A message containing a first estimate of the track parameters for a track candidate is generated. Since in the pretrigger and FLT chain only information from subdetectors behind the magnet is available, the determination of the track parameters is done assuming that the track originates from the target. The message is based on the coincidence position in the detector and the coincidence pattern, i.e. the hit pattern in the three MU4 columns in the outer part or in four pseudo-pads respectively. The message defines an RoI in MU4 that serves as a starting-point for FLT tracking. The muon pretrigger has been designed to serve as a starting-point for a muon pair trigger, e.g. for muons from J/ψ decays, but also a single high-p_{T} lepton trigger based on the muon pretrigger has been used in the 2000 run [HB00a].

The First Level Trigger

The FLT is built as a network of specialized hardware boards that perform tracking in various layers of the HERA – B tracking detectors. The electron part includes four superlayers of the main tracker (TC2, TC1, PC4, PC1). For muon triggering, three superlayers of the muon system (MU4, MU3, MU1) are used in addition. An overview is given in Fig. 2.6.

The principle of FLT tracking for muons shall serve as an example of the FLT operation: The FLT stores the wire information of all superlayers that are used in the trigger in a so-called wire memory. A muon track seed in a certain region is defined by the muon pretrigger. This instructs the FLT to read out the wire memory in MU4 in this region. The wire information in MU4 is used to extrapolate the track candidate to MU3. The wire information in this superlayer is added to recalculate the track parameters. With the improved information, the track is extrapolated to MU1. Wire information within the RoI in MU1 resulting from the extrapolation is added to further improve the tracking information. After that, main tracker information is added in the same way. In the end, a trigger decision based on the track parameters of one or more tracks is made. Such an iterative track fit is an application of the Kalman filter technique. An overview of the application of Kalman filters in particle physics can be found e.g. in [Boc00] and references therein.

The trigger concept of the FLT is implemented with three types of electronics boards: The Track Finding Units (TFUs) perform the tracking in the various superlayers of the muon system and main tracker. The Track Parameter Units (TPUs) calculate the track parameters for the track. The Trigger Decision Unit (TDU) can be operated in two different trigger modes: In the count trigger mode the number of accepted tracks per event determines the trigger decision, while in the pair trigger mode the decision is based on the kinematic properties of track pairs, e.g. their invariant masses.

The Second Level Trigger and Third Level Trigger

If an event is accepted by the FLT, the complete detector information is written to the Second Level Buffer (SLB), which is accessible to the SLT. The information that is used in the SLT comes from the RoIs defined by the previous trigger steps. The SLT algorithm encloses several packages [HB00a]:

- The SLICER package performs a fast removal of ghost tracks. Using information from PC1 to PC4 and from TC1 and TC2, the FLT RoI is divided into 8 slices in the x direction. The slices are combined with each other in all possible ways, and the compatibility with the hypothesis of a straight track is checked for every combination.

- REFIT-X and REFIT-Y perform a Kalman filter based track fit in the x view and in the stereo views of the main tracker respectively.

- The L2MAGNET package allows a fast traversal of track candidates through the magnetic field. It uses a parametrization of the effective field integrals as a function of the track slopes $t_x \equiv \tan\theta_x$ and $t_y \equiv \tan\theta_y$, where $\tan\theta_x = p_x/p_z$ and $\tan\theta_y = p_y/p_z$ are the slopes of the track candidates in the x and in the y direction respectively.

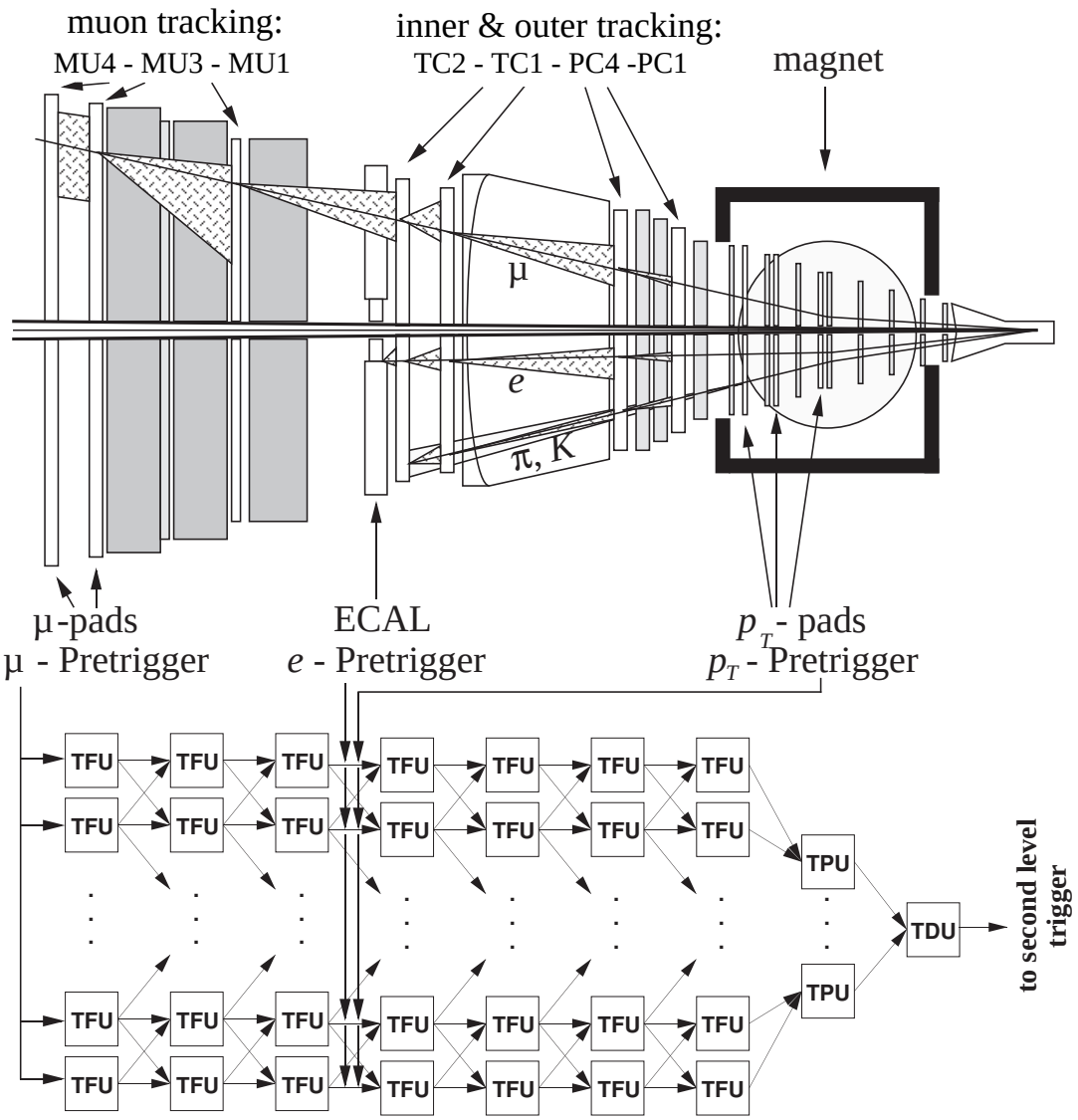

Figure 2.6: *Schematic overview of the FLT [HB00a]. The three pretrigger systems provide seeds for the FLT tracking. Three layers of Track Finding Units (TFUs) in the muon system and four layers of TFUs in the main tracker follow tracks opposite to their flight direction in restricted windows (RoIs). Finally, the Track Parameter Units (TPUs) calculate the track parameters, and the Trigger Decision Unit (TDU) decides which events are passed to the SLT.*

- The SLT is the first trigger step to utilize information from the VDS. The track candidates are followed through the VDS by the L2SILI package, which is based on Kalman filter methods.

- L2VERTEX decides via a χ^2 cut whether two trigger tracks come from a common vertex and calculates their impact parameters with respect to the target wire.

The SLT accepts events, where a track pair passes the tracking and vertexing algorithms explained above.

The Third Level Trigger – included in the same executable on the SLT/TLT PC farm – uses data from the whole detector to refine the trigger decision of the SLT [HB00a]. This is especially needed for event classes without a common vertex formed by two trigger particles, for example for semileptonic B decays.

The Fourth Level Trigger

Events that pass the SLT and the TLT undergo full reconstruction in the Fourth Level Trigger. The software package ARTE used for triggering is the same that is used for offline analyses [Alb95b]. The 4LT selects events by classifying them after the full online reconstruction. Accepted events are written to tape at a data rate of up to 10 MByte/s [Gel00].

2.3.3 The data acquisition system

The data acquisition (DAQ) system is closely connected to the triggers. The exchange of data between the trigger levels and the synchronization of the triggers in the individual subdetectors is provided by the DAQ. It consists of four parts:

- The Fast Control System (FCS) serves as an interface between the front-end electronics of the detector and the DAQ. The FCS distributes the bunch crossing number (BX) to the detector front-end to synchronize the front-end pipelines that buffer the detector information during the trigger decision.

- The buffering of data for the SLT in the SLB and the data switching to the SLT nodes is done by a cluster of 1200 digital signal processors (DSPs)[3].

- The SLT farm consists of of 240 PCs with the Linux operating system[4] with PCI interfaces to the DSPs.

- The 4LT farm consists of single and dual processor Linux PCs, adding up to 200 CPUs. A switched fast ethernet network provides the data transfer between the SLT and 4LT nodes and between the 4LT nodes and the tape archiver.

[3] In HERA – B ADSP-21060 SHARC DSPs are used. SHARC (Super Harvard Architecture) is a registered trademark of Analog Devices Inc.

[4] The SLT farm is built of Intel Pentium II based PCs. Pentium is a registered trademark of Intel Corp. Linux is a registered trademark of Linus Torvalds.

Chapter 3

The Drell-Yan process

The main intention of this thesis is to evaluate prospects of HERA – B in the field of Drell-Yan physics. Therefore, this chapter contains a review of the main theoretical issues concerning the Drell-Yan process. Starting from the quark-parton model, QCD corrections are introduced. The second part of the chapter focuses on the question of angular distributions and the Lam-Tung relation in the Drell-Yan process. Results from fixed-target experiments prior to HERA – B, that show a violation of the Lam-Tung relation, are compared with theoretical predictions.

3.1 Basic theory

3.1.1 Naïve quark-parton model

The parton model [Fey69] is very successful in explaining the phenomenology of deep-inelastic electron-nucleon scattering (DIS). It assumes that a nucleon consists of constituents called "partons", later identified as the quarks [Bjo69b]. The parton model is based on the kinematic assumption that the impulse approximation holds for the interaction between electrons and partons, i.e. the assumption that the interaction time between the electron and the parton is small compared to the typical time scale of binding effects of the partons in the nucleon. In this case the electron can probe each parton independently. An introduction to the quark-parton model and to DIS can be found in many text books, e.g. in [Hal84, Ell96].

Drell and Yan were the first to apply this concept to the annihilation of a parton-antiparton pair in hadron-hadron collisions [Dre70], and the Drell-Yan cross section was the first hadron-hadron cross section that could be derived from first principles. In the language of Feynman diagrams, the process can be considered as the annihilation of a quark-antiquark pair into a virtual photon with a subsequent decay into a lepton pair[1], as depicted in Fig. 3.1. In proton-nucleon scattering, the quark carries a fraction x_1 of the proton's longitudinal momentum, and a fraction x_2 of the nucleon's longitudinal momentum is carried by the antiquark. The virtuality of the exchanged photon, or equivalently the invariant mass squared M^2 of the lepton pair, is then given by

$$M^2 = x_1 x_2 s, \tag{3.1}$$

$\sqrt{s}$ being the center-of-mass energy of the proton-nucleon collision. The impulse approximation remains valid in the kinematic region of large s and M^2 but finite $\tau \equiv M^2/s$.

[1] The expressions "Drell-Yan process" and "lepton pair production process" are used synonymously in the following.

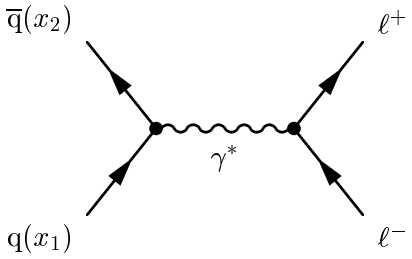

Figure 3.1: *Feynman diagram of the lowest order Drell-Yan process: annihilation of a quark-antiquark pair* ($\mathrm{q}(x_1)$, $\bar{\mathrm{q}}(x_2)$) *into a virtual photon* (γ^*) *and subsequent decay into a lepton pair* ($\ell^+\ell^-$).

The general structure of the cross section formula for the collision of a beam A with a target B can be expressed as a convolution of the cross section for the partonic subprocess $\hat{\sigma}(\mathrm{q}\overline{\mathrm{q}} \to \ell^+\ell^-)$ with the parton distribution functions $f_{\mathrm{q}}(x)$, i.e. the probabilities of finding a quark q with a momentum fraction x in the proton [Ell96]:

$$\sigma_{AB}(\,\ell^+\ell^-) = \sum_{\mathrm{q}} \int \mathrm{d}x_1 \mathrm{d}x_2 \, f_{\mathrm{q}}(x_1)\, f_{\overline{\mathrm{q}}}(x_2)\, \hat{\sigma}(\mathrm{q}\overline{\mathrm{q}} \to \ell^+\ell^-). \tag{3.2}$$

The decomposition into subprocess cross section and parton distribution functions in the quark-parton model is called "factorization". For a review see e.g. [Col89]. In the parton model, the cross section for the subprocess is given by

$$\hat{\sigma}(\mathrm{q}(x_1)\,\overline{\mathrm{q}}(x_2) \to \ell^+\ell^-) = \frac{N}{N^2}\,\frac{4\pi\alpha^2}{3\,x_1 x_2 s}\,e_{\mathrm{q}}^2, \tag{3.3}$$

where e_{q} is the electric charge of quark q. N/N^2 is a color factor, $N = 3$ being the number of quark colors, which reflects that only three out of nine combinations of a color and an anticolor lead to a color singlet state. The differential cross section is then given by:

$$M^4 \frac{\mathrm{d}\sigma}{\mathrm{d}M^2} = \frac{1}{N}\,\frac{4\pi\alpha^2}{3}\,\tau\mathcal{F}(\tau), \tag{3.4}$$

$$\text{with } \mathcal{F}(\tau) = \int_0^1 \mathrm{d}x_1 \mathrm{d}x_2\, \delta(x_1 x_2 - \tau) \left[\sum_{\mathrm{q}} e_{\mathrm{q}}^2 \left\{f_{\mathrm{q}}(x_1) f_{\overline{\mathrm{q}}}(x_2) + (\mathrm{q} \leftrightarrow \overline{\mathrm{q}})\right\}\right]. \tag{3.5}$$

Thus, the cross section reveals scaling in the variable τ, i.e. it only depends on τ but not on $\sqrt{s}$ – in exact analogy with the approximate Bjorken scaling in DIS [Bjo69a].

The angular distribution of the leptons in lowest order can be obtained directly from the naïve quark-parton model. In the quark-parton model picture, two uncorrelated massless spin $\frac{1}{2}$ partons interact. With the same probability both can have positive and negative helicities resulting in the following angular dependence of the cross section:

$$\frac{\mathrm{d}\sigma}{\mathrm{d}\Omega} \sim 1 + \cos^2\theta, \tag{3.6}$$

θ denoting the angle between the parton-parton annihilation axis and the direction of the outgoing ℓ^+.

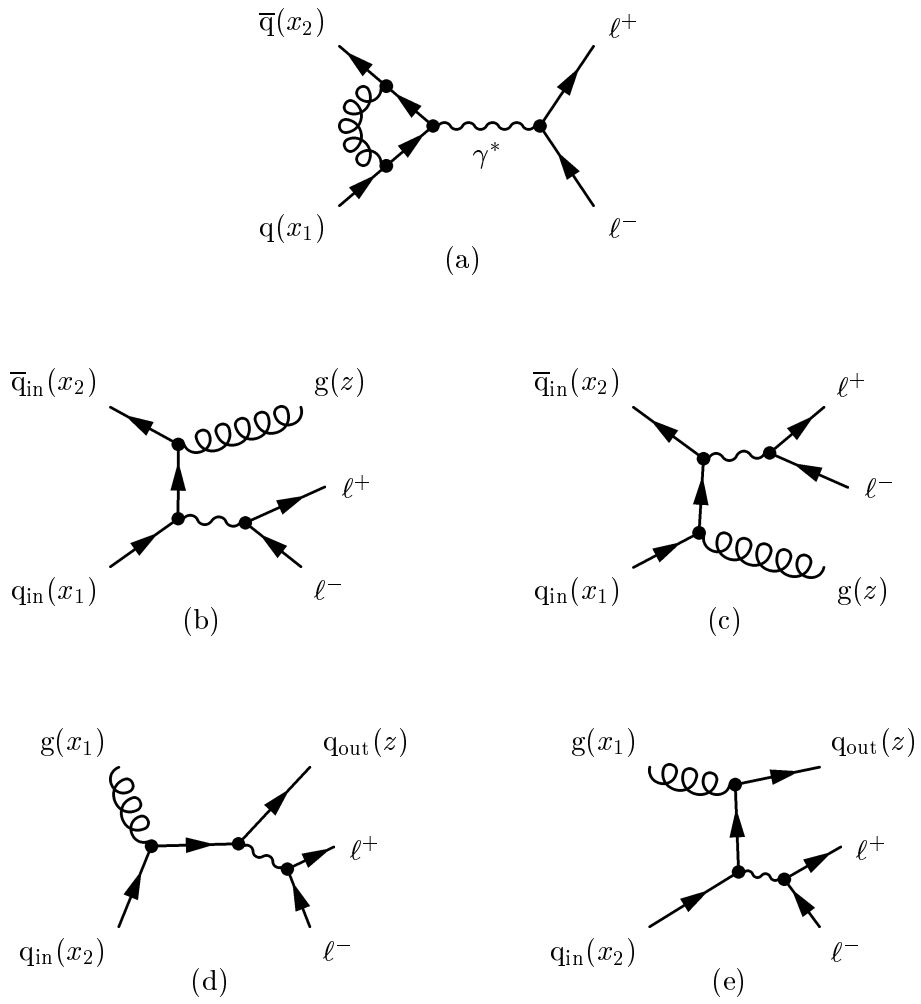

Figure 3.2: *Leading and next-to-leading order QCD corrections to the Drell-Yan process: (a) vertex correction, (b) and (c)* $\mathrm{q\overline{q}}$ *corrections, (d) and (e)* qg *corrections (QCD Compton scattering)*

3.1.2 Perturbative QCD

Perturbative QCD can be included in the cross section calculation if additional gluon exchange is allowed. The relevant Feynman diagrams for $\mathcal{O}(\alpha_s)$ corrections to the quark-parton model are shown in Fig. 3.2. The most striking result of the calculations is the fact that the quark-parton model formalism and the factorization hypothesis remain valid if QCD corrections are included. The technical reason for this is the following: The singularities that occur in these calculations turn out to be the same as in the calculation of structure functions in DIS and can thus be absorbed into the same universal "renormalized", scale-dependent parton distribution functions $f_{\mathrm{q}}(x, M^2)$. This results in the general structure for the total cross section:

$$\sigma_{AB}(\,\ell^+\ell^-) = \sum_{\mathrm{q}} \int \mathrm{d}x_1 \mathrm{d}x_2 \, f_{\mathrm{q}}(x_1, M^2)\, f_{\overline{\mathrm{q}}}(x_2, M^2) \left[\hat{\sigma}_0 + \frac{\alpha_s(M^2)}{2\pi}\,\hat{\sigma}_1 + \ldots\right]_{\mathrm{q\overline{q}} \to\, \ell^+\ell^-} . \tag{3.7}$$

The derivation of the full result to $\mathcal{O}(\alpha_s)$ in the $\overline{\text{MS}}$ renomalization scheme with the renormalization scale $\mu^2 = M^2$ can be found e.g. in [Ell96]. For calculations to $\mathcal{O}(\alpha_s^2)$ refer to [Ham91].

Note that Equation (3.7) includes a genuine $\mathcal{O}(\alpha_s)$ correction to the cross section that is referred to as the "theoretical K-factor". Experimentally, the K-factor is determined as the ratio of the measured to the tree level cross section. At fixed-target values for $\sqrt{s} \approx 10$–$40\,\text{GeV}$ and $M > 4\,\text{GeV}/c^2$ the theoretical K-factor is large and positive, of the order of 50% or more [Ell96]. It turns out that the real and virtual corrections to the $\text{q}\overline{\text{q}}$ process, as shown in Fig. 3.2 (a)-(c), contribute most to the K-factor, while considering in addition the qg process, depicted in Fig. 3.2 (d) and (e), reduces the correction by a small amount [Alt78].

3.1.3 Angular distributions and the Lam-Tung relation

Due to the large corrections from perturbative QCD, the integrated Drell-Yan cross section alone is not a very stable testing ground for the parton model. Therefore, Lam and Tung suggested studying the angular distributions of the outgoing leptons in addition [Lam78, Lam80]. From a measurement of the angular distributions, certain aspects of the structure of the hadrons that take part in the interaction can be derived.

This structure is described by the so-called hadronic tensor $W^{\mu\nu}$, in DIS as well as in lepton pair production processes. $W^{\mu\nu}$ can be decomposed into a sum of tensor components with the coefficients W_1 and W_2, the so-called structure functions:

$$W^{\mu\nu} = W_1 \left(-g^{\mu\nu} + \frac{q^\mu q^\nu}{q^2} \right) + \frac{W_2}{{M_\text{p}}^2} \left(p^\mu - \frac{p \cdot q}{q^2}\, q^\mu \right) \left(p^\nu - \frac{p \cdot q}{q^2}\, q^\nu \right). \tag{3.8}$$

Here M_p denotes the mass and p^μ the momentum four-vector of the proton, and q^μ is the four-momentum of the virtual photon. This decomposition has the advantage of a clear separation of the kinematics and dynamics of the hadronic process. The structure functions W_1 and W_2 only contain the dynamics of the process, but they do not separate leptonic and hadronic degrees of freedom [Lam78]. An alternative description uses "helicity structure functions", which have a direct interpretation in terms of longitudinal and transverse polarization of the virtual photon. However, in general this description is not Lorentz-invariant.

Both sets of structure functions obey certain relations derived from the parton model. An important relation that results from the parton model is the Callan-Gross relation [Cal69], which is a consequence of the quarks having spin $\frac{1}{2}$. The Callan-Gross relation states that the longitudinal structure function W_L, i.e. the contribution of longitudinally polarized virtual photons to the cross section, vanishes:

$$W_\text{L} = \left(\frac{\nu^2}{q^2} - 1 \right) W_2 - W_1 = 0, \qquad \text{with } \nu \equiv \frac{p \cdot q}{M_\text{p}}. \tag{3.9}$$

This equation can also be stated as [Lam80]

$$W^\mu_\mu = 2W_1, \tag{3.10}$$

where W^μ_μ is the trace of the hadronic tensor, which is proportional to the total cross section. The Callan-Gross relation as given in Equation (3.10) is a general consequence of the quark-parton model and holds also for lepton pair production [Lam78].

Lam and Tung demonstrated that – contrary to the Callan-Gross relation in DIS – Equation (3.10) is not modified by first order QCD corrections in the case of lepton pair

production [Lam80], although W_μ^μ – and therefore the total cross section – is subject to large corrections. In lepton pair production, Equation (3.10) is called the "Lam-Tung relation".

The invariant structure functions W_1 and W_2 or the helicity structure functions are related to the angular distribution of the leptons in the rest frame of the virtual photon. This results in the following expression for the cross section [Fal86]:

$$\frac{1}{\sigma}\frac{\mathrm{d}\sigma}{\mathrm{d}\Omega} = \left[\frac{3}{4\pi}\frac{1}{\lambda+3}\right]\left(1+\lambda\cos^2\theta+\mu\sin 2\theta\cos\phi+\frac{\nu}{2}\sin^2\theta\cos 2\phi\right). \tag{3.11}$$

Here θ is the polar angle and ϕ the azimuth angle of the momentum vector of the positively charged lepton, σ is the total cross section. Details of the choice of the reference frame to measure θ and ϕ and an introduction in general fixed-target kinematics can be found in Appendix A. The coefficients λ, μ, and ν depend on the structure of the hadrons involved in the interaction and are predicted by theory. The naïve quark-parton model predicts the values $\lambda = 1$ and $\mu = \nu = 0$. This leads to the angular distribution given in Equation (3.6). The Lam-Tung relation (3.10) can also be expressed in terms of λ, μ, and ν:

$$1 - \lambda - 2\nu = 0. \tag{3.12}$$

3.2 Violation of the Lam-Tung relation

3.2.1 Experimental results

In the 1980's, the Lam-Tung relation has been tested in two experiments using a pion beam on a fixed target.

- The E615 experiment, carried out by the Chicago-Iowa-Princeton collaboration in the Proton-West High Intensity Area at FNAL, used a 252 GeV/c pion beam on a tungsten target [Bii86].
- The NA10 experiment was located in the CERN North Area High-Intensity Facility. A 140 GeV/c, 194 GeV/c, or 286 GeV/c pion beam was used on tungsten and deuterium targets [And84].

Both experiments were typical fixed target spectrometers with a target followed by a beam dump and a hadron absorber to suppress most of the hadronic background. Behind the dump/absorber a muon spectrometer was situated, which consisted of one or more analyzing magnets, and wire chambers and hodoscope counters for triggering and tracking. The acceptance of such a spectrometer typically included the forward hemisphere in the proton-nucleon center-of-mass frame, i.e. x_F values of $0 \lesssim x_\mathrm{F} \lesssim 1$. For a definition of x_F cf. Appendix A.

In the 1990's, the E866 (NUSEA) experiment, using an improved version of the fixed-target spectrometer E605/E772/E789 with a new trigger and better acceptance, was set up at FNAL [Mor91, Gag98]. In E866 an 800 GeV/c proton beam interacted with a copper target.

In the following, some details of the analyses of E615, NA10, and E772/E866 concerning angular distributions of muon pairs and the violation of the Lam-Tung relation are discussed.

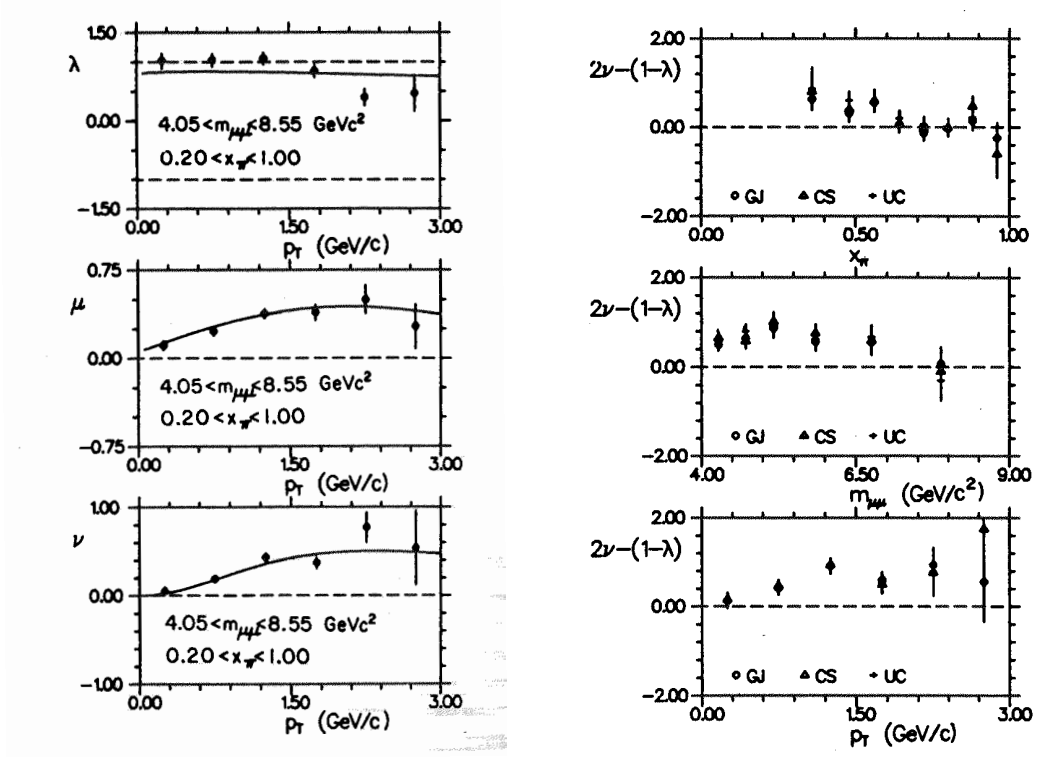

(a) (b)

Figure 3.3: *Results of the E615 experiment [Con89]: (a) λ, μ, and ν as functions of p_{T} in the Gottfried-Jackson frame. The curves are empirical fits that have been used by E615 to optimize the generation of Monte Carlo events. (b) Test of the Lam-Tung relation in the range of $0.2 < x_1 < 1.0$ for the momentum fraction x_1 of the parton in the pion (upper plot), in the invariant mass region $4.05\,\mathrm{GeV}/c^2 < M < 8.55\,\mathrm{GeV}/c^2$ (middle plot) and in the photon transverse momentum region of $0\,\mathrm{GeV}/c < p_{\mathrm{T}} < 5\,\mathrm{GeV}/c$ (lower plot). The results are given in the Gottfried-Jackson, the Collins-Soper, and the u-channel reference frames. For the definitions of the reference frames cf. Appendix A.*

The E615 analysis

The E615 analysis [Con89] includes data from a run with a $252\,\mathrm{GeV}/c$ beam of negatively charged pions. Accepted events are required to include muon pairs in the acceptance region of $0 < x_{\mathrm{F}} < 1$ with an invariant mass of $4.05\,\mathrm{GeV}/c^2 < M < 8.55\,\mathrm{GeV}/c^2$. About 28,000 events fulfill these requirements.

The main source of background events is accidental combinations of muons from different physics processes, e.g. a muon from an interaction in the target combined with a muon from a decay of a beam pion. The shape of the background in the angular distributions is estimated by randomly combining tracks from a prescaled single track trigger. Background events show clustering near polar angles of $|\cos\theta| = 1$ and azimuth angles in the laboratory frame of $\phi_{\mathrm{lab}} = 0$. They account only for a few percent of the data and can be easily subtracted. To avoid large background subtraction while determining the angular distributions, a cut of $|\cos\theta| < 0.9$ is applied.

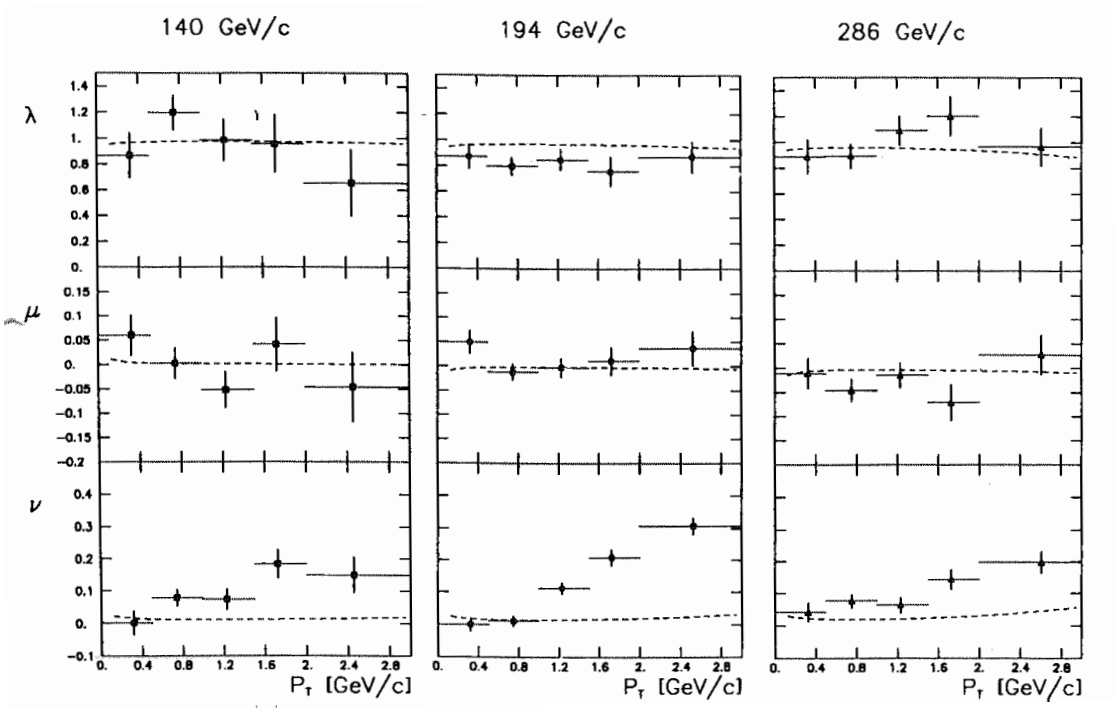

Figure 3.4: *Results of the NA10 experiment [Gua88]: λ, μ, and ν as functions of p_{T} in the Collins-Soper frame for three different momenta of the incident pions:* 140 GeV/c, 194 GeV/c, *and* 286 GeV/c *(from left to right). For the definitions of the reference frames cf. Appendix A. The dashed curves are predictions from perturbative QCD to $\mathcal{O}(\alpha_s)$ including soft gluon resummation [Chi86].*

A Monte Carlo simulation of the E615 detector is used to determine the acceptance, and the distributions of the kinematic variables in question are corrected accordingly, neglecting kinematic regions with acceptances below 0.75%.

Fig. 3.3 shows results of the E615 analysis. On the left side the parameters λ, μ, and ν are plotted as functions of p_{T} in the Gottfried-Jackson reference frame. A detailed description of the reference frames can be found in Appendix A. The Gottfried-Jackson frame is chosen because the detector has the largest acceptance in this frame. The right side plots show explicit tests of the Lam-Tung relation (3.12) as functions of the momentum fraction x_1 of the struck parton in the pion, the invariant mass M of the muon pair, and the virtual photon's transverse momentum p_{T}. The deviations from zero are expected to be less than 0.05. For large values of p_{T}, the Lam-Tung relation is violated in all three reference frames.

The NA10 analysis

The data for the NA10 analysis [Fal86, Gua88] were collected with 140 GeV/c and 194 GeV/c π^- beams on a tungsten target and with a 286 GeV/c π^- beam on deuterium and tungsten targets. The discussion in this section will concentrate on the largest sample, which was collected with the 194 GeV/c beam and consists of about 148,000 di-muon events.

Events with a muon pair in the invariant mass range of $4.05\,\mathrm{GeV}/c^2 < M < 8.55\,\mathrm{GeV}/c^2$ and $M > 11\,\mathrm{GeV}/c^2$ are accepted. For acceptance reasons only the re-

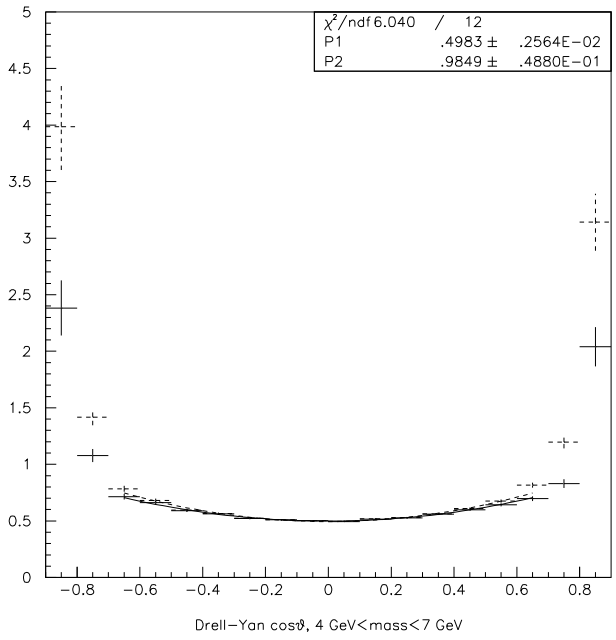

Figure 3.5: $\cos\theta$ *distribution of Drell-Yan muon pairs in the E866 experiment [Cha99]. A fit to the function* $N(1+\lambda\cos^2\theta)$ *results in* $\lambda = 0.98 \pm 0.04$*. Solid line: after subtraction of background from random combinations of muons. Dashed line: before random subtraction. The rise at* $|\cos\theta| \to 1$ *is a consequence of resolution effects of the E866 spectrometer.*

gions of $|\cos\theta| \leq 0.5$ and $x_\mathrm{F} > 0$ are considered. The cut in $\cos\theta$ results in a rather inaccurate measurement of the coefficient λ. To suppress "higher-twist" effects (cf. Section 3.2.2), events with momentum fractions x_1 of the struck parton in the pion larger than 0.7 are rejected.

The distributions of λ, μ, and ν as functions of the transverse momentum p_T of the virtual photon for the different beam energies are shown in Fig. 3.4. The Collins-Soper frame has been chosen for these plots because the influence of biases and smearing effects of the detector, indicated by the angular resolution, is the smallest in this frame. For the coefficient ν a clear deviation from the predictions of perturbative QCD is seen for large p_T values, while λ and μ are compatible with the QCD predictions. The effect is largest in the 194 GeV/c data. Thus, as in the case of E615, the data show a violation of the Lam-Tung relation. The data from the deuterium and the tungsten targets agree well, i.e. the violation of the Lam-Tung relation shows no strong dependence on the number of nucleons in the target.

The analyses of E866 and 772

E866 was mainly designed to measure asymmetries in the sea quark distributions of nucleons. However, a measurement of the angular distribution of J/ψ decays has also been performed, including a measurement of the Drell-Yan angular distributions as a cross-check [Cha99].

In E866, di-muon candidates are accepted in the kinematic range of $0.2 < x_\mathrm{F} < 1.0$ and $-0.95 < \cos\theta < 0.95$. A total of 10 million J/ψ events was collected during a four week dedicated run in 1997. This sample contains about 200,000 di-muon pairs

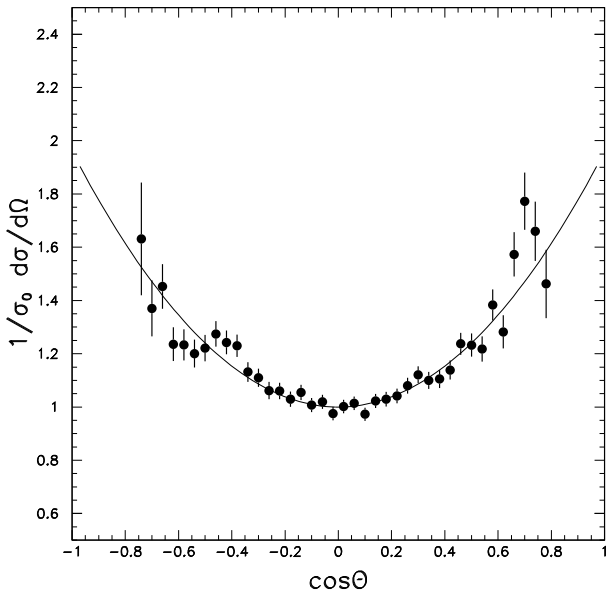

Figure 3.6: $\cos\theta$ *distribution of high-mass Drell-Yan muon pairs in the E772 experiment [McG99]. The muon pairs cover the mass region of* $11\,\mathrm{GeV}/c^2 < M < 17\,\mathrm{GeV}/c^2$ *with* $-0.3 \leq x_\mathrm{F} \leq 0.8$ *and* $p_\mathrm{T} < 6\,\mathrm{GeV}/c$. *A fit to the function* $N(1 + \lambda\cos^2\theta)$ *yields* $\lambda = 0.96 \pm 0.04\,(\mathrm{stat.}) \pm 0.06\,(\mathrm{sys.})$

in the mass range from $4.0\,\mathrm{GeV}/c^2$ to $7.5\,\mathrm{GeV}/c^2$. The main background in this mass regime results from random combinations of muons from pion or kaon decays in flight and is controlled by the number of like-sign muon pairs and normalized by a single muon trigger.

The angular distribution was fitted to the function $N(1 + \lambda\cos^2\theta)$ in the range $-0.7 < \cos\theta < 0.7$ in the Collins-Soper frame. A result of $\lambda = 0.98 \pm 0.04$ was obtained, consistent with $\lambda = 1$ as predicted by the parton model. The result is shown in Fig. 3.5. The influence of the parameters μ and ν of Equation (3.11), as functions of e.g. the transverse momentum of the virtual photon, has not been studied. Therefore, the validity of the Lam-Tung relation has not been checked in this experiment.

The angular distribution for Drell-Yan events with masses above $11\,\mathrm{GeV}/c^2$ was measured by the E772 experiment. About 50,000 events were recorded, using a copper beam dump as the target. From a fit similar to the E866 analysis, a value of $\lambda = 0.96 \pm 0.04\,(\mathrm{stat.}) \pm 0.06\,(\mathrm{sys.})$ is obtained, as shown in Fig. 3.6 [McG96, McG99].

3.2.2 Theoretical models

After the measurements of E615 and NA10 several theoretical explanations for the violation of the Lam-Tung relation came up, partly based on concepts that had been developed before. In the following, some of these models and their relevance to HERA–B are discussed.

Higher-twist contributions

In quantum field theory, a "twist" τ can be assigned to each operator that occurs in matrix elements for cross section calculations. The twist is defined as the difference

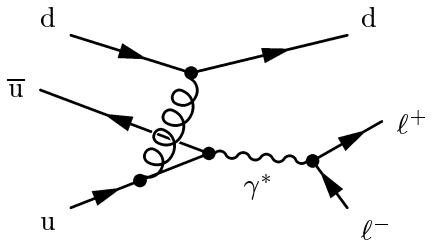

Figure 3.7: *Feynman diagram of a "higher-twist" contribution to pion-nucleon scattering. The incoming* u *quark of the nucleon and the spectator* d *quark in the pion exchange a gluon.*

between the dimension d and the spin s of an operator: $\tau = d - s$. The current operator of QED may serve as an example: The expression $\overline{\psi}\,\gamma^\mu\,\psi$ is bilinear in the fermion field operators ψ and contains one spin index μ. Since fermion field operators have the dimension $\frac{3}{2}$, the twist of the current operator is $\left(2 \times \frac{3}{2}\right) - 1 = 2$. In QED as well as in QCD, twist-two operators give the largest contribution to the cross section, hence they are called "leading-twist" contributions.

The quark-parton model allows a more intuitive approach to the twist. It is assumed that only one quark in the nucleon participates in the interaction, while the other quarks take the role of spectators. This assumption holds for leading-twist contributions. In higher-twist contributions, however, the spectators take part in the interaction [Itz80, Rey81].

In [Ber79] the influence of higher-twist effects on the decay angular distribution in lepton pair production is evaluated. In the limit $x_\mathrm{F} = x_1 - x_2 \to 1$, the quark or the antiquark in the hard subprocess is far off its mass shell. Consequently, the short distance internal dynamics of the hadronic wave function are probed. The dominant process in pion-nucleon scattering is the single gluon exchange between a u quark of the nucleon and the spectator d quark of the meson, as depicted in Fig. 3.7.

The differential cross section including higher-twist effects reads

$$\frac{\mathrm{d}\sigma}{\mathrm{d}\Omega} \sim (1 - x_1)^2 \left(1 + \cos^2\theta\right) + \frac{4}{9}\,\frac{\langle {k_\mathrm{T}}^2 \rangle}{M^2}\,\sin^2\theta. \tag{3.13}$$

The higher-twist contribution bears a polar angle dependence proportional to $\sin^2\theta$, indicating a longitudinal polarization of the virtual photon. This contribution is suppressed by a factor $1/M^2$, typical for higher twist effects. Furthermore, the contribution is proportional to the average of the square of the transverse momentum $\langle {k_\mathrm{T}}^2 \rangle$ of the antiquark in the meson.

These ideas are extended in [Bra94], where predictions for the coefficients λ, μ, and ν of Equation (3.11) are made under certain assumptions regarding the pion wave function. Fig. 3.8 shows a fit to the E615 data [Con89]. The higher-twist model fails to explain the high values of ν for large transverse momenta of the photon.

The relevance to HERA–B of higher-twist effects is expected to be small since the detector covers the central x_F region of $-0.4 < x_\mathrm{F} < 0.3$, where these effects should be suppressed. Predictions of the impact of higher-twist effects on the angular distribution of Drell-Yan lepton pairs in proton-nucleon scattering have not yet been made.

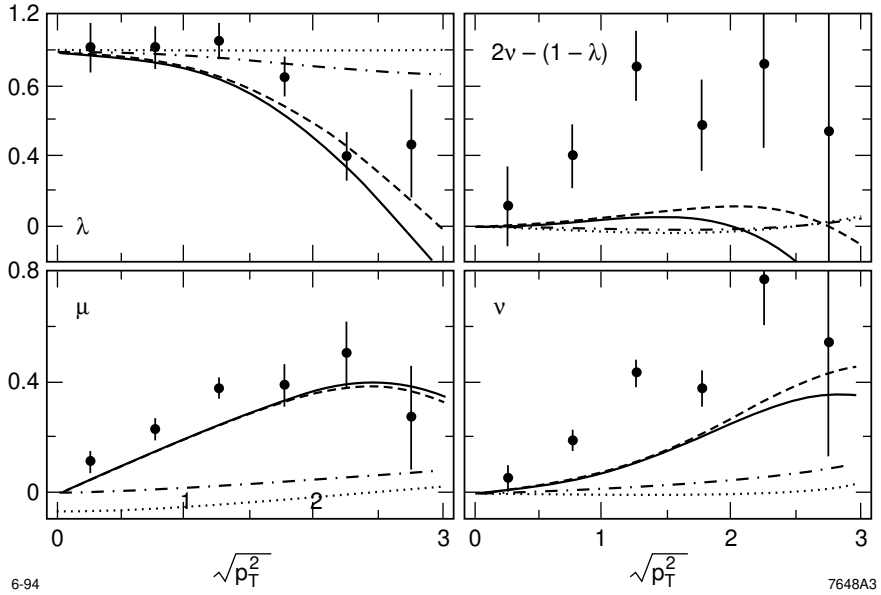

Figure 3.8: *Higher-twist model fits to the E615 data [Bra94]. The coefficients λ, μ, and ν and the Lam-Tung relation are plotted against the transverse momentum of the virtual photon. The different lines correspond to different models for the pion wave function.*

Color domains

Another theoretical explanation is based on the concept of color domains in the QCD vacuum. The basic ideas of this approach are elaborated in [Nac84]. The QCD vacuum is regarded as a kind of "ether" that shows a domain structure. Inside a domain, a constant chromomagnetic field is expected. The domain size should be of the order of $\hbar c/\Lambda_{\mathrm{QCD}} \approx 1\,\mathrm{fm}$, where $\Lambda_{\mathrm{QCD}} \approx 200\,\mathrm{MeV}$ is the QCD scale parameter. Highly energetic quarks that cross this domain structure acquire a transverse spin polarization, similar to the Sokolov-Ternov effect [Sok64] in a synchrotron.

Furthermore, in $\mathrm{q\overline{q}}$ scattering as in the Drell-Yan process, the chromomagnetic field introduces a correlation between the transverse momenta of the quark and the antiquark. The quark and the antiquark, moving in opposite directions in space, are bent in the same direction by the chromomagnetic Lorentz force if they carry color and corresponding anticolor.

A phenomenological model which is based on these assumptions is presented in [Bra93]. The spin correlation parameter κ is introduced, $\kappa = 0$ corresponding to no correlation between the quark and the antiquark spin and $\kappa = 1$ corresponding to maximal correlation. The parameters λ and μ in (3.11) are nearly unaffected by κ, whereas ν is strongly altered. A simple ansatz for the p_{T} dependence of κ is used:

$$\kappa = \kappa_0 \frac{{p_{\mathrm{T}}}^4}{{p_{\mathrm{T}}}^4 + {m_{\mathrm{T}}}^4}, \tag{3.14}$$

where p_{T} is the transverse momentum of the quark-antiquark pair and κ_0 and m_{T} are free parameters. The model predicts a modification of the Lam-Tung relation (3.12):

$$1 - \lambda - 2\nu \approx -4\kappa. \tag{3.15}$$

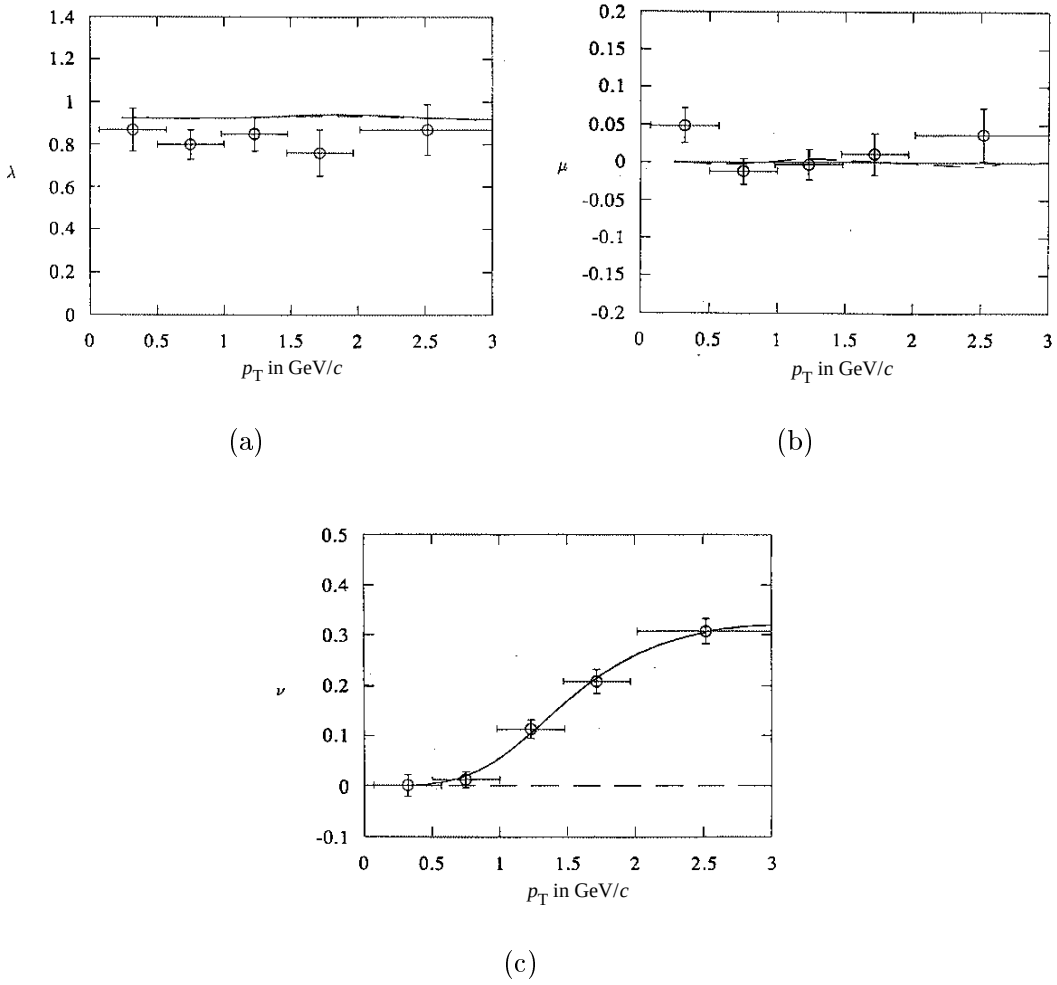

Figure 3.9: *Fit to the* 194 GeV/c π^- *data of NA10 (circles), cf. Fig. 3.4, from the color domain model of [Bra93]. The values of the parameters* λ, μ, *and* ν *are depicted as functions of the transverse momentum of the virtual photon* p_T. *(a) shows a fit to the parameter* λ, *in (b) the parameter* μ *is plotted, and in (c)* ν *is depicted. The solid lines are the fits, the dashed lines are the predictions of the parton model.*

The predictions have been checked with the NA10 data from the 194 GeV/c π^- beam. As shown in Fig. 3.9, the results agree well with the data. In particular, the increase of the parameter ν with the transverse momentum of the virtual photon p_T – indicating the violation of the Lam-Tung relation – is described well by the model.

Intrinsic transverse momentum-dependent parton distribution functions

In [Boe99] the origin of the violation of the Lam-Tung relation is attributed to large single transverse spin asymmetries, which have been observed in inclusive pion production by transversely polarized 200 GeV/c antiprotons in the E704 experiment [Bra96]. The size of these asymmetries cannot be explained by perturbative or higher-twist effects.

The origin of the asymmetries is seen in a special set of parton distribution functions which are odd under the chiral and the time reversal symmetries. In addition, they

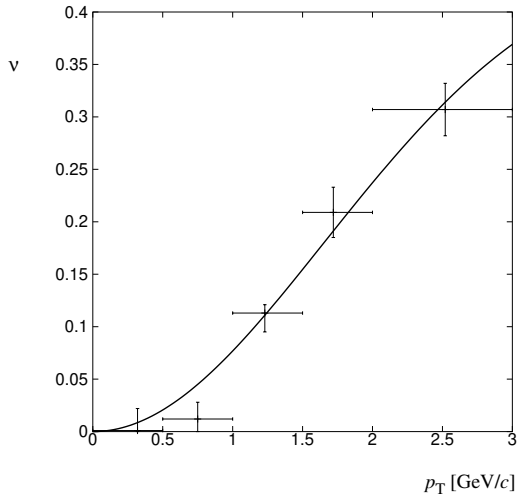

Figure 3.10: *Fit to the* 194 GeV/c π^- *data of NA10, cf. Fig. 3.4, using the model of intrinsic transverse momentum-dependent parton distribution [Boe99]*

depend on the intrinsic transverse momentum of the partons. Hence, these distribution functions connect the transverse spin and the transverse momentum of partons.

The predictions of this model describe the rise of ν with the transverse momentum of the virtual photon in the NA10 data [Gua88] quite well, cf. Fig. 3.10. However, the chiral-odd T-odd parton distributions have the conceptual problem that they are expected to vanish due to time reversal symmetry.

Coherent states

A fourth theoretical model is based on ideas from quantum statistical mechanics. The expression for the angular dependence of the cross section as a function of the transverse momentum of the lepton pair is obtained by a non-perturbative quantum statistical treatment of the virtual photon [Bla89].

Due to the quantum statistical properties of the virtual photon, the lepton pair in the Drell-Yan process is in a coherent state. Thus viewed in phase-space, the coordinates and the momentum of the lepton pair are subject to a non-vanishing correlation as a function of the transverse momentum of the pair. The lowest order approximation of the exact result is compared with the NA10 data [Gua88] in Fig. 3.11. The rise of ν as a function of the transverse momentum is reproduced to a good extent.

3.2.3 Concluding remarks

The Lam-Tung relation has been explicitly tested in pion-nucleon scattering by the E615 and the NA10 experiments. The results of these tests show a clear violation of the Lam-Tung relation in the coefficient ν.

There are different theoretical approaches to explain the violation of the Lam-Tung relation on the basis of diverse non-perturbative effects. Most of these models succeed in describing the experimental data, but the data are not precise enough to verify or to exclude the different models.

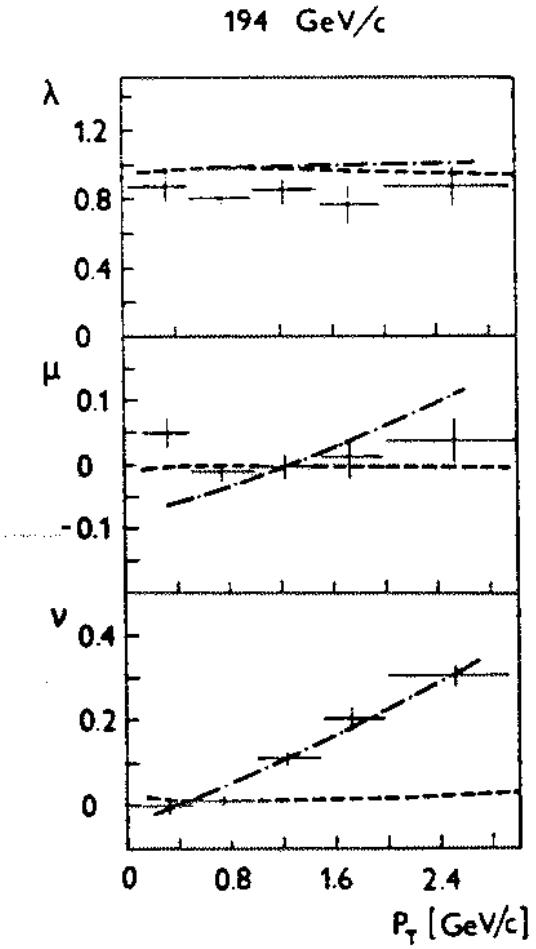

Figure 3.11: *Fit to the* 194 GeV/c π^- *data of NA10 (cf. Fig. 3.4) in a coherent state model [Bla89]. The dashed lines correspond to the predictions of perturbative QCD [Chi86], and the dashed-dotted lines are the predictions of the coherent state model.*

Measurements of the violation of the Lam-Tung relation in proton-nucleon scattering have not yet been published. In the E772 and the E866 experiments, only the coefficient λ has been determined. Furthermore, the theoretical expectations for violation effects in proton-nucleon scattering are only vague: The effect is expected to be smaller than in pion-nucleon scattering, since in pion-proton scattering two valence partons are involved while in proton-nucleon scattering the antiquark is from the sea [Boe01].

Thus, a test of the Lam-Tung relation in proton-nucleon scattering is of interest both from a theoretical and an experimental point of view. The prospects of HERA–B to perform such a measurement will be evaluated in Chapter 6.

Chapter 4

The HERA – B di-muon trigger in the 2000 data-taking period

In this chapter, the HERA – B di-muon trigger in the 2000 data-taking period will be described. Starting from the status of the detector and trigger commissioning in spring 2000, the idea of a combination of the Second Level Trigger (SLT) and the pretriggers together with a software substitute for the First Level Trigger (FLT) will be illustrated. A description of the evolution of the analysis software and techniques in this period will also be included. The chapter will close with a review of the basic analysis ideas for the di-lepton data and some results.

4.1 Status of the trigger commissioning in spring 2000

In spring 2000 the HERA – B experiment was in its commissioning phase. Several subdetectors were already completed, and others became ready in this time. However, the most complex part of the trigger chain, the FLT, was not fully operational. In this period, it was equally important to complete the HERA – B detector and trigger and to take data with the working parts of the detector in order to finalize the commissioning and to begin physics studies. Therefore, ways had to be found to bypass the non-working FLT track finding algorithm and to substitute the FLT tracking with software.

4.1.1 The pretrigger–SLT di-electron trigger

The idea to use the SLT together with the pretriggers and to emulate the FLT in the SLT had already arisen in 1998. With the help of the ECAL pretrigger and some of the SLT algorithms, a search for signatures of high mass electron-positron pairs was performed. Tracks in the vertex detector system (VDS), identified with the L2Sili package, were matched to clusters with large transverse momenta in the electromagnetic calorimeter (ECAL) [HB00a]. Some early results of the analysis of these data can be found in [Sch99].

The SLT algorithm for the default FLT-SLT trigger also includes tracking in the main tracker via the Slicer/Refit packages. The Slicer/Refit packages use hits from six superlayers of the main tracker for their tracking algorithms. Hence, they are sensitive to the correct mapping of detector channels and to the detector alignment. The performance and alignment of the Outer Tracker (OTR) became sufficiently stable for the SLT in spring 2000. From this point on the Slicer/Refit algorithms in the OTR were also included in the search for electron pairs. The Inner Tracker system (ITR)

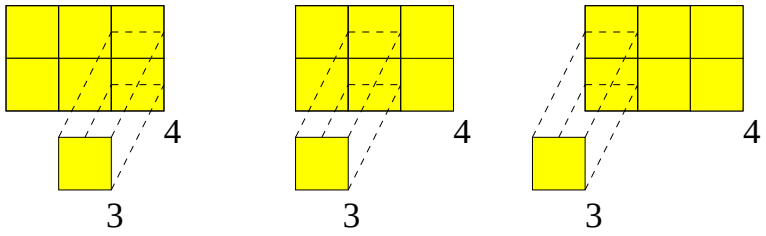

Figure 4.1: *Coincidence logic of the muon pretrigger emulation: in the outer regions of the detector, the MU4 pads are shifted outwards by one pad (left and right picture). In the central region of the detector, the coincidence logic is the same as in the muon pretrigger hardware.*

became ready late in the run and was not included in the SLT in the 2000 data-taking period.

4.1.2 Trigger based on the muon pretrigger emulation

During the commisioning of the muon pretrigger in late 1999, a software algorithm to emulate the muon pretrigger coincidence logic was also developed [Eig99]. In the inner columns of the muon detector, the coincidence logic of the emulation is the same as implemented in the muon pretrigger hardware, as depicted in Fig. 2.5. In the outer parts, the logic of the emulation differs from the hardware logic in order to retain the efficiency of the coincidence algorithm. To improve the projectivity of the coincidence scheme, the three columns of the superlayer MU4 are shifted outwards by one column, as shown in Fig. 4.1.

The emulation code could be run on the SLT farm. With the help of this tool a simple di-muon trigger could be set up, demanding two or more separated coincidences as the trigger condition. The input rate of the trigger was limited to the maximum input rate of the SLT farm, which equals approximately 30 kHz. The rate reduction from the typical interaction rate of 5 MHz to about 30 kHz was achieved by using a default trigger option of the HERA – B data acquisition system (DAQ) that forces the DAQ to write randomly chosen events at an adjustable rate to the Second Level Buffer (SLB) where the data are accessible to software that runs on the SLT farm. Thus the number of primary interactions was prescaled by a factor of 150–200. In runs with the muon pretrigger emulation as the active trigger, the test trigger rate was tuned to saturate the input of the SLT.

The analysis of data taken with this trigger concentrated on matching the slopes of track segments that were reconstructed stand-alone in different subdetectors [Eig99]. In the VDS, the tracks were reconstructed with CATS [Kis99, Eme00a]; the RICH reconstruction was carried out with RISE [Duj00]. In the muon system, the tool MUREC-A [Fom97] was used.

The di-muon invariant mass spectrum obtained in this analysis was still dominated by combinatorial background. Due to the random trigger and the large prescaling factor, the quality of events that were passed to the SLB was varying, a certain fraction being even empty. The muon pretrigger emulation derives its trigger decision solely from a coincidence of hits in two superlayers of the muon system. The coincidence condition can be fulfilled not only by correct tracks that come from the target, but also by secondary particles produced for example in the muon absorbers. As a consequence, the purity of

the triggered events was poor, and the muon pretrigger emulation was estimated to be about a factor of 10 away from observing a J/ψ signal [Eig99].

The replacement of the pretrigger emulation by the real hardware was expected to accelerate the pure software trigger because the starting-point for the software trigger would now be provided by a fast hardware trigger. This would increase the quality of the data passed to the SLT farm and leave time for a more sophisticated trigger decision by the software trigger, using information from additional subdetectors [Buc00]. This improved trigger concept for muon pairs, a combination of the muon pretrigger and a software trigger on the SLT farm, was implemented as the counterpart to the di-electron trigger described above. A detailed description of the di-muon trigger based on the muon pretrigger and the SLT will be given in Section 4.2.

4.1.3 Commissioning of the muon pretrigger

The muon pretrigger system was first installed only in the outer part of the muon detector, which consists of pad chambers. The trigger in the pixel system, the inner part of the muon detector, was added and tested within the experiment at the end of the 2000 run. Since the ITR was not included in the SLT, the acceptance of the muon pretrigger would have been increased only by the overlap between the OTR and the muon pixel system. The size of the overlap was estimated with the help of Monte Carlo simulations of the detector acceptance for muon pairs from the process $gg \to J/\psi \to \mu^+\mu^-$. An expected relative increase in the acceptance gain by only 7%, corresponding to a total acceptance gain of 2.9% [Kla00], led to the decision to concentrate on the reliable operation of the muon pretrigger in the pad system and to perform tests with the pixel system part only at the end of the data-taking period.

The first commissioning runs with the full muon pretrigger chain but only a small part of the system were performed in November and December 1999. Analyses of these runs consisted of tests of the pretrigger chain on the bit level. The tests included checks of the pretrigger logic and the integrity of the data as well as studies of the data transmission between the hardware modules. Parts of the results are discussed, e.g. in [Kla00] and [Hus00a]. The configuration of the muon pretrigger system in the end of the test period mid December 1999 is shown in Fig. 4.2 (a). The area covered by the muon pretrigger consists of several disconnected parts, corresponding to missing channels on the Pretrigger Coincidence Units (PCUs), the electronics boards that perform the coincidence calculations.

The coverage of the muon pad system by the muon pretrigger was extended in several steps. As shown in Fig. 4.2 (b), the configuration in April 2000 covered almost the whole outer part of the muon detector. The missing parts at the periphery of the muon pad system resulted in a loss of less than 5% of the events, because the detector occupancy in this region is small [Ada99]. The pretrigger hardware for these parts was added in July 2000.

After April 2000 the commissioning work concentrated on improvements of the stability of the muon pretrigger system. On the hardware side some broken electronics devices were replaced, and the integration of the system into the HERA–B DAQ was finalized [Sch01b, Bec01]. In addition, the reliability of the optical links which transmit the muon pretrigger data from the detector front-end to the electronics trailer was improved. Afterwards, an average of 252 out of the 264 optical links worked without detectable errors [Bec00].

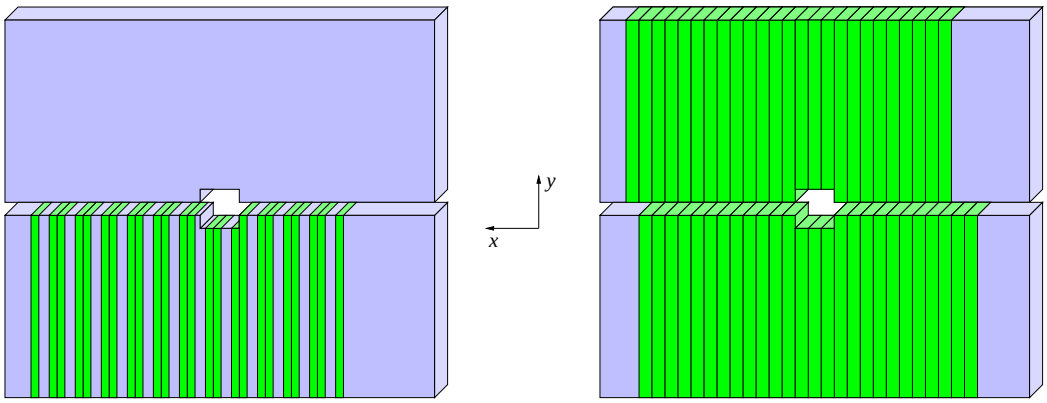

(a) December 1999 (b) April 2000

Figure 4.2: *Coverage of the muon pad system by the muon pretrigger: (a) December 1999, (b) April 2000. The marked detector columns were covered by the muon pretrigger. In December 1999 only half of the channels on each electronics board that performs the coincidence calculations were equipped.*

The efficiency of the muon pretrigger was determined in special runs where the muon pretrigger emulation was the active trigger. The efficiency calculation was based on a pad-by-pad comparison of the pretrigger information stored in the data record and the output of MUPRESIM, a detailed simulation of the muon pretrigger, cf. Appendix C. A measurement of the muon pretrigger efficiency in August 2000 yielded a value of 92%, including all problems and non-working channels and an average value of 98.5% for all working channels [Ada01b].

4.2 The First Level Trigger emulation

In this section, the emulation of the FLT that was used as a part of the the di-muon trigger in the 2000 data-taking period will be described. The expression "emulation" in this context does not mean an imitation of the FLT operation in software but rather an alternative simplified tracking algorithm that serves as a substitute for the FLT.

A substitute for the FLT is needed because the muon pretrigger alone is not designed to provide a significant rate reduction but rather a starting-point for the FLT tracking. Together with the FLT, the expected rate reduction adds up to 200, sufficient to match the maximum input rate of the SLT. This rate reduction clearly cannot be achieved with the muon pretrigger alone. The average single coincidence rate of the pretrigger for a target rate of 5 MHz was about 600 kHz in the 2000 data-taking [Sch01b], and the input rate of the SLT was limited to approximately 30 kHz.

In addition, the SLT algorithms in the OTR Slicer/Refit expect a small Region of Interest (RoI) in the rearmost superlayer of the OTR (TC2) as a starting-point for their tracking. The RoIs provided by the FLT have a size of approximately $\pm 2.5\,\mathrm{cm}$ both in the x and the y direction. Since the resolution of the muon pretrigger is limited by the pad size of about $12 \times 10\,\mathrm{cm}^2$ and by multiple scattering effects in the three muon absorber layers, the RoI obtained from a projection of the position of the muon

pretrigger coincidence to TC2 is not precise enough for the SLT. Therefore, the position information delivered by the muon pretrigger has to be refined.

Sufficient rate reduction and RoI sizes are provided by the First Level Trigger emulation in the muon system (FLTm), which works in two steps:

1. The pretrigger provides a seed for a software trigger in the first two layers of the muon system.

2. The combined information of the muon system is translated into an RoI for the SLT.

Technically, the FLTm code is part of the SLT code, hence it is executed on the SLT farm.

4.2.1 Utilization of the muon pretrigger

As in the normal FLT operation mode, the muon pretrigger generates messages out of coincidences between hits in projective cathode pads in the last two superlayers of the muon system, MU3 and MU4. In the FLT mode, up to three messages per coincidence may be sent. This permits effectively increasing the size of the RoI for the FLT to account for multiple scattering of low-momentum tracks. For the SLT di-muon trigger, the number of messages was restricted to one, because a larger RoI was not needed for the FLTm algorithm. Such changes in the number of messages and in the message format can be implemented via an alternative programming of the lookup tables that are used to generate the pretrigger messages.

Among other information the messages contain the x and y position of the MU3 pad from which the coincidence originates, the "coincidence position". Details of the meaning and the format of the messages in the FLT can be found in [Ger98, Sch98b].

The accuracy of the coincidence position is limited by the size of a single pad, approximately $12 \times 10\,\mathrm{cm}^2$. The information in the yz plane, where tracks are not bent by the magnet, referred to as the "non-bending plane" in the following, is considered to be precise enough for the SLT. Thus the y range of the RoI for the SLT is determined by a projection onto TC2 of the upper and lower boundaries of the pad in MU3 where the coincidence was generated.

4.2.2 The "transparent" First Level Trigger

In the 2000 di-muon trigger, the FLT is used as an interface between the pretrigger and the SLT, running in a "transparent" mode that passes the pretrigger messages to the SLT without modifying the relevant parts of the messages. The muon pretrigger messages are collected on two Track Finding Units (TFUs) in MU4, which serve as multiplexers for the messages. The TFUs are directly connected to a Trigger Decision Unit (TDU). The standard configuration of the connection is shown in Fig. 4.3. Because the FLT commissioning took place in parallel to the J/ψ trigger running, some minor changes in the configuration occurred during the run. Details of the connection and connection tests can be found in [Sch01b].

The TDU is operated in the count trigger mode and requires at least two coincidence messages. The average trigger rate can be reduced to about 80 kHz by this double coincidence requirement. A further reduction of the output rate was achieved by prescaling the muon pretrigger in the TDU. The prescaling factor was 2^2 or 2^3 for most of the di-muon runs, i.e. the TDU accepts only one out of four or eight double coincidences from the muon pretrigger.

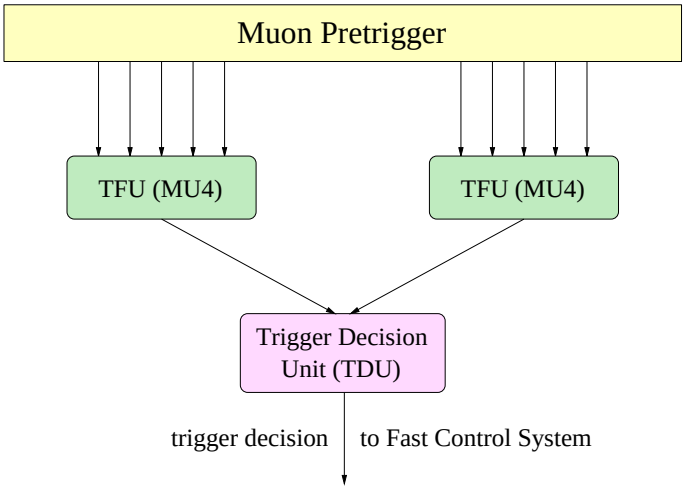

Figure 4.3: *Default "transparent" FLT setup for the di-muon trigger (after [HB00a]). The pretrigger messages are passed through two Track Finding Units (TFUs) in MU4 without modifications of the relevant parts. A Trigger Decision Unit (TDU) is operated in the count trigger mode, i.e. it causes the Fast Control System to pass events with two or more pretrigger messages to the higher trigger levels.*

4.2.3 Tracking in the muon system

Before the detector data is transferred from the SLB to the nodes of the SLT farm, the FLTm algorithm imposes a cut on the distance d between two tracks of $d \geq 50\,\text{cm}$ in the muon detector superlayer MU3, i.e. at $z = 1880\,\text{cm}$. Monte Carlo simulations show that 95% of the muons from direct J/ψ decays are emitted with a laboratory frame angle with respect to each other that corresponds to this distance between the tracks in MU3. Therefore the distance cut can be used to suppress background from random combinations of coincidences.

To determine the momentum of a track, good knowledge of the tracking parameters in the bending plane of the magnet is important. Consequently, the FLTm algorithm improves the x information on the track provided by the muon pretrigger by reading out the 0° wires in the first and second superlayer of the muon system (MU1 and MU2). The stereo layers are neglected because the y position has to be determined through a combination with the tilted wires. This procedure is less accurate [Tit00] and more complicated than analyzing only the vertical wires. The tracking in the muon system consists of the following steps [Eig00, Ada00b], for an illustration cf. Fig. 4.4:

(a) The muon pretrigger delivers the position of a coincidence in MU3.

(b) The x position of the muon pretrigger coincidence is projected to MU2. The size of the RoI in MU2 takes into account the size of the pads and multiple scattering in the muon absorber layer between MU2 and MU3. The size of the RoI was obtained from a Monte Carlo simulation as $\pm 20\,\text{cm}$ from the x position of the coincidence [Ada00a]. The algorithm searches for isolated single or double hits in the 0° wires in this region. MU2 has been chosen because the occupancy of this superlayer is the smallest in the muon system. Compared to the situation in MU1, where Monte Carlo simulations of inelastic interactions show that only 5% of the hits are from muons, the environment of MU2 is cleaner, i.e. the fraction of muon hits is 21%.

(c) Next the algorithm searches for all hits in the 0° wires of MU1. The coordinates of the current hit in MU1 and the hit in MU2 define a straight line which serves as a track hypothesis. This line is extended to MU3. The algorithm checks if there is a coincidence at the pad position where the line crosses MU3. Events with a collinear MU1 hit, MU2 hit, and pretrigger coincidence are accepted.

(d) The straight line defined by the hits in MU1 and MU2 and the pretrigger coincidence is used to extrapolate the track candidate to TC2, where the SLT tracking with SLICER/REFIT starts. The size of the RoI in TC2 is about $10 \times 10\,\mathrm{cm}^2$.

The efficiency of this trigger has been determined by a Monte Carlo simulation [Pet01a]. A compilation of the results is given in Table 4.1. The total efficiency is composed of several contributions:

- The geometrical acceptance of the outer muon system for muon pairs from J/ψ decays, including hot and dead detector channels, which are masked out,
- the efficiency of the cathode pads in the muon detector to detect at least four hits for two tracks,
- the efficiency of the muon pretrigger system to detect a coincidence,
- and the efficiency of the FLTm algorithm in linking the hits in MU1 and MU2 to the coincidence and projecting the resulting track candidate to TC2.

The geometrical acceptance of the muon pretrigger in the outer muon system for muon pairs from the decay $J/\psi \to \mu^+\mu^-$ has been determined by a Monte Carlo simulation [Ada01b]. The efficiency of the cathode pads used in the muon pretrigger was measured in July 2000 with a provisional tracking algorithm. The cathode pads showed an average efficiency of $(71 \pm 11)\%$ [Zai00]. This rather low efficiency is due to masked channels in certain parts of the muon detector. To obtain the efficiency for a pair of tracks, having hits in two superlayers each, this figure has to be taken to the fourth power. The muon pretrigger efficiency has been determined from data recorded with the muon pretrigger emulation as the active trigger and the muon pretrigger operating in parallel [Ada01b]. The overall efficiency of the FLTm code has been obtained from a Monte Carlo simulation of the full FLTm and SLT trigger chain [Pet01a]. Since no direct measurement of the FLTm tracking efficiency in the superlayers MU1 and MU2 of the muon detector was available, this figure could only be inferred from the other efficiencies. The value of approximately 0.3 agrees well with direct measurements for an ideal detector description; see Table 6.5.

Table 4.1: *Two-track efficiency of the muon pretrigger and the FLTm algorithm. The errors are statistical errors from the single independent measurements only. The efficiency for hits in MU1 and MU2 has been estimated from the other figures.*

Trigger element	Efficiency
Geometrical acceptance [Ada01b]	0.42 ± 0.01
Muon pads [Zai00]	0.26 ± 0.16
Muon pretrigger [Ada01b]	0.92 ± 0.05
Hits in MU1 and MU2	$\approx$ *0.30*
Two tracks from FLTm [Pet01a]	0.03 ± 0.04

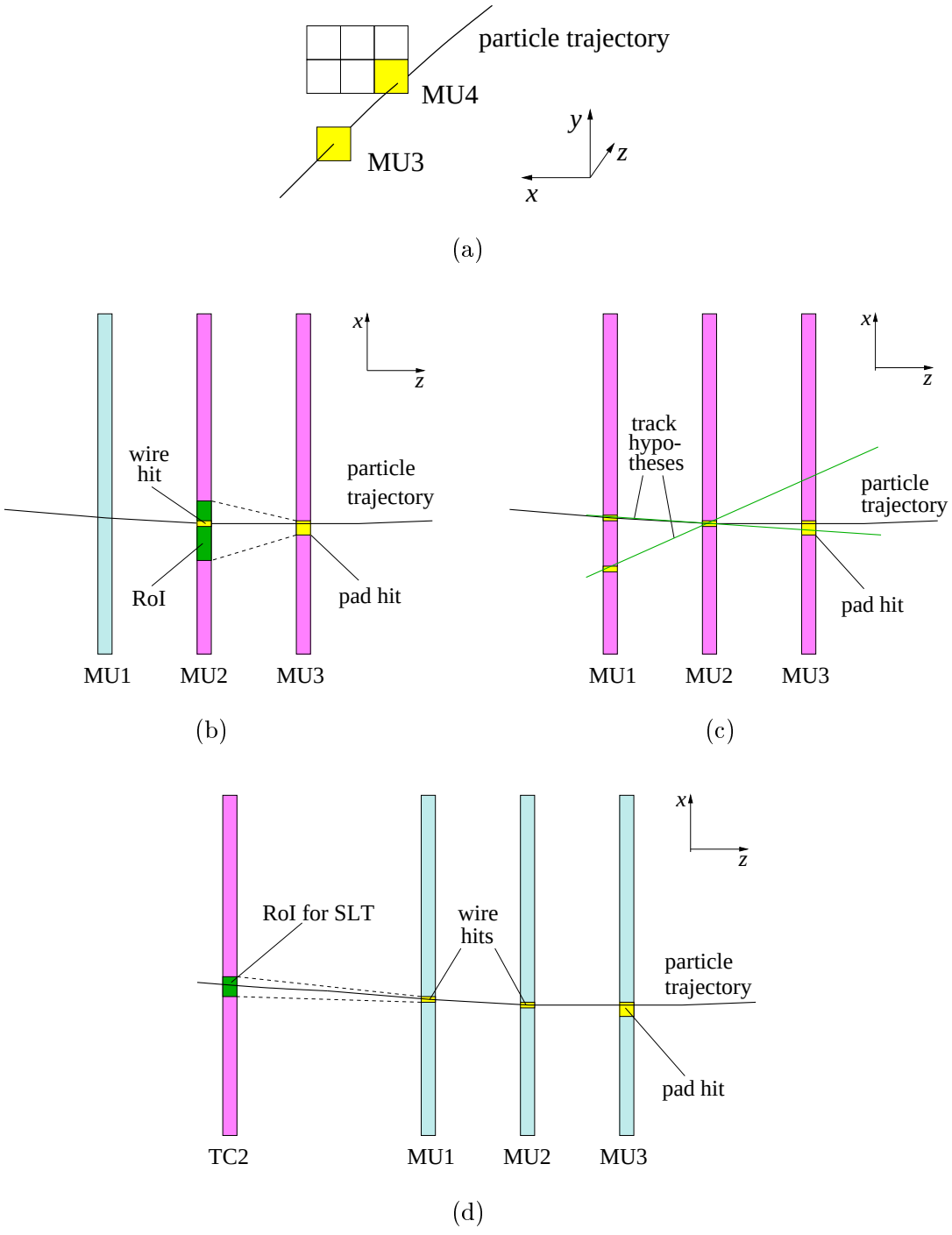

Figure 4.4: *Illustration of the FLTm algorithm: (a) A muon pretrigger coincidence serves as a seed. (b) The seed is projected to MU2. In the region of interest (RoI) a search for isolated hits in the 0° wires is performed. (c) For each hit in MU1 a track hypothesis is formed by a straight line connecting the current MU1 hit and the MU2 hits. The hypothesis is accepted if the extension of the line to MU3 crosses the position of the muon pretrigger coincidence. (d) The track candidate is projected to TC2, using information from MU1-MU3 in the x direction and from the MU3 pad only in the y direction.*

4.2.4 Tracking in the Second Level Trigger

Contrary to the di-electron trigger, the SLICER/REFIT algorithms in the OTR were used by the SLT for the di-muon trigger from the beginning of its operation. Information on the drift time in the OTR cells is not employed, and the magnet chambers ware not used in the SLT algorithm. To account for unstable OTR running conditions in the 2000 run, the cuts applied in the SLICER/REFIT hit counting have been relaxed compared to the default cuts for the standard FLT-SLT trigger chain. A completely empty superlayer is allowed for, and the search window in the OTR is enlarged to $\pm 2.5\,\mathrm{cm}$ to deal with alignment problems [HB00a].

A matching between the SLICER/REFIT tracks and tracks in the VDS is performed by L2SILI. An event is accepted by the SLT if at least two tracks from the VDS can be matched with OTR tracks. The L2VERTEX algorithm performs a vertex fit which is, however, not included in the trigger decision. Contrary to the di-electron trigger, which only accepts pairs of "outwards"-bending tracks, all four combinations of track charges, $(++)$, $(+-)$, $(-+)$, and $(--)$, are accepted by the di-muon trigger.

The efficiency of the components of the SLT algorithm in the configuration described above has been estimated by a Monte Carlo simulation with a realistic description of the HERA–B detector. The simulation included efficiencies and hot channel masks of the VDS, the OTR, and the muon system as used in July and August 2000. The study was performed on a sample of 10,000 events from the process $\mathrm{gg} \to \mathrm{J}/\psi \to \mu^+\mu^-$ [Pet01a]. The results are shown in Table 4.2

Table 4.2: *Estimates of the SLT two-track triggering efficiencies with a realistic simulation of the HERA–B detector (as of July/August 2000) for the decay* $\mathrm{J}/\psi \to \mu^+\mu^-$ *[Pet01a]. The errors are statistical errors only.*

Algorithm	Efficiency
SLICER	0.67 ± 0.05
REFIT-X	0.67 ± 0.06
REFIT-Y	0.76 ± 0.07
L2SILI	0.93 ± 0.07
Overall SLT	0.31 ± 0.13

The low efficiencies in the OTR algorithms are mainly due to the quality of the RoIs provided by FLTm which are rather large and uncertain, about $\pm 5\,\mathrm{cm}$, In combination with the efficiencies of the FLTm algorithm, which are shown in Table 4.1, the overall efficiency of the di-muon trigger ϵ_{trig} can be obtained:

$$\epsilon_{\mathrm{trig}} = 0.009 \pm 0.015. \tag{4.1}$$

To summarize, the di-muon trigger in the 2000 data-taking period – as described in this chapter – provided the possibility to take data with the HERA–B detector without the FLT in full operation. As will be pointed out in the following, even with the quite low efficiency of 1%, resulting in a number of 25 detected J/ψ mesons per hour, an interesting physics program can be started. In addition, the well-defined muon tracks from J/ψ decays can be used as reference tracks in the commissioning of the HERA–B detector.

4.3 Analysis strategies

While the HERA – B detector and trigger were being commissioned, the tools that were needed to analyze the data were further developed. The search for J/ψ mesons in di-muon triggered data began with methods where the track segments from different subdetectors were combined manually, since there was no standard combination procedure available. The succeeding method was based on the tracking information collected in the SLT. In the end, a "standard" procedure was established where tracks were formed out of a proper combination of all relevant subdetectors by the default reconstruction chain, so that track-based analyses could be performed.

In this section, the main ideas of these analysis strategies will be reviewed. Following the evolution of tracking methods, some basic principles of the stand-alone reconstruction in the individual subdetectors, the combination of track segments and the momentum determination will be described. These principles are used only implicitly in the final analysis since they are hidden in the reconstruction chain. Some results from the methods that are no longer employed can be found at the end of the corresponding subsections. The results obtained with the most recent analysis techniques can be found in Chapter 5.

4.3.1 Matching of track segments

In an inhomogeneous detector system like the HERA – B detector, the track reconstruction can be divided into two steps which are equally important. As a first step, detailed knowledge of the subdetectors is needed to implement pattern recognition and stand-alone tracking algorithms for each subdetector. In a second step, the information from the subdetectors has to be combined to obtain the parameters of the track as a whole.

The choice of subdetectors

Without a standard procedure to link the track segments, the combination of tracks from the individual subdetectors had to be done manually. For most physics analyses it is vital to know the track parameters and the identities of the particles in the final state. In HERA – B the tracking detectors in front of and behind the magnet are used to determine the momentum and the position of the track while the particle identification detectors help to identify the particle.

In the search for muon pairs that originate from a vertex close to the target, the following subdetectors can be employed. The VDS allows measurement of the track parameters of charged particles that are produced in primary and secondary interactions close to the target. To determine the slope of the tracks behind the magnet, the main tracker is the most important device. In the data-taking period under consideration, i.e. from November 1999 to May 2000, only the OTR was used, the ITR became operational at a later date. The RICH is a particle identification device for pions, kaons, protons, and in part also for muons. Moreover, the RICH provides information on the track slopes behind the magnet. The slopes and positions of muons behind the magnet can be measured by the muon system. Since almost no other particles from interactions near the target reach the muon detector, the reconstruction of track segments in the muon detector also helps to identify muons.

The energy of neutral particles, electrons, and some hadrons can be measured by the ECAL. The energy deposition of muons in the ECAL is usually small. Therefore,

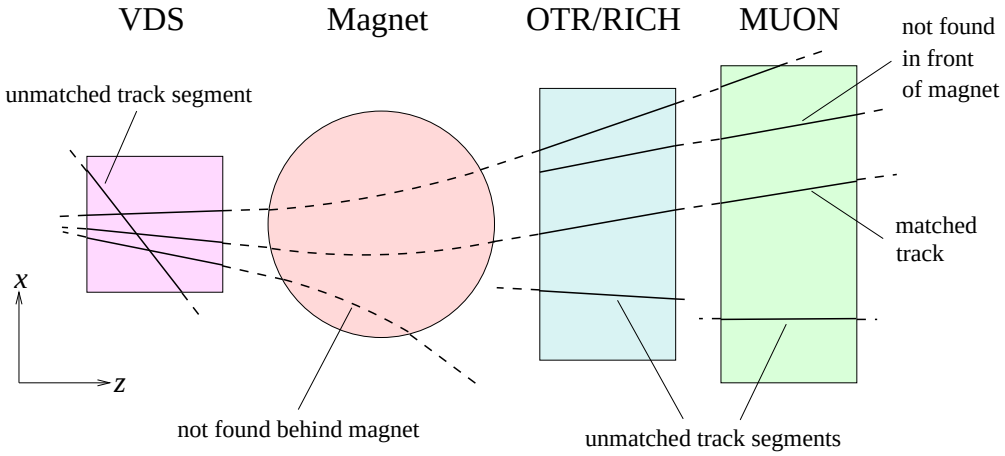

Figure 4.5: *Illustration of the track parameter matching procedure: Matching between two subdetectors behind the magnet filters out unmatched track segments in these subdetectors. Matching between subdetectors in front of and behind the magnet allows tracking through the magnet. Finally, the momentum of the track can be determined by the slope difference in front of and behind the magnet.*

the VDS, the RICH, the OTR, and the muon detector are chosen as subdetectors for the analysis of muon pairs.

The track parameter matching procedure

The basic idea of parameter matching between different subdetectors is a comparison of the slopes of the track segments in the bending and in the non-bending planes of the HERA−B magnet and a comparison of the points of intersection of tracks with the xy plane at a given z position, after the tracks have been extrapolated to this z position.

Generally, there are two categories in the matching of track segments from two subdetectors:

A) The matching of tracks from subdetectors on the same side of the magnet helps to reduce the number of wrong combinations of track segments, because track segments of one subdetector that have no continuation in the other subdetector are filtered out.

B) If tracks from subdetectors on both sides of the magnet are matched, their slopes in the non-bending plane of the magnet can be used to follow the tracks through the magnet. The slope differences in front of and behind the magnet in the bending plane can be employed to determine the momenta of the tracks.

For an illustration of the matching categories cf. Fig. 4.5.

Based on these ideas two independent analyses [Eig99, Hus00b] were developed in HERA−B. The sequence of the matching steps and the cuts differ in these analyses. Moreover, both analyses evolved over time. In the following, the procedure of the final analysis of [Hus00b] will be described.

The track parameters in the subdetectors that are used in the matching are obtained from a stand-alone reconstruction of track segments in these subdetectors. As a first step, pairs of these track segments are matched:

1. First the track slopes in the RICH and the muon detector are matched. The RICH tracking is expected to be more precise than the muon tracking because multiple scattering is larger in the muon system due to the muon absorbers. On the other hand, the number of tracks in the muon system is much smaller than in the RICH. So the precise slope measurement of the RICH is combined with the simple particle identification criterion that the track can be extended to the muon system. Since both subdetectors are situated on the same side of the magnet, the RICH-MUON matching belongs to the matching category A. In order not to reject tracks that are deflected by multiple scattering, the cuts on slope differences in the x direction $\Delta t_{x,\,\mathrm{RICH-MUON}}$ and in the y direction $\Delta t_{y,\,\mathrm{RICH-MUON}}$ were relatively weak compared to the widths of the Δt_x and Δt_y distributions of approximately ± 15 mrad in $\Delta t_{x,\,\mathrm{RICH-MUON}}$ and ± 8 mrad in $\Delta t_{y,\,\mathrm{RICH-MUON}}$:

$$|\Delta t_{x,\,\mathrm{RICH-MUON}}| = |t_{x,\,\mathrm{MUON}} - t_{x,\,\mathrm{RICH}}| < 30\,\mathrm{mrad}, \tag{4.2}$$

$$|\Delta t_{y,\,\mathrm{RICH-MUON}}| = |t_{y,\,\mathrm{MUON}} - t_{y,\,\mathrm{RICH}}| < 20\,\mathrm{mrad}, \tag{4.3}$$

   where the slopes are defined as $t_x \equiv p_x/p_z$ and $t_y \equiv p_y/p_z$ with the three-momentum of the track in the laboratory frame (p_x, p_y, p_z). An overview of the tracking parameters that are commonly used in HERA – B can be found in Appendix B.

2. Since also the OTR is situated behind the magnet, the OTR can be used together with the muon system similarly to the RICH. Therefore, OTR-MUON matching also belongs to category A. To employ the RICH and the OTR in a complementary way improves the efficiency of the matching algorithms, since it partly compensates for the disadvantages of the single detectors. Among other improvements, inefficiencies of the individual subdetectors can be corrected for, e.g. inefficiencies due to the different acceptances of the OTR and the RICH, due to the inherent momentum cut in the RICH from the threshold for the emission of Čerenkov photons, and due to low tracking efficiencies in the OTR. Similar to the RICH-MUON matching, weak cuts on $\Delta t_{x,\,\mathrm{OTR-MUON}}$ and $\Delta t_{y,\,\mathrm{OTR-MUON}}$ ensure high efficiencies for correct combinations of track segments:

$$|\Delta t_{x,\,\mathrm{OTR-MUON}}| = |t_{x,\,\mathrm{MUON}} - t_{x,\,\mathrm{OTR}}| < 30\,\mathrm{mrad}, \tag{4.4}$$

$$|\Delta t_{y,\,\mathrm{OTR-MUON}}| = |t_{y,\,\mathrm{MUON}} - t_{y,\,\mathrm{OTR}}| < 30\,\mathrm{mrad}. \tag{4.5}$$

3. Track segments from the VDS are matched with segments from the RICH and the OTR in the non-bending plane of the magnet. Once two segments are matched, the difference of their slopes in the bending plane is used to determine the momentum of the track. Hence, this matching procedure belongs to category B. The cuts that were applied in the VDS-OTR matching were less tight than in the VDS-RICH matching, taking into account alignment problems and larger multiple scattering effects in the OTR:

$$|\Delta t_{y,\,\mathrm{VDS-RICH}}| = |t_{y,\,\mathrm{VDS}} - t_{y,\,\mathrm{RICH}}| < 10\,\mathrm{mrad}, \tag{4.6}$$

$$|\Delta t_{y,\,\mathrm{VDS-OTR}}| = |t_{y,\,\mathrm{VDS}} - t_{y,\,\mathrm{OTR}}| < 20\,\mathrm{mrad}. \tag{4.7}$$

   An example of VDS-RICH matching in a Monte Carlo simulation is shown in Fig. 4.6.

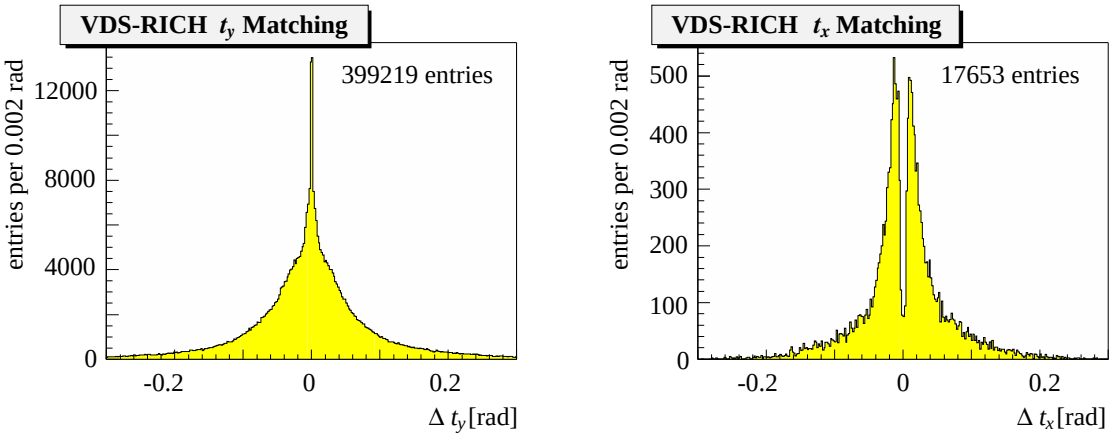

Figure 4.6: *Monte Carlo simulation of the matching of track segments from the VDS and the RICH. The left plot shows the difference of the y slopes from the VDS and RICH,* $\Delta t_{y,\,\mathrm{VDS-RICH}}$*. The difference of the x slope* $\Delta t_{x,\,\mathrm{VDS-RICH}}$ *is shown on the right plot for all combinations of track segments with* $\Delta t_{y,\,\mathrm{VDS-RICH}} < 1\,\mathrm{mrad}$*. The separation of positively and negatively charged particles is clearly visible.*

4. Since in both the muon system and the VDS the position of tracks is measured, a position matching between these subdetectors is possible. The MUREC-A package performs an extrapolation of the positions of track segments in the muon system to $z = 1300\,\mathrm{cm}$, the z position of TC2. The VDS segment is also extrapolated to $z = 1300\,\mathrm{cm}$, assuming a straight line in the non-bending plane of the magnet and neglecting the tracking errors. The y positions of the track segments are compared:

$$|\Delta y_{\mathrm{VDS-MUON}}| = |\, y_{\mathrm{MUON,\,TC2}} - (y_{\mathrm{VDS}} + (z_{\mathrm{TC2}} - z_{\mathrm{VDS}})\; t_{y,\,\mathrm{VDS}})| < 25\,\mathrm{cm}. \quad (4.8)$$

Here $y_{\mathrm{MUON,\,TC2}}$ denotes the extrapolated y position of the track segment in the muon system to the z position of TC2, $z_{\mathrm{TC2}} = 1300\,\mathrm{cm}$; $t_{y,\,\mathrm{VDS}}$ is the y slope in the VDS and y_{VDS} and z_{VDS} are the y and z positions where the y slope is measured in the VDS.

Next, one-to-one matches are combined to form track candidates. All VDS-OTR-MUON combinations are constructed by searching for track segments that occur in the VDS-OTR matching, the VDS-MUON matching, and in the OTR-MUON matching. Through this triple matching the number of possible combinations of track segments is further reduced. If no track pair is found that fulfills the above requirements, a similar algorithm, employing the same cuts, is applied to the VDS-RICH-MUON combinations in the events in order to use the RICH and the OTR in a complementary manner.

Momentum determination

For all matched combinations of track segments of the VDS, the OTR or the RICH, and the muon system, the momentum of the track candidate is calculated. The deflection of a charged particle in a homogeneous magnetic field is inversely proportional to the momentum. Since the field is assumed to be homogeneous, the deflection can be regarded as a single "kick" of the particle's transverse momentum, cf. Fig. 4.7. If the deflection angles are small, the z position where the kick occurs is approximately the middle of the region of the magnetic field.

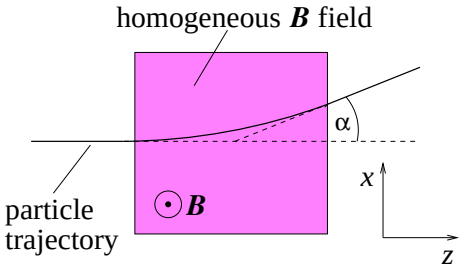

Figure 4.7: *Deflection of a charged particle in a magnetic field by the angle α. The view is along the direction of the field lines.*

Although the magnetic field in the HERA–B magnet is not exactly homogeneous, as a first approximation the momentum of charged particles can be described by a single p_T-kick at $z = 450\,\text{cm}$ that changes the slope of the particle in the x direction by the angle α :

$$p = \frac{\alpha_0}{\alpha} \qquad \text{with } \alpha_0 = (0.6334 \pm 0.0016)\,\text{GeV}/c. \tag{4.9}$$

α_0 has the meaning of a field integral, i.e. the effective influence of the entire magnetic field on the particle. Hence in the single-kick method, it is assumed that the integral influence of the magnetic field is constant and does not depend on the slope of the particles.

The value of the constant α_0 has been determined with a Monte Carlo simulation of the production of direct J/ψ mesons decaying into a muon pair. A fit to the deflection angle α as a function of the momentum p is shown in Fig. 4.8. For convenience, the arithmetic mean of the fit results for the positively and negatively charged muons has been chosen as the value for α_0, which is used to calculate the track momenta. However, due to the different acceptances of the HERA–B detector for positively and negatively charged particles, the values differ significantly. Therefore, the error of α_0 has been estimated by the difference of the mean value and the fit results.

The single-kick method for the momentum determination can be improved by a "swimming algorithm" as provided in the RANGER package [Man97a, Man97b]. Swimming means the extension of a track through a static inhomogeneous magnetic field via the integration of the equations of motion for the particle in the magnetic field. A swimming algorithm can be used to transport the track parameters and their covariance matrix from a position z_0 in front of the magnet to another position z_1 behind the magnet. The accuracy of this approach is superior to the single-kick method described above, since it takes into account the inhomogeneous structure of the magnetic field and depends on the track slopes.

The swimming algorithm that was used for the momentum determination in the matching analysis works in two steps: Since the extrapolation distance from the VDS to the OTR or the muon system is long (5–15 m), the track is first clipped into small pieces. The size of the track pieces depends on the momentum of the track. Then a numerical integration of the equations of motion is performed separately for each piece, employing a fifth order Runge-Kutta algorithm. The algorithm disregards energy loss and multiple scattering during the extrapolation. Details about the mathematical foundation of the swimming algorithm can be found in [Spi98] and references therein.

The actual momentum determination for a track candidate is performed iteratively:

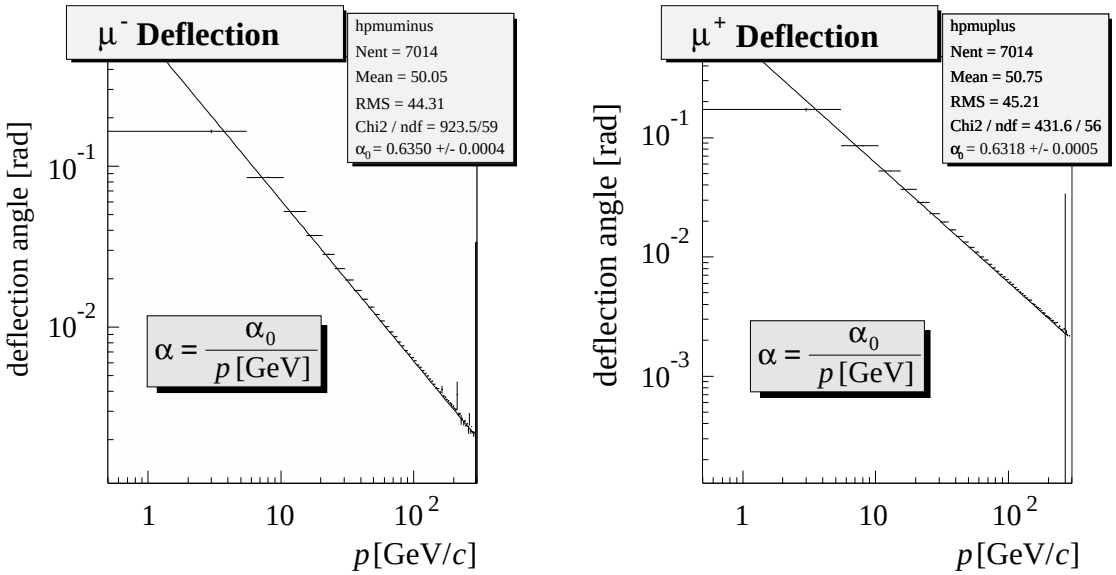

Figure 4.8: *Fits to the momentum dependence of the deflection angle: On the abscissae the logarithms of the μ^- momentum (left side) and the μ^+ momentum (right side) are plotted. On the ordinates the deflection angles α are plotted.*

The track parameters obtained from the VDS and the momentum estimate by the single-kick method serve as input parameters for the swimming algorithm. The swimming algorithm returns the track parameters behind the magnet that the track would have if the momentum were correct. The value of the track slope in the bending plane obtained by the integration of the equations of motion is compared with the value of the track segment from the RICH or OTR that has been matched with the VDS segment. The swimming algorithm is iterated with an improved momentum estimate until the agreement between the two values is better than 0.1 mrad, which is better than the accuracy of the matching, or the number of iterations reaches a given limit.

Cuts on track parameters and vertex position

After the momentum calculation, some cuts on the kinematics of the track and the vertex position are applied:

- Both tracks must have momenta larger than 5 GeV/c and transverse momenta p_{T} larger than 0.5 GeV/c. The muon absorbers filter out practically all muons with momenta smaller than 4–5 GeV/c. In addition, the missing inner part of the detector introduces an effective p_{T} cut of 0.7 GeV/c. Track segment combinations that result from wrongly matched segments also have momenta or transverse momenta that are smaller than the intrinsic cuts of the detector.

- To suppress wrong combinations of a real track and its own clones, i.e. other tracks reconstructed from the same detector hits, which have similar slopes, muon pairs with a slope difference of less than 0.5 mrad are neglected.

- For the VDS segments of the track pair, the position and closest distance of approach are determined. The explicit formula to calculate these quantities is given in Appendix B. This method neglects the covariance matrices of the tracks. The

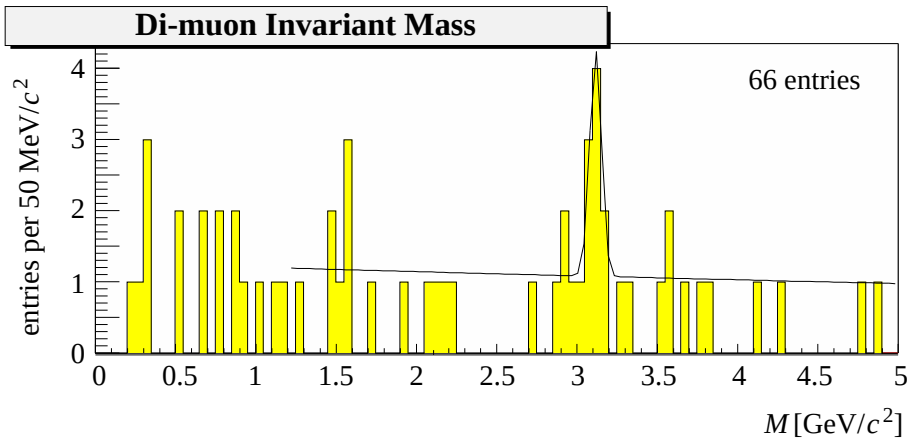

Figure 4.9: *First observation of a* J/ψ *signal with a predecessor of the matching algorithm described in the text. On the abscissa of the histogram, the invariant mass of the muon pair is plotted. A peak can be observed at a mass of about* 3.1 GeV/c^2 *[Hus00b].*

position of closest approach $(x_{\mathrm{CDA}}, y_{\mathrm{CDA}}, z_{\mathrm{CDA}})$ is demanded to lie within a box around the HERA–B target from -1 cm to 1 cm in x and y and from -6 cm to 2 cm in the z direction. Furthermore, the distance of closest approach must not exceed 0.02 cm. These cuts serve as a simple substitute for a full vertex fit.

Discussion

The matching of stand-alone reconstructed track segments was the first method which led to the observation of a J/ψ signal in the di-muon channel [Eig00]. The first signal that was observed during the development of the analysis described in this chapter is shown in Fig. 4.9 [Hus00b]. To obtain the J/ψ signal, a predecessor of the method described above was used, where only the matching between the VDS, the RICH, and the muon system is performed and the cuts are very tight to suppress background. Large values for the p_{T} cut are used to reduce the background of non-J/ψ track pairs since the average transverse momentum for a track pair from the decay of a J/ψ meson of mass $M = 3.09687\,\mathrm{GeV}/c^2$ [Gro00] is expected to be $\langle p_{\mathrm{T}} \rangle \approx Mc/2 \approx 1.5\,\mathrm{GeV}/c$. The following cuts have been used in the analysis that led to the result of Fig. 4.9:

$$\begin{aligned}
\Delta t_{x,\,\mathrm{RICH-MUON}} &< 5\,\mathrm{mrad},\\
\Delta t_{y,\,\mathrm{RICH-MUON}} &< 15\,\mathrm{mrad},\\
\Delta t_{y,\,\mathrm{VDS-RICH}} &< 1\,\mathrm{mrad},\\
\Delta x_{\mathrm{VDS-MUON}} &< 15\,\mathrm{cm},\\
p &> 10\,\mathrm{GeV}/c,\\
p_{\mathrm{T}} &> 1.2\,\mathrm{GeV}/c,\\
-6\,\mathrm{cm} < z_{\mathrm{CDA}} &< 2\,\mathrm{cm}.
\end{aligned}$$

Despite its success in observing the first J/ψ signals and the advantage of being independent of a special trigger, the matching method suffers from several drawbacks. It relies on stand-alone reconstruction packages in four subdetectors which bear certain inefficiencies:

- At an interaction rate of 5 MHz, 7.4% of the reconstructed track segments in the VDS are ghost tracks, i.e. tracks that do not belong to an actual track, and 3.1% of the track segments are track clones, i.e. more than one reconstructed track for the same "real" track [Eme00a].

- The stand-alone RICH reconstruction is inefficient near the threshold for the emission of Čerenkov photons, i.e. momenta of approximately 2.0 GeV/c for muons, 2.7 GeV/c for pions and 9.6 GeV/c for kaons.

- In the 2000 run, 5–10% of the chambers in the OTR were not operational due to problems with the high-voltage. In addition, the offline tracking algorithms in the OTR turned out to be less efficient on the di-muon triggered data than expected from Monte Carlo simulations. Most probably, the reason for this behavior is a poor interplay between the OTR, which included inefficient regions, and the pattern recognition algorithms in the main tracker.

- The stand-alone muon reconstruction suffers from inefficiencies in the muon detector: the cathode pads in MU3 and MU4 that showed low efficiency values in the year 2000 data-taking are used as a starting-point for the MUREC-A tracking.

Furthermore, a certain part of the tracks are lost through the matching cuts. The matching criteria are not momentum-dependent, while e.g. effects of multiple scattering that can spoil the matching are inversely proportional to the momentum. Hence, the matching method can be considered as a first temporary solution for the reconstruction of muon tracks.

4.3.2 Second-Level-Trigger-based tracking

The succeeding tracking method used for the analysis of di-muon triggered data was based on information from the SLT. Since the SLT algorithm performs a complete tracking in the VDS and the OTR including the momentum determination through the matching of track segments in front of and behind the magnet, the SLT information can be used as a substitute for the offline tracking. The SLT tracking information can be supplemented by a comparison with the track parameters in the subdetectors where the offline tracking is under good control, mainly the VDS. The signal quality can be further improved by some simple cuts. Details of this analysis can be found in Chapter 5.

The SLT in the event structure

A schematic overview of the SLT record, the data structure in which SLT information is stored in an event record, can be found in Fig. 4.10. The SLT record consists of the following elements: In a header, the status of the SLT for each event is stored, including the trigger decision, the number of triggers issued, and the number of tracks in the event. The basic object of the SLT record is a trigger, i.e. all information that is involved in a single trigger decision by the SLT. Each event contains a number of data structures to store the single triggers (SLT_TRIGGER) along with the trigger type, e.g. a di-muon or a di-electron trigger, and the trigger status (accepted or rejected). Each SLT_TRIGGER structure usually contains two SLT_TRACK structures which consist of information about the track seeds from the earlier trigger levels (SLT_SEEDTRACK), the fitted track segments in the main tracker from the Slicer/Refit algorithms (SLT_REFITTRACK), the fitted track segments in the VDS provided by L2Sili (SLT_SILITRACK) and the

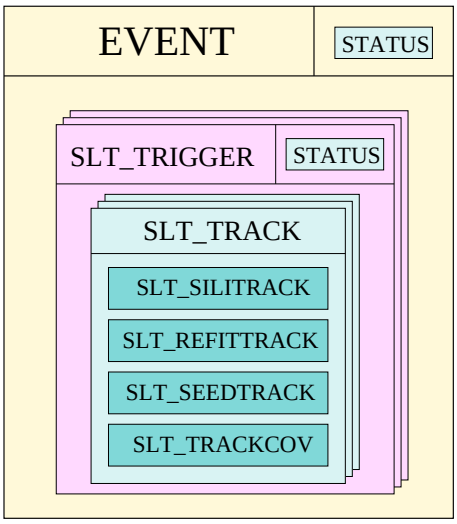

Figure 4.10: *Sketch of the SLT event structure: The SLT record of each event contains the event status and several track combinations that fulfill the trigger conditions of the SLT* (SLT_TRIGGER). *Each of these triggers consists of tracks* (SLT_TRACK). *Each* SLT_TRACK *contains tracking information from the track seeds provided by the earlier trigger levels* (SLT_SEEDTRACK), *the* L2Sili *algorithm in the VDS* (SLT_SILITRACK), *and of the* Slicer/Refit *packages in the main tracker* (SLT_REFITTRACK). *In addition, the track covariance matrix is stored in the* SLT_TRACKCOV *data structure.*

covariance matrix of the track parameters (SLT_TRACKCOV). If there is more than one positive trigger decision by the SLT in an event, the SLT_TRIGGER data structures are ordered by increasing quality.

Momentum determination

The momentum determination that is used by the SLT algorithms is based on the field map method. The basic idea of this method is to model the influence of the magnetic field on charged particles in a slope-dependent way. The field map contains a parametrization of the effective magnetic field integral in the HERA – B magnet as a function of an array of track slopes $(t_{x,\mathrm{front}}, t_y)$ in front of the magnet. The field integrals are stored in look-up tables, and interpolations are needed between the discrete points $(t_{x,\mathrm{behind}}, t_y)$. Consequently, the momentum of a track is calculated in a modified, slope-dependent version of Equation 4.9:

$$p(t_{x,\,\mathrm{front}}, t_{x,\,\mathrm{behind}}, t_y) = \frac{\alpha_0(t_{x,\,\mathrm{front}}, t_y)}{\alpha} = \frac{\alpha_0(t_{x,\,\mathrm{front}}, t_y)}{t_{x,\,\mathrm{behind}} - t_{x,\,\mathrm{front}}}. \tag{4.10}$$

Here $\alpha_0(t_{x,\,\mathrm{front}}, t_y)$ is the field integral, and $t_{x,\,\mathrm{front}}$ and $t_{x,\,\mathrm{behind}}$ are the x slopes in front of and behind the magnet.

To improve the momentum measurement of the SLT, the field map method is used again in the offline analysis. Similar to the swimming method, the slopes in x and y of the track in front of the magnet and the momentum as determined by the SLT algorithm are fed into the field map. The field integral obtained from the field map is used to calculate a new momentum via Equation 4.10. This modus operandi is iterated

three times. Finally, all components of the momentum vector of the track (t_x, t_y, p) are measured to a sufficient accuracy, so that the invariant mass of the combination of tracks can be calculated.

Discussion

The events that pass the SLT trigger still include events without real muon pairs. Most of the events include more than one trigger of one type, since the SLT trigger decision keeps all charge combinations $(++)$, $(+-)$, $(-+)$, and $(--)$ that pass the SLT algorithms. Furthermore, the SLT tracking is not free of ghost tracks and track clones. Therefore, clones and combinatorial background, e.g. from decays in flight of charged pions or kaons, also occur in the invariant mass spectrum of track pairs. A deeper discussion of the background can be found in Section 5.2.4. The quality of the invariant mass spectrum can be improved by applying some additional cuts in the offline analysis. Details will be described in Chapter 5.

4.3.3 The "standard" procedure

The "standard" procedure to perform the reconstruction of events relies on the offline reconstruction of tracks and correct determination of the track parameters through a combination of the information that the subdetectors provide. In the following, the track reconstruction as implemented in the HERA–B reconstruction and simulation environment ARTE [Alb95b] will be briefly described. Note that the details of the reconstruction process may change with different ARTE versions. All analyses which will be presented in the following are performed within the framework of the release ARTE-03-08-r5.

The ARTE event record

All information about a recorded or simulated event that is relevant to further analysis is stored in a data structure commonly called the event record. The event record includes tables for different classes of data, e.g. the raw detector hits, trigger information, and the results of the event reconstruction. The discussion of the event record in this chapter will be restricted to the part that allows offline analysis based on tracks and vertices. A sketch of the ARTE event record can be found in Fig. 4.11.

All important parameters of a track that are determined in the reconstruction chain are written into the track table RTRA (Reconstructed Tracks). The contents of the RTRA table include the following information:

- For each subdetector the number of hits that are assigned to the track is stored.
- The tracking parameters include the coordinates of the initial point of the track $(x_\mathrm{f}, y_\mathrm{f}, z_\mathrm{f})$, the momentum vector at the initial point of the track $(t_{x,\mathrm{f}}, t_{y,\mathrm{f}}, p_\mathrm{f})$ and the slope $(t_{x,\mathrm{r}}, t_{y,\mathrm{r}})$ and the Čerenkov angle measured in the RICH.
- The quality of the track reconstruction and the errors are given in terms of the χ^2 value of the track fit and the covariance matrix of the track parameter vector $(x, y, t_x, t_y, p_\mathrm{f})$. The meaning of χ^2 is described in Section B.3.
- The particle identification devices, i.e. the RICH, the ECAL, the TRD, and the muon system, provide likelihoods for several particle hypotheses. The ECAL can

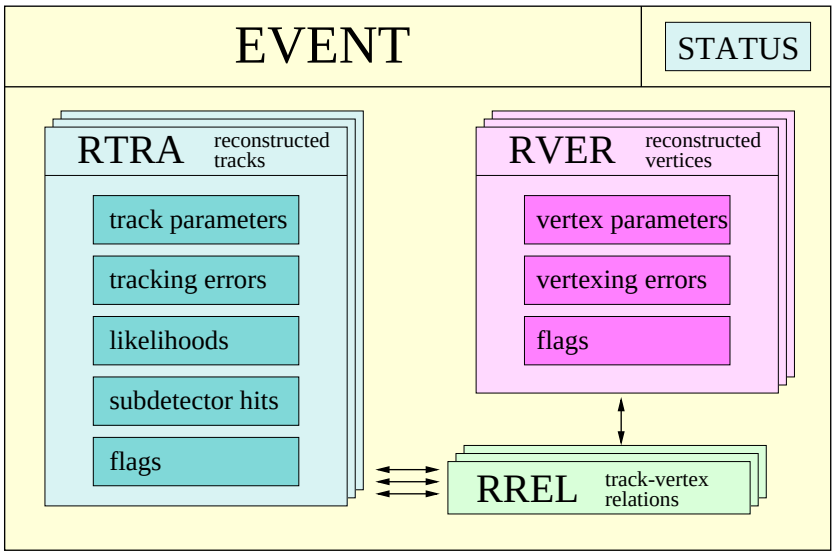

Figure 4.11: *Illustration of a part of the ARTE event record: The most important tables in the event record are RTRA, which contains the track parameters and their errors, the numbers of hits in the individual subdetectors, and the likelihoods for different particle hypotheses, and RVER, where the reconstructed vertex data is stored, mainly the vertex positions and their errors. A relationship between a vertex and the tracks that have been used to fit the vertex is provided by the RREL table.*

identify electrons, hadrons, and minimally ionizing particles, the TRD provides likelihoods for electrons and hadrons, and in the muon system likelihoods for muons and hadrons are calculated. The RICH provides likelihoods for electrons, muons, pion, kaons, and protons.

- Additional information from the reconstruction steps is stored, e.g. the probability of the track to be a clone, details of the likelihood calculations, and the way the track momentum was calculated.

- RTRA contains relations – often called "ARTE relations" – to several other ARTE tables, e.g. to a list of the detector hits that were used for the reconstruction, a list of the reconstructed track segments from which the track was linked together, and the decay vertex in the case of short-lived particles.

Besides the RTRA table, the table for reconstructed vertices, RVER (Reconstructed Vertices), is the most important ARTE table for physics analyses. The vertex parameters that are stored in RVER include the position and the mass. For primary vertices the closest target wire is also stored. Furthermore, there is a relation to the ARTE track table that contains a list of the tracks that have been used to fit the vertex.

Hit preparation and stand-alone reconstruction

Before the reconstruction of track segments can start, the raw detector data have to be prepared. In the OTR for example the hit and time-to-digital converter information of the detector channels have to be translated into drift times and space points. The hits in a single layer only contain position information perpendicular to the sensitive materials

of the detectors, i.e. the VDS silicon strips and the wires in drift chamber detectors. However, combining the three wire orientations allows extraction of the point in space where the hit occurred. This procedure is called hit preparation.

After the hit preparation, the stand-alone reconstruction programs for the individual subdetectors are called in the following order:

1. The reconstruction in the VDS is carried out by the CATS (Cellular Automaton for Tracking in Silicon) package. In CATS a cellular automaton algorithm is used for pattern recognition, and Kalman filter methods are employed to fit the track parameters [Kis99, Eme00a].

2. The CARE (Calorimeter Reconstruction) package performs the reconstruction in the ECAL. In a first step, the CARE algorithm searches for all showers in the ECAL. Depending on the particle type, the energy deposition in the cells of the ECAL varies. While minimally ionizing particles only deposit energy in one or two isolated cells of the ECAL, energy from electromagnetic or hadronic showers is deposited in a cluster of cells. If several clusters overlap, the signature in the ECAL is even more complex. CARE provides an algorithm to classify these clusters [Vil97].

3. The reconstruction of tracks in the main tracker is performed by the RANGER package. The tracking in RANGER uses the Kalman filter technique in combination with "concurrent track evolution", a mechanism that allows efficient tracking even in a high-occupancy environment with up to 200 charged tracks per event in the main tracker. The Kalman filter algorithm fits track segments in steps by propagating them from one detector layer to the next. The basic idea of the concurrent track evolution is to store all plausible combinations of detector hits that form a track in parallel and keep only the best track candidates in each step of the Kalman filter [Man97a, Man97b].

   RANGER is able to work in a seeded mode, in which prior knowledge of the track parameters is used to define regions in the main tracker where tracks can be potentially found. This feature has been used extensively in the reconstruction of the 2000 data. The SLT tracks in the main tracker, as obtained from SLICER/REFIT, serve as seeds for the offline reconstruction with RANGER. The "SLT seeded" mode helps to increase the reconstruction efficiency and to decrease the computing time needed by the RANGER algorithm.

4. The stand-alone ring search in the RICH is done by the RISE (Ring Search) package. RISE identifies the radius and the center of RICH rings from which the track slope and the Čerenkov angle can be deduced [Duj00].

5. In the muon system, the MUREC-A (Muon Reconstruction) package is employed to reconstruct tracks. Hits in the pads or pixels of the superlayers MU3 and MU4 are used as starting-points for a Kalman filter algorithm that follows the tracks to MU2 and MU1 [Fom97].

After the track segments in the OTR are reconstructed, the CARE package tries to link them with ECAL clusters. Consequently, neutral particles can be distinguished from charged particles. In addition, the charged particles are separated into high and low energy clusters.

Matching, track selection, and refit

Following the stand-alone reconstruction the track segments are matched. Similar to the simple matching routines described in Section 4.3.1, track segments from different subdetectors can be matched to define a track. The matching is carried out by the MARPLE package [Igo98]. The extrapolation and parameter matching methods in MARPLE include the effects of multiple scattering and depend on the details of the track parameters. After the matching of track segments, the momentum of the track as a whole can be determined. In the default setting in ARTE-03-08-r5, segments in the VDS and in the PC chambers of the main tracker are matched. Finally, the track bank is filled with the tracks that were formed by the matching of track segments.

At this point, all tracking information for a track is available. With the global track parameters, especially the track momentum, the tracking results from the subdetectors can be updated and further improved. While the Kalman-filter-based tracking in the individual subdetectors is an iterative procedure, the refit of the track is a global operation. Currently, the refit is based on track segments from the VDS and the OTR.

Particle identification

The particle identification in the RICH relies on a measurement of the angles of the Čerenkov photons. In a medium with refractive index n, particles with a velocity $\beta \equiv v/c$ – c being the velocity of light in the vacuum – emit photons at the Čerenkov angle θ_{C}:

$$\cos\theta_{\mathrm{C}} = \frac{1}{n\beta}. \tag{4.11}$$

For small Čerenkov angles, the relation

$$\theta_{\mathrm{C}}{}^2 = \theta_0{}^2 - \frac{m^2}{p^2} \tag{4.12}$$

holds, where θ_0 is the Čerenkov angle for particles with the velocity $\beta = 1$, and m and p are the mass and the momentum of the particles to be identified. Therefore, particles of a given momentum can be distinguished by their mass if the Čerenkov angles are known.

The Čerenkov angles can be measured in two different ways. In the stand-alone method provided by RISE, the slope of a track and the Čerenkov angle are deduced from a measurement of the center and the radius of a RICH ring. RISE also works in a seeded mode, where the center of the rings are constrained by the slopes of external tracks and the radii are constrained by the momenta of these tracks. The RIRE [Ari99] and the RITER algorithms [Pes01] do not reconstruct rings, but use the accumulation of Čerenkov photons to calculate likelihoods for several particle hypotheses. This method has the advantage of being more efficient for particles near the Čerenkov threshold, where the number of photons produced via the Čerenkov effect is small. However, the method relies on the quality of the seed tracks. Therefore the alignment and accuracy of the tracking detectors enter into the efficiency of the RIRE and RITER algorithms.

In the ECAL, the shape of the showers of secondary particles is used for the separation of particles which interact via the electromagnetic force, mainly electrons and photons, or via the strong force, e.g. pions. The energy deposition in the individual ECAL cells caused by a shower is combined to form clusters. The number of clusters is significantly larger for hadrons than for electrons and photons, while minimal ionizing

particles like muons deposit energy in only one ECAL cell. From this information the likelihood probability for the different particle types can be calculated.

The muon identification is performed by the MuonID program. The main idea of MuonID is to carry out a seeded search for tracks in the muon system. The algorithm of MuonID works in five steps [Fom01]:

1. The raw hits in the muon system are prepared for the algorithm.

2. The seed for the hits in the muon system comes from the main tracker. Track segments from the main tracker are extrapolated to the muon detector, preferably from the TC chambers, which are closest to the muon chambers, but also from the PC chambers.

3. The extrapolation of the seed tracks to the muon detector is implemented as a Kalman filter propagation. From one superlayer to the next, an RoI is calculated which takes into account errors due to multiple scattering and alignment. All reasonable propagation possibilities are kept as a track tree.

4. The muon likelihood is calculated for all track candidates in the track tree. The likelihood is a function of the quality of the track, measured by the χ^2 of the track fit, and the distribution of hits in the individual superlayers of the muon system around the point where the track trajectory and the superlayer intersect.

5. The best branch of the track tree is kept, and the muon likelihood is stored in the track bank, along with flags that indicate the result of the extrapolation of the track seed.

Vertexing

In HERA–B there are several vertexing packages available, all of which rely on Kalman filter techniques. The VT package [Loh95] is a FORTRAN-based tool, which has been recently re-implemented in C++, resulting in the VT++ package [Gle00]. Independently, the ROVER (Reconstruction of Vertices) package was developed [Per00, Eme00b]. A common C++ interface to both VT/VT++ and ROVER is provided by the GROVER (Generic Reconstruction of Vertices) environment [San00].

Since the combination of ROVER with the GROVER front-end is established as the standard vertexing package in HERA–B, the description of the vertexing will be restricted to a short overview of this tool.

The primary vertex reconstruction is a purely geometrical procedure, i.e. no information about the track momenta is involved. Hence vertices can be reconstructed on the basis of the well-determined positions and slopes of VDS track segments alone. GROVER also accepts tracks from the RTRA table or a mixture of RTRA tracks and track segments in the VDS. The reconstruction of primary vertices starts with a pattern recognition algorithm that assigns a track to a target wire if the distance to the wire in the wire plane is smaller than $3.5\,\sigma_{\mathrm{T}}$, σ_{T} being the error of the intersection point of the track and the wire plane. A cluster algorithm searches for clusters of intersection points and combines them with primary vertex candidates if they consist of at least three tracks. The vertex positions and their covariance matrices serve as starting-points for a Kalman filter algorithm, where the fitted track parameters are "virtual measurements" of the vertex position. New tracks are assigned to the vertex, and the vertex position

is updated. Good knowledge of the wire positions is essential for the successful reconstruction of primary vertices. However, the actual wire position is only poorly known in the reconstruction. Therefore ROVER applies a mechanism to follow the movement of the target wire and to reconstruct the actual position.

The reconstruction of secondary vertices is not included in the standard reconstruction chain. However, tools for this task are available in GROVER. Secondary vertices can be reconstructed by a momentum-dependent Kalman filter based algorithm. Mass constraints can be introduced for a fit of secondary vertices. A mass constraint decreases the number of free fit parameters by one by fixing the invariant mass of the vertex. Hence, the precision of the parameters obtained in a constrained vertex fit is often better than the precision obtained in an unconstrained fit.

The implementation of mass constraints in GROVER is realized as an additional pseudo-measurement directly in the filtering procedure. This is more general than the standard way of Lagrange multipliers in the calculation of the individual χ^2 contributions of tracks since it allows incorporation of any type of constraint [Eme00b].

The results of the primary and secondary vertex fits are stored in the RVER table, including relations to the tracks that have been used in the fits.

4.3.4 Summary

The development of analysis strategies started from simple algorithms that match track segments from different subdetectors. With these algorithms, the first J/ψ signal in the muon channel could be observed. Using the pretrigger-SLT di-muon trigger and tracking information for the analysis was a second step towards the final analysis chain.

The final analysis chain is based on reconstructed tracks. Thus, it makes use of several complex reconstruction packages, which perform reconstruction steps mainly based on the same ideas as the simple algorithms but are implemented on a more sophisticated level. The results obtained with the SLT tracking and the "standard" procedures will be discussed in detail in Chapter 5.

Chapter 5

Analysis of the di-muon triggered data in the 2000 data-taking period

After the main analysis strategies have been discussed in Chapter 4, this chapter deals with the most recent analysis of the di-muon triggered data that has been developed in the context of this Diploma thesis. The analysis chain for the data will be described, and the analysis of the complete di-muon triggered data sample from 2000 will be presented. The results will be compared with the outcome of the SLT-based tracking discussed in Chapter 4. Furthermore, this chapter includes a comparison of the results to Monte Carlo simulations of the HERA–B detector and trigger as well as a preliminary discussion of background processes and systematic effects affecting the di-muon invariant mass spectrum.

5.1 Analysis chain

The main strategy of the analysis presented in this chapter is to identify candidates for muon tracks and to match pairs of these track candidates to vertices. The invariant mass spectrum of the vertices includes the J/ψ resonance, the properties of which will be examined. The background underneath the J/ψ peak and in the sidebands of the peak also contains interesting physics signals, e.g. muon pairs from the Drell-Yan process.

The analysis of the data can be divided into two parts. The first part is carried out within the ARTE environment [Alb95b]. It consists of a preselection of tracks and vertices mainly from the ARTE tables RTRA (Reconstructed Rracks) and RVER (Reconstructed Vertices). In this step, a data structure, which is suited for the final analysis, is filled with the relevant information. The second part of the analysis is done within the framework of the ROOT physics analysis package [Bru97]. In ROOT, further selection cuts are applied to the preselected tracks and vertices to obtain the final observables.

5.1.1 Preselection of tracks and vertices

After a short description of the ROOT event structure that serves as an interface between the two analysis parts, the preselection of tracks and vertices within the ARTE framework will be discussed.

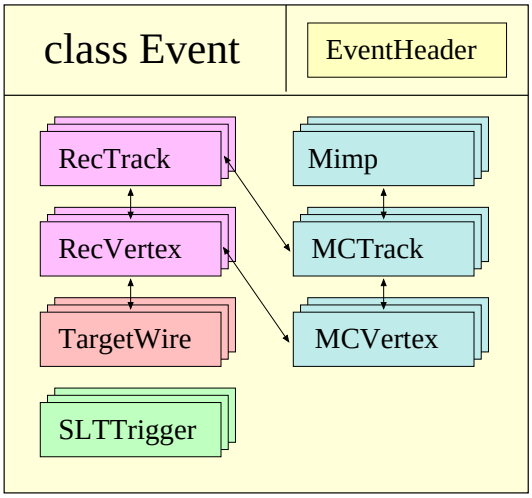

Figure 5.1: *Simplified picture of the structure of the ROOT event class used for the analysis described in this chapter: An event contains a header (*EventHeader*), where general information, e.g. the event number, is stored. There are containers for reconstructed tracks and vertices (*RecTrack, RecVertex*), for Monte Carlo tracks and vertices (*MCTrack, MCVertex*), for Monte Carlo impact points (*Mimp*), for the target wires (*TargetWire*), and for SLT information (*SLTTrigger*). Some of the containers include subcontainers. There are relations between tracks and vertices, vertices and target wires, and between Monte Carlo objects and their corresponding reconstructed objects, as indicated by arrows.*

The ROOT event class

To keep the final analysis independent of the large environment of the HERA – B software, the track and vertex data are stored in a ROOT event object. The object-oriented approach of ROOT is more flexible than the previous n-tuple based analysis, because it allows a more natural modeling of the hierarchical structure of events in a particle physics experiment. An event contains general information on the top level and several containers for tracking objects. The number of objects in each container is unknown a priori, and each container may include a set of subcontainers, e.g. a container for reconstructed tracks may contain a collection of likelihoods.

The design of an event class depends on the problem under investigation. For most four-vector-based physics analyses and Monte Carlo studies in HERA – B, the following structure – shown in Fig. 5.1 – is suitable: The event contains a header, where general information about the event is stored. Several containers for physics analysis objects are implemented, like containers for reconstructed tracks and vertices, containers for Monte Carlo tracks and vertices, for Monte Carlo impact points, and for the target wires. In order to use the information from the SLT, an additional container for the SLT_TRIGGER structure, as described in Section 4.3.2, is needed. The connections between different analysis objects, e.g. between a vertex and the tracks that have been used to fit the vertex, are modeled via relations between the corresponding entries in the different containers.

Track preselection

In the track preselection step, a subset of the tracks that are stored in the RTRA table is chosen for further analysis. In order to keep as much flexibility as possible for the second part of the analysis, this track sample contains all tracks that might be useful for the final analysis, i.e. tracks which are reconstructed at least in the VDS and in the main tracker and fulfill minimal quality criteria. However, the RTRA table in its present form (ARTE-03-08-r5) also contains track segments which are reconstructed in the VDS only or in the VDS and subdetectors the information of which is not used in the analysis. About 20% of the tracks originate in the matching of VDS and main tracker segments, 30% are VDS–ECAL matches, 20% VDS–RICH matches and the remaining 30% are track segments from the stand-alone reconstruction in the VDS and the main tracker. This choice has been made for historical reasons, since the first track definition in HERA–B was based on the matching of VDS and ECAL information. The composition of the RTRA table is expected to be changed in the future [Mas01]. The following cuts are applied to preselect track candidates for the second part of the analysis:

- The tracks must carry a flag indicating a reconstructed charged track. This cut discards track candidates without momentum determination and disconnected track segments in the VDS and the main tracker.
- The χ^2 of the track fits must be better than 200 in order to cut away tracks with extremely bad fit quality. The definition of χ^2 for tracking in HERA–B can be found in Section B.3.
- Since the VDS tracking information is essential to determine the track parameters close to the target and in front of the HERA–B magnet, the tracks must have more than five hits in the VDS.

The preselected tracks are stored in a ROOT event object.

Vertex selection

In the online reconstruction in the Fourth Level Trigger (4LT) and in the reprocessing of the data, primary vertices are reconstructed by the Grover (Generic Reconstruction of Vertices) package. The vertex selection step starts with copying all primary vertices from the online reconstruction into the event object.

The goal of the analysis described in this chapter is to extract the di-muon invariant mass spectrum produced in primary interactions on the target wires. Hits in the muon system serve as a first indicator for a muon track candidate. Therefore, only a subsample of the preselected tracks, containing tracks with hits in the muon system, is fitted by a two-prong secondary vertex fitting algorithm, which is only used to determine the kinematics of track pairs close to the target. These vertices are not expected to be displaced from the closest primary vertex. For the vertex fit, the quality of the tracks is required to be better than for the track preselection. Furthermore, only tracks from the VDS–RICH and VDS–main tracker segments which have a continuation in the muon system should be used in the fit. Hence, the following cuts are applied after the track preselection:

- The tracks must have more than five hits in the muon system. This cut serves as a simplified muon identification, since hits in the muon system reflect the successful continuation of a track to the muon system by the the muon identification package MuonID.

- The quality of the tracks for the vertex fit must be better than the quality of the preselected tracks, indicated by a cut on the χ^2 of the tracks of $\chi^2 < 100$.
- Sometimes wrong combinations of track segments result in very low or very large reconstructed momenta, even violating four-momentum conservation. Particles with these momenta are either unphysical or would never reach the muon detector. Therefore, the selected tracks must have momenta in the range of $2\,\mathrm{GeV}/c < p < 333\,\mathrm{GeV}/c$.

Each combination of tracks that fulfill these criteria is fitted to a secondary vertex. In addition, it is checked if the tracks have already been fitted to a primary vertex. If both tracks point to the same primary vertex, the other tracks belonging to the primary vertex are added to the track pair, and the vertex fit is performed again. Because of the larger number of tracks in the vertex the number of degrees of freedom for the fit is increased, and the vertex quality is expected to improve.

The vertex is rejected if the χ^2 per degree of freedom of the vertex fit is larger than 200 or the reconstructed invariant mass is outside the widest mass range of interest for the analysis, i.e. from $2\,\mathrm{GeV}/c^2$ to $10\,\mathrm{GeV}/c^2$. If the vertex mass is close to the J/ψ mass, in the range of $2.9\,\mathrm{GeV}/c^2$ to $3.3\,\mathrm{GeV}/c^2$, an additional constrained fit is performed to improve the vertex quality. The constraint consists of fixing the mass of the vertex – and hence the mass of the track pair – to the J/ψ mass. The results of the vertex fit are stored in the ROOT event object.

Extraction of the SLT triggers

After the reprocessing of the di-muon triggered data, the SLT information, i.e. the SLT_TRIGGER and SLT_TRACK structures, are stored in the ARTE tables RSLI and RSLA, which provide information on the SLT track parameters that are equivalent to the SLT record described in Section 4.3.2.

Similar to the "standard" analysis, the first part of the analysis of the SLT triggers is carried out within the ARTE framework. For both tracks in each trigger the SLT_SEEDTRACK, the SLT_REFITTRACK, and the SLT_SILITRACK are extracted. The momenta of the tracks are re-determined via the field map method, and the invariant mass of the track pair is calculated. The tracks are kept if the track momenta are smaller than $300\,\mathrm{GeV}/c$. Events that pass these criteria are stored in SLTTrigger objects in the ROOT event class.

5.1.2 The final analysis

A ROOT event object is written to disk after the preselection if it contains at least one successfully reconstructed muon pair vertex or one SLTTrigger object that passes the cuts. The final analysis is done on these event objects.

In the final analysis, additional quality cuts are applied to the vertex and the tracks that form the vertex. The cuts are ordered in the following hierarchy:

1. Event-based cuts select events by their global properties.
2. In selected events, track-based cuts select tracks from muon candidates using kinematic and particle identification criteria.
3. Vertex-based cuts select vertices fitted from selected tracks by checking the quality of the vertex fit.

The cuts have been tuned by optimizing the significance Σ of the J/ψ signal. Since no appropriate Monte Carlo simulation of the background in the invariant mass spectrum was existing that included the trigger, cf. Section 5.2.4, the cut optimization had to be performed on real data. A common choice for the definition of the significance has been used for this analysis:

$$\Sigma = \frac{S}{\sqrt{B}}, \tag{5.1}$$

where S is the number of signal events in the J/ψ peak, and B is the number of background events underneath the peak in the range of 2.9–3.3 GeV/c^2. Assuming S and B are Poisson-distributed with the variances ${\sigma_S}^2 = \sqrt{S}$ and ${\sigma_B}^2 = \sqrt{B}$, Σ measures the strength of the signal compared to a one-sigma fluctuation of the background. With $\Sigma^2 = S \times S/B$ the optimization of the significance can also be interpreted as the simultaneous optimization of the signal strength and the signal-to-background ratio.

Fits to the invariant mass spectrum

To evaluate the effects of the cuts in the analysis, the numbers of signal and background events have to be measured. This is done by fitting the invariant mass spectrum of the vertices to a model of the J/ψ signal and the background shape. Furthermore, the position and width of the signal are determined, leading to conclusions about the response and resolution of the HERA–B detector.

The fit function f is a product of a parametrization of the background by an exponential function g and a Gaussian function h which describes the signal:

$$f(M; p_0, p_1, N_{\mathrm{J}/\psi}, M_0, \sigma) = g\,(M; p_0, p_1) \times h(M; N_{\mathrm{J}/\psi}, M_0, \sigma), \tag{5.2}$$

where the functions g and h are defined by

$$g\,(M; p_0, p_1) = \exp\left[p_0 + p_1 M\right] \quad \text{and} \tag{5.3}$$

$$h(M; N_{\mathrm{J}/\psi}, M_0, \sigma) = \frac{N_{\mathrm{J}/\psi}}{n_{\mathrm{bins}}} \frac{1}{\sqrt{2\pi}\sigma} \exp\left[-\frac{1}{2}\frac{(M - M_0)^2}{\sigma^2}\right]. \tag{5.4}$$

Here M denotes the invariant mass of the muon pair, and n_{bins} is the number of bins per GeV/c^2 in the mass spectrum histogram. This number has been fixed to $n_{\mathrm{bins}} = 40$. The free parameters of the background function g are the constant $\exp[p_0]$ and the slope p_1. The signal function h depends on the number of J/ψ mesons $N_{\mathrm{J}/\psi}$, the mass M_0 of the J/ψ and the width σ of the J/ψ signal.

The description of the background with an exponential function is purely empirical and accounts for the suppression of large invariant masses in the combinatorial background from meson decays in flight. The J/ψ signal is a rather sharp resonance in the mass spectrum, having a width of only $(87 \pm 5)\,\mathrm{keV}/c^2$ [Gro00]. Therefore detector resolution effects dominate the measured width of the J/ψ signal, which is already approximately $40\,\mathrm{MeV}/c^2$ in Monte Carlo simulations, cf. Section 5.2.3. Hence, a Gaussian function for the signal assumes only statistical errors in the measurement, neglecting systematic effects on distortions of the mass spectrum.

The number of background events is given by the area under the graph of the background function g in the region $2.9\,\mathrm{GeV}/c^2 < M < 3.3\,\mathrm{GeV}/c^2$ as

$$N_{\mathrm{bkg}} = n_{\mathrm{bins}} \int_{2.9\,\mathrm{GeV}/c^2}^{3.3\,\mathrm{GeV}/c^2} \exp\left[p_0 + p_1 M\right]\,\mathrm{d}M. \tag{5.5}$$

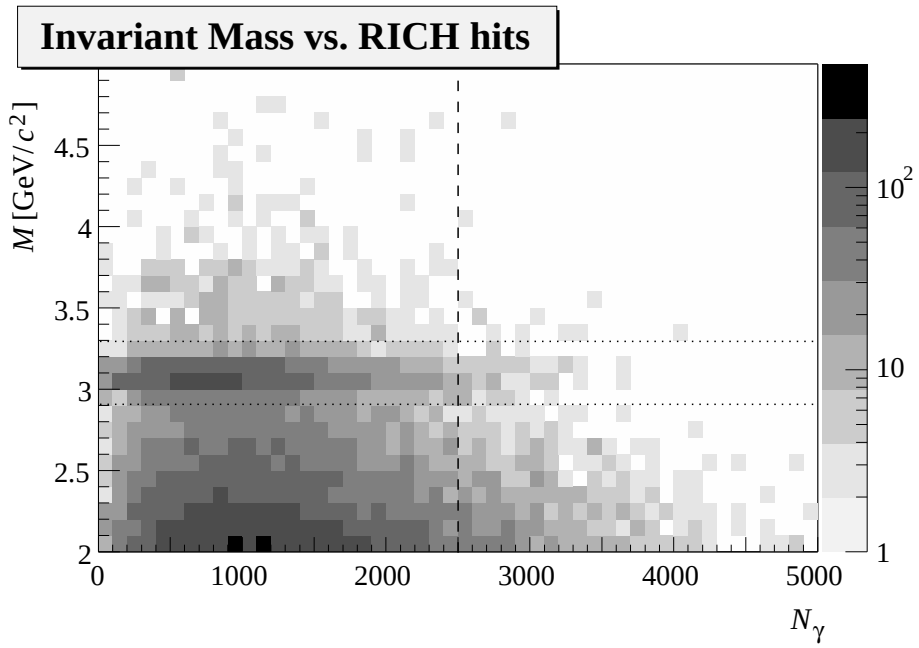

Figure 5.2: *The invariant mass of muon pairs as a function of the number of RICH photons N_γ: The dotted horizontal lines delimit the* J/ψ *mass region, and the dashed vertical line indicates the multiplicity cut $N_\gamma < 2500$. Most events with more than 2,500 RICH photons do not contain* J/ψ *decays.*

The limits of the above integral have been fixed instead of using e.g. a 3σ region around the signal peak. The reason for this is to have a defined range where the background is evaluated, while the measured width of the signal varies from run to run; see Table D.1.

Multiplicity cut

In events with extremely high multiplicities of charged particles, there is an increased chance for the di-muon trigger to be issued by a wrong combination of hits from different tracks. Less than 5% of the high-multiplicity events in the 2000 data sample contain a J/ψ signal [Ada01a]. Therefore, a cut that rejects high-multiplicity events is desirable.

The number of photons per event in the RICH, N_γ, is chosen as an indicator for the multiplicity. In the analysis, all events with $N_\gamma > 2,500$ are neglected. Plotting the dependence of the reconstructed invariant mass on the RICH multiplicity, cf. Fig. 5.2, shows that most events with more than 2,500 RICH photons do not contain a J/ψ signal.

In other analyses, the multiplicity is measured by counting the number of hits per event in the main tracker [Fom00].

Kinematic cuts

Only loose cuts were applied to the momenta of the track pair. The cuts reflect the acceptance of the outer muon detector, which is only reached by particles with momenta larger than 4–5 GeV/c and transverse momenta larger than 0.7 GeV/c. It is required that

- the momenta p of both tracks are greater than 5 GeV/c, and
- the transverse momenta p_T are in the range of 0.7–10.0 GeV/c.

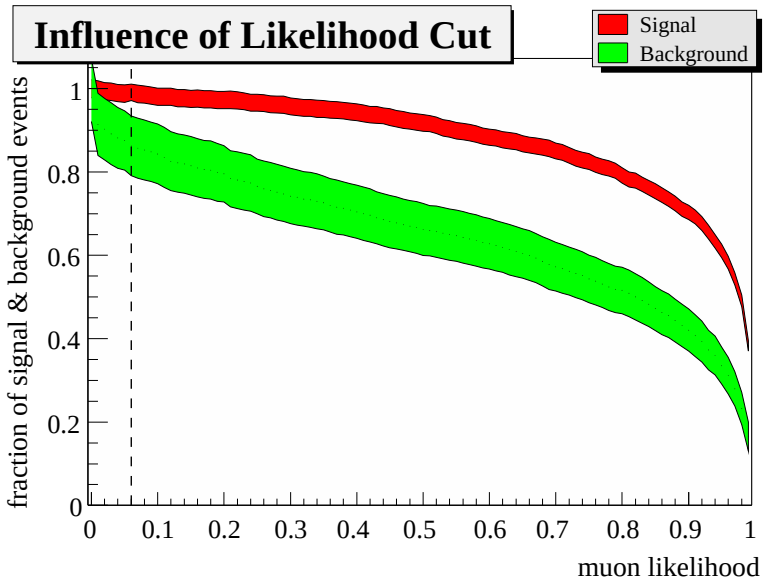

Figure 5.3: *Dependence of the signal and background efficiencies on the muon likelihood. The efficiency is normalized to tracks which are successfully propagated to the muon system. The numbers of signal and background events have been determined by fits to the invariant mass spectrum. The error intervals of the signal and background efficiencies are depicted as error bands.*

The signal-to-background ratio cannot be improved by momentum cuts tighter than the ones described above. Background in the low-mass region could be rejected by a cut on the sum of the transverse momenta of the two tracks, e.g. $\sum p_{\mathrm{T}} > 2.5\,\mathrm{GeV}/c$. However, this cut has a strong influence on the background shape at masses below the J/ψ peak. Since the background will be used for studies of Drell-Yan physics, a cut on the sum of the transverse momenta is not applied.

Likelihood cuts

While the muon identification in the preselection of tracks is restricted to requiring hits in the muon system, in the final analysis also the likelihoods of the tracks to be a muon – as calculated by the MuonID package – is employed. Using MuonID, the following cuts are applied:

- The propagation of tracks from the PC or the TC chambers of the OTR to the muon system must be successful.
- The calculated muon likelihood has to be greater than 0.06. The dependence of the fraction of signal events and the fraction of background events on the likelihood cut is shown in Fig. 5.3. By this choice of the likelihood cut, almost all possible candidates for muons are selected, while the number of background events drops by 14%. Thus, further confirmation of the muon identification is gained while the signal strength is reduced by less than 1%. If a better background rejection is needed, the likelihood cut can also be set to higher values. However, then also the signal strength is noticeably reduced.

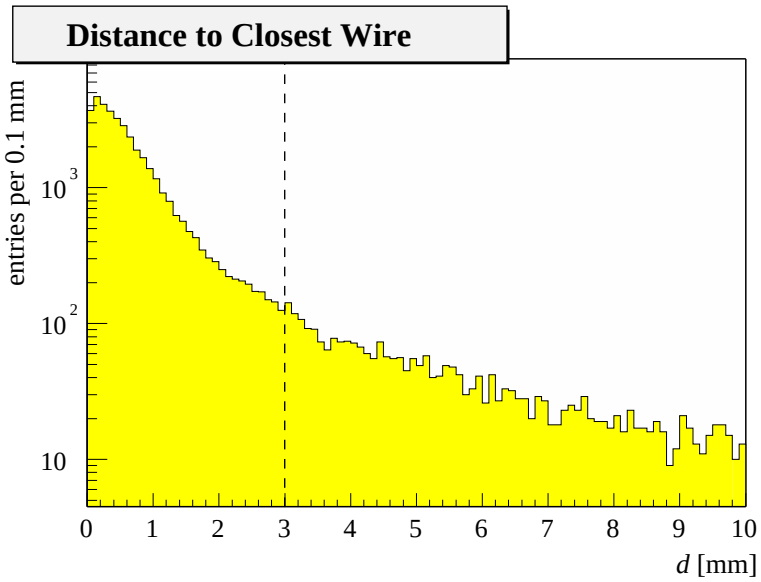

Figure 5.4: *Distribution of the distance d between a vertex and the closest target wire. Vertices with distances greater than 3 mm (dashed line) are being rejected.*

Vertex cuts

Additional cuts on the vertex quality help to further reduce the background.

- The χ^2 probability of the vertex fit is required to be greater than 0.005 to exclude extremely bad vertices. The definition of the χ^2 probability in the HERA–B tracking and vertexing is given in Section B.3.
- The distance to the closest target wire must be smaller than 3 mm, see Fig. 5.4. By this cut background from wrong track combinations is reduced. The vertex-target distance allowed by this cut is greater than the resolution of vertices on the target wires to account for the uncertainties introduced by a two-prong vertex fit and difficulties during the reconstruction of the exact wire positions. With further improvements of the vertex-wire relation also background from secondary vertices, e.g. semileptonic D meson decays from open charm production $c\overline{c} \rightarrow D\overline{D}$, could be rejected.

The positions of the vertices that pass these cuts in Run 16784 are shown in Fig. 5.5. The wires Inner II and Below I used in this run are clearly visible.

Results of the final analysis

The whole data sample taken in the di-muon triggered runs in 2000 has been analyzed in this thesis. The data have been reprocessed in January and February 2001 using improved detector alignment and reconstruction software. An exhaustive list of the analyzed runs is given in Table D.1 The results are summarized in Table 5.1. The whole data sample contains approximately 4.1 million events, out of which 193,946 are preselected for the final analysis. The data have been taken at an interaction rate of 4–5 MHz, using the target wire Inner II in the first part and the wires Inner II and Below I in the second part of the runs. The total number of J/ψ mesons in the sample after all

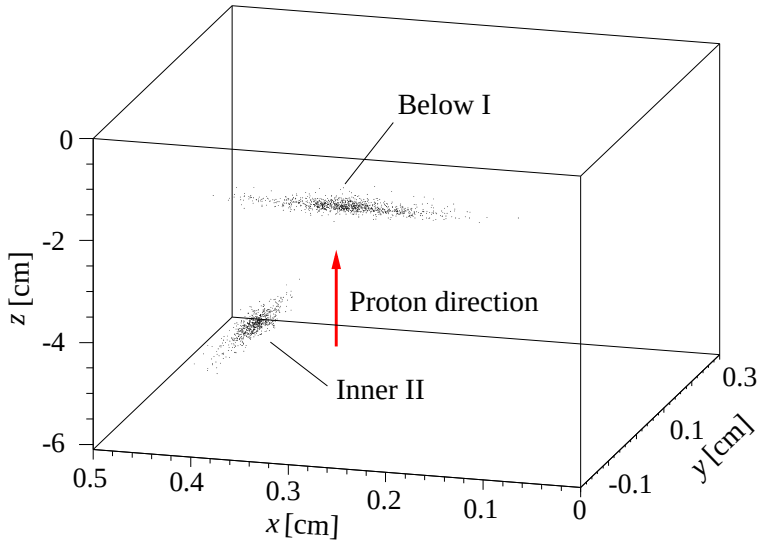

Figure 5.5: *Position of the reconstructed* J/ψ *vertices after cuts in Run 16784. The wires Inner II and Below I, which were used for the data-taking, are clearly visible.*

Table 5.1: *Total statistics of the reprocessed di-muon triggered runs in the 2000 data-taking period. The errors are statistical errors of the fit.*

Number of runs	201
Number of events	4,093,800
Number of preselected events	193,946
Number of J/ψ mesons after cuts: $N_{J/\psi}$	$2,688 \pm 58$
Average J/ψ mass: M_0	$(3081 \pm 1)\,\mathrm{MeV}/c^2$
Average J/ψ width: σ	$(51 \pm 1)\,\mathrm{MeV}/c^2$
Signal-to-background ratio: S/B	3.77 ± 0.35
Significance: Σ	101 ± 3

cuts amounts to $2,688 \pm 58$. The mass spectrum obtained from the analysis is shown in Fig. 5.6, and a detailed discussion of the mass spectrum will follow in Section 5.2.3.

5.1.3 Relation to the SLT information

The final analysis has two points of contact with the SLT information, where the results of both methods can be compared:

1. The SLT tracks are used as seeds for the OTR reconstruction.

2. The SLT-based tracking method was used before the offline reconstruction in the OTR was working with a sufficient efficiency.

Effects of the SLT seed for RANGER

The main tracker reconstruction during the reprocessing has been performed in the "SLT seeded" mode, where the tracks from the SLT algorithm SLICER/REFIT serve as seeds

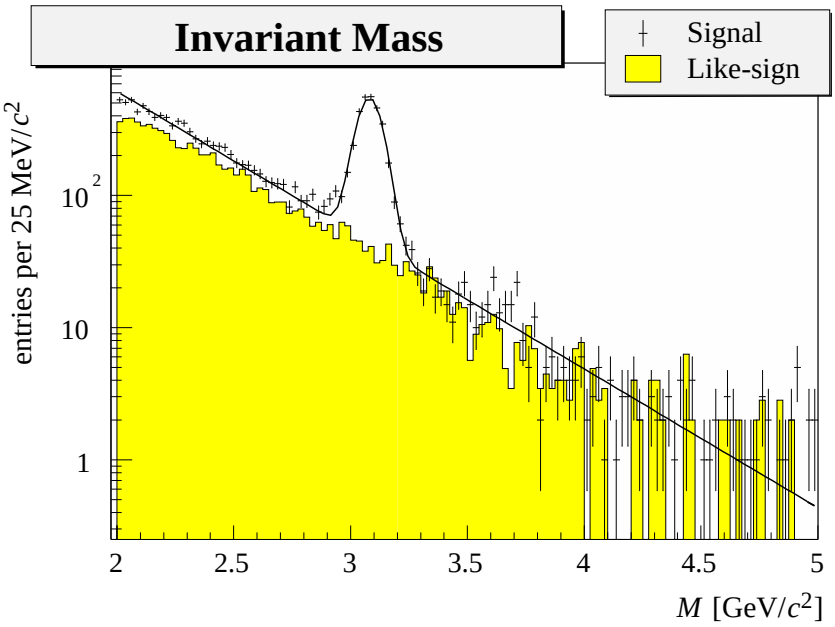

Figure 5.6: *The J/ψ signal in the 2000 data after the final analysis. On the abscissa the invariant mass of track pairs is plotted. The filled histogram contains the number of like-sign muon pairs in the spectrum as an estimate for the number of background events. For a discussion of the shape of the background cf. Section 5.2.4.*

for the RANGER pattern recognition algorithm in the main tracker. Therefore, the number of seeded tracks in a secondary vertex which enters the invariant mass spectrum can be checked. A list of the number of J/ψ mesons and background events after a fit to the invariant mass spectrum is shown in Table 5.2.

Table 5.2: *Effects of the SLT seed for RANGER: For vertices with zero, one or both tracks seeded by the SLT, the number of* J/ψ *mesons and the number of background events from a fit to the invariant mass spectrum are compared.*

# seeded tracks	J/ψ Signal	Background
0	–	≈ 3
1	146 ± 14	53 ± 26
2	2542 ± 56	657 ± 66

In approximately 94% of the cases both tracks are SLT-seeded. For runs where the SLT was the active trigger, the number of J/ψ mesons found by the SLT is the maximum number of J/ψ mesons available in the data sample. Hence, the number of J/ψ mesons cannot be increased by using the RANGER offline reconstruction. The fact that some vertices are found where only one of the tracks is SLT seeded is probably caused by two effects:

- RANGER reconstructs a clone of the track that issued the SLT.
- One of the tracks that issued the SLT is a ghost track or a track that does not originate from the J/ψ decay, and RANGER finds the correct track.

This hypothesis is confirmed by the fact that the signal-to-background ratio is the same for vertices with one or two seeded tracks, indicating that these events belong to the same class of events, i.e. events where the SLT was the active trigger.

SLT triggers in the final analysis

The final analysis step for the SLT trigger information includes some additional quality cuts. For all events with an SLTTrigger of unlike-sign muon pairs, the same multiplicity cut as in the "standard" analysis is applied, as well as the same kinematic cuts for the track pair:

- $N_\gamma < 2,500$,
- $p > 5\,\mathrm{GeV}/c$, and
- $p_\mathrm{T} > 0.7\,\mathrm{GeV}/c$.

For all SLTTriggers that pass these cuts, the invariant mass is calculated. The invariant mass spectrum will be compared with the results of the "standard" analysis in Section 5.2.3.

5.1.4 Comparison with Monte Carlo simulations

A comparison of the data with a Monte Carlo simulation is performed in order to test the quality of the cuts and the background rejection on simulated events. An introduction to Monte Carlo simulations in the HERA–B experiment is given in Appendix C.

The Monte Carlo sample used for the comparison has been generated and reconstructed with ARTE-03-08-r5 [Pet01a]. The geometry version used for the detector description was 99.1014, which contains the most accurate knowledge – as of January 2001 – on the HERA–B detector during the data-taking in July and August 2000.

Hot and dead channels in the OTR and in the muon system were masked according to the setup used in Run 16665. The efficiency of working channels in the muon system was set to 100%, disregarding the efficiency problems of the muon pad chambers in the real data-taking.

Two data samples were generated, 100,000 events for single-wire and two-wire running each. In this analysis only the single-wire sample is used, because the results obtained from the two-wire simulation are very similar. The events were mixed with inelastic interactions. The number of J/ψ signals per event was set to one while the number of inelastic interactions was generated according to a Poisson distribution with the mean value of $\lambda = 0.5$, cf. Equation (C.2). This value corresponds to an interaction rate of 4.3 MHz, while the data sample in the 2000 runs was recorded mostly with 5 MHz interaction rate, and other parts were also recorded with 4 MHz. After the simulation of the detector and the SLT, the number of events left in the Monte Carlo sample is approximately 1,800. This rather small number reflects the acceptance of the detector and the efficiencies of the detector and trigger chain, as explained in Section 4.2.4.

The track and vertex multiplicities, the properties of the invariant mass spectrum from the Monte Carlo simulation, and the effects of the cuts will be discussed in the following section.

5.2 Discussion of the results

In this section, the results of the final analysis will be evaluated in detail. The track and vertex multiplicities of the preselected events and the efficiencies of the cuts will be compared to the corresponding results from Monte Carlo simulations. The properties of the invariant mass spectrum from data and Monte Carlo simulations will be compared both for the "standard" analysis and for the SLT-based analysis. In addition, possible sources of background in the mass spectrum and the influence of systematic effects on the analysis will be discussed.

5.2.1 Track and vertex multiplicities

Tracks

The average number of tracks per event is given in Table 5.3. Because the track number distribution cannot be described by the usual distribution functions and has long tails, the average has been approximated by a robust estimator, the median of the track number distribution. The median is defined as the number of tracks where in half of the events there are less and in half of the events there are more tracks. The variances are defined by the range in the track number distributions where 68.3% of the events are situated, 34.15% on each side of the median [Fri74].

Table 5.3: *Average numbers of tracks per event for 193,946 events in real data and 1,771 events from the Monte Carlo simulation (MC).*

	Data	MC
Tracks per event	70^{+39}_{-35}	37^{+19}_{-11}
Preselected tracks per event	39^{+21}_{-20}	24^{+12}_{-8}

The track multiplicities in real data are 60–90% higher than in the Monte Carlo simulations. Similar results have been obtained by independent studies on the numbers of detector hits [Pet01b]. This general mismatch between data and Monte Carlo simulations has not yet been resolved.

Vertices

The average number of primary and secondary vertices, including those where both tracks point to the same primary vertex, as well as those obtained from a constrained fit, can be found in Table 5.4.

The difference in the numbers of primary vertices corresponds to the difference in the numbers of tracks. The larger number of events in the Monte Carlo simulation in which both tracks point to the same primary vertex can be explained by the smaller clone rate. Since the Monte Carlo simulation contains a J/ψ signal in every event, the number of events where a constrained fit is applied is larger than in real data.

Table 5.4: *Average numbers of preselected vertices per event for 193,946 events in real data and 1,771 events in the Monte Carlo simulation (MC). The numbers of vertices and their variances are given by the mean and the RMS (root mean square) values of the distributions.*

	Data	MC
Preselected primary vertices per event	1.8 ± 0.8	1.1 ± 0.5
Preselected secondary vertices per event	1.9 ± 0.4	1.0 ± 0.4
Both tracks point to the same primary vertex	0.06 ± 0.24	0.87 ± 0.34
Secondary vertex from constrained fit	0.02 ± 0.13	0.88 ± 0.33

5.2.2 Effects of the cuts

Efficiency on real data

Based on fits to the invariant mass spectrum, the influence of the cuts on the J/ψ signal and the background is evaluated. The results are summarized in Table 5.5 and in Fig. 5.7. The influence of a cut is always calculated in addition to the cuts applied before, according to the cut hierarchy described above. The absolute efficiency of the individual cuts, i.e. the effect of the cuts without any other cut, has not been evaluated. Since the cut hierarchy defines a "natural" order of the cuts, the efficiency relative to the previous cut is also a meaningful measure for the cut efficiency.

Table 5.5: *Efficiency of the cuts on the numbers of signal and background events and on the signal-to-background ratio S/B and the significance Σ. The cuts are ordered by the hierarchy described in the text. The errors are statistical errors of the fit.*

Cut	J/ψ Signal	Background	S/B	Σ
Unlike sign track pair	$2,961 \pm 65$	$1,310 \pm 99$	2.3 ± 0.2	81.8 ± 3.6
$N_\gamma < 2,500$	$2,913 \pm 63$	$1,211 \pm 93$	2.4 ± 0.2	83.7 ± 3.7
$p > 5\,\mathrm{GeV}/c$	$2,915 \pm 63$	$1,208 \pm 93$	2.4 ± 0.2	83.9 ± 3.7
$p_\mathrm{T} > 0.7\,\mathrm{GeV}/c$	$2,919 \pm 63$	$1,183 \pm 87$	2.5 ± 0.2	84.9 ± 3.6
MuonID	$2,896 \pm 62$	$1,089 \pm 86$	2.7 ± 0.2	87.8 ± 3.9
muon likelihood > 0.06	$2,869 \pm 58$	938 ± 78	3.1 ± 0.3	93.7 ± 4.3
$d < 3\,\mathrm{mm}$	$2,825 \pm 59$	881 ± 75	3.2 ± 0.3	95.2 ± 4.5
$\mathrm{prob}(\chi^2, N_\mathrm{dof}) > 0.005$	$2,688 \pm 58$	713 ± 66	3.8 ± 0.4	100.7 ± 5.1

The most effective cuts for the rejection of background are the cuts on the muon likelihood and on the χ^2 probability of the vertex fit. The likelihood cut leads to a 14% reduction of the background, while the signal is only reduced by 1%. The cut on the χ^2 probability of the vertex fit reduces the background by 19% but the signal by only 5%.

Real data vs. Monte Carlo simulations

The results of a comparison of the cut efficiencies in the analysis of real data and of Monte Carlo simulations are shown in Fig. 5.8. The efficiencies for real data and Monte Carlo simulations agree within the errors. However, the efficiencies on real data are always

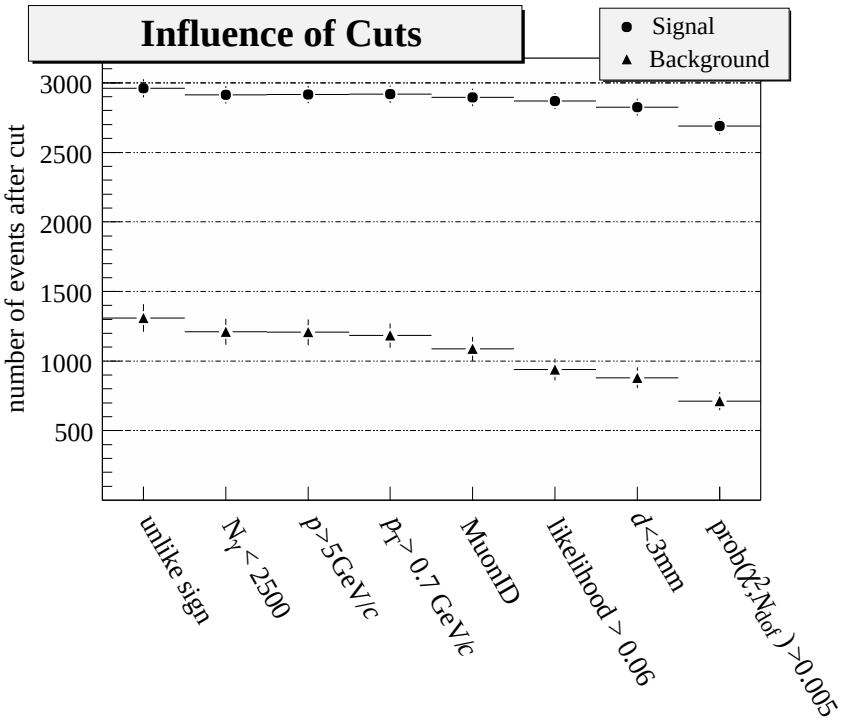

Figure 5.7: *Influence of the selection cuts on the* J/ψ *signal and the background. The plot shows the number of signal and background events obtained from a fit to the invariant mass spectrum after applying all cuts including the actual cut.*

smaller than on simulated events. The main differences occur after the multiplicity cut and the vertex cuts. As already shown, the fraction of high-multiplicity events in real data is larger than in the simulation. Therefore, the chance to cut away a J/ψ event by the multiplicity cut is higher in real data. The detector resolution in the Monte Carlo simulation is better than in real data, as is visible from the width of the J/ψ signal of $(40 \pm 1)\,\mathrm{MeV}/c^2$ compared to $(51 \pm 1)\,\mathrm{MeV}/c^2$ in the data, cf. Table 5.7. Thus, the cuts on the vertex-wire distance and the χ^2 probability of the vertex fit are expected to be more efficient in the simulation.

5.2.3 Properties of the invariant mass spectrum

The final results on the invariant mass spectrum have been given in Table 5.1 and in Fig. 5.6. In this section, the spectrum will be compared with the results from the SLT-based analysis and Monte Carlo simulations.

The invariant mass spectrum from the SLT

Since the SLT was the active trigger in the data-taking, the total number of J/ψ mesons recorded with this trigger is the theoretical upper limit for the total number of J/ψ mesons found in the data sample. However, the J/ψ signal may be hidden by an insufficient suppression of background, leading to a smaller total number of J/ψ mesons after a fit to the invariant mass spectrum in the SLT-based analysis compared to the "standard" analysis. Fig. 5.9 shows the invariant mass spectrum of SLT triggers compared to the spectrum obtained by the "standard" analysis.

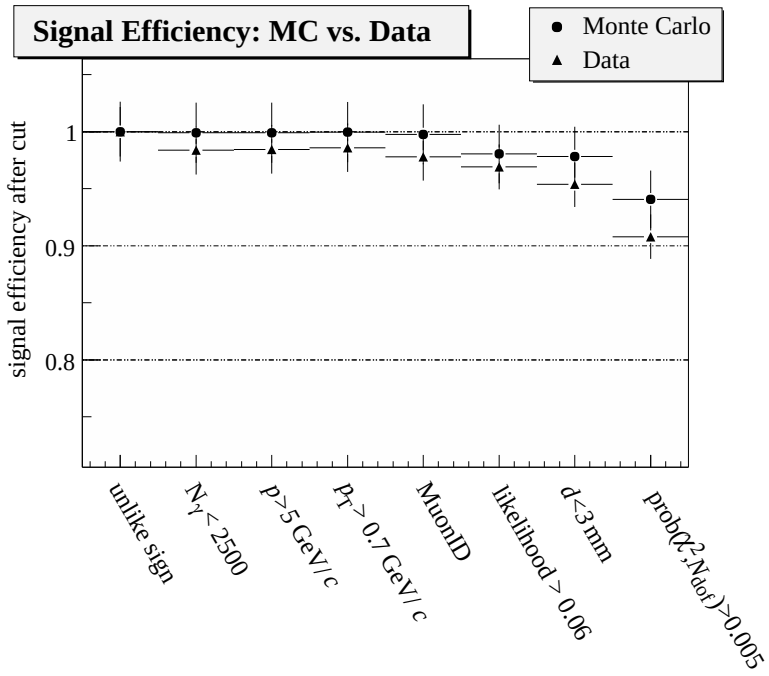

Figure 5.8: *Influence of the selection cuts on the* J/ψ *signal efficiency in data and reconstructed Monte Carlo events. The plot shows the signal efficiencies obtained from a fit to the invariant mass spectrum after applying all cuts up to and inclusive of the actual cut.*

The parameters of the J/ψ signal for both methods are compared in Table 5.6. The number of signal events obtained from the fit is smaller in the SLT trigger, due to the insufficient background suppression with the multiplicity and kinematic cuts only. The SLT triggers contain ghost tracks in the VDS, which could be suppressed via matching with offline reconstructed track segments from the CATS package. This cut is impossible with the condensed "MINI" format of the reprocessed data, since the track segments are not stored in the event record. Thus, the use of the SLT triggers as a reference for the efficiency of the offline cuts is not possible.

Table 5.6: *Comparison of the* J/ψ *peak from SLT-based and the "standard" analysis.*

Property	SLT-based	"Standard"
Number of J/ψ mesons after cuts: $N_{J/\psi}$	$1,813 \pm 72$	$2,688 \pm 58$
Average J/ψ mass: M_0	$(3072 \pm 3)\,\mathrm{MeV}/c^2$	$(3081 \pm 1)\,\mathrm{MeV}/c^2$
Average J/ψ width: σ	$(66 \pm 3)\,\mathrm{MeV}/c^2$	$(51 \pm 1)\,\mathrm{MeV}/c^2$
Signal-to-background ratio: S/B	0.61 ± 0.04	3.77 ± 0.35
Significance: Σ	33 ± 2	101 ± 3

The width of the J/ψ peak is considerably larger than in the "standard" analysis after the reprocessing because the detector alignment is hard-coded in the SLT algorithm. Therefore, the SLT-based analysis cannot take advantage of later improvements in the alignment of the HERA–B detector.

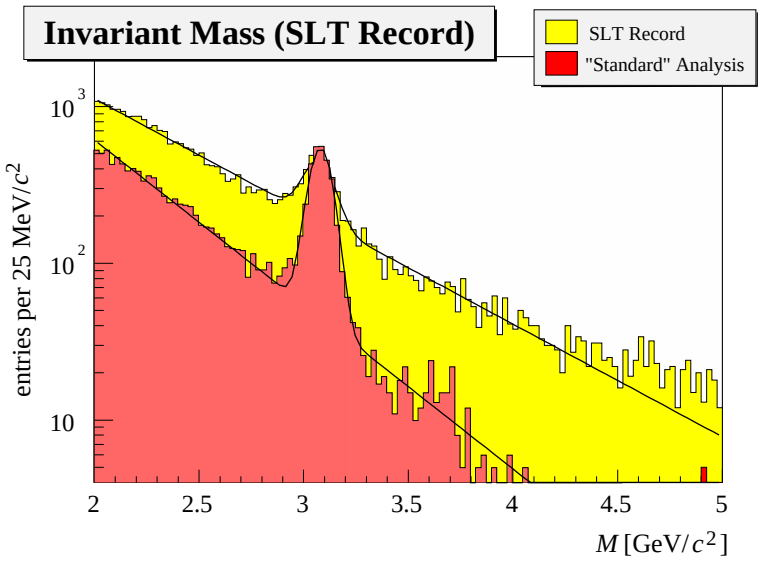

Figure 5.9: *Invariant mass spectrum obtained from the SLT trigger information: Events with more than 2,500 RICH photons are neglected, the like-sign triggers are subtracted, and the momentum and transverse momentum of the SLT tracks are demanded to have* $p > 5\,\mathrm{GeV}/c$ *and* $p_\mathrm{T} > 0.7\,\mathrm{GeV}/c$*. For comparison, the invariant mass spectrum from the "standard" analysis is also shown.*

To summarize the comparison between the SLT-based and the "standard" analysis, the latter has evolved into an analysis strategy which is superior to the SLT-based analysis in the main physics observables. Nevertheless, the SLT information is still valuable for the offline reconstruction, since by using the SLT seeds for RANGER the tracking efficiency in the main tracker can be improved.

The simulated invariant mass spectrum

The invariant mass spectrum obtained from the Monte Carlo simulation was fitted to a Gaussian function only, since the background in the sidebands is negligible. The result of the fit is shown in Fig. 5.10. In Table 5.7, the properties of the J/ψ signal from real data and from the Monte Carlo simulation are compared. The width of the signal is significantly smaller in the simulation, reflecting the ideal assumptions concerning the detector alignment in the Monte Carlo simulation. Hence, the signal in real data is still about 30% too wide, compared to Monte Carlo simulations. A further improvement of the detector alignment may help to improve the signal width. The position of the J/ψ peak in the Monte Carlo simulation, $M_0 = (3095 \pm 1)\,\mathrm{MeV}/c^2$, agrees with the literature value of $(3096.87 \pm 0.04)\,\mathrm{MeV}/c^2$.

5.2.4 Background in the invariant mass spectrum

As can be seen from Fig. 5.6, even with several cuts, the background in the invariant mass spectrum cannot be fully removed. Possible sources of background include

- other physics processes with a continuous di-muon spectrum, e.g. Drell-Yan processes,
- combinatorial background from pion and kaon decays in flight,

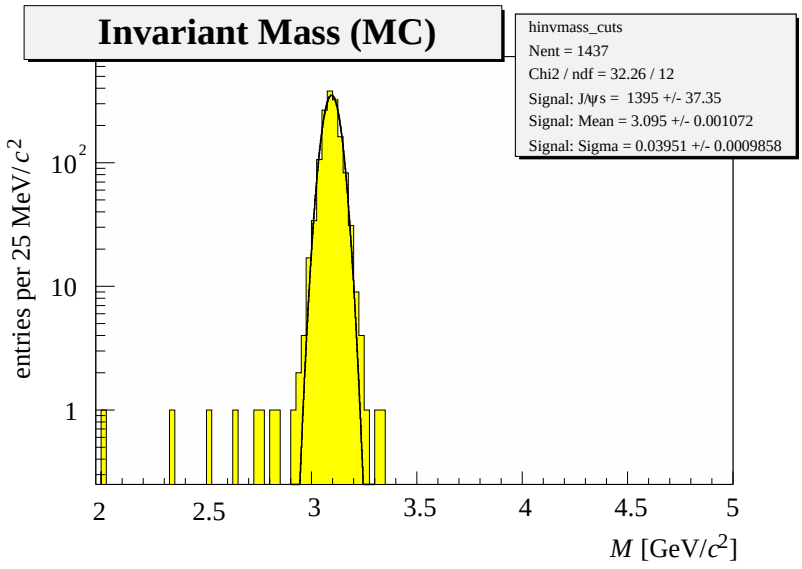

Figure 5.10: *Invariant mass spectrum obtained from a Monte Carlo simulation of the process* $J/\psi \to \mu^+\mu^-$ *including a simulation of the full detector and trigger chain. For the fit, only a Gaussian function has been used.*

Table 5.7: *Properties of the* J/ψ *signal in Monte Carlo simulations and in data. The signal efficiency after all cuts is normalized to the number of unlike-sign muon pairs after the track and vertex preselection.*

Property	Monte Carlo Simulation	Data
Average J/ψ mass: M_0	$(3095 \pm 1)\,\mathrm{MeV}/c^2$	$(3081 \pm 1)\,\mathrm{MeV}/c^2$
Average J/ψ width: σ	$(40 \pm 1)\,\mathrm{MeV}/c^2$	$(51 \pm 1)\,\mathrm{MeV}/c^2$
Signal efficiency	0.94 ± 0.03	0.91 ± 0.02

- combinatorial background from leptonic or semileptonic decays of charmed mesons, and
- other unknown sources.

Physics background

The typical physics background in a fixed-target spectrometer consists mainly of Drell-Yan muon pairs and semileptonic decays of charmed mesons [Abr01]. A detailed analysis of the Drell-Yan background can be found in Chapter 6. The influence of charmed mesons has not been studied in the framework of this thesis.

Combinatorial background

Charged pions and kaons are the most abundant particles in the HERA−B detector. Approximately 70% of the particles in an inelastic interaction with the target are pions, about 15% are kaons [HB00a]. The properties of these particles are listed in Table 5.8. Kaons decay into muons either directly via the channel $K \to \mu\nu_\mu$ or via an intermediate

decay into charged pions. More than 99.9% of all charged pions decay into muons by the reaction $\pi \to \mu\nu_\mu$.

Table 5.8: *Properties of muons, charged pions, and charged kaons [Gro00]*

Particle	Mass [MeV/c^2]	Mean life [ns]	Branching fraction into $\mu\,\nu_\mu$
$\mu^\pm$	105.658357 ± 0.000005	2197.03 ± 0.04	–
$\pi^\pm$	139.57018 ± 0.00035	26.033 ± 0.005	0.9998770 ± 0.0000004
$K^\pm$	493.677 ± 0.016	12.386 ± 0.024	0.6351 ± 0.0018

The probability of a particle of mass m, mean lifetime τ, and momentum p to decay within a flight path of the length L is given by

$$P(L) = 1 - \exp\left[-\frac{m}{p}\,\frac{L}{\tau}\right]. \tag{5.6}$$

Hence, a pion with $p = 10\,\mathrm{GeV}/c$ decays within the 13 m between the target and the ECAL with a probability of about 2%.

The mass difference between pions and muons is only $34\,\mathrm{MeV}/c^2$. Therefore, the transverse momentum kick by the pion decay is small, and the muons from pion decays keep approximately the flight direction of the pions. The mean deflection of the muon track with respect to the pion track is about 1 mrad [Boh01]. The deflection by multiple scattering is of the same order of magnitude; the width of the distribution of multiple scattering angles θ_0 can be approximated by [Lyn91]

$$\theta_0 = \frac{13.6\,\mathrm{MeV}}{\beta c p}\sqrt{\frac{x}{X_0}}\left[1 + 0.038\,\ln\left(\frac{x}{X_0}\right)\right], \tag{5.7}$$

where p and β are the momentum and the velocity of the particle, and x/X_0 is the thickness of the material in radiation lengths. Hence, for a particle with $p = 10\,\mathrm{GeV}/c$, the mean deflection angle in one radiation length of material is about 1.36 mrad.

The tracking algorithms might not be able to reconstruct the "kink" in the track at the position where the pion decays. From an early Monte Carlo study of a "kink-finder" algorithm, a reduction factor of 2–3 for pions and 10 for kaons is expected [Tit96]. However, this study assumes an OTR resolution as given in the HERA–B Proposal [Loh94] of 120 μm, much better than the value of 350 μm, which was achieved in the 2000 run [HB00a].

If in addition the pions are produced in primary interactions, the combination of a pion track and the track of the muon the pion decays into can hardly be distinguished from a real muon track from the target. Thus, combinations of muons from the target with muons from decays in flight or combinations of two muons from decays in flight can pass the whole trigger, reconstruction and analysis chain, and enter the final invariant mass spectrum. In that sense the background from decays in flight is "irreducible".

However, the background can be estimated from the number of like-sign tracks which pass all cuts. Suppose the number of tracks with positive charge is independent of the number of tracks with negative charge, the multiplicities of both track charges are Poisson-distributed, and the detector has the same acceptance for positively and negatively charged tracks. Then the number of background events N_{bkg} introduced by

opposite sign pairs of decays in flight can be estimated from the number of like-sign pairs as follows [Abr98]:

$$N_{\mathrm{bkg}} = 2\sqrt{N^{++}N^{--}}, \tag{5.8}$$

where N^{++} and N^{--} are the numbers of pairs with positive and negative signs respectively. In Fig. 5.6 the distribution of like-sign pairs in the background is shown. The number of like-sign pairs is calculated with Equation (5.8) for each bin in the mass spectrum. The combinatorial background can be subtracted from the signal, resulting in an almost background-free J/ψ peak, as shown in Fig. 5.11. However, the background in the sideband on the low-mass side of the J/ψ peak cannot be fully explained by decays in flight. About 25% of this background is not reproduced by the distribution of like-sign muon pairs. The expectation for physics background from Drell-Yan processes in this mass regime can be estimated by 5–20% [Abr01].

This background subtraction method shows a drawback in treating empty bins in the signal histogram, which occur frequently in the high-mass region. If the corresponding bin in the background histogram is filled, there are negative entries after the subtraction. The background subtraction can be improved, if in this case filled neighboring bins are included: If a bin is empty, the neighboring bin is used for the background subtraction. If the background to be subtracted is larger than the data content of this bin, only the part of the background equal to the cell content is subtracted. The method results in invariant mass spectra, where the bin contents are always positive or zero [Abr98].

Combinatorial background can also be estimated by mixing tracks with similar kinematics from different events. The invariant mass spectrum from event mixing depends strongly on the correlation between the kinematic properties of the mixed tracks. In addition, the spectrum is difficult to normalize, since the signal events are mixed with background events which leads to an underestimation of the background close to the peak [Dri84]. Hence, without a detailed analysis, no conclusions concerning the combinatorial background should be drawn from event mixing methods.

Background in the Monte Carlo simulation

The background in hadronic interactions is very difficult to model correctly in a Monte Carlo simulation of the detector and trigger system. For the real trigger, the ratio of signal to background events can be estimated by comparing the cross sections for inelastic interactions with the production cross section for J/ψ mesons and the branching fraction for a decay into a muon pair. The inelastic cross section in proton-carbon interactions is 19 mb [HB00a] per nucleon, the J/ψ production cross section amounts to 422 nb [Sch95], and the branching fraction of $\mathrm{J}/\psi \to \mu^+\mu^-$ is 6%. Hence, in the experiment, only one of about 750,000 events that is processed by the trigger contains a J/ψ meson. This situation cannot be modeled properly with a reasonable amount of Monte Carlo events. However, first attempts to modify the Monte Carlo simulation in order to increase the background to the experimentally observed level have been undertaken.

5.2.5 Systematic effects

Effects of the binning

The choice of a fixed bin size, $n_{\mathrm{bins}} = 40$, has been checked for systematic effects in the fits to the invariant mass spectrum. To estimate the influence of binning effect, the

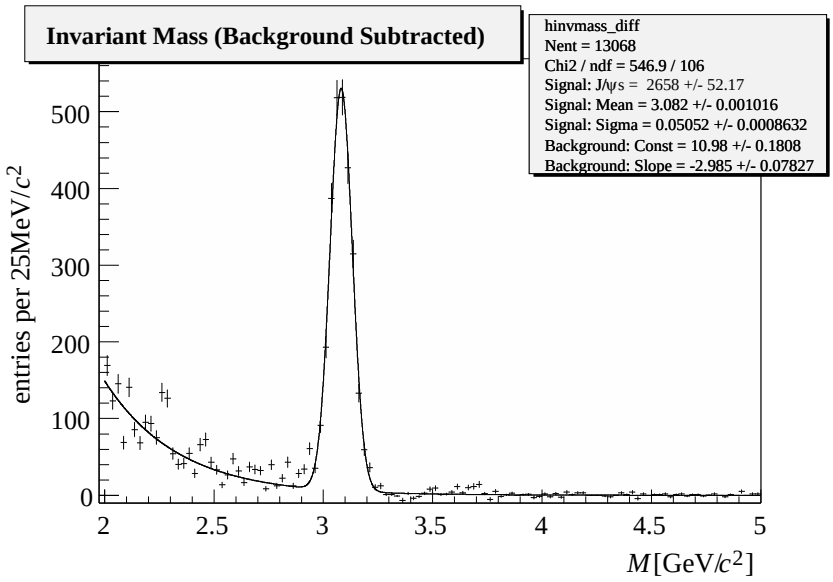

Figure 5.11: *Invariant mass spectrum after the subtraction of combinatorial background, estimated from the distribution of like-sign muon pairs.*

analysis has been performed with bin sizes of $n_{\text{bins}} = 20$ and $n_{\text{bins}} = 100$. The results are summarized in Table 5.9. The number of J/ψ events after the fit is stable, and the quality of the fit improves with the number of bins. However, since the same bin size is used for single runs and for the whole sample, $n_{\text{bins}} = 40$ is a good compromise between sufficient statistics per bin and the resolution of the mass spectrum.

Table 5.9: *Systematic effects of the bin size in the invariant mass spectrum on the number of* J/ψ *events after the fit (*J/ψ *Signal) and on the fit quality (χ^2/N_{dof}).*

n_{bins}	J/ψ Signal	χ^2/N_{dof}
20	$2,680 \pm 58$	144.9/55
40	$2,688 \pm 58$	188.4/110
100	$2,684 \pm 57$	332.7/249

Normalization of the mass spectrum

The position of the J/ψ peak in the invariant mass spectrum is significantly different for the SLT-based and the "standard" analysis, and for data and Monte Carlo simulations respectively. The different results are summarized in Table 5.10.

A shift in the invariant mass is expected if the calibration of the magnetic field is different in different scenarios or if the detector is misaligned. As an example, the effect of the magnetic field is evaluated in the following. Possible reasons for a poor calibration include:

Table 5.10: *Systematic effects on the position of the* J/ψ *peak in the invariant mass spectrum. The measured positions have to be compared to the literature value of* $(3096.87 \pm 0.04)\,\mathrm{MeV}/c^2$.

Analysis	$M\,[\mathrm{MeV}/c^2]$
"Standard" (Data)	3081 ± 1
"Standard" (Monte Carlo)	3095 ± 1
SLT-based (Data)	3072 ± 3
SLT-based (Monte Carlo)	3099 ± 1

1. The "standard" and the SLT-based analyses use different momentum determination methods, swimming algorithms in the "standard" analysis and field maps in the SLT-based analysis.

2. The magnetic field in the detector and the model of the magnetic field in the GEANT simulation are different.

The results of Table 5.10 show that there are differences in the trends for data and Monte Carlo simulations but not for the "standard" and the SLT-based analyses. Since the mass obtained from the Monte Carlo simulation agrees with the expected value, the calibration of the magnetic field in the HERA–B detector seems to induce a shift in the invariant mass spectrum:

$$M_{\mathsf{HERA-B}} = (0.9955 \pm 0.0005)\, M_{\mathrm{real}}. \tag{5.9}$$

5.2.6 Concluding remarks

In this chapter, an analysis of the complete di-muon triggered data sample of the HERA–B experiment taken in the 2000 run has been presented. In a total of 4.1 million events, a clean J/ψ sample of about 2,700 events has been found. The absolute number of J/ψ mesons and thus the total efficiency of the analysis described in this chapter could be evaluated if the analysis were compared to other independent analyses. However, for further studies of the di-muon invariant mass spectrum the understanding of the background is much more important than the absolute normalization.

Although the selection cuts in the analysis presented in this chapter reject a huge fraction of the background, the absolute number of background events is still large, especially for masses lower than the J/ψ mass. Additional background rejection may be achieved by more sophisticated use of the vertexing routines.

In order to extract "physics" out of the continuum in the mass spectrum, e.g. Drell-Yan events, a detailed understanding of the background is absolutely necessary. In this chapter it has been shown that approximately 75% of the background can be explained by random combinations of meson decays in flight. However, from this explanation no strategy to suppress combinatorial background on a non-statistical basis has been derived so far, and the absolute height of the background has serious effects on the further studies.

A comparison to Monte Carlo simulated data shows that the mass of the J/ψ peak is significantly shifted towards lower masses. A possible reason for this effect may be a poor calibration of the HERA–B magnetic field. This hypothesis can be checked by examining the positions of other prominent peaks in the invariant mass spectrum, e.g. the $\mathrm{K}^0_{\mathrm{S}}$ signal.

The width of the J/ψ signal has been reduced by reprocessing the data with an improved detector alignment, but it is still 30% larger than the width expected from Monte Carlo simulations. The Monte Carlo simulation of inelastic background events in its present form cannot be used for background studies including a full trigger simulation. However, first ideas to modify the Monte Carlo simulation have been developed.

In the next chapter, the techniques developed in and the result obtained from the J/ψ analysis will be applied to studies of Drell-Yan physics with the HERA–B detector.

Chapter 6

Prospects of HERA – B in the field of Drell-Yan physics

Based on the analyses presented in the previous chapter and on independent Monte Carlo studies, in this chapter the prospects of HERA – B in the field of Drell-Yan physics will be evaluated. The main point of the studies will be measurements of angular distributions of Drell-Yan muon pairs, connected with the possibility of studying the violation of the Lam-Tung relation in HERA – B. The emphasis of this chapter will be on the discussion of the feasibility of Drell-Yan measurements in HERA – B and on preliminary tests of some analysis strategies.

6.1 Acceptance studies

Not all particles that are produced in interactions with the target can be found by the HERA – B detector. The main reason for this is that the detector does not cover the full solid angle in the center-of-mass frame of the interaction. In the HERA – B detector, there are for example cut-outs for the HERA proton and electron beam pipes. Moreover, each subdetector has certain insensitive areas, e.g. gaps between modules of the subdetectors or frames on which the detectors are mounted. This inefficiency of the detector is expressed as the geometrical acceptance ϵ_{acc}. The geometrical acceptance is defined as the ratio of the number of particles N which can be recorded with the detector to the number of particles N_0 that are produced in interactions with the target:

$$\epsilon_{\mathrm{acc}} = \frac{N}{N_0}. \tag{6.1}$$

The geometrical acceptance ϵ_{acc} depends especially on the kinematics of the outgoing particles and therefore on the physics process under consideration.

Since the number of particles produced in interactions with the target is unknown in real data, the geometrical acceptance has to be determined via a Monte Carlo simulation. A common way to extract the geometrical acceptance is to extrapolate the particle trajectories to different subdetector and to check whether these subdetectors are sensitive in the areas where the trajectories cross. The extrapolation of tracks is performed by the GEANT detector simulation. To determine the geometrical acceptance, the number of Monte Carlo impact points (MIMPs) in the individual layers of the subdetectors are counted, because in GEANT, MIMPs represent the entry and exit points of particle trajectories in the sensitive detector volumes.

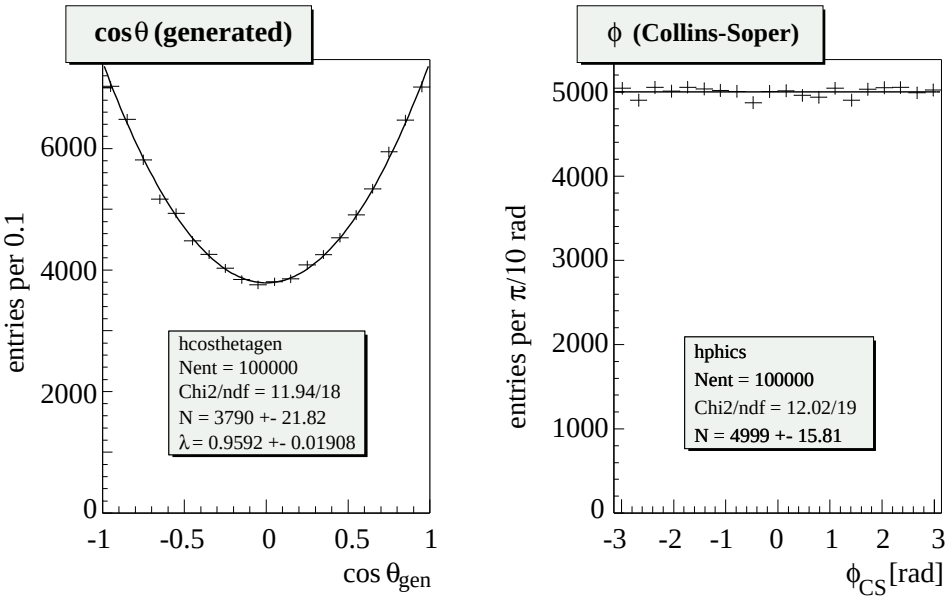

Figure 6.1: *Angular distributions of Drell-Yan muons at the generator level. The distribution of* $\cos\theta$ *in the partonic center-of-mass frame (left) is consistent with Equation (6.2), where* $\lambda = 0.96 \pm 0.2$. *The distribution of* ϕ *in the Collins-Soper frame (right) is flat.*

6.1.1 The Drell-Yan process in the HERA – B event generators

The Drell-Yan process has become a standard process in the HERA – B Monte Carlo simulation environment since ARTE version 03-08-r5. An overview of the implementation of Monte Carlo simulations in HERA – B can be found in Appendix C. The Drell-Yan process can be chosen with the KUIP command '`LUND dy`'. This command activates the PYTHIA process $q\overline{q} \rightarrow \gamma^*/Z^0$ with q = u, d, s, c. The interference between the virtual photon γ^* and the Z^0 boson can be safely neglected at a maximal center-of-mass energy of the partonic subsystem of 41.6 GeV in HERA – B. The default minimal invariant mass of the virtual photon is $2\,\mathrm{GeV}/c^2$, and initial state radiation from the incoming quarks is allowed for. The KUIP command '`PARTICLE mu+ mu-`' forces the virtual photon to decay into a muon pair. The generated angular distributions of Drell-Yan events follow

$$\frac{\mathrm{d}\sigma}{\mathrm{d}\Omega} \sim 1 + \lambda \cos^2\theta, \tag{6.2}$$

where the polar angle θ of the positively charged muon is measured in the center-of-mass system of the partonic subprocess. The distribution of $\cos\theta$ in the partonic center-of-mass frame is shown in Fig. 6.1. The value of λ varies with the invariant mass of the virtual photon. For a lower mass cut-off of $2\,\mathrm{GeV}/c^2$, $\lambda = 0.96 \pm 0.02$ is obtained, while increasing the mass cut-off to $4\,\mathrm{GeV}/c^2$ results in a value $\lambda = 0.99 \pm 0.02$. The origin of this effect within the event generator is presently not understood. The internal functionality of the PYTHIA/JETSET package with respect to the Drell-Yan process has to be further investigated.

Since the partonic center-of-mass frame is invariant under rotations around the collision axis of the partons, the distribution of the azimuth angle ϕ is isotropic. The ϕ distribution is shown in the Collins-Soper frame instead, where the partons are no longer antiparallel. For an overview of the kinematics of the Drell-Yan process cf. Appendix A.

The Monte Carlo simulations of the HERA–B detector in this chapter were performed with the version 99.1014 of the detector geometry, which has also been used for the simulation of direct J/ψ events in Section 5.1.4. In the simulation, the primary interactions take place on the wire Inner II. The complete Monte Carlo sample comprises 55,000 events with masses larger than 2 GeV/c^2, which were generated and traced through the detector simulation, as described in Appendix C.

6.1.2 Definition of the acceptance requirements

The definition of the requirements for a track to be accepted by the HERA–B detector is somewhat arbitrary. The definition which has been chosen for this study is guided by the following idea. Both muon tracks from the Drell-Yan process are required to pass the most important subdetectors needed to trigger on, detect, and identify muons. Therefore, the geometrical acceptance of muons from the Drell-Yan process is derived from the following requirements, which are also summarized in Table 6.1:

- Both muons have to be accepted in the vertex detector (VDS), since a measurement of the kinematics and a vertex fit are impossible without precise tracking information close to the target. The VDS is built from double-layers of double-sided detector structures. Hence, in many cases double hits in two VDS superlayers are sufficient to reconstruct a track. Therefore, hits are required in at least two superlayers of the VDS. The hit sum must be greater than or equal to six, allowing for missing hits in the detector layers. In the geometry version 99.1014, the VDS is not in its final position at 10 mrad from the proton beam, but rather at about 15 mrad. Since in the 2001/2002 run the VDS is expected to be positioned at 12 mrad or closer to the beam [Brä01], all tracks which have slopes between 12 and 15 mrad in the x or the y direction are also declared as accepted by the VDS.

- MIMPs in the PC and the TC region of the main tracker are required in order to guarantee tracking information after the HERA–B magnet. In the main tracker, at least three superlayers have to be crossed, and the minimum number of MIMPs is 15 in the ITR and 18 in the OTR. The number in the ITR is lower, since one of the trigger chamber layers of the ITR was missing in the detector in July and August 2000, hence also in the Monte Carlo simulation. To account for tracks where the first part is detected by the ITR and the second part by the OTR exclusively, tracks that cross three or more superlayers with more than 18 hits where either the ITR or the OTR is crossed exclusively are accepted in addition.

- To allow the identification of muons with the muon detector, both tracks have to pass at least three layers of the muon system. The minimum number of hits is six in the muon tube chambers in the outer detector and three in the pixel chambers in the inner muon detector. This is a conservative assumption, since for each tube chamber, the sensitive volumes are modeled by two shifted rectangular boxes, resulting in four MIMPs per single layer. The pixel chambers in the inner muon detector are implemented as single boxes, hence they contain two hits per superlayer at most.

- Since the di-muon trigger chain starts with the muon pretrigger in the superlayers MU3 and MU4 of the muon detector, the minimal requirement for a positive muon pretrigger decision is MIMPs in the pad system or in the pixel system of both MU3 and MU4.

Table 6.1: *Definition of the acceptance requirements for Drell-Yan muon pairs. For all relevant subdetectors, the number of hits for a track to be accepted is given. To be accepted in the main track, a track has to pass the ITR or the OTR or a combination of both. In the muon system, each track can be accepted either by the inner pixel chambers or by the outer tube chambers.*

Subdetector	MIMPs	Superlayers	Comment
VDS	≥ 6	≥ 2	
ITR	≥ 15	≥ 3	logical OR with OTR, ITR & OTR
OTR	≥ 18	≥ 3	logical OR with ITR, ITR & OTR
ITR & OTR	≥ 18	≥ 3	logical OR with ITR, OTR
Muon tubes	≥ 6	≥ 3	logical OR with pixels
MU3/MU4	≥ 1 each	–	
Muon pixels	≥ 3	≥ 3	logical OR with tubes
MU3/MU4	≥ 1 each	–	

6.1.3 The acceptance as a function of the kinematic variables

The kinematics of the virtual photon in the Drell-Yan process are completely determined by the four-vectors of the outgoing leptons; hence, the acceptance for the process is a function of eight variables. This number decreases to six, since the masses of the leptons are known. In Drell-Yan analyses, a typical choice for the variables consists of the invariant mass M, the transverse momentum p_{T}, the Feynman variable x_{F}, and the rapidity y of the virtual photon. Furthermore, the azimuth and polar angles of the positively charged muon in the Collins-Soper frame $\cos\theta_{\mathrm{CS}}$ and ϕ_{CS} can be chosen. For a definition of these variables cf. Appendix A.

The easiest approach to determine the acceptance for the Drell-Yan process is to calculate the acceptance as a function of one of these variables, integrating over the others. The results of this acceptance calculation can be found in Fig. 6.2. The results can be interpreted as follows:

- As a function of M or p_{T}, the acceptance increases. This reflects the wider spread of the muon pairs in the laboratory frame due to larger masses and transverse momenta, so that fewer muons escape through the beam pipe cut-out. Since the HERA–B detector is designed for B physics, where the average transverse momenta are smaller than half the B^0 mass, the outer limits of the HERA–B acceptance are only reached in very few events. Due to the limited statistics, this effect is not visible in Fig. 6.2.

- The acceptance as a function of x_{F} and y is almost symmetric around zero with a slightly broader tail for negative values. From the definitions of x_{F} and y follows that in the center-of-mass frame, the HERA–B detector covers the central region. The acceptance in the forward region is limited by the closest possible distance to the beam pipe, and the acceptance limits in the backward region are defined by the outer borders of the tracking devices.

- Plotted as a function of $\cos\theta_{\mathrm{CS}}$, the acceptance is also symmetric. The acceptance drop close to $\cos\theta_{\mathrm{CS}} = \pm 1$ corresponds to HERA–B's acceptance limits in the

forward and the backward regions, since the z axis in the Collins-Soper frame is approximately parallel to the z direction in the laboratory frame. The orientation of the coordinate system in the Collins-Soper frame is given by the proton-nucleon axis in the rest frame of the virtual photon, which can have an arbitrary orientation with respect to the laboratory frame. Hence, the acceptance in the polar angle ϕ_{CS} is almost flat. The larger acceptance of HERA–B e.g. with respect to NA10 is clearly visible in Fig. 6.2.

In general, the kinematic variables are correlated, and the acceptance has to be evaluated as a function of more than one variable. The amount of correlation between two variables x and y can be calculated via the correlation coefficient ρ_{xy} from a two-dimensional histogram of the variables. Let (x_i, y_j) be the center of a bin in the histogram and w_{ij} the weight of this bin. The correlation coefficient is then given by

$$\rho_{xy} = \frac{\mathrm{cov}[x,y]}{\mathrm{rms}(x)\,\mathrm{rms}(y)}, \tag{6.3}$$

where the covariance $\mathrm{cov}[x,y]$ of the variables x and y is defined as

$$\mathrm{cov}[x,y] \equiv \frac{\sum_{ij} w_{ij}\, x_i\, y_j}{\sum_{ij} w_{ij}} - \frac{\left(\sum_{ij} w_{ij}\, x_i\right)\left(\sum_{ij} w_{ij}\, y_j\right)}{\left(\sum_{ij} w_{ij}\right)^2}, \tag{6.4}$$

and the root mean square e.g. of the variable x is given by

$$\mathrm{rms}(x) \equiv \sqrt{\frac{\sum_{ij} w_{ij}\, {x_i}^2}{\sum_{ij} w_{ij}} - \left(\frac{\sum_{ij} w_{ij}\, x_i}{\sum_{ij} w_{ij}}\right)^2}. \tag{6.5}$$

The correlation coefficients between the kinematic variables in the Drell-Yan process are summarized in Table 6.2. The largest correlation is visible between M and p_{T}, since for a photon the larger the virtuality is, the larger is the expected average p_{T}. The Feynman-x variable is omitted in Table 6.2, since it is strongly correlated with y, the correlation coefficient being $\rho_{x_{\mathrm{F}}y} = 0.96$. The rapidity y is chosen, because of its logarithmic dependence on the momenta. Therefore, the central region of the detector in the center-of-mass frame can be resolved better with y than with x_{F}, which depends linearly on the momenta.

Table 6.2: *Correlations between the kinematic variables. For each pair of kinematic variables the correlation coefficient ρ is given.*

	p_{T}	y	$\cos\theta_{\mathrm{CS}}$	ϕ_{CS}
M	0.0872	0.0110	0.0048	0.0052
p_{T}	–	0.0246	0.0051	0.0001
y	–	–	0.0001	0.0016
$\cos\theta_{\mathrm{CS}}$	–	–	–	0.0007

For studies of the angular distributions, the correlations of $\cos\theta_{\mathrm{CS}}$ and ϕ_{CS} with each other and with the other kinematic variables have to be considered. Both $\cos\theta_{\mathrm{CS}}$ and ϕ_{CS} show relatively large correlations with M, while the correlation between these variables is about a factor seven smaller. Therefore, all acceptance corrections applied to the angular distributions are performed in a mass-dependent way.

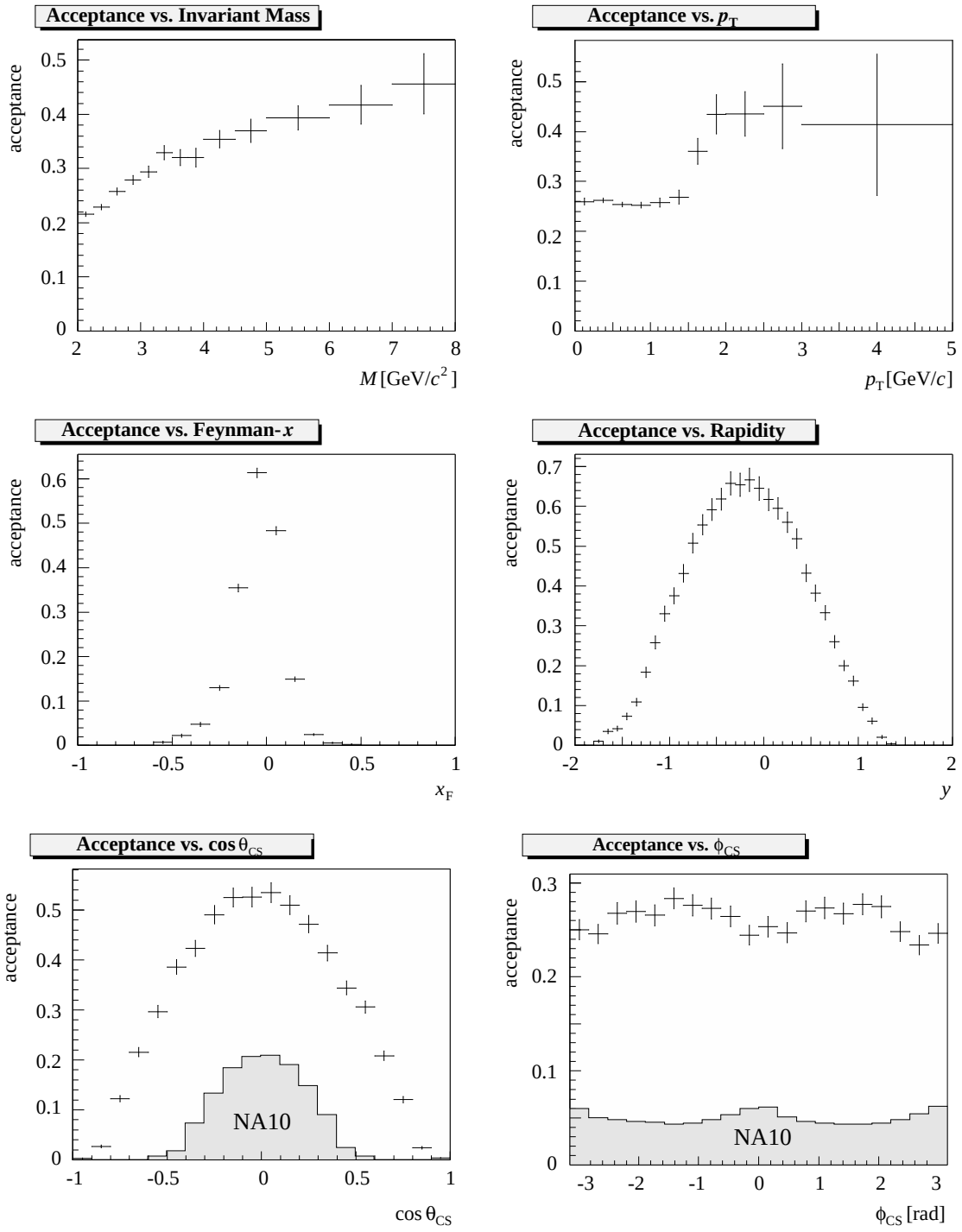

Figure 6.2: *Geometrical acceptance for Drell-Yan events as a function of the kinematic variables: Invariant mass M (upper left), transverse momentum p_T (upper right), Feynman-x (middle left), and rapidity y (middle right) of the virtual photon and polar angle $\cos\theta_{CS}$ (lower left) and azimuth angle ϕ_{CS} (lower right) of the positively charged muon in the Collins-Soper frame. The angular acceptances of NA10 [Fal86] are shown for comparison.*

6.1.4 Acceptance corrections

The geometrical acceptance has an impact on the response of a detector to a physics signal. In order to reconstruct as much as possible of the original signal, acceptance effects have to be corrected for. Acceptance corrections are essential for all measurements for which the shape of the distribution of interest depends strongly on the detector acceptance. Since the HERA–B detector does not cover the full solid angle in the center-of-mass frame of the interactions, angular distributions show such an acceptance dependence.

From a description of the detector response, strategies for acceptance corrections can be derived. Since the response of a detector is also influenced by resolution effects, additional boundary conditions for the acceptance corrections are introduced by the detector resolution. In the following, the parametrization of detector effects by the response matrix of a detector will be described, and the methods of correction factors, relying on the properties of the response matrix, will be introduced.

The response matrix

For vectors of discrete measurements, the detector response can be described by a matrix. Suppose the measurement of a distribution is represented by a histogram with n bins. Then the result of the measurement is given by an n-dimensional vector $\mathbf{f} = (f_1, f_2, \ldots, f_n)$. For each bin of the histogram there is a true value g_i, resulting in a true distribution $\mathbf{g} = (g_1, g_2, \ldots, g_n)$. The influence of detector effects on the true values that causes the measurement of $\mathbf{f}$ can be written as

$$f_i = \sum_{j=1}^{n} R_{ij}\, g_j. \tag{6.6}$$

The $n \times n$ matrix (R_{ij}) is called the response matrix of the detector for a measurement of the true distribution $\mathbf{g} = (g_1, g_2, \ldots, g_n)$. A straightforward method to extract the true distribution $\mathbf{g}$ would be the inversion of (R_{ij}). However, this method is numerically unstable [Sch98a]. Therefore, other methods have to be applied.

If the measurements f_i in different bins are independent, the response matrix is diagonal. Correlations between "neighboring" measurements are introduced by limited detector resolution. Due to smearing effects, there is a certain probability for a measurement of a kinematic variable to be found in a neighboring bin. If the bin widths are chosen such that these effects are small, the response matrix is still almost diagonal.

The detector response is derived from a Monte Carlo simulation, where the "true" values of kinematic variables from the event generator can be compared with the values obtained from the reconstruction. For a single kinematic variable, the response matrix can be visualized by a two-dimensional histogram, where the "true" values are plotted versus the reconstructed values. In Fig. 6.3, the response matrices for the angular variables $\cos\theta_{\mathrm{CS}}$ and ϕ_{CS} are shown. 5,000 Drell-Yan events from a Monte Carlo simulation are mixed with an average number of 0.58 inelastic interactions, cf. Equation (C.2), to take into account the more realistic reconstruction situation by the superposition of multiple interactions. After that the events are reconstructed with the standard reconstruction chain, as described in Section 4.3.3.

The angular distributions in $\cos\theta_{\mathrm{CS}}$ and ϕ_{CS} are plotted for all reconstructed tracks which have ARTE relations to the "true" Monte Carlo tracks, momenta larger than $5\,\mathrm{GeV}/c$, and transverse momenta larger than $0.7\,\mathrm{GeV}/c$. The correlations between the

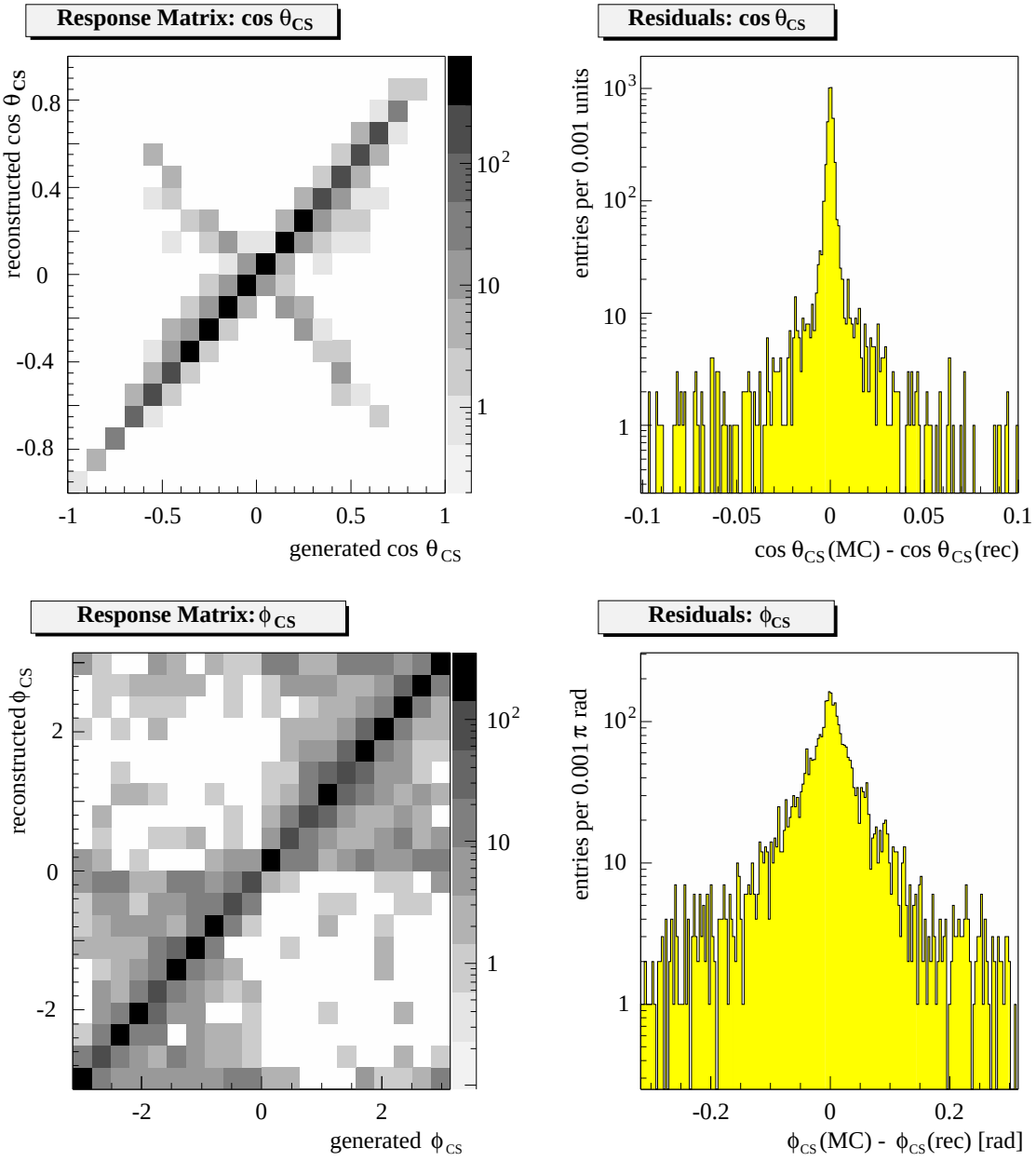

Figure 6.3: *Illustration of the response matrix for the angular variables* $\cos\theta_{\rm CS}$ *and* $\phi_{\rm CS}$*. The reconstructed* $\cos\theta_{\rm CS}$ *is plotted versus the generated* $\cos\theta_{\rm CS}$ *(upper left), and the reconstructed* $\phi_{\rm CS}$ *is plotted versus the generated* $\phi_{\rm CS}$ *(lower left). Even on a logarithmic scale, the correlation between the generated and the reconstructed distributions is clearly visible. On the right hand side the corresponding residuals are shown, i.e. the difference between generated and reconstructed angles.*

true and the reconstructed angular variables are clearly visible. In Fig. 6.3, also the residuals, i.e. the differences between the true and the reconstructed values, are shown. The full widths at half maximum of the residuals – 0.004 for $\cos\theta_{\mathrm{CS}}$ and 40 mrad for ϕ_{CS} – are much smaller than the bin sizes chosen for the response matrix, i.e. 0.1 for $\cos\theta_{\mathrm{CS}}$ and $\pi/10$ mrad for ϕ_{CS}. This information is needed to legitimate the use of correction factors for the acceptance, which will be introduced in the following.

Corrections factors

The easiest way to correct for acceptance effects is the method of correction factors. The idea of this method is to scale up the content of each bin i of a measured distribution m_i by the ratio of the true bin content g_i and the accepted bin content f_i. The correction factor C_i for bin i is then given by

$$C_i = \frac{g_i}{f_i}. \tag{6.7}$$

In order to obtain a reliable result from this method, the contents of the individual bins have to be uncorrelated. This condition can often be fulfilled, at least approximately, by choosing the widths of the bins accordingly.

The method of correction factors for the acceptance is also limited by the errors of the correction factors. The errors are composed of the error of the number of entries f_i and g_i in a given bin i and of the size of the correction factor C_i. In principle, the error on the number of entries can be made small by generating a sufficiently large sample of Monte Carlo events. However, if the correction factor is large, the errors on the distribution to be corrected for are amplified, and these errors are always limited by the statistics of the data sample and by systematic errors.

Acceptance corrections of the angular variables

The residuals in Fig. 6.3 show that the bin sizes chosen for the response matrix are much larger than the smearing introduced by the detector response. To be conservative and to account for the limited size of the Monte Carlo sample for the study, the bin sizes for the angular distributions are doubled.

Due to the correlations between the angular distributions and M, correction factors C_{ij} are calculated on two-dimensional grids in the $\cos\theta_{\mathrm{CS}} - M$ and the $\phi_{\mathrm{CS}} - M$ planes. The mass range includes 6 bins from 2 GeV/c^2 to 8 GeV/c^2. The distribution of the polar angle $\cos\theta_{\mathrm{CS}}$ is divided in 10 bins from -1 to 1, and the distribution in the azimuth angle ϕ_{CS} from $-\pi$ to π also contains 10 bins.

The correction factor C_{ij} for each bin $(\cos\theta_{\mathrm{CS}\,i}, M_j)$ and $(\phi_{\mathrm{CS}\,i}, M_j)$ is calculated as the ratio of the true bin content g_{ij} and the accepted bin content f_{ij}. The correction factors obtained from a sample of 55,000 Monte Carlo events are shown in Fig. 6.4. In order to avoid large errors, all bins with acceptances smaller than 0.1 or relative Gaussian errors larger than 0.3 are not corrected, i.e. the correction factor is set to zero.

Applications of the correction factor method to Monte Carlo simulated and real data can be found in Fig. 6.5. A Monte Carlo sample of 5,000 Drell-Yan events with masses larger than 2 GeV/c^2 has been analyzed, using a different track and vertex preselection but the same offline analysis chain as the real data. After all cuts, the sample of reconstructed Drell-Yan events comprises 1,351 events, 1,334 of which have ARTE relations to both "true" Monte Carlo simulated tracks. For comparison, the acceptance correction is applied to the 2000 data sample, containing 13,068 events after all cuts.

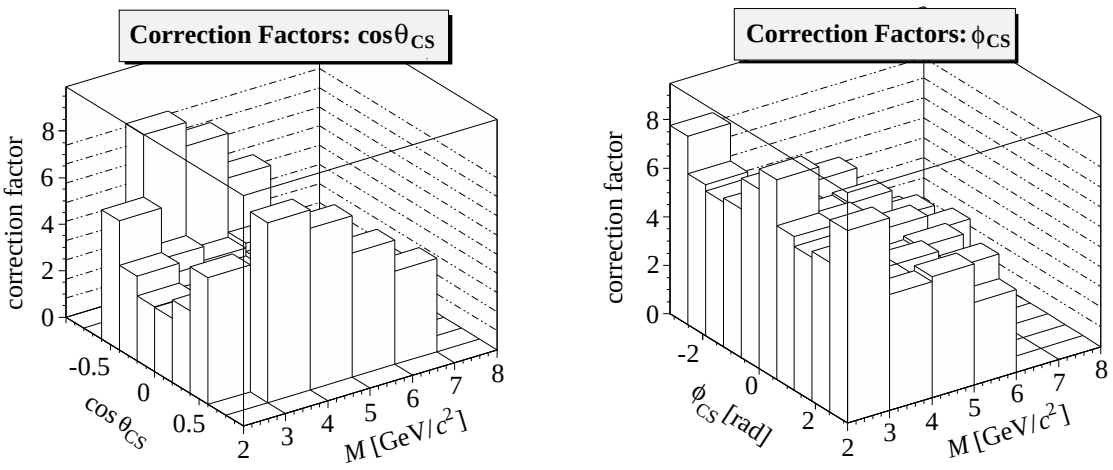

Figure 6.4: *Correction factors for the geometrical acceptance. The correction factors are calculated on* 6×10 *grids in the* $\cos\theta_{\mathrm{CS}} - M$ *plane (left) and in the* $\phi_{\mathrm{CS}} - M$ *plane (right).*

The acceptance correction is calculated for the first mass bin only, i.e. for invariant masses from $2\,\mathrm{GeV}/c^2$ to $3\,\mathrm{GeV}/c^2$, where the statistics are large enough to obtain a meaningful result from the acceptance correction. Since the geometrical acceptance depends strongly on the kinematics of the process, the same kinematic cuts as in the offline analysis are applied to calculate the correction factors, i.e. the track momenta have to be larger than $5\,\mathrm{GeV}/c$ and the transverse momenta larger than $0.7\,\mathrm{GeV}/c$. The acceptance corrected data are fitted by the following function:

$$f(\cos\theta_{\mathrm{CS}}; N, \lambda) = N(1 + \lambda \cos^2\theta_{\mathrm{CS}}), \tag{6.8}$$

where the normalization N and the coefficient λ are the free parameters. The value of the coefficient λ is 1.6 ± 1.4 for the Monte Carlo sample and 3.2 ± 1.2 for the real data sample. Within the large errors, the Monte Carlo result is consistent with $\lambda \approx 1$, as expected from the Monte Carlo generator. The fit result from real data shows a large λ value. The reason for this effect is that the invariant mass region regarded in this analysis contains approximately 75% random combinations of muons. The acceptance correction is specific for a particular physics process – in the case of this analysis the Drell-Yan process – and is not necessarily valid for other processes. The trend towards a large fit value for λ, corresponding to a larger $\cos\theta_{\mathrm{CS}}$ acceptance for the combinatorial background, is consistent with the result of [Cha99]; see Fig. 3.5.

Systematic errors and possible improvements

Since the values f_{ij} and g_{ij} may be strongly correlated, only a lower bound of the error introduced by the correction factor method can be obtained by using Gaussian error propagation. The systematic error of the correction factors can be estimated by calculating the correction factors for different distributions in the same kinematic variable [Sch01a].

The systematic error of the acceptance correction for $\cos\theta_{\mathrm{CS}}$ is estimated by calculating correction factors $C_{ij}(n)$ for three different $\cos\theta_{\mathrm{CS}}$ distributions. Assuming that the generated distribution follows the distribution function $\mathrm{d}\sigma/\mathrm{d}\Omega \sim 1 + \cos^2\theta_{\mathrm{CS}}$, the

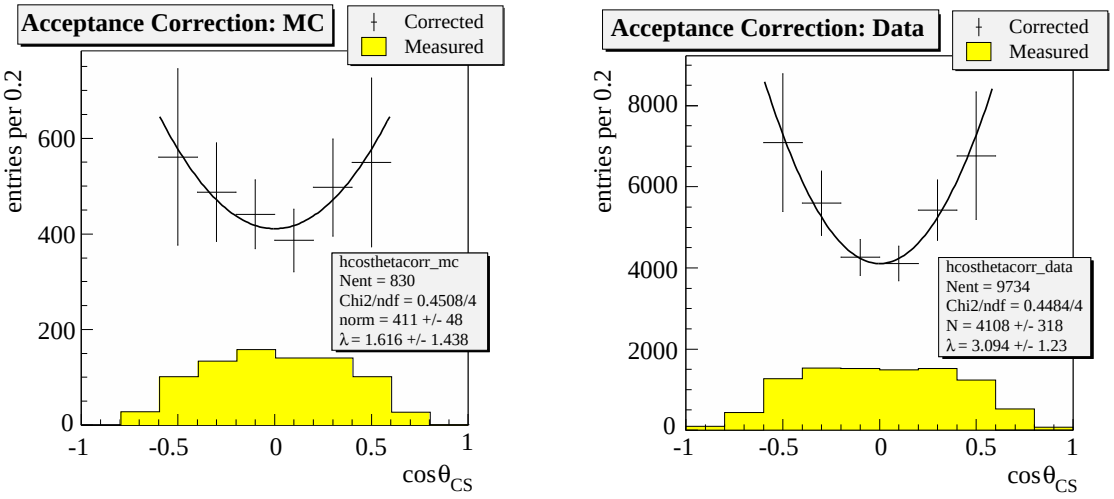

Figure 6.5: *Application of the acceptance correction to Monte Carlo simulations and data in the range of 2–3 GeV/c^2: The acceptance correction is applied to a sample of 830 reconstructed Drell-Yan events from a Monte Carlo simulation (left) and 9,734 reconstructed events from the year 2000 data sample (right). The acceptance corrected data are fitted using the function* $f(\cos\theta_{\mathrm{CS}}; N, \lambda) = N(1 + \lambda\cos^2\theta_{\mathrm{CS}})$.

generated $\cos\theta_{\mathrm{CS}}$ distribution is re-weighted with the factor

$$w(n; \cos\theta_{\mathrm{CS}}) = \frac{1 + n\cos^2\theta_{\mathrm{CS}}}{1 + \cos^2\theta_{\mathrm{CS}}}, \quad n = 0, 1, 2, \tag{6.9}$$

where $n = 1$ corresponds to the generated $\cos\theta_{\mathrm{CS}}$ distribution. The re-weighting procedure according to Equation (6.9) is performed on three Monte Carlo samples of 5,000 events each. The systematic error is defined as the maximum of the deviations of the $n = 0$ and the $n = 2$ sample from the $n = 1$ sample for each bin:

$$\sigma_{ij,\mathrm{sys}} = \max\left(|C_{ij}(1) - C_{ij}(0)|, |C_{ij}(1) - C_{ij}(2)|\right). \tag{6.10}$$

In this definition, the limited statistics still have an influence on the systematic error, so that an increase in statistics is expected to result in a smaller systematic error.

Due to the limited statistics, only the first mass bin, which includes the mass range from 2 GeV/c^2 to 3 GeV/c^2, is used in the analysis. The results of the study are shown in Fig. 6.6. The error bars correspond to the statistical errors only, while the error bands denote the quadratic sum of the statistical and the systematic error. The plot shows that for a sample of 5,000 events, the statistical and the systematic errors are of the same order of magnitude in the forward and backward regions, while in the central region of $\cos\theta_{\mathrm{CS}} \approx 0$, the statistical error dominates. The average total error is approximately 30%. With a sample of 100,000 events, the statistical error of the acceptance correction can be reduced to less than 9%. The influence of increased statistics on the systematic error has not yet been evaluated.

To summarize, it has been shown that the acceptance correction via correction factors is feasible if enough statistics can be generated in the Monte Carlo simulations. In general, the Monte Carlo simulations needed for acceptance corrections suffer from small statistics especially in the high-mass range. With Monte Carlo samples in which different

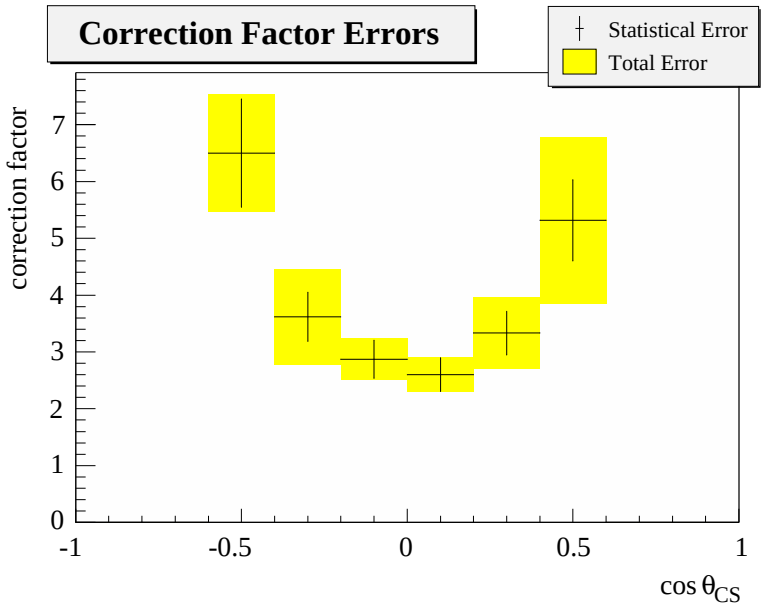

Figure 6.6: *Estimate of the systematic error of the correction factor method for the distribution of* $\cos\theta_{\mathrm{CS}}$*. The plot includes the mass range of 2–3* GeV/c^2*. The error bars account for statistical errors only. The error band denotes the quadratic sum of the statistical error and the systematic error, which is given by the maximum deviation of the re-weighted* $\cos\theta_{\mathrm{CS}}$ *distribution with* $n = 0$ *and* $n = 2$ *– see Equation (6.9) – relative to the unmodified* $n = 1$ *sample.*

mass cut-offs larger than $2\,\mathrm{GeV}/c^2$ are used, the error of the acceptance correction in these mass regions can be sufficiently decreased.

The correction factor method is the easiest method for acceptance corrections. Acceptance corrections are a special case of deconvolution of multi-dimensional distributions. A large number of more sophisticated deconvolution methods, which also have applications in image restoration, can be found in the literature, see e.g. [Abr98, Cow98, Sch98a].

6.2 Experimental observables

After the reconstructed data are corrected for the geometrical acceptance of the detector, observables have to be extracted from the data that allow a reliable test of the Lam-Tung relation. In this section, two strategies to test the Lam-Tung relation will be introduced, a fit-based and a moments-based method. The foundations of these methods as well as first tests will be discussed.

6.2.1 Fits to the angular distributions

A straightforward way to test the Lam-Tung relation is a fit to the acceptance-corrected data, using a least-squares or maximum-likelihood algorithm. From a two-dimensional distribution of the angular variables $\cos\theta$ and ϕ in an arbitrary reference frame, the coefficients λ, μ, and ν of the angular distribution can be obtained by a fit. The fit

function f is given by

$$f(\cos\theta, \phi; N, \lambda, \mu, \nu) = N\left[1 + \lambda\,\cos^2\theta + \mu\,\sin 2\theta\,\cos\phi + \frac{\nu}{2}\,\sin^2\theta\,\cos 2\phi\right], \qquad (6.11)$$

where the normalization N and the coefficients λ, μ, and ν are the free parameters of the fit. As a first test, f is fitted to a sample of 100,000 events from a Monte Carlo simulation of the Drell-Yan process. The simulated events contain Drell-Yan muon pairs with invariant masses larger than $4\,\mathrm{GeV}/c^2$. The fit is applied to the angular distribution of the generated events in the Collins-Soper frame, which is represented by two-dimensional histograms of 20 bins for $\cos\theta_{\mathrm{CS}}$ and ϕ_{CS}.

The fit results are summarized in Table 6.3. Within the errors, the Lam-Tung relation is conserved at the generator level. However, since the fit function (6.11) contains four free parameters, the fit might be unstable if the errors of the measured angular distributions are large. In addition, a problem may arise from the fact that the acceptance corrections for $\cos\theta_{\mathrm{CS}}$ and ϕ_{CS} are done independently, while in the fit, the correlation between $\cos\theta_{\mathrm{CS}}$ and ϕ_{CS} is used to determine the coefficients λ, μ, and ν. In the present stage of the analysis, these effects are hidden by the errors of the acceptance correction and have been neglected.

Table 6.3: *Results of a direct fit to the generated angular distribution of 100,000 Drell-Yan muon pairs. The function f – see Equation (6.11) – is fitted to a two-dimensional histogram of $\cos\theta_{\mathrm{CS}}$ and ϕ_{CS} using a least-squares algorithm.*

Fit variable	Value
λ	0.9551 ± 0.0191
μ	-0.0106 ± 0.0077
ν	0.0049 ± 0.0128
$1 - \lambda - 2\nu$	0.0351 ± 0.0319

The "classical" invariant mass range for Drell-Yan processes includes masses larger than $4\,\mathrm{GeV}/c^2$. Due to the small statistics in this range both in the Monte Carlo simulated and in the real data, an application of the fit method to these samples is dominated by the statistical errors and does not yet lead to meaningful results.

6.2.2 The method of moments

Instead of fitting the angular distributions directly with a least-squares or a maximum-likelihood algorithm, the method of moments can be applied to test the Lam-Tung relation. In the method of moments, the Lam-Tung relation is checked by calculating the first moments, i.e. the expectation values, of a suitable set of linearly independent functions p_i. From a computational point of view, this technique is often simpler than a fit [Cow98]. To describe angular distributions in the Drell-Yan process, the functions p_i have to be functions of the solid angle Ω. Legendre polynomials have been chosen as these functions, since they are used in multipole expansions of radially symmetric problems. Therefore, they are suitable for parametrizing angular distributions [Boh01]. The first moments of $p_i(\Omega)$ are given by

$$\alpha_i \equiv \langle p_i(\Omega)\rangle = \int \mathrm{d}\Omega\, p_i(\Omega)\, f(\Omega), \qquad (6.12)$$

where $f(\Omega)$ is the function used to parametrize the angular distributions, i.e. the angular part of the cross section (3.11). $f(\Omega)$ is rewritten as a function of Legendre polynomials

$$f(\cos\theta,\phi) = \frac{1}{4\pi}\left[1 + \frac{2\lambda}{\lambda+3}P_2(\cos\theta) + \frac{2\mu}{\lambda+3}P_2^1(\cos\theta)\cos\phi + \frac{\nu}{2(\lambda+3)}P_2^2(\cos\theta)\cos 2\phi\right], \tag{6.13}$$

where P_n is a Legendre polynomial, and P_l^m is an associated Legendre polynomial:

$$P_n(\cos\theta) = \frac{1}{2^n\, n!}\frac{\mathrm{d}(\cos^2\theta-1)^n}{\mathrm{d}(\cos\theta)^n}, \tag{6.14}$$

$$P_l^m(\cos\theta) = \frac{(-1)^m}{2^l\, l!}(1-\cos^2\theta)^{m/2}\ \frac{\mathrm{d}^{l+m}(\cos^2\theta-1)^l}{\mathrm{d}(\cos\theta)^{l+m}}. \tag{6.15}$$

Since the Legendre polynomials are orthogonal, linear combinations of the three coefficients λ, μ, and ν can be projected out by calculating the first moments of the Legendre polynomials. As a result, the Lam-Tung relation can be tested by calculating the mean values of the three variables

$$P_2(\cos\theta) = \frac{1}{2}(3\cos^2\theta - 1), \tag{6.16}$$

$$P_2^1(\cos\theta)\ \cos\phi = \frac{3}{2}\sin 2\theta\ \cos\phi, \text{ and} \tag{6.17}$$

$$P_2^2(\cos\theta)\ \cos 2\phi = 3\sin^2\theta\ \cos 2\phi. \tag{6.18}$$

The first moments of these variables are connected to the coefficients λ, μ, and ν by

$$\alpha_0 = \langle P_2(\cos\theta)\rangle = \int \mathrm{d}\Omega\, P_2(\cos\theta)\, f(\cos\theta,\phi) = \frac{1}{5}\frac{2\lambda}{3+\lambda}, \tag{6.19}$$

$$\alpha_1 = \langle P_2^1(\cos\theta)\cos\phi\rangle = \int \mathrm{d}\Omega\, \left(P_2^1(\cos\theta)\cos\phi\right) f(\cos\theta,\phi) = \frac{3}{5}\frac{2\mu}{3+\lambda}, \tag{6.20}$$

$$\alpha_2 = \langle P_2^2(\cos\theta)\cos 2\phi\rangle = \int \mathrm{d}\Omega\, \left(P_2^2(\cos\theta)\cos 2\phi\right) f(\cos\theta,\phi) = \frac{3}{5}\frac{2\nu}{3+\lambda}. \tag{6.21}$$

Hence, the Lam-Tung relation (3.12) can also be formulated using the moments α_0, α_1, and α_2, where it reads:

$$2\alpha_0 + \alpha_2 - 0.2 = 0. \tag{6.22}$$

In Fig. 6.7, the distributions of (6.16)–(6.18) are shown for a sample of 100,000 Monte Carlo Drell-Yan events simulated on the event generator level with masses larger than $4\,\mathrm{GeV}/c^2$. The Collins-Soper frame has been chosen as the reference frame to measure the angular variables. The moments α_i, $i = 0, 1, 2$ are given by the mean values of the distributions i. The errors of these values can be estimated by the root mean square of the corresponding histogram divided by the square root of the number of entries N_i, assuming that α_i are uncorrelated:

$$\sigma(\alpha_i) \approx \frac{\mathrm{rms}(i)}{\sqrt{N_i}},\ i = 0, 1, 2. \tag{6.23}$$

A test of the Lam-Tung relation in these variables is summarized in Table 6.4. Within the errors, the Lam-Tung relation is fulfilled at generator level. The moments α_i have

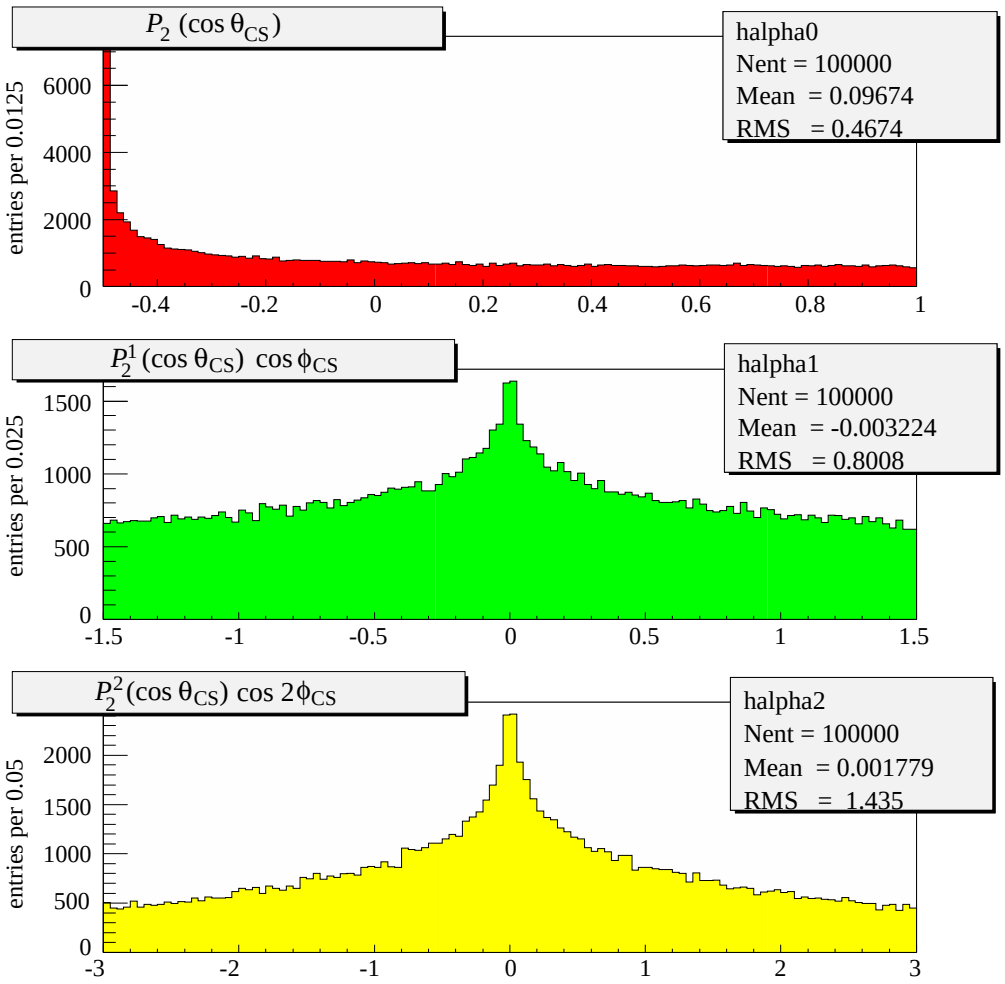

Figure 6.7: *Distribution of the angular components of the Drell-Yan cross section. For 100,000 generated Drell-Yan events with invariant masses larger than 4 GeV/c^2, the distributions in* $P_2(\cos\theta_{\mathrm{CS}})$ *(upper plot), in* $P_2^1(\cos\theta_{\mathrm{CS}})\cos\phi_{\mathrm{CS}}$ *(middle plot), and in* $P_2^2(\cos\theta_{\mathrm{CS}})\cos 2\phi_{\mathrm{CS}}$ *are shown (lower plot).*

been translated into the usual coefficients λ, μ, and ν, which can be compared to the results of Table 6.3, assuming that the moments α_i are uncorrelated. The results of the method of moments and the fit method agree within errors for all three coefficients. The errors calculated by both methods are approximately of the same size.

To summarize, the method of moments is an alternative technique to test the Lam-Tung relation, which is simpler than fitting methods, since only the mean values of three distributions have to be calculated. However, further studies are needed in order to apply the method to acceptance corrected data. The main questions to be addressed are:

- How robust is the method of moments regarding measurement errors?
- How many events are needed to obtain a significant result?
- What is the influence of the number of "irreducible" background events, i.e. combinatorial background from meson decays in flight, on the statistical power of the method of moments?

Table 6.4: *Test of the Lam-Tung relation with the method of moments. On the left side, the moments α_i are given, while on the right side, the values of the corresponding coefficients can be found. The errors of α_i are given by the root mean square of the distribution divided by the square root of the number of events. The errors of λ, μ, and ν are obtained from a Gaussian error propagation, assuming that the moments α_i are uncorrelated.*

Fit variable	Value	Corresp. coefficient	Value
α_0	0.0967 ± 0.0015	λ	0.9570 ± 0.0193
α_1	-0.0032 ± 0.0025	μ	-0.0106 ± 0.0084
α_2	0.0018 ± 0.0045	ν	0.0059 ± 0.0150
$2\alpha_0 + \alpha_2 - 0.2$	-0.0047 ± 0.0054	$1 - \lambda - 2\nu$	0.0312 ± 0.0356

6.3 Expectations for HERA – B

The expectations for HERA – B in the field of Drell-Yan physics are estimated, extrapolating the detector and reconstruction performances achieved in the 2000 run. The guide-line for these studies is to use measured values whenever possible and to make conservative assumptions concerning the progress in detector and trigger commissioning otherwise. Some of the figures that will be presented may be modified in the future due to better understanding of the detector and trigger performances. Therefore, the calculation of the expectations will be described as transparently as possible to allow the replacement of any obsolete figure with an updated estimate or measurement in the future.

J/ψ decays into muon pairs have the same signature in the trigger as Drell-Yan processes, if no cut on an invariant mass window is applied within the trigger chain. In addition, from the J/ψ peak in the di-muon invariant mass spectrum, the number of J/ψ events can be determined reliably by a fit; see Section 5.2. Therefore, J/ψ rates can be used as a normalization for the expected Drell-Yan rates.

The first estimate of HERA – B's potential in the field of Drell-Yan physics was given in the HERA – B letter to the DESY directorate in December 2000 [HB00b]. With improved understanding of the detector and trigger performances and with the improved analysis of the di-muon triggered data in the 2000 run developed in Chapter 5, a new estimate will be given in this section, which refers to the knowledge of March 2001. The estimate of the December 2000 analysis will be reviewed and compared to the new numbers.

6.3.1 The December 2000 estimate for J/ψ and Drell-Yan rates

The December 2000 strategy to get an estimate of the number of expected Drell-Yan events included the following steps:

1. The anticipated improvements in the detector, trigger, and data acquisition systems are assumed to have the same influence on the rates of Drell-Yan and J/ψ events.

2. The number of Drell-Yan candidates in the 2000 data is determined directly from the measured di-muon invariant mass spectrum. The improvement factor expected for the J/ψ rate is used to obtain the anticipated number of Drell-Yan events in the 2001/2002 data-taking period.

The starting-point of the December 2000 analysis was a sample of 1,060 reconstructed J/ψ mesons. This sample was obtained from data of the runs 16012–16677, cf. Table D.1, corresponding to a total running time of approximately 75.8 hours. Hence, after all cuts, the resulting average rate was 14 J/ψ mesons per hour.

This number was scaled up by several factors, reflecting the expected improvements of the detector and trigger chain. The results are summarized Table 6.6.

Expected improvements

The improvements in the efficiencies of the detector and trigger chain up to the FLT were expected to result in an improvement factor of 1.0–2.6. Thereby, the range of the possible improvement factor accounted for scenarios with "low" and "high" efficiencies in the FLT. The anticipated FLT improvements included mainly progress in the muon tube and pad chamber efficiencies and a better trigger performance via the replacement of the FLT emulation code by the real FLT.

The pure SLT efficiency, i.e. without the emulation of the FLT in the muon system, was expected to increase from 75% to 100%, leading to a factor of 1.3. Using the additional acceptance of the ITR and the muon pixel system a gain of 1.0–2.3 was expected, where 1.0 corresponds to no utilization of the inner detectors in the trigger, and a gain of 2.3 implies the full utilization of the inner detectors in the trigger and reconstruction chain. The efficiency of the DAQ was expected to improve by a factor of 1.5 by reducing the dead-time from 50% to 33% and by an additional factor of 8 because no prescaling is needed on the Trigger Decision Unit (TDU) if the FLT tracking is used. Altogether these factors resulted in an anticipated improvement factor of 15.6–93.3. Given a measured J/ψ rate of 14 per hour, this corresponds to an expected J/ψ rate of 218–1,306 per hour. In all these considerations, an interaction rate of 5 MHz was assumed. To compare these studies to the most recent studies, where running at 10 MHz is assumed, the expected rates have to be doubled, resulting in a J/ψ rate of 436–2,612 per hour.

Expected Drell-Yan event rates

The number of Drell-Yan muon pairs in the sidebands next to the J/ψ mass of the invariant mass plot was estimated by a simple event mixing algorithm. The invariant mass of a combination of the positively charged muon of the previous event with the negatively charged muon of the current event was calculated. The spectrum obtained from the mixing algorithm served as an estimate for the combinatorial background in the invariant mass spectrum, since it was constructed from a pair of uncorrelated particles. The invariant mass spectrum and the background estimate from event mixing are shown in Fig. 6.8.

It was assumed that all events that remain after the subtraction of the mixing background are Drell-Yan events. The sidebands included the mass range below the J/ψ mass of 2–2.9 GeV/c^2. In this range, the mass is large enough so that the invariant mass spectrum is not influenced by the intrinsic momentum and transverse momentum cuts of the HERA – B detector. The sidebands also included the mass range of 4.0–8.5 GeV/c^2, i.e. the range above the J/ψ and ψ' resonances and below the mass of the Υ family, since in this range, only continuum processes contribute to the total cross section. The number of Drell-Yan muon pairs obtained from the background subtraction amounted to 230 in the low-mass sideband and 30 in the high-mass sideband. In this study, the low-mass region was always included in the calculation, because it was believed that due

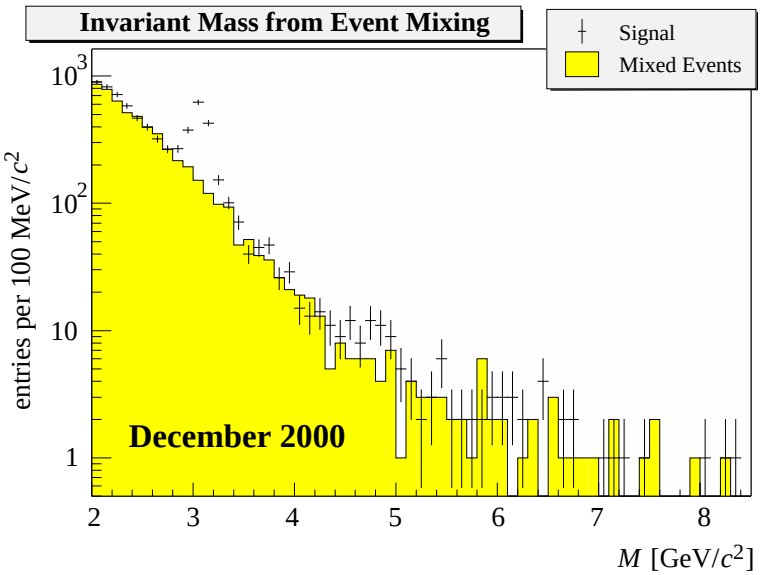

Figure 6.8: *Invariant mass spectrum of December 2000. The underlying histogram contains background events estimated from event mixing.*

to the higher detector resolution, Drell-Yan events from this region could also be used. This decision had a large impact on the number of expected Drell-Yan events, since the low-mass region contains more than 85% of the total statistics. The feasibility of using this mass range in the analysis will be discussed in Section 6.3.3.

The number of 260 Drell-Yan events had to be multiplied by 15.6–93.3 accounting for the anticipated improvements in the detection of J/ψ events and by approximately 20 for 5×10^6 seconds of running per year. As a result of the December 2000 study, a total number of approximately 81,000–485,000 Drell-Yan events per year were expected at an interaction rate of 5 MHz, corresponding to 162,000–970,000 events per year at 10 MHz.

Prospects for testing the Lam-Tung relation

To estimate the feasibility of testing the Lam-Tung relation in HERA – B, these expectations were compared to the statistics acquired in the NA10 experiment. In the NA10 analysis, the violation of the Lam-Tung relation was a 10-sigma effect for large p_T, cf. Fig. 3.4. The data sample for the analysis consisted of 148,000 Drell-Yan events. It was concluded that a test of the Lam-Tung relation in proton-nucleon scattering is possible for HERA – B, if approximately the same number of Drell-Yan events are collected with the HERA – B detector. Since HERA – B has a larger acceptance and a higher center-of-mass energy than NA10 and, in addition, the NA10 measurement has a large significance, it was expected that the number of events needed for a significant test of the Lam-Tung relation could even be smaller. It was concluded that with the expected number of 162,000–970,000 Drell-Yan events per year, a measurement would be possible.

6.3.2 The March 2001 estimate

Many of the figures presented above have been re-evaluated after December 2000, resulting in more detailed expectations for the J/ψ rate improvement [Eis01]. The starting-

point for the study is the most probable trigger scenario for the detector startup in 2001/2002. It consists of a single-track FLT, i.e. the FLT follows a single track seed of the muon pretrigger through the muon system and the OTR and defines RoIs for the SLT tracking from that. The SLT runs in a mode in which two muon tracks are required to issue the SLT. One of the tracks is seeded by the FLT, while the second track has to be found by the combination of the FLTm code and the SLT algorithms. This configuration, referred to as "$\mathrm{FLT}_{1\mu} + \mathrm{SLT}_{2\mu}$" in the following, was tested in August 2000 [HB00a].

In the new evaluation presented in this thesis, the strategy to determine the expected Drell-Yan rates is modified compared to the December 2000 estimate:

1. Improvements in the J/ψ rates in the 2001/2002 run are used to extrapolate the Drell-Yan rate, this time taking into account the different kinematics of the two processes.

2. The expected number of Drell-Yan events in the di-muon triggered data is obtained from the measured number of J/ψ events and from the ratio of the Drell-Yan and the J/ψ cross sections. This strategy is chosen because estimating the number of Drell-Yan events from the subtraction of background, which is only partially under control, leads to a large error already at the starting-point of the estimate. In contrast, the cross section ratios are based on independent measurements of other experiments.

The efficiency of the $\mathrm{FLT}_{1\mu} + \mathrm{SLT}_{2\mu}$ trigger configuration is composed of the detector and pretrigger efficiencies, the FLT efficiency, and the SLT efficiency. The efficiency of the di-muon trigger that is based on the muon pretrigger and the SLT is 0.009, see Section 4.2.4. This efficiency includes the single-track efficiency of the muon pad system and the muon pretrigger and the efficiencies of the FLTm and the SLT algorithms. The measured single-track efficiency of the FLT is 0.23. If both numbers are combined, the resulting two-track efficiency for the complete trigger chain is $0.009 \times \left(1 - (1 - 0.23)^2\right) = 0.004$. With an additional dead-time correction of approximately 0.5, the efficiency of the $\mathrm{FLT}_{1\mu} + \mathrm{SLT}_{2\mu}$ scenario is 0.002 [Eis01]. The J/ψ rate measured in the test of this trigger configuration during the 2000 run was 37 per hour. This number included 44% dead-time, hence running without dead-time would result in an improvement factor of $1/(1 - 0.44) = 1.78$.

Expected improvements in the 2001/2002 run

The anticipated improvements of the J/ψ rate include refinements in the muon system and the OTR. The acceptance of the detector is increased by including the ITR and the muon pixel system in the trigger. In addition, more efficient use of the SLT and the DAQ is taken into account:

- In the muon system, the average efficiency of the muon pads is expected to increase from 0.71 to 0.75, resulting in a factor of 1.12. Note that the single pad efficiencies have to be squared to obtain the efficiency for a pretrigger coincidence, since in the muon pretrigger, a coincidence of pads in two superlayers is required. By repairing broken channels, the average efficiency of the muon tube chambers is anticipated to go up from 0.62 to 0.88, resulting in a factor of 1.43. Improvements in the mapping of the detector geometry to the FLT account for another factor of 1.1.

- In the OTR, the improved mapping of detector and readout channels accounts for a factor of 1.08. Repairing dead channels in the OTR results in another factor of 1.28, while improvements in the mapping to the FLT increase the efficiency by a factor of 1.04. An efficiency gain of the OTR chambers from 90% to 93% contributes an additional factor of 1.06.

Hence, the FLT can take advantage of a total gain factor of 2.68 per track.

The efficiency of the SLT can be improved by a better input to this trigger level. Since the FLT is able to provide smaller RoIs than the FLTm code, tighter cuts can be applied in the SLT, and the SLT efficiency is increased. If detector effects are separated from trigger effects, i.e. an "ideal" detector without problematic channels is assumed, the efficiencies of the FLTm and the SLT algorithms are given by the values of Table 6.5 [Kre01].

Table 6.5: *Two-track efficiencies of the SLT algorithms obtained from Monte Carlo simulations, assuming an ideal detector without problematic channels [Kre01].*

Algorithm	Efficiency
FLTm	0.34 ± 0.03
Slicer	0.68 ± 0.04
Refit-X	0.93 ± 0.04
Refit-Y	0.90 ± 0.04
L2Sili	0.93 ± 0.05
Overall SLT	0.53 ± 0.13

The resulting two-track efficiency for the complete SLT chain amounts to 0.53 (0.73 for a single track). This chain does not include the FLTm algorithm, which has a two-track efficiency of 0.34 (0.58 for a single track). With smaller RoIs, the single track efficiency of the SLT is expected to increase from 0.73 to 0.84. If both tracks were triggered by a combination of the FLTm algorithm and the SLT, the combined efficiency would be $0.58^2 \times 0.73^2 = 0.18$. In the $\mathrm{FLT}_{1\mu} + \mathrm{SLT}_{2\mu}$ scenario, only one track has to be triggered by the FLTm algorithm, the other track is found by the FLT, which increases the SLT efficiency for this track to 0.84. Therefore, the efficiency of this scenario is $(0.58 \times 1) \times (0.73 \times 0.84) = 0.36$. The result is an improvement by a factor of 2.0 from the SLT. The SLT improvement may serve as an example of the possible variations of the estimates presented in this chapter. The improvement factor of 2.0 corresponds to conservative assumptions concerning the improvement of the SLT algorithms. For an optimistic extrapolation of the SLT performance, the factor would be replaced by 4.0 [Kre01].

The additional acceptance of the inner detector, i.e. the ITR and the muon pixel system, accounts for a factor of 2.2. Increasing the interaction rate to 10 MHz, the J/ψ rate is doubled, if the dead-time of the trigger chain is unchanged. To summarize, the improvements of the efficiency of the HERA−B detector in the detection of J/ψ decays into a muon pair add up to a factor of 42.0. This corresponds to an anticipated J/ψ rate of 1,554 per hour in the data-taking of the years 2001/2002. The estimates of March 2001 for the J/ψ rate in 2001/2002 are compared to the estimates of December 2000 in Table 6.6.

Table 6.6: *Comparison of the J/ψ rate estimates of December 2000 [HB00b] and March 2001 [Eis01, Kre01].*

	December 2000	March 2001
Trigger scenario (5 MHz)	SLT	$\mathrm{FLT}_{1\mu} + \mathrm{SLT}_{2\mu}$
Measured rate [J/ψ's per hour]	14	37
Trigger & detector improvements	1.0–2.6	2.68
SLT improvement	1.3	2.0
Prescaling	8	–
DAQ dead-time	1.5	1.78
Inner acceptance (ITR & Pixel)	1.0–2.3	2.2
10 MHz interaction rate	2.0	2.0
Expected rate [J/ψ's per hour]	436–2,612	1,554

Translation of the improvements from J/ψ events into Drell-Yan events

In the December 2000 study, the expected rate of Drell-Yan events was derived from the expected J/ψ rate by using the same scaling factors. This approach assumes that the detector improvements have exactly the same impact on J/ψ and on Drell-Yan events. However, this assumption is not true in general. Therefore, the relevance of the scaling factors for Drell-Yan events is discussed in the following. In addition, importance is attached to the option of using only invariant masses larger than 4 GeV/c.

Improvements in the muon system and in the OTR affect muons from Drell-Yan processes and from J/ψ decays in the same way, if only the average improvements of the chamber performances are regarded. Since the distributions of intersection points of muon trajectories in the subdetectors are different for different physics processes, local efficiency variations may have a small effect on the improvements in the detector performance. However, a more accurate estimate of this effect is difficult to formulate, and therefore it is neglected in the following. Hence, the total gain factor of 2.68 per track in the pretrigger and FLT chain is unchanged for Drell-Yan events.

The SLT improvement are caused by a better seeding from the FLT, which, again apart from local effects, is the same for Drell-Yan and J/ψ events.

Since the Drell-Yan process contributes to the continuum in the di-muon invariant mass spectrum, the Drell-Yan kinematics and the J/ψ kinematics are different. This effect can be illustrated e.g. by the Monte Carlo simulated p_{T} distributions of the muons from both processes, as shown in Fig. 6.9. The mean value of the transverse momentum of the positively charged muon from a Drell-Yan process is (1.49 ± 0.02) GeV/c, compared to a mean value of (1.63 ± 0.01) GeV/c for the positively charged J/ψ muon. Hence, the probability for a Drell-Yan muon to pass the inner detector is larger, and the expected improvements by using the ITR and the muon pixel system are larger for Drell-Yan events than for J/ψ events.

A detailed comparison of the acceptances for Drell-Yan and J/ψ events, using the definition of the acceptance requirements of Section 6.1.2, is shown in Table 6.7. Since the total acceptances with and without the inner detectors are very sensitive to the acceptance requirements in the VDS, these numbers are also given for a VDS acceptance of 1.0. The overall acceptance for Drell-Yan muon pairs is smaller than for muon pairs from J/ψ decays. The relative improvements by including the inner detector result in

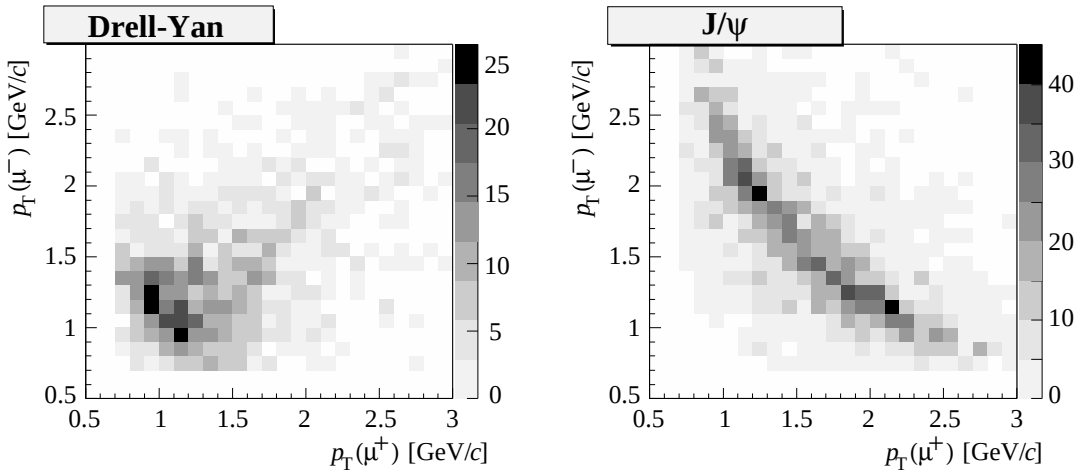

Figure 6.9: *Comparison of the reconstructed muon p_T distributions for Drell-Yan and J/ψ events from a Monte Carlo simulation. The mean transverse momentum of the positively charged muon in Drell-Yan events of* $(1.49 \pm 0.02)\,\mathrm{GeV}/c$ *is smaller than the mean value for J/ψ events, which amounts to* $(1.63 \pm 0.01)\,\mathrm{GeV}/c$.

a factor of 1.42 for J/ψ decays. This number should be used instead of the factor of 2.2 given in [Eis01], if the gain for the J/ψ rate is calculated. The overall improvement factor decreases from 42.0 to 27.1 accordingly, leading to an expected J/ψ rate of 1,003 per hour.

For Drell-Yan processes, the relative gain by using the inner detectors is 1.44 including invariant masses larger than $2\,\mathrm{GeV}/c^2$ and 1.52 if only masses larger than $4\,\mathrm{GeV}/c^2$ are considered. Hence, the improvement factor for Drell-Yan events is $1.44/1.42 \times 27.1 = 27.5$ including the low-mass Drell-Yan events and $1.52/1.42 \times 27.1 = 29.0$ including only high-mass Drell-Yan events.

In addition, the reconstruction efficiency may be different for muons from Drell-Yan and J/ψ events. However, since the geometrical acceptance is already expected to discard muons which cannot be reconstructed, and the signature of the remaining muons in the HERA – B detector is the same for Drell-Yan and J/ψ events, the same reconstruction efficiency is assumed for both processes.

Cross section ratios

While in the December 2000 estimate the number of Drell-Yan events in the di-muon data was obtained from event mixing and background subtraction, for the new estimate, the anticipated Drell-Yan rate is derived from the ratio of the Drell-Yan to the J/ψ cross section. The reason for this policy change is the following. As already discussed in Section 5.2.4, the results of the event mixing procedure are difficult to interpret. Background estimates based on the number of like-sign muon pairs rely on Poisson statistics, which is problematic to apply, given the small number of events in the high-mass region of the di-muon spectrum.

The cross sections used for the estimate presented in this chapter are obtained from independent measurements of other experiments. The expectations for the HERA – B experiment include extrapolations to the energy regime of HERA – B and corrections for HERA – B's acceptance.

Table 6.7: *Detailed comparison of the geometrical acceptances for muon pairs from Drell-Yan processes and J/ψ events. The study is based on 40,000 simulated J/ψ events and 55,000 simulated Drell-Yan events, 4,754 of which have invariant masses larger than 4 GeV/c^2. The sum of the acceptances in the inner and outer parts of the main tracker and the muon system do not add up to the acceptance of the whole subdetector, because the inner and outer parts of these subdetectors overlap. Since the total acceptance is very sensitive to the acceptance requirements in the VDS, the total acceptances assuming a VDS acceptance of 1.0 are shown for comparison.*

	$J/\psi \to \mu^+\mu^-$	Drell-Yan ($M > 2\,\mathrm{GeV}/c^2$)	Drell-Yan ($M > 4\,\mathrm{GeV}/c^2$)
VDS	0.712 ± 0.004	0.421 ± 0.007	0.55 ± 0.02
Main tracker	0.673 ± 0.006	0.401 ± 0.007	0.55 ± 0.02
both in OTR	0.433 ± 0.008	0.246 ± 0.009	0.32 ± 0.03
one ITR – one OTR	0.391 ± 0.008	0.232 ± 0.009	0.34 ± 0.03
both in ITR	0.103 ± 0.016	0.069 ± 0.016	0.09 ± 0.05
Muon system	0.676 ± 0.006	0.429 ± 0.007	0.59 ± 0.02
both in pad system	0.427 ± 0.008	0.231 ± 0.009	0.33 ± 0.03
one pixel – one pad	0.244 ± 0.010	0.172 ± 0.010	0.26 ± 0.03
both in pixel system	0.044 ± 0.024	0.052 ± 0.019	0.05 ± 0.06
Accepted in HERA – B	0.481 ± 0.008	0.261 ± 0.009	0.38 ± 0.02
Without inner detectors	0.338 ± 0.008	0.181 ± 0.010	0.25 ± 0.03
VDS	1.0	1.0	1.0
Accepted in HERA – B	0.604 ± 0.006	0.347 ± 0.007	0.50 ± 0.02
Without inner detectors	0.353 ± 0.008	0.190 ± 0.010	0.27 ± 0.03

The cross section for the Drell-Yan process has been measured in numerous experiments. A compilation of the data is given in [Sti93]. To derive the expected Drell-Yan cross section for HERA – B, data from an experiment in a similar energy regime has been chosen. The E772 experiment used a 800 GeV proton beam on a deuterium target. The published cross sections are given in the differential form [Ald90]

$$\frac{\mathrm{d}\sigma}{\mathrm{d}M} = \frac{8\pi\alpha^2}{9M^3} \int_{x_1}^{1} \frac{\mathrm{d}x_1}{x_1} \left[\sum_{\mathrm{q}} e_{\mathrm{q}}^2 \left\{ f_{\mathrm{q}}(x_1) f_{\overline{\mathrm{q}}}(\tau/x_1) + (\mathrm{q} \leftrightarrow \overline{\mathrm{q}}) \right\} \right] \tag{6.24}$$

and in the double-differential form [McG94]

$$M^3 \frac{\mathrm{d}^2\sigma}{\mathrm{d}M\,\mathrm{d}x_{\mathrm{F}}} = \frac{8\pi\alpha^2}{9} \frac{x_1 x_2}{x_1 + x_2} \left[\sum_{\mathrm{q}} e_{\mathrm{q}}^2 \left\{ f_{\mathrm{q}}(x_1) f_{\overline{\mathrm{q}}}(x_2) + (\mathrm{q} \leftrightarrow \overline{\mathrm{q}}) \right\} \right]. \tag{6.25}$$

The data are shown in Fig. 6.10 together with theoretical predictions of the Drell-Yan cross section based on Equation (6.24). The parton distribution functions $f_{\mathrm{q}}(x, M^2)$ used for the prediction are the leading order parton distributions of the GRV98 [Glü98] and the CTEQ5 [Lai00] sets. The theoretical predictions are smaller than the measured values of E772 by a factor of 1.5–2.0, leaving space for an additional K-factor from

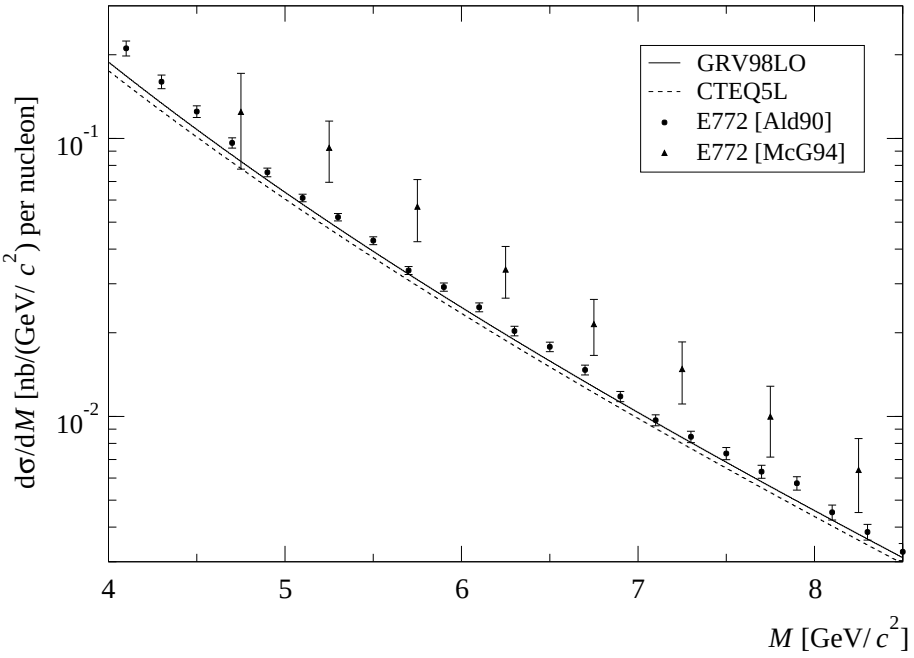

Figure 6.10: *Differential Drell-Yan cross section from the E772 experiment [Ald90, McG94]. The data points and errors of [McG94] (triangles) are obtained from the double-differential cross section* $M^3\,\mathrm{d}^2\sigma/\mathrm{d}M\mathrm{d}x_\mathrm{F}$ *by summing all* x_F *bins for the same mass and assuming that the cross section is symmetric in* x_F*. The theoretical predictions are calculated from Equation (6.24), using the leading order parton distribution functions of [Glü98, Lai00].*

next-to-leading order cross section contributions. This result gives further confidence in the strategy of using cross section ratios as a starting-point for the evaluation of the Drell-Yan expectations.

The differential cross section was measured in the range of 4.0–15.1 GeV/c^2, and the double-differential data enclose the kinematic region in M and x_F which was accessible to E772, i.e. invariant masses in the range of 4.5–16.0 GeV/c^2 and a large fraction of the forward region in x_F, i.e. $0.0 < x_\mathrm{F} < 0.7$. The acceptance of the HERA – B detector includes the central region $-0.4 < x_\mathrm{F} < 0.3$. Since Equation (6.25) is invariant under the exchange of x_1 and x_2, the cross section is symmetric in x_F, so that the double-differential E772 results for positive x_F have to be doubled to account also for negative x_F values. In Fig. 6.10, the x_F bins for each mass bin have been summed. The errors are calculated by Gaussian error propagation, assuming that the x_F bins are uncorrelated.

To obtain the total cross section, the data of Fig. 6.10 are fitted by an analytic function which is integrated afterwards. To control the systematic errors connected to the integration, two different fit functions have been chosen, for an exponential and for a power law dependence. Both have two free parameters a and b:

$$f_1(M;a,b) = a\,e^{bM}, \tag{6.26}$$

$$f_2(M;a,b) = a\,M^b. \tag{6.27}$$

The results of the fits and the integrated cross sections are summarized in Table 6.8. Since the fit parameters have large errors and are strongly correlated, the error of the

cross section integration is large. It can by estimated by taking half the difference between the integrated cross section values obtained from the different parametrizations, which vary by approximately 10–15%.

The older differential E772 data sample [Ald90], which has been used in [HB00a], shows a significantly smaller cross section than the data of the newer double differential E772 analysis [McG94]. The E772 collaboration recommends using the data of the newer analysis for evaluations of the Drell-Yan cross section [Mos01]. Therefore, the integrated Drell-Yan cross section from E772 used in the following analysis is 0.3 nb per nucleon.

The Drell-Yan cross section shows scaling in the variable $\tau \equiv M^2/s$. Since the center-of-mass energy in HERA – B is larger than in E772, $\sqrt{s} = 41.6\,\text{GeV}$ instead of $\sqrt{s} = 38.8\,\text{GeV}$, the same τ value corresponds to a higher mass in HERA – B. Therefore, the mass scale of E772 has to be shifted by the inverse ratio of the center-of-mass energies, i.e. the interval of 4.0–8.5 GeV/c^2 in HERA – B corresponds to 3.7–7.9 GeV/c^2 in E772. Thus, the expected Drell-Yan cross section in HERA – B from the E772 measurements is approximately

$$\sigma_{\text{Drell-Yan}} = (0.40 \pm 0.05)\,\text{nb/nucleon}. \tag{6.28}$$

Table 6.8: *Integrated cross sections for the Drell-Yan process from E772 and extrapolation to HERA – B energies. The cross sections for HERA – B are calculated for the mass range of* $3.7-7.9\,\text{GeV}/c^2$*, corresponding to* $4.0-8.5\,\text{GeV}/c^2$ *in E772.*

	E772 [Ald90]	E772 [McG94]
Data range [GeV/c^2]	4.0–8.5	4.5–8.5
Scaling factor for HERA – B	0.933	0.933
σ for exponential function (6.26)	≈ 0.19 nb/nucleon	≈ 0.28 nb/nucleon
σ (scaled for HERA – B)	≈ 0.25 nb/nucleon	≈ 0.36 nb/nucleon
Parameter a	7.1 ± 0.7	8.0 ± 1.0
Parameter b [(GeV/c^2)$^{-1}$]	-0.917 ± 0.015	-0.866 ± 0.018
σ for power law (6.27)	≈ 0.21 nb/nucleon	≈ 0.32 nb/nucleon
σ (scaled for HERA – B)	≈ 0.29 nb/nucleon	≈ 0.45 nb/nucleon
Parameter a [(GeV/c^2)$^{-b}$]	582.2 ± 50.5	768.5 ± 273.4
Parameter b	-5.602 ± 0.047	-5.495 ± 0.193

To evaluate the expectations of HERA – B on the basis of cross section ratios, the expected Drell-Yan cross section has to be compared to the J/ψ cross section. Results from a kinematic range similar to HERA – B were obtained by the E789 experiment, where 800 GeV protons are collided with a gold target. In E789, the measured J/ψ production cross section was [Sch95]

$$\sigma_{\text{J}/\psi} = (422 \pm 2\,(\text{stat.}) \pm 88\,(\text{sys.}))\,\text{nb/nucleon}. \tag{6.29}$$

This number compares well with a preliminary HERA – B measurement in the di-electron channel, which yields [Sam01]

$$\sigma_{\text{J}/\psi} = (415 \pm 58\,(\text{stat.}) \pm 30\%\,(\text{sys.}))\,\text{nb/nucleon}. \tag{6.30}$$

The branching fraction of J/ψ mesons into muon pairs is $(5.88 \pm 0.10)\%$ [Gro00]. Therefore, the cross section for the direct production of J/ψ mesons with a subsequent

decay into muon pairs is 24.8 nb per nucleon, 62 times larger than the cross section for Drell-Yan muons in the range of 4.0–8.5 GeV/c^2 in HERA – B. To obtain the expected number of Drell-Yan events from the number of J/ψ events, also the different acceptances have to be taken into account. Since in the 2000 run the inner detectors have not been used, the acceptances of Table 6.7 without these subdetectors have to be compared for the high-mass region. The acceptance for muon pairs from Drell-Yan processes is 0.25 ± 0.03, while the J/ψ acceptance is 0.338 ± 0.008. Therefore, the cross section ratio has to be scaled by the ratio of the acceptances which is $0.34/0.25 = 1.36$. The resulting "effective" cross section ratio of muon pairs from J/ψ decays and Drell-Yan processes is 84.3, i.e. the number of reconstructed J/ψ mesons has to be divided by 84.3 to obtain the expected number of Drell-Yan muon pairs in the range of 4.0–8.5 GeV/c^2. Hence, a total number of $2,688/84.3 = 31.9$ Drell-Yan events is expected in this range in the 2000 data sample.

The expected number of muon pairs from Drell-Yan events in 2001/2002

From the measurements and considerations collected in this chapter, the expected number of Drell-Yan events in the data-taking period of 2001/2002 can be derived. The number of 31.9 events expected in the 2000 data sample from the ratio of the Drell-Yan and the J/ψ cross sections is scaled up by a factor of 27.1 from the anticipated improvements in the detector and trigger systems and by a factor of 8.9 due to the longer time for data-taking – 5×10^6 seconds instead of 5.62×10^5 seconds – resulting in an expectation of

7,694 muon pairs from Drell-Yan processes

with masses in the the range of 4.0–8.5 GeV/c^2 in the 2001/2002 data sample. A compilation of these numbers can be found in Table 6.9.

Table 6.9: *Expectations for the number of Drell-Yan events in 2001/2002. The expected number of Drell-Yan events is derived from the ratio of the Drell-Yan and the* J/ψ *cross sections. The numbers assume the standard analysis cuts and take into account only the high-mass region of* $4.0 - 8.5\,\mathrm{GeV}/c^2$.

Expected number of Drell-Yan candidates in the 2000 data sample	31.9
Expected improvement factor for 2001/2001	241.2
Detector & trigger improvements	27.1
One year of data-taking	8.9
Number of Drell-Yan events in 2001/2002	7,694

The errors of these expectations are large, since a small number of events is scaled up using a set of factors which include uncertainties, e.g. the cross section ratio. In addition, since the extrapolation of the detector and trigger improvements is conservative, the overall improvement factor may be underestimated by a factor of two or more. However, the numbers presented above represent the best knowledge of the HERA – B detector and trigger as of March 2001.

6.3.3 Discussion of the prospects of HERA – B in the field of Drell-Yan physics

After the discussion of the number of Drell-Yan events expected in the 2000 data sample and the anticipated improvements of the detector and trigger system of the HERA – B experiment, in this section, the prospects of HERA – B in the field of Drell-Yan physics that result from these measurements and extrapolations to the future will be evaluated.

Prospects of the event selection

The ratio of signal events to background events is an important input to all evaluations of the prospects of Drell-Yan physics, because it has an impact on the statistical power of practically all measurements. Therefore, better selection cuts are desirable, which would suppress a larger fraction of the background in the mass range relevant for Drell-Yan physics than the cuts of the analysis chain described in Chapter 5.

One of the possible improvements is a tighter cut on the muon likelihood. The muon likelihood is calculated from the extension of tracks to the muon system and the distribution of hits in the muon system which are used to reconstruct these tracks. A tighter cut on the muon likelihood can be used to select a very clean sample of muons. A comparison of the invariant mass spectrum obtained with the standard cut, i.e. a likelihood larger than 0.06 for both tracks, to the spectrum from the tighter likelihood cut of 0.9 is shown in Fig. 6.11. The number of events for both cuts are summarized in Table 6.10. While the number of events in the J/ψ peak is reduced from 2,688 events to 1,912 events (a factor of 1.4), the number of background events in the sideband is reduced from 9,188 to 3,945 (a factor of 2.3). The background fraction calculated from the number of like-sign events keeps a constant value of approximately 75% for both cuts.

The number of background events obtained from the combination of like-sign muon pairs in the high-mass range is larger than the number of expected Drell-Yan events from the cross section ratio and the number of unlike-sign muon pairs in this range. Since the absolute numbers are small, the influence of statistical fluctuations on the signal-to-background ratio is large. Hence, it is not yet possible to draw any conclusions concerning the purity of the expected Drell-Yan signal from the 2000 data sample.

Further background suppression is expected from more sophisticated vertexing, which would allow a tighter cut on the distance between the di-muon vertex and the closest target wire. In the "standard" analysis, a vertex-target distance of less than 3 mm is required. A tighter cut is expected to suppress muon pairs which include muons from semileptonic D meson decays close to the target wire.

A large fraction of the background is combinatorial background from pion and kaon decays in flight. An implementation of a "kink-finder" algorithm in the VDS and main tracker tracking packages may help to suppress this background. While multiple scattering takes place in every layer of the HERA – B detector, only a single kink occurs at the decay position of the pion or kaon. Further efforts are needed to evaluate the prospects of such an algorithm. The theoretical limit of the background suppression, which is given by the construction of HERA – B as an open-aperture spectrometer, i.e. without thick hadron absorbers directly behind the target, is currently unknown.

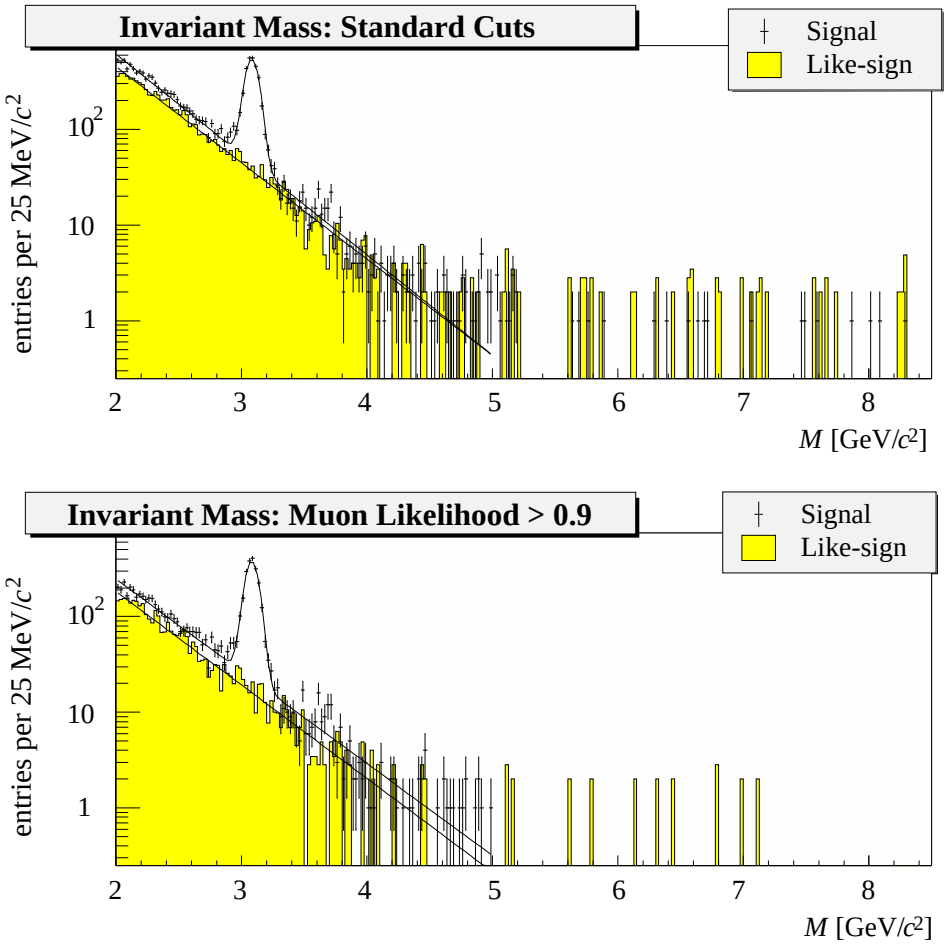

Figure 6.11: *Invariant mass spectra for different muon likelihood cuts. In the upper plot, the standard cuts of Chapter 5 have been applied, where the muon likelihood is required to be larger than 0.06, while in the lower plot the muon likelihood is larger than 0.9 for both muons. The filled histograms represent the estimated number of background events obtained from the number of like-sign muon pairs.*

Table 6.10: *Number of events in the sidebands of the* J/ψ *peak for the standard cuts of Chapter 5 and for a tight cut on the muon likelihood (*lmmu > 0.9*). The "signal & background" sample includes all unlike-sign muon pairs that pass the cuts, while the "like-sign background" sample contains the background estimate from the number of triggered like-sign muon pairs. In brackets the number of expected Drell-Yan events from the cross section ratio.*

	2.0–2.9 GeV/c^2	4.0–8.5 GeV/c^2
Standard cuts: signal & background	9079	109 (31.9 Drell-Yan expected)
Standard cuts: like-sign background	6915	128
lmmu > 0.9: signal & background	3897	48 (22.7 Drell-Yan expected)
lmmu > 0.9: like-sign background	2870	36

Prospects of testing the Lam-Tung relation in HERA – B

Based on the current expectations for the improvements of the HERA – B detector and trigger and on the year 2000 $J/\psi \to \mu^+\mu^-$ data sample, approximately 8,000 fully reconstructed Drell-Yan events with invariant masses larger than $4\,\mathrm{GeV}/c^2$ are anticipated in the 2001/2002 data-taking.

In the NA10 experiment, a significant result has been obtained from a sample of 148,000 Drell-Yan events. Using a sample of 28,000 events, the E615 experiment obtained a result with a smaller significance. Both experiments have only a very small fraction of background events in the invariant mass spectrum, due to the thick hadron absorbers. In the NA10 experiment, less than 1% combinatorial background from decays in flight is expected [Gua88]. The expected number of Drell-Yan events per year in HERA – B is of the same order of magnitude as the number of events in the E615 data sample, but with a larger background. The excess of events that is needed to compensate for this drawback is currently unknown. The calculation of this quantity is also influenced by other factors, e.g. HERA – B's better detector resolution and larger geometrical acceptance.

To summarize, from the number of expected 8,000 Drell-Yan events and the uncertainty in the signal-to-background ratio – see Table 6.10 and Fig. 6.11 – precise conclusions concerning the feasibility of a measurement of the Lam-Tung relation in the HERA – B experiment cannot be drawn yet.

Chapter 7

Summary

In this Diploma thesis, data analysis issues of the data-taking during the 2000 run of the HERA – B experiment have been treated. In the year 2000, the HERA – B experiment was in its commisioning phase, including regular data-taking as well as tests of the detector and the trigger. The year 2000 was also the year of a major decision for the HERA – B experiment, i.e. the definition of a new physics program for the data-taking in 2001/2002, including interesting topics from QCD and charm physics, while at the same time also taking into account delays and problems in the commisioning of the detector and trigger systems. This thesis comprises an analysis of the 2000 data as well as an evaluation of the prospects in one of the new physics topics of HERA – B, i.e. the measurement of the angular distribution of muon pairs from the Drell-Yan process.

During the 2000 run, a special di-lepton trigger was set up, which substituted the tracking of the First Level Trigger (FLT). This trigger consisted of a combination of the pretriggers and the Second Level Trigger (SLT), where the starting-points for tracking in the SLT are defined by the electron and the muon pretriggers instead of the FLT. In the muon system, the pure hardware information of the muon pretrigger was further improved by a simple substitute of the FLT tracking, the FLTm algorithm.

The analysis techniques in HERA – B evolved in parallel with the trigger strategies. Starting from algorithms in which track segments in different subdetectors were matched manually, with the development of the SLT di-lepton trigger, the SLT tracking information was used directly in the data analysis. Finally, the complete offline reconstruction chain could be used efficiently for the "standard" analysis of the di-lepton triggered data.

The direct production of J/ψ mesons with a decay into a lepton pair was the most important "benchmark process" to evaluate the performance of the trigger and reconstruction chain in the HERA – B experiment. In this thesis, results of the J/ψ search with the matching-based, the SLT-based, and the "standard" procedures have been presented. After all cuts are applied, the complete di-muon triggered data sample of the 2000 run contains about 2,700 J/ψ mesons. The measured width of the J/ψ signal is approximately $51\,\mathrm{MeV}/c^2$, while from Monte Carlo simulations of the HERA – B detector, a J/ψ width of about $40\,\mathrm{MeV}/c^2$ is obtained. The position of the J/ψ peak is slightly shifted from the literature value of $3096.87\,\mathrm{MeV}/c^2$ to $3081\,\mathrm{MeV}/c^2$. Most probably, the reason for this shift is connected with the calibration of the magnetic field.

Studying events in the continuum underneath the J/ψ resonance requires good understanding of the background in the di-muon invariant mass spectrum. Combinatorial background arises from muons which are produced by meson decays in flight. Their number can be controlled via the number of like-sign muon pairs in the spectrum. It

has been shown in this thesis that approximately 75% of the background events in the mass range of 2.0–8.5 GeV/c^2 originate from random combinations of muons from different physics processes in the same event.

The Drell-Yan process is the most abundant continuum process in the mass range above the J/ψ and the ψ' resonances. Drell-Yan processes are a fertile testing ground for the predictions of perturbative QCD. In the 1980's, pion-nucleon scattering experiments have measured a discrepancy between data and QCD predictions in the angular distributions of Drell-Yan muon pairs. The experiments showed that the Lam-Tung relation, which connects different contributions to the angular distribution, is violated. Since no test of the Lam-Tung relation in proton-nucleon scattering exists so far, HERA–B has the opportunity to contribute to this field, provided that the number of reconstructed Drell-Yan events is large enough, and background events can be suppressed efficiently.

Based on the analysis of the di-muon triggered data of 2000 and on Monte Carlo studies, the prospects of HERA–B in the field of Drell-Yan physics have been evaluated. This evaluation includes the development of analysis tools as well as a detailed analysis of the expected event rates and of the problem of background rejection.

Techniques for the correction of the geometrical acceptance on the basis of bin-wise correction factors have been evaluated. In addition, strategies for the actual measurement of the Lam-Tung relation have been discussed. Besides direct fits to the acceptance-corrected angular distributions, a method using the first moments of certain components of the angular distribution has been tested. On the generator level, both methods lead to very similar results.

The expected event rates have been determined from the measured J/ψ rate in the 2000 run and some assumptions of improvements in the detector and trigger performance. The number of Drell-Yan events in the 2000 data sample has been estimated from the number of J/ψ events via the ratio of the cross sections for these processes and an additional acceptance correction. To calculate the expected number of Drell-Yan events in the 2001/2002 data-taking period, this number has been scaled up by a factor that takes into account the anticipated improvements in the detector and the trigger. From this study, 7,694 Drell-Yan muon pairs with invariant masses above 4 GeV/c^2 are expected. Due to the low statistics in this invariant mass range in the 2000 data sample, the ratio of Drell-Yan events to the combinatorial background cannot be derived with sufficient precision. Therefore, it is not yet possible to draw any conclusions concerning the ideal mass range to study Drell-Yan physics in HERA–B.

A test of the Lam-Tung relation is difficult given the expected number of signal events and the large uncertainty of the measured amount of background. However, with further improvements in the detector and trigger chain and in the offline analysis, a measurement may be possible in the future.

Appendix A

Kinematics of the Drell-Yan process

In this chapter the most important kinematic variables relevant to the analyses in this thesis are summarized. After a short overview of general fixed-target kinematics, the variables and reference frames used for measurements of the angular distributions of the final state leptons in Drell-Yan processes are introduced.

A.1 General fixed-target kinematics

The kinematics of inclusive scattering measurements are described by a suitable set of two independent variables. In fixed-target experiments the Feynman-x variable x_{F} and τ are chosen. Feynman-x is defined as the longitudinal momentum p_z, normalized to its maximum value $p_{z,\mathrm{max}}$:

$$x_{\mathrm{F}} \equiv \frac{p_z}{p_{z,\mathrm{max}}}. \tag{A.1}$$

In the center-of-mass frame, the maximum longitudinal momentum is given by $p_{z,\mathrm{max}} \approx \sqrt{s}/2$. τ is defined as the square of the ratio of the invariant mass M and the center-of-mass energy $\sqrt{s}$:

$$\tau \equiv \frac{M^2}{s}. \tag{A.2}$$

An alternative choice for the two independent variables is the momentum fractions of the scattering partons x_1 and x_2 in the infinite momentum frame. They are related to x_{F} and τ by:

$$x_{\mathrm{F}} = x_1 - x_2, \tag{A.3}$$

$$\tau = x_1\, x_2. \tag{A.4}$$

Several other combinations of variables can be found in the literature. A separation of the kinematics parallel and perpendicular to the beam axis is achieved by choosing x_{F} together with the transverse momentum $p_{\mathrm{T}} \equiv \sqrt{{p_x}^2 + {p_y}^2}$.

Another measure for the kinematics parallel to the beam axis is the rapidity y or the pseudo-rapidity η. y is defined as

$$y = \frac{1}{2} \ln\left(\frac{E + p_z}{E - p_z}\right) \overset{\text{CM frame}}{\approx} \frac{1}{2} \ln\left(\frac{x_1}{x_2}\right), \tag{A.5}$$

where E is the energy of the particle. If p is large compared to the mass of the particle, y can be approximated by the pseudo-rapidity η which is completely determined by the scattering angle θ:

$$\eta = -\ln \tan\left(\frac{\theta}{2}\right). \tag{A.6}$$

A.2 Angular distributions

In the Drell-Yan process, the kinematics of the virtual photon are of interest, which cannot be measured directly. However, the kinematics are completely determined by the four-momenta of the outgoing leptons, leading to six free parameters if the masses of the leptons are known. Therefore, also the angular distributions of the outgoing leptons are needed to determine the kinematics of the virtual photon.

The angular variables in the Drell-Yan process can be expressed in different reference frames. All angular distributions are expressed in the rest frame of the virtual photon. However, the choice of the three-dimensional coordinate system in this frame is ambiguous. Three common choices can be found in the literature.

The ideal frame would be based on the parton-parton annihilation axis as the z axis. This axis is not necessarily parallel to the proton and the nucleon momentum directions, because the partons bear an intrinsic transverse momentum. Therefore, this axis is unknown. The confinement of the partons in the proton and the nucleons accounts for an intrinsic transverse momentum of $\langle p_{\mathrm{T}} \rangle \approx 200\,\mathrm{MeV}/c$ via Heisenberg's uncertainty relation. As a consequence, the proton and the nucleon axes are tilted in the virtual photon rest frame. The angle 2β between the proton and the nucleon momentum (cf. Fig. A.1) is given by

$$\tan\beta = \frac{p_{\mathrm{T}}}{M}. \tag{A.7}$$

Here p_{T} is the transverse momentum of the virtual photon in the proton-nucleon center-of-mass frame, and M is the invariant mass of the lepton pair, i.e. the virtuality of the photon. A proof of this relation can be found in [Fal86].

The three common choices for the z axis in the rest frame of the virtual photon are shown in Fig. A.1:

- In the Gottfried-Jackson frame [Got64], the z axis is parallel to the momentum three-vector of the incoming proton.
- In the u-channel frame, the negative of the three-momentum of the nucleon defines the z axis.
- The Collins-Soper frame [Col77] represents a "compromise" between the Gottfried-Jackson and the u-channel frames: The z axis is the bisector of the proton momentum vector and the negative of the nucleon's momentum vector.

If both angles θ and ϕ are measured in an experiment, the choice of the reference frame is only a matter of convenience. Angular distributions can be translated from one reference frame to another. If only the polar angle θ is measured, the choice of the frame becomes important, because strictly speaking the angular distributions are only correct in the unknown frame with the parton-parton annihilation axis as the z axis [Fal86]. Therefore kinematic and dynamical relations, e.g. the Lam-Tung relation (3.12), can only be checked by measuring both angles.

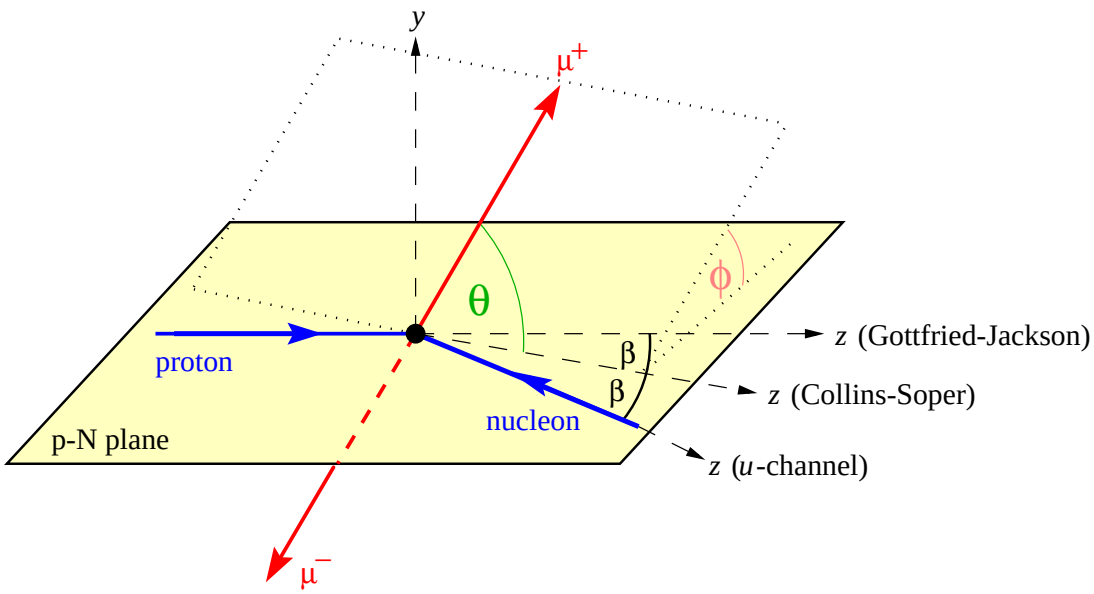

Figure A.1: *The three common frames for angular distributions (all defined in the rest frame of the virtual photon): The Gottfried-Jackson frame [Got64] has the z axis parallel to the momentum three-vector of the incoming proton. The z axis of the u-channel frame is antiparallel to the momentum three-vector of the nucleon, and the z axis of the Collins-Soper frame [Col77] is the bisector of the momentum three-vector of the proton and the negative of the momentum three-vector of the nucleon. If the proton and nucleon momenta are not antiparallel, the x and y axes are well-defined: y is perpendicular to the proton-nucleon plane, and x is chosen to define a right-handed orthogonal coordinate system. In this coordinate system the angles θ and ϕ are the conventional polar and azimuth angles (after [Con89]).*

Appendix B

Track parameters

B.1 The basic track parameters

The tracking properties of elementary particles of a given mass are completely determined by their positions in space $\mathbf{x} = (x, y, z)$ and their momenta $\mathbf{p} = (p_x, p_y, p_z)$.

The tracking algorithms in HERA–B do not use the positions and the momenta of the tracks but rather a different set of parameters which is more convenient for the tracking algorithms. The filter equations of the Kalman filter, which is used in most of the tracking packages in HERA–B, are closer to being linear in $1/|\mathbf{p}|$ than in $|\mathbf{p}|$ [Loh95]. Therefore, a typical choice for the vector ξ of tracking parameters is

$$\xi = (b_x, b_y, t_x, t_y, Q/p)\,, \tag{B.1}$$

where b_x and b_y are the points of intersection of the track and the xy plane at $z = 0$, Q the charge of the track, and $p = |\mathbf{p}|$ is the modulus of the momentum vector. In HERA–B, Q/p is often denoted as p_{f}. t_x and t_y are the slopes of the tracks in the x and y directions:

$$t_x = \tan\theta_x = \frac{p_x}{p_z}, \tag{B.2}$$

$$t_y = \tan\theta_y = \frac{p_y}{p_z}. \tag{B.3}$$

The inversion of (B.2) and (B.3) yields:

$$p_z = \left(\sqrt{1 + {t_x}^2 + {t_y}^2}\,\left|\frac{Q}{p}\right|\right)^{-1}, \tag{B.4}$$

$$p_x = t_x\, p_z, \tag{B.5}$$

$$p_y = t_y\, p_z. \tag{B.6}$$

The extrapolated position of a track to a given z position z_0 is given by the equation of a straight line:

$$x(z_0) = b_x + t_x\, z_0, \tag{B.7}$$

$$y(z_0) = b_y + t_y\, z_0. \tag{B.8}$$

B.2 The position of closest approach

A first test of the compatibility of two tracks with a common vertex and an estimate of the vertex position can be obtained from the position and the closest distance of

approach of these tracks. In front of the HERA–B magnet, tracks can be regarded as straight lines. Hence, they can be characterized by their intersection points with the xy plane at $z = 0$, $\mathbf{x}_1 = (x_1, y_1, 0)$ for track 1 and $\mathbf{x}_2 = (x_2, y_2, 0)$ for track 2, and the direction vectors of the tracks $\mathbf{t}_i = (t_{x,i}, t_{y,i}, 1)$, $i = 1, 2$. The closest distance of approach d_{CDA}, and the position of closest approach $\mathbf{x}_{\mathrm{CDA}}$ can be obtained from the solution vector $(s_{\mathrm{CDA}}, t_{\mathrm{CDA}}, d_{\mathrm{CDA}})$ of the equation

$$(\mathbf{x}_1 + s\,\mathbf{t}_1) - (\mathbf{x}_2 + t\,\mathbf{t}_2) = d\,\frac{\mathbf{t}_1 \times \mathbf{t}_2}{|\mathbf{t}_1 \times \mathbf{t}_2|}, \tag{B.9}$$

where the position on track 1 is parametrized by s and the position on track 2 by t. Hence, the position of closest approach is located on a line which is perpendicular to the plane defined by the two tracks. The position of closest approach is defined as the middle of this line:

$$\mathbf{x}_{\mathrm{CDA}} = (\mathbf{x}_1 + s_{\mathrm{CDA}}\mathbf{t}_1) - \frac{d_{\mathrm{CDA}}}{2}\,\frac{\mathbf{t}_1 \times \mathbf{t}_2}{|\mathbf{t}_1 \times \mathbf{t}_2|}. \tag{B.10}$$

B.3 The χ^2 of tracks and vertices

The χ^2 of a track or vertex is a measure of the fit quality. The exact definition depends on the tracking or vertexing algorithm under consideration. For a series of n measurements $\mathbf{m} = (m_1, m_2, \ldots, m_n)$ for the true value m with the vector of measurement errors $\sigma = (\sigma_1, \sigma_2, \ldots, \sigma_n)$ the χ^2 function is given by

$$\chi^2 = \sum_{i=1}^{n} \frac{(m - m_i)^2}{{\sigma_i}^2}, \tag{B.11}$$

i.e. the square sum of the deviations from the true value m, normalized by the measurement error. Since in general the true value m is not known, a minimization of χ^2 from (B.11) with respect to m leads to an estimate $\overline{m}$ for m. The quality of this fit is given by Equation (B.11), where m is substituted by $\overline{m}$.

In the Kalman filter tracking, a vector ξ of the tracking or vertexing parameters is determined in each measurement. A straightforward generalization of Equation (B.11) for this case of a measurement of a vector $(\xi_1, \xi_2, \ldots, \xi_n)$ of values yields:

$$\chi^2 = \sum_{i=1}^{n} (\overline{\xi} - \xi_i)^{\mathrm{T}}\, {\mathbf{C}_i}^{-1}\, (\overline{\xi} - \xi_i), \tag{B.12}$$

where $\mathbf{C}_i$ is the covariance matrix of the measurement ξ_i, and $\overline{\xi}_i$ is an estimate for the true vector ξ.

The probability that some observed χ^2 value exceeds the measured χ^2 value by chance, even if the model for the fit is correct, is given by the χ^2 probability $\mathrm{prob}(\chi^2, N_{\mathrm{dof}})$ for N_{dof} degrees of freedom in the fit:

$$\mathrm{prob}(\chi^2, N_{\mathrm{dof}}) = 1 - P\left(\frac{N_{\mathrm{dof}}}{2}, \frac{\chi^2}{2}\right), \tag{B.13}$$

where

$$P(n,x) = \frac{1}{\Gamma(n)} \int_0^x t^{n-1} e^{-\frac{t}{2}} \, \mathrm{d}t \tag{B.14}$$

is the incomplete gamma function.

In a vertex fit with N_{tracks} tracks with $d \equiv \dim(\xi_i)$ parameters, the fit procedure employs the vertex position (three parameters), and the track parameters constrained to the vertex position $\tilde{\xi}$ ($d-2$ parameters) are as free parameters. The number of degrees of freedom is then given by [Loh95]

$$N_{\text{dof}} = d\, N_{\text{tracks}} - ((d-2) \times N_{\text{tracks}} + 3) = 2 \times N_{\text{tracks}} - 3. \tag{B.15}$$

With N_{constr} additional constraints, the number of degrees of freedom increases to

$$N_{\text{dof,constr}} = 2 \times N_{\text{tracks}} + N_{\text{constr}} - 3. \tag{B.16}$$

Appendix C

Monte Carlo simulations in HERA – B

To extract a meaningful physics result from a particle physics experiment, the behavior of the underlying complex physics processes has to be understood. Furthermore, the signatures of these processes in a likewise complex collection of materials and electronic devices in the detector have to be interpreted correctly. Therefore, the physics processes and the detector undergo detailed Monte Carlo simulations. The goal of a Monte Carlo simulation in particle physics experiments is to provide simulated detector data for arbitrary physics processes. In order to be processed by the same reconstruction chain, the simulated data is delivered in the same format as the signals from the detector.

The basic idea of the Monte Carlo method, the numerical calculation of probabilities based on random numbers, is well suited for the production of elementary particles and their interactions in matter, since they follow the laws of quantum mechanics which are probabilistic themselves. The foundations of the Monte Carlo method can be found in many text books, e.g. in [Cow98], and will not be further described here. In the following, the implementation of Monte Carlo simulations within the HERA – B experiment will be briefly sketched. The complete chain of the Monte Carlo simulation and the corresponding chain for the preparation of real data is depicted in Fig. C.1.

C.1 Event generators

The Monte Carlo simulation of physics processes within the HERA – B detector starts with an event generator, i.e. a program to simulate the kinematics and dynamics of a physics process. The event generators used in HERA – B are based on the PYTHIA/JETSET package [Sjö94]. PYTHIA is the standard generator for hard scattering processes in many particle physics experiments, while JETSET is used internally by PYTHIA to simulate the fragmentation of hadronic jets. Since PYTHIA is restricted to interactions between nucleons and their constituents, the FRITIOF package [Pi92] is needed to simulate nuclear effects in the target nuclei.

In HERA – B the interplay of PYTHIA/JETSET and FRITIOF is implemented as follows: The hard subprocess, e.g. the production of heavy quarks, is simulated by PYTHIA. The remaining energy is passed to FRITIOF to generate the underlying event. This cannot be done in a fully consistent manner, so that the inclusive transverse momentum spectra have to be corrected by event weights. Most interactions in the HERA – B detector are inelastic proton-nucleus interactions, i.e. a mixture of soft and hard interactions. The

FRITIOF event generator is able to treat soft and hard interactions of protons with the target nuclei simultaneously. Therefore, for the simulation of inelastic interactions only the FRITIOF event generator is used. Further details of the event generators used and adapted for HERA–B can be found in [Iva99].

Before the events are passed to the detector simulation they can be mixed with events from other physics processes. Hence the superposition of a signal event with a number of inelastic interactions can be simulated. The number of mixed events N_{mix} can be set to a fixed value or determined by a random number generated according to a Poisson distribution with the mean value λ:

$$P(N_{\mathrm{mix}};\lambda) = \frac{\lambda^{N_{\mathrm{mix}}}}{N_{\mathrm{mix}}!}\, e^{-\lambda}. \tag{C.1}$$

Provided 180 of the 220 HERA proton bunches are injected and bunches are crossing the target every 96 ns, the mean number of interactions λ as a function of the interaction rate ν is given by

$$\lambda(\nu) = \nu \cdot \frac{220}{180} \cdot 96\,\mathrm{ns} \approx 0.117\,\frac{\nu}{\mathrm{MHz}}. \tag{C.2}$$

C.2 Detector simulation

In a second step the interactions of the particles which were produced with the event generator are simulated in the detector. The simulation of the HERA–B detector is carried out by HBGEAN [Now94], a detector simulation package based on the standard detector description tool GEANT [GEA94]. A proper simulation of the detector response relies on a precise description of the position and amount of material included in the individual subdetectors, often called the "detector geometry". With the help of the GEANT package and a complete description of the geometry of the HERA–B detector, the interactions of the particles with the various materials in the detector can be simulated. The individual elements of the detector are represented by simple geometrical objects, e.g. cubes. Whenever the particles cross a sensitive GEANT volume in one of the subdetectors, the entry point and the exit point are stored in an ARTE table as so-called "Monte Carlo impact points" (MIMPs). The Monte Carlo tracks and vertices are stored in the MTRA (Monte Carlo Tracks) and MVER (Monte Carlo Vertices) tables. These tables are similar to the RTRA and RVER tables for reconstructed tracks and vertices. They contain the "Monte Carlo truth" about the tracks and vertices, i.e. the parameters as they were generated by the event generator and the detector simulation.

To provide data for the reconstruction chain which is equivalent to real data, the MIMPs, being space points along the trajectory of the particles through the detector, have to be translated into discrete hits in the detector. This step of the detector simulation is called digitization and is the counterpart of the read-out and the hit preparation in the real detector. The simulation of the detector resolution, the hit efficiencies of the individual chambers and hot and dead detector channels are also included in the digitization step.

C.3 Trigger simulation

The purpose of a trigger is to select events of interest while effectively rejecting uninteresting background events. Therefore, data that are recorded with a trigger are usually

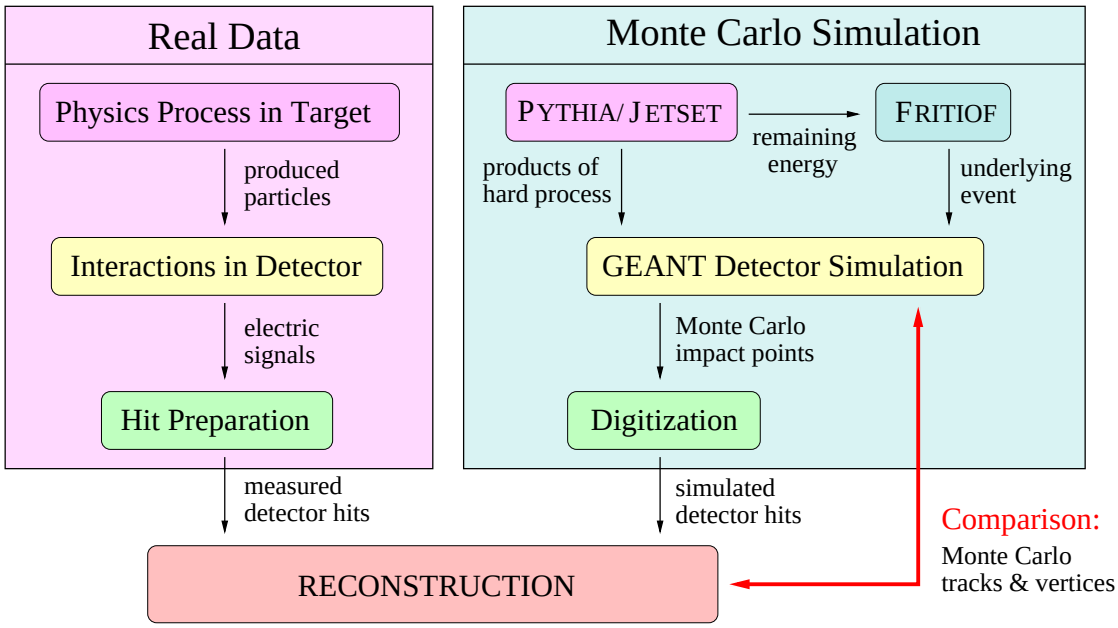

Figure C.1: *Graphical illustration of the data path from the physics process to the reconstruction in real data (left) and in Monte Carlo simulations (right). The event generation is the counterpart of the interactions of protons with the HERA–B target. Interactions in the detector are modeled by the GEANT detector simulation, and the digitization simulates the effects of the detector read-out and the hit preparation.*

biased towards a certain class of events, and not every event that is generated in a Monte Carlo simulation is able to pass the trigger. In order to interpret the triggered data correctly, the bias that is introduced by the trigger has to be understood. The understanding can be achieved either analytically or by means of a simulation of the trigger logic. Data-taking with a real detector often includes a certain fraction of dead-time, i.e. part of the trigger or data acquisition system (DAQ) is blocked during the processing of the detector data. To model these effects the timing of a trigger has to be simulated.

A trigger simulation can be used together with the Monte Carlo simulation of the detector to determine the trigger efficiency. The efficiency of the trigger system is an important number for most physics analyses. The "inherent" efficiency of a trigger is given by the trigger algorithm and can be determined by running a trigger simulation on Monte Carlo simulated events. The efficiency of a real working trigger compared to an ideal trigger can be obtained by the comparison of the behavior of the trigger and the trigger simulation on the same sample of real data. To be independent of the trigger bias, data for such studies have to be triggered with an independent trigger.

The muon pretrigger simulation

The behavior of the muon pretrigger can be simulated by the muon pretrigger simulation tool MUPRESIM [Ada01b]. In MUPRESIM, the individual components of the muon pretrigger system are modeled in C++ classes. The simulation can be configured via the HERA–B database in the same way as the pretrigger hardware, using the same lookup-tables to generate the pretrigger messages and the same masks for hot channels in the

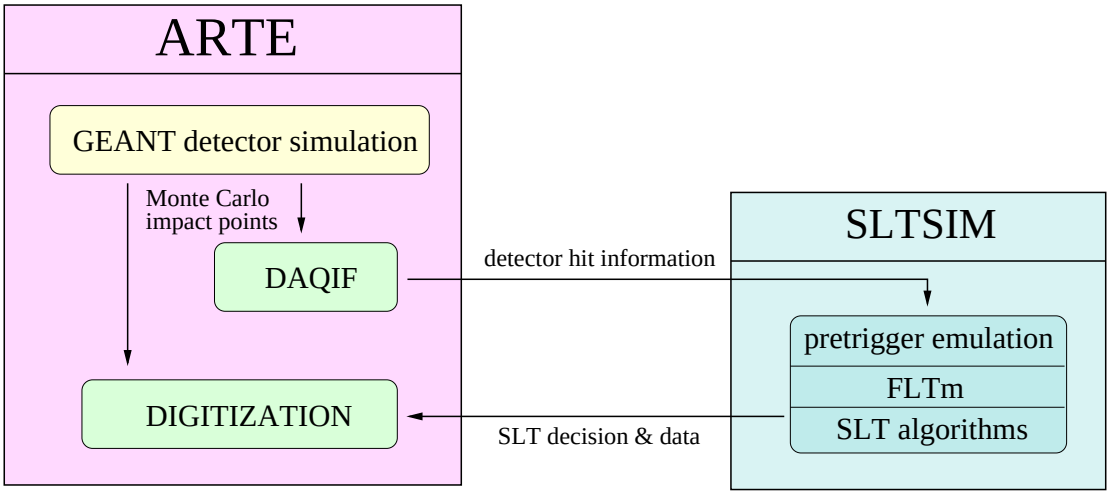

Figure C.2: *Data flow in the simulation of the SLT: The DAQIF package translates the Monte Carlo impact points into raw detector hits. The hit information is piped to the SLT simulation program, which consists of the pretrigger emulation and the FLTm code, in addition to the usual SLT algorithms. The trigger decision and data are returned to the reconstruction chain.*

muon detector and the trigger. The main input to the simulation is hits in the muon pad and pixel chambers from the hit preparation. MUPRESIM can be also employed in the framework of Monte Carlo simulations.

The SLT simulation

In HERA – B, the SLT is simulated by providing an interface between the detector simulation and the SLT algorithm running as a separate program. The data flow in the SLT simulation is shown in Fig. C.2. The DAQIF package [Soe00] provides a translation of the MIMPs, as delivered by the GEANT detector simulation, into the raw detector hit format, which the detector frond end also yields. Data of this format, the so-called DAQ format, can be processed with the same SLT programs that are used in the data-taking. The special SLT programs that are used in the SLT emulation of the di-muon trigger consist of the emulation of the muon pretrigger, cf. Section 4.1.2, the FLT emulation algorithm FLTm, as described in Section 4.2, and the usual SLT packages Slicer/Refit and L2Sili.

The raw detector information of DAQIF is piped to the SLT program. After the trigger calculations the result of the trigger algorithms is passed back to the digitization step, followed by the reconstruction chain.

Appendix D

List of di-muon triggered runs in the 2000 data-taking

This appendix contains a list of the di-muon triggered runs in the 2000 data-taking period, taken at an interaction rate of 4–5 MHz partly with the target wire Inner II only and partly with Inner II and Below I. The data have been reprocessed in January and February 2001 with ARTE-03-08-r5. For each run the J/ψ yield has been calculated with a fit to a histogram of the invariant mass spectrum of opposite-sign muon pairs after cuts. The fit has been performed with the ROOT physics analysis package [Bru97]. The fit functions and the cuts are described in Section 5.1.

Table D.1: *List of reprocessed di-muon triggered runs in the 2000 data-taking period. The fit results are only stated for runs where the number of triggered events was sufficient to let the fit converge, a rough estimate for this number being more than 1,000 di-muon events. The errors are statistical errors of the fit only.*

Run	DSTs	Events	Di-muon	$N_{\mathrm{J}/\psi}$	M_0 [MeV/c^2]	σ [MeV/c^2]	N_{bkg}
16012	9	25,100	433	–	–	–	–
16013	5	12,500	211	–	–	–	–
16014	4	9,900	188	–	–	–	–
16062	1	4,000	431	–	–	–	–
16067	1	2,500	98	–	–	–	–
16068	1	2,000	84	–	–	–	–
16069	1	1,500	160	–	–	–	–
16073	3	10,700	875	–	–	–	–
16078	11	36,700	2,570	25 ± 6	3086 ± 10	36 ± 8	19 ± 26
16258	2	7,600	127	–	–	–	–
16262	2	4,000	218	–	–	–	–
16265	13	13,200	1,140	–	–	–	–
16279	2	7,900	311	–	–	–	–
16280	6	26,400	1,107	–	–	–	–
16282	1	700	6	–	–	–	–
16284	3	10,900	454	–	–	–	–

continued on next page

continued from previous page

Run	DSTs	Events	Di-muon	$N_{J/\psi}$	M_0 [MeV/c^2]	σ [MeV/c^2]	N_{bkg}
16291	4	11,500	866	–	–	–	–
16327	1	3,500	92	–	–	–	–
16330	6	27,900	1,772	19 ± 8	3078 ± 19	47 ± 17	14 ± 42
16331	2	5,700	228	–	–	–	–
16332	2	6,400	351	–	–	–	–
16333	3	10,500	682	8 ± 6	3119 ± 25	36 ± 33	14 ± 49
16346	1	200	21	–	–	–	–
16347	55	151,900	5,983	67 ± 9	3083 ± 10	70 ± 12	8 ± 14
16351	2	3,300	156	–	–	–	–
16352	3	6,300	173	–	–	–	–
16358	1	3,100	–	–	–	–	–
16367	2	4,200	140	–	–	–	–
16368	1	700	22	–	–	–	–
16369	1	100	3	–	–	–	–
16370	16	45,100	1,331	15 ± 6	3078 ± 23	51 ± 15	21 ± 21
16371	30	85,500	3,648	82 ± 11	3081 ± 8	54 ± 7	19 ± 21
16374	1	200	12	–	–	–	–
16382	8	19,200	850	–	–	–	–
16383	2	5,800	155	–	–	–	–
16384	21	45,100	1,371	–	–	–	–
16385	5	6,400	318	–	–	–	–
16386	5	4,700	328	–	–	–	–
16387	1	400	24	–	–	–	–
16388	2	3,500	187	–	–	–	–
16389	1	500	29	–	–	–	–
16390	1	500	24	–	–	–	–
16391	3	5,300	249	–	–	–	–
16392	14	28,000	1,676	–	–	–	–
16395	3	4,400	257	–	–	–	–
16396	2	2,000	129	–	–	–	–
16410	9	5,600	4	–	–	–	–
16411	23	11,200	301	–	–	–	–
16412	14	6,600	148	–	–	–	–
16413	25	58,800	2,148	17 ± 8	3068 ± 28	58 ± 33	16 ± 36
16414	6	13,700	2	–	–	–	–
16470	6	18,000	2	–	–	–	–
16471	13	33,300	1,463	17 ± 5	3061 ± 9	28 ± 8	16 ± 25
16472	12	30,300	1,445	12 ± 7	3099 ± 36	50 ± 29	15 ± 29
16475	7	14,100	1,075	13 ± 11	3068 ± 28	50 ± 49	12 ± 53
16480	1	2,600	92	–	–	–	–
16482	5	13,600	470	–	–	–	–
16493	4	8,100	3	–	–	–	–
16494	1	500	27	–	–	–	–

continued on next page

continued from previous page

Run	DSTs	Events	Di-muon	$N_{J/\psi}$	M_0 [MeV/c^2]	σ [MeV/c^2]	$N_{\rm bkg}$
16495	8	18,300	947	–	–	–	–
16497	1	100	13	–	–	–	–
16498	1	600	25	–	–	–	–
16500	2	3,500	141	–	–	–	–
16501	3	6,500	365	–	–	–	–
16502	4	8,600	401	–	–	–	–
16503	2	2,500	160	–	–	–	–
16504	1	1,800	123	–	–	–	–
16505	6	10,200	709	–	–	–	–
16506	8	22,800	752	–	–	–	–
16510	9	22,800	1,005	–	–	–	–
16511	1	700	27	–	–	–	–
16512	2	3,100	129	–	–	–	–
16513	1	600	35	–	–	–	–
16516	3	7,100	286	–	–	–	–
16521	1	200	11	–	–	–	–
16522	9	4,000	124	–	–	–	–
16523	7	5,000	374	–	–	–	–
16524	3	3,500	198	–	–	–	–
16527	17	15,900	727	–	–	–	–
16529	10	25,000	1,327	19 ± 17	3136 ± 36	32 ± 22	17 ± 32
16538	7	24,000	2	–	–	–	–
16540	2	4,400	217	–	–	–	–
16541	1	400	6	–	–	–	–
16542	10	27,700	1,222	–	–	–	–
16545	1	1,800	26	–	–	–	–
16546	1	800	22	–	–	–	–
16568	38	103,900	5,198	87 ± 11	3087 ± 6	46 ± 5	26 ± 25
16571	4	9,900	534	–	–	–	–
16572	26	63,800	3,209	49 ± 8	3081 ± 6	36 ± 5	15 ± 20
16573	9	21,000	1,526	24 ± 6	3072 ± 12	41 ± 8	15 ± 27
16575	7	18,200	1,273	18 ± 10	3117 ± 45	88 ± 61	8 ± 21
16600	2	5,000	217	–	–	–	–
16601	1	600	39	–	–	–	–
16602	9	21,600	1,127	13 ± 7	3061 ± 28	51 ± 24	12 ± 26
16603	1	2,000	90	–	–	–	–
16605	19	53,200	2,635	47 ± 8	3068 ± 7	37 ± 6	17 ± 23
16607	1	2,700	123	–	–	–	–
16621	1	1,700	82	–	–	–	–
16622	6	16,000	756	–	–	–	–
16629	6	16,500	819	–	–	–	–
16630	9	26,700	1,474	18 ± 5	3075 ± 7	23 ± 6	18 ± 23
16631	4	10,900	560	–	–	–	–

continued on next page

continued from previous page

Run	DSTs	Events	Di-muon	$N_{J/\psi}$	M_0 [MeV/c^2]	σ [MeV/c^2]	N_{bkg}
16632	4	10,800	455	–	–	–	–
16640	1	2,300	130	–	–	–	–
16645	3	5,100	303	–	–	–	–
16648	5	12,700	631	–	–	–	–
16649	5	13,500	647	–	–	–	–
16651	3	6,700	367	–	–	–	–
16652	1	300	16	–	–	–	–
16653	20	47,800	1,978	34 ± 9	3074 ± 20	76 ± 16	11 ± 21
16655	6	14,600	816	–	–	–	–
16658	4	10,300	502	–	–	–	–
16659	5	11,300	606	15 ± 8	3044 ± 27	49 ± 25	10 ± 31
16660	1	1,900	117	–	–	–	–
16662	5	11,300	641	–	–	–	–
16663	8	20,700	1,140	–	–	–	–
16665	55	140,600	7,899	150 ± 14	3079 ± 5	53 ± 5	31 ± 24
16674	3	6,500	474	–	–	–	–
16675	10	24,900	1,790	34 ± 9	3093 ± 17	66 ± 21	9 ± 26
16677	5	11,200	725	–	–	–	–
16679	31	75,100	5,612	87 ± 11	3073 ± 6	51 ± 7	21 ± 21
16681	29	70,800	4,828	69 ± 9	3089 ± 6	42 ± 6	15 ± 19
16684	9	22,500	1,579	–	–	–	–
16686	15	37,800	1,756	14 ± 5	3102 ± 16	40 ± 19	11 ± 26
16688	6	14,700	1,066	–	–	–	–
16690	19	45,500	3,058	30 ± 8	3099 ± 13	46 ± 14	14 ± 26
16700	9	21,700	987	–	–	–	–
16702	5	9,800	583	–	–	–	–
16704	8	17,400	1,122	–	–	–	–
16707	10	24,900	1,457	15 ± 5	3072 ± 7	20 ± 7	21 ± 27
16708	30	75,000	4,614	76 ± 10	3095 ± 7	50 ± 7	18 ± 21
16710	11	26,800	1,426	24 ± 7	3074 ± 13	42 ± 9	16 ± 22
16713	16	33,700	1,797	17 ± 6	3080 ± 12	33 ± 10	15 ± 26
16715	13	28,800	1,674	–	–	–	–
16716	9	22,200	1,235	–	–	–	–
16717	36	90,900	4,281	42 ± 9	3066 ± 12	50 ± 9	19 ± 22
16739	10	25,900	1,373	–	–	–	–
16740	8	22,600	1,068	13 ± 6	3071 ± 18	41 ± 19	15 ± 34
16748	3	7,600	351	–	–	–	–
16750	18	49,100	2,498	29 ± 6	3073 ± 7	29 ± 7	20 ± 22
16751	8	19,100	1,235	–	–	–	–
16756	30	69,300	3,964	49 ± 8	3088 ± 7	41 ± 8	19 ± 25
16758	14	33,200	1,793	16 ± 5	3093 ± 13	41 ± 13	9 ± 24
16760	22	57,300	3,147	30 ± 7	3075 ± 10	39 ± 10	27 ± 25
16761	1	3,500	104	–	–	–	–

continued on next page

continued from previous page

Run	DSTs	Events	Di-muon	$N_{J/\psi}$	M_0 [MeV/c^2]	σ [MeV/c^2]	$N_{\rm bkg}$
16765	6	18,500	505	–	–	–	–
16766	3	8,000	423	–	–	–	–
16767	5	11,700	608	–	–	–	–
16768	2	4,200	205	–	–	–	–
16783	6	16,100	779	–	–	–	–
16784	90	255,700	12,521	188 ± 16	3078 ± 4	48 ± 4	63 ± 31
16785	2	5,400	257	–	–	–	–
16793	11	25,500	1,142	–	–	–	–
16798	20	57,800	2,334	35 ± 7	3078 ± 8	35 ± 11	18 ± 22
16838	3	7,300	494	–	–	–	–
16854	1	3,100	48	–	–	–	–
16855	2	3,800	68	–	–	–	–
16857	1	300	18	–	–	–	–
16858	1	300	14	–	–	–	–
16859	1	300	17	–	–	–	–
16863	5	11,500	268	–	–	–	–
16865	9	21,800	530	5 ± 5	3088 ± 47	34 ± 40	16 ± 36
16866	6	14,700	172	–	–	–	–
16868	3	7,200	204	–	–	–	–
16881	10	23,600	952	–	–	–	–
16882	1	200	10	–	–	–	–
16883	26	68,100	2,500	23 ± 7	3065 ± 16	48 ± 13	16 ± 24
16886	5	10,900	422	–	–	–	–
16887	14	34,900	1,388	–	–	–	–
16888	1	3,000	99	–	–	–	–
16889	17	49,200	1,578	13 ± 4	3067 ± 5	14 ± 4	18 ± 31
16894	12	35,200	1,166	–	–	–	–
16897	29	73,000	3,985	43 ± 8	3083 ± 11	54 ± 10	14 ± 22
16899	5	11,800	665	10 ± 7	3066 ± 39	41 ± 35	13 ± 42
16911	3	6,100	142	–	–	–	–
16921	15	41,800	1,611	19 ± 6	3094 ± 13	40 ± 13	17 ± 26
16924	1	700	24	–	–	–	–
16927	7	19,300	715	–	–	–	–
17006	8	18,600	989	–	–	–	–
17008	9	26,000	281	–	–	–	–
17009	50	133,100	5,980	40 ± 7	3109 ± 10	54 ± 9	7 ± 13
17010	8	19,600	859	–	–	–	–
17013	4	9,000	426	–	–	–	–
17014	5	13,600	479	–	–	–	–
17015	5	12,700	530	–	–	–	–
17017	5	13,700	544	–	–	–	–
17018	3	6,000	299	–	–	–	–
17019	1	2,200	118	–	–	–	–

continued on next page

continued from previous page

Run	DSTs	Events	Di-muon	$N_{J/\psi}$	M_0 [MeV/c^2]	σ [MeV/c^2]	N_{bkg}
17020	3	6,600	302	–	–	–	–
17021	28	75,700	3,338	–	–	–	–
17048	5	14,000	653	–	–	–	–
17054	17	45,400	1,980	–	–	–	–
17057	2	4,900	115	–	–	–	–
17075	12	31,000	1,077	–	–	–	–
17077	9	19,600	1,224	–	–	–	–
17081	4	12,000	569	–	–	–	–
17152	4	8,400	417	–	–	–	–
17159	13	40,700	6	–	–	–	–
17168	1	500	11	–	–	–	–
17169	6	7,100	202	–	–	–	–
17170	4	5,000	127	–	–	–	–

runs:	201
events:	4,093,800
selected:	194,000
J/ψ mesons:	2,688

List of Acronyms

Acronym	**Explanation**
4LT	Fourth Level Trigger
ARTE	Analysis and Reconstruction Tool
BX	Bunch Crossing (Number)
CARE	Calorimeter Reconstruction
CATS	Cellular Automaton for Tracking in Silicon (VDS reconstruction package)
CDA	Closest Distance of Approach
CERN	Conseil Européen pour la Recherche Nucléaire (European Laboratory for Particle Physics)
CKM	Cabibbo-Kobayashi-Maskawa (matrix)
DAQ	Data Acquisition
DAQIF	Data Acquisition Interface
DESY	Deutsches Elektronen-Synchrotron
DIS	Deep-Inelastic Scattering
DSP	Digital Signal Processor
ECAL	Electromagnetic Calorimeter
FCNC	Flavor Changing Neutral Current
FCS	Fast Control System
FLT	First Level Trigger
FLTm	First Level Trigger emulation in the muon system
FNAL	Fermi National Accelerator Laboratory
GEM	Gas Electron Multiplier
GROVER	Generic Reconstruction of Vertices (vertexing package)
HERA	Hadron-Elektron-Ring-Anlage
HPT	High-p_{T}
ITR	Inner Tracker
LHC	Large Hadron Collider
MC	Monte Carlo
MCn	Outer Tracker Magnet Chamber n
MIMP	Monte Carlo Impact Points (ARTE table)

continued on next page

continued from last page

Acronym	**Explanation**
MSGC	Micro-strip Gaseous Chamber
MTRA	Monte Carlo Tracks (ARTE table)
MUn	Muon Chamber Superlayer n
MUPRESIM	Muon Pretrigger Simulation Package
MVER	Monte Carlo Vertices (ARTE table)
NLO	Next-to-leading Order
OTR	Outer Tracker
PCn	Outer Tracker Pattern Recognition Chamber n
QCD	Quantum Chromodynamics
QED	Quantum Electrodynamics
QFD	Quantum Flavor Dynamics
RANGER	main tracker reconstruction package
RICH	Ring-imaging Čerenkov Hodoscope
RISE	Ring Search (RICH reconstruction package)
RoI	Region of Interest
ROVER	Reconstruction of Vertices (vertexing package)
RSLA	Reconstructed SLT Tracks (ARTE table)
RSLI	Reconstructed SLT Triggers (ARTE table)
RTRA	Reconstructed Tracks (ARTE table)
RVER	Reconstructed Vertices (ARTE table)
SHARC	Super Harvard Architecture (digital signal processor)
SLB	Second Level Buffer
SLT	Second Level Trigger
TCn	Outer Tracker Trigger Chamber n
TDU	Trigger Decision Unit
TFU	Track Finding Unit
TLT	Third Level Trigger
TPU	Track Parameter Unit
TRD	Transition Radiation Detector
VDS	Vertex Detector System

Bibliography

[Abr98] M.C. Abreu et al. (NA38 Collaboration), *A four-dimensional deconvolution method to correct NA38 experimental data*, Nucl. Instrum. Meth. **A405** (1998) 139

[Abr99] M.C. Abreu et al. (NA50 Collaboration), *Latest results from NA50 on* J/ψ *suppression in Pb-Pb collisions*, Nucl. Phys. **A661** (1999) 93

[Abr01] M.C. Abreu et al. (NA50 Collaboration), *Transverse momentum distributions of* J/ψ, ψ', *Drell-Yan and continuum dimuons produced in Pb-Pb interactions at the SPS*, Phys. Lett. **B499** (2001) 85

[Abt97] I. Abt et al. (H1 Collaboration), *The H1 detector at HERA*, Nucl. Instrum. Meth. **A386** (1997) 310

[Ada99] M. Adams, Universität Dortmund, private communication (October 1999)

[Ada00a] M. Adams, Universität Dortmund, private communication (April 2000)

[Ada00b] M. Adams, Universität Dortmund, private communication (August 2000)

[Ada01a] M. Adams, *Studies on hit multiplicities*, talk given at the HERA – B collaboration meeting, February 19-23, 2001, DESY, Hamburg (2001)

[Ada01b] M. Adams, Dissertation, Universität Dortmund (in preparation)

[Alb87] H. Albrecht et al. (ARGUS Collaboration), *Observation of* $B^0 - \overline{B^0}$ *mixing*, Phys. Lett. **192** (1987) 245

[Alb92] H. Albrecht et al., *HERA – B – An experiment to study CP violation in the B system using an internal target at the HERA proton ring*, Letter of Intent, DESY-PRC 92/04 (October 1992)

[Alb95a] H. Albrecht et al., *HERA – B – An experiment to study CP violation in the B system using an internal target at the HERA proton ring*, Design Report, DESY-PRC 95/01 (January 1995)

[Alb95b] H. Albrecht, *ARTE Analysis and Reconstruction Tool*, HERA – B Note 95-008 (1995)

for a more recent online reference see (status: Dec 28, 2000):
`http://www-hera-b.desy.de/subgroup/software/`

[Ald90] D.M. Alde et al., *Nuclear dependence of dimuon production at 800-GeV FNAL-772 experiment*, Phys. Rev. Lett. **64** (1990) 2479

[Ale97] T. Alexpoulos et al. (E771 Collaboration), *A measurement of the* $b\overline{b}$ *cross section in 800 GeV/c proton-silicon interactions*, Phys. Rev. **D55** (1997) 3927

[Alt78] G. Altarelli, R.K. Ellis, and G. Martinelli, *Leptoproduction and Drell-Yan processes beyond the leading approximation in chromodynamics*, Nucl. Phys. **B143** (1978) 521

G. Altarelli, R.K. Ellis, and G. Martinelli, *Large perturbative corrections to the Drell-Yan process in QCD*, Nucl. Phys. **B157** (1979) 461

[And84] L. Anderson et al. (NA10 Collaboration), *A high-resolution spectrometer for the study of high-mass muon pairs produced by intense hadron beams*, Nucl. Instrum. Meth. **A223** (1984) 26

[Ari99] I. Ariño and L. Garrido, *Particle identification with the HERA−B RICH*, HERA−B Note 99-108, DESY, Hamburg (1999)

[Ari00] I. Ariño et al. (HERA−B RICH Group), *The HERA−B RICH*, Nucl. Instrum. Meth. **A453** (2000) 289

[Bal00a] V. Balagura et al., *High-p_T trigger for HERA−B experiment*, Nucl. Instrum. Meth. **A453** (2000) 412

[Bal00b] P. Ball et al., B *decays at the LHC*, CERN-TH 2000-101, preprint hep-ph/0003238 (2000)

[Bau00] C. Bauer et al., *The HERA−B vertex detector system*, Nucl. Instrum. Meth. **A453** (2000) 103

[Bec00] P. Bechtle, *DAQ integration and online monitoring of the HERA−B muon pretrigger system*, talk given at the Special Seminar of the Max-Planck-Institut für Kernphysik, November 8, 2000, Heidelberg

[Bec01] P. Bechtle, *Inbetriebnahme des HERA−B Myon-Pretrigger-Systems*, Diplomarbeit, Universität Dortmund (March 2001), in German

[Ber79] E.L. Berger and S.J. Brodsky, *Quark structure functions of mesons and the Drell-Yan process*, Phys. Rev. Lett. **42** (1979) 940

E.L. Berger, *Higher-twist effects in deep-inelastic scattering*, Phys. Lett. **89B** (1980) 241

[Ber98] E.L. Berger, L.E. Gordon, and M. Klasen, *Massive lepton pairs as a prompt photon surrogate*, Phys. Rev. **D58** (1998) 074012

[Ber00] S. Bergmann et al., *Lessons from FOCUS and CLEO measurements of* $D^0 - \overline{D^0}$ *mixing parameters*, Phys. Lett. **B486** (2000) 418

[Bii86] C. Biino et al. (Chicago-Iowa-Princeton Collaboration), *An apparatus to measure the structure of the pion*, Nucl. Instrum. Meth. **A243** (1986) 323

[Bjo69a] J.D. Bjorken, *Asymptotic sum rules at infinite momentum*, Phys. Rev. **179** (1969) 1547

[Bjo69b] J.D. Bjorken and E.A. Paschos, *Inelastic electron proton and gamma proton scattering, and the structure of the nucleon*, Phys. Rev. **185** (1969) 1975

[Bla89] M. Blazek, M. Biyajima, and N. Suzuki, *Angular distributions of muon pairs produced by negative pions on deuterium and tungsten in terms of coherent states*, Z. Phys. **C43** (1989) 447

[Boc00] R.K. Bock et al., *Data-analysis techniques for high-energy physics*, 2nd edition, Cambridge Univ. Press (2000), p. 244ff.

[Boe99] D. Boer, *Investigating the origins of transverse spin asymmetries at RHIC*, Phys. Rev. **D60** (1999) 014012

[Boe01] D. Boer, RIKEN-BNL Research Center, private communication (January 2001)

[Boh01] G. Bohm, DESY Zeuthen, private communication (February 2001)

[Bra93] A. Brandenburg, O. Nachtmann, and E. Mirkes, *Spin effects and factorization in the Drell-Yan process*, Z. Phys. **C60** (1993) 697

[Bra94] A. Brandenburg et al., *Angular distributions in the Drell-Yan process: A closer look at higher twist effects*, Phys. Rev. Lett. **73** (1994) 939

[Bra96] A. Bravar et al. (E704 Collaboration), *Single spin asymmetries in inclusive charged pion production by transversely polarized anti-protons*, Phys. Rev. Lett. **77** (1996) 2626

[Brä01] M. Bräuer, Dissertation, Universität Heidelberg (in preparation)

[Bru97] R. Brun and F. Rademakers, *ROOT: an object oriented data analysis framework*, Nucl. Instrum. Meth. **A389** (1997) 81

For a more recent reference manual see `http://root.cern.ch`.

[Buc00] P. Buchholz, Universität Dortmund, private communication (February 2000)

[Bur97] A.J. Buras and R. Fleischer, *Quark mixing, CP violation and rare decays after the top quark discovery*, in: Heavy Flavours II, eds. A.J. Buras and M. Lindner, World Scientific (1997) 65

[Cab63] N. Cabibbo, *Unitary symmetry and leptonic decays*, Phys. Rev. Lett. **10** (1963) 531

[Cal69] C.G. Callan and D.J. Gross, *High-energy electroproduction and the constitution of the electric current*, Phys. Rev. Lett. **22** (1969) 156

[Cha99] T.-H. Chang, *Angular distributions of J/ψ decays in dimuon channel in 800 GeV proton-copper collisions*, PhD thesis, New Mexico State University (1999)

[Chi86] P. Chiappetta and M. Le Bellac, *Angular distribution of lepton pairs in Drell-Yan-like processes*, Z. Phys. **C32** (1986) 521

[Col77] J.C. Collins and D.E. Soper, *Angular distribution of dileptons in high-energy hadron collisions*, Phys. Rev. **D16** (1977) 2219

[Col89] J.C. Collins, D.E. Soper, and G. Sterman, *Factorization of hard processes in QCD* in: Perturbative QCD, ed. A.H. Mueller, World Scientific (1989) 1

[Con89] J.S. Conway et al. (Chicago-Iowa-Princeton Collaboration), *Experimental study of muon pairs produced by 252-GeV pions on tungsten*, Phys. Rev. **D39** (1989) 92

[Cow98] G.D. Cowan, *Statistical data analysis*, Oxford Univ. Press (1998)

[DES00] Abteilung Presse und Öffentlichkeitsarbeit, DESY, Hamburg (2000)

[Dit00] M. Dittmar, *Perspectives of Standard Model Higgs measurements at the LHC*, Pramana J. Phys. **55** (2000) 151

[Dre70] S.D. Drell and T.-M. Yan, *Massive lepton-pair production in hadron-hadron collisions at high energies*, Phys. Rev. Lett. **25** (1970) 316

[Dri84] D. Drijard, H.G. Fischer, and T. Nakada, *Study of event mixing and its application to the extraction of resonance signals*, Nucl. Instrum. Meth. **A225** (1984) 367

[Duj00] D. Dujmić and R. Eckmann, *Software for standalone RICH reconstruction*, HERA–B Note 00-004, DESY, Hamburg (2000)

[Dür96] M. Düren, *HERMES – ein neues HERA-Experiment zur Klärung des Spinrätsels*, Phys. Bl. **52** (1996) Nr. 3, p. 243ff., in German

[Eig99] V. Eiges, *MUON-RICH matching*, talk given at the HERA–B collaboration meeting, October 11-15, 1999, HERA–B Note 99-203, DESY, Hamburg (1999)

V. Eiges, *Muon track reconstruction using matching with VDS and RICH*, talk given at the HERA–B muon reconstruction and analysis meeting, February 2-3, 2000, Universität Dortmund

[Eig00] V. Eiges, *Muon J/ψ triggering*, talk given at the HERA–B muon analysis meeting, May 20, 2000, DESY, Hamburg

[Ein05] A. Einstein, *Zur Elektrodynamik bewegter Körper*, Annalen der Physik **17** (1905) 891

[Eis01] F. Eisele, *How many ψ's per life hour can we expect in 2002 in the muon channel*, plenary talk given at the HERA–B collaboration meeting, February 19-23, 2001, DESY, Hamburg HERA–B Note 01-039 (2001)

[Ell96] R.K. Ellis, W.J. Stirling, and B.R. Webber, *QCD and collider physics*, Cambridge Univ. Press (1996), p. 301ff.

[Eme00a] D. Emeliyanov and I. Kisel, *CATS track fitting algorithm based on the discrete Kalman filter*, HERA–B Note 00-032, DESY, Hamburg (2000)

[Eme00b] D. Emeliyanov et al., *Primary vertex reconstruction by Rover*, HERA–B Note 00-139, DESY, Hamburg (2000)

V. Eiges et al., *Test of vertex reconstruction and fitting algorithms on J/$\psi \to \mu^+\mu^-$ data*, HERA–B Note 00-052, DESY, Hamburg (2000)

[Fal86] S. Falciano et al. (NA10 Collaboration), *Angular distributions of muon pairs produced by 194 GeV/c negative pions*, Z. Phys. **C31** (1986) 513

[Fey49] R.P. Feynman, *Space-time approach to quantum electrodynamics*, Phys. Rev. **76** (1949) 769

[Fey69] R.P. Feynman, *Very high-energy collisions of hadrons*, Phys. Rev. Lett. **23** (1969) 1415

R.P. Feynman, *Photon-hadron interactions*, W.A. Benjamin, Reading, MA (1972)

[Fom97] B. Fominykh, *MUREC-A reconstruction program for HERA−B muon detector operating in stand-alone mode*, HERA−B Note 97-167, DESY, Hamburg (1997)

[Fom00] B. Fominykh, *Study of muon identification program (MuonID.C) on di-muon SLT triggered events*, talk given at the HERA−B collaboration meeting, October 2-6, 2000, in HERA−B Note 00-171, DESY, Hamburg (2000)

[Fom01] B. Fominykh, *Muon identification*, talk given at the HERA-B Tracking Meeting, January 15, 2001, DESY, Hamburg

[Fri74] J. Friedman, *Data analysis techniques for high energy particle physics*, in: Proc. 1974 CERN School of Computing, CERN 74-23, CERN, Genève (1974)

[Gag98] G.A. Gagliardi et al., *Hardware trigger system for Fermilab E866*, Nucl. Instrum. Meth. **A418** (1998) 322

[GEA94] *GEANT 3.21 detector description and simulation tool*, CERN Program Library Long Writeup W5093, CERN, Genève (1994)

[Gel00] A. Gellrich et al., *Full online event reconstruction at HERA−B*, Proc. 1. International Conference On Computing In High Energy Physics And Nuclear Physics (CHEP2000), Pisa, 7-11 February 2000, ed. M. Mazzucato (Povda, INFN, 2000) 597

[Ger98] E.K.E. Gerndt et al., *Description of messages and process-logic for the First Level Trigger of HERA−B*, FLT internal note, DESY, Hamburg (1998)

[Gla61] S.L. Glashow, *Partial symmetries of weak interactions*, Nucl. Phys. **22** (1961) 579

[Gle00] T. Glebe, *Vt++ Version 1.0*, HERA−B Note 00-175, DESY, Hamburg (2000)

for a more recent documentation see (status: February 3, 2001)
`http://www.mpi-hd.mpg.de/herab/vt++`

[Glü98] M. Glück, E. Reya, and A. Vogt, *Dynamical parton distributions revisited*, Eur. Phys. J. **C5** (1998) 461

[Got64] K. Gottfried and J.D. Jackson, *On the connection between production mechanism and decay of resonances at high-energies*, Nuovo Cim. **33** (1964) 309

[Gro73] D.J. Gross and F. Wilczek, *Ultraviolet behavior of nonabelian gauge theories*, Phys. Rev. Lett. **30** (1973) 1343

[Gro00] D.E. Groom et al., *Review of particle physics*, Eur. Phys. J. **C15** (2000) 1

[Gua88] M. Guanziroli et al. (NA10 Collaboration), *Angular distributions of muon pairs produced by negative pions on deuterium and tungsten*, Z. Phys. **C37** (1988) 545

[Gur00] A. Gurtu, *Precision tests of the electroweak gauge theory*, talk given at the XXXth International Conference on High Energy Physics (ICHEP), July 27 – August 2, 2000, Osaka

[Hal84] F. Halzen and A.D. Martin, *Quarks & leptons: an introductory course in modern particle physics*, J. Wiley & Sons, New York (1984)

[Ham91] R. Hamberg, T. Matsuura, and W.L. van Neerven, *A complete calculation of the $\mathcal{O}(\alpha_s^2)$ correction to the Drell-Yan K factor*, Nucl. Phys. **B359** (1991) 343

[Har98] The BABAR Physics Book, *Physics at an asymmetric* B *factory*, Eds. P.F. Harrison and H.R. Quinn, SLAC-R-504 (1998)

[Has95] C. Hast et al., *Test of internal halo targets in the HERA proton ring*, Nucl. Instrum. Meth. **A354** (1995) 224

[HB00a] HERA–B Collaboration, *HERA–B report on status and prospects*, DESY-PRC 00/04 (October 2000)

[HB00b] HERA–B Collaboration, *HERA–B physics in 2001/2002*, letter to the DESY directorate (December 2000)

[Hei26] W. Heisenberg, *Über quantentheoretische Umdeutung kinematischer und mechanischer Beziehungen*, Z. Phys. **33** (1926) 879

[Hol93] U. Holm et al. (ZEUS Collaboration), *ZEUS: A detector for HERA – status report 1993*, ZEUS-STATUS-REPT-1993, DESY, Hamburg (1993)

[Hus00a] U. Husemann, *Muon pretrigger simulation and analysis*, talk given at the HERA–B collaboration meeting, February 28 – March 3, 2000, in HERA–B Note 00-015, DESY, Hamburg (2000)

[Hus00b] U. Husemann, J/ψ *search*, talk given at the HERA–B muon analysis meeting, June 22, 2000, DESY, Hamburg

U. Husemann, J/ψ *search - an update*, talk given at the HERA–B muon analysis meeting, July 25, 2000, DESY, Hamburg

[Igo98] O. Igonkina, *MARPLE – Version 1.03*, HERA–B Note 98-129, DESY, Hamburg (1998)

for a more recent online manual see (status Jan 28, 2001):
`http://www-hera-b.desy.de/subgroup/software/arte/MARPLE/`

[Igo00] P. Igo-Kemenes (LEP Higgs Working Group), *Status of Higgs boson searches*, talk given at the LEPC meeting, November 3, 2000, CERN, Genève

[Itz80] C. Itzykson and J.-B. Zuber, *Quantum field theory*, McGraw-Hill, New York (1980)

[Iva99] J. Ivarsson, P. Kreuzer, and T. Lohse, *PYTHIA and FRITIOF: event generators for HERA−B*, HERA−B Note 99-067, DESY, Hamburg (1999)

[Jar88] C. Jarlskog and R. Stora, *Unitarity polygons and CP violation areas and phases in the standard electroweak model*, Phys. Lett. **208** (1988) 268

[Kap94] D.M. Kaplan, B *cross-section from E789*, presented at the HQ94 Workshop, Charlottesville, VA, October 7-10, 1994, IIT-HEP-94-2

[Kis99] I. Kisel and S. Masciocchi, *CATS - A cellular automaton for tracking in silicon for the HERA−B vertex detector*, HERA−B Note 99-242, DESY, Hamburg (1999)

[Kla00] E. Klaus, *Untersuchungen zur Inbetriebnahme des HERA−B-Myon-Pretriggers und Monte-Carlo-Studien zum Zerfall* $B^0 \to K^{0*} \mu^+\mu^-$, Diplomarbeit, Universität Dortmund (November 2000), in German

[Kob73] M. Kobayashi and T. Maskawa, *CP violation in the renormalizable theory of weak interaction*, Prog. Theor. Phys. **49** (1973) 652

[Kre01] P. Kreuzer, DESY Hamburg, private communication (March 2001)

[Lai00] H. Lai et al. (CTEQ Collaboration), *Global QCD analysis of parton structure of the nucleon: CTEQ5 parton distributions*, Eur. Phys. J. **C12** (2000) 375

[Lam78] C.S. Lam and W.-K. Tung, *Systematic approach to inclusive lepton pair production in hadronic collisions*, Phys. Rev. **D18** (1978) 2447

[Lam80] C.S. Lam and W.-K. Tung, *Parton-model relation without quantum-chromodynamic modifications in lepton pair production*, Phys. Rev. **D21** (1980) 2712

[Loh94] T. Lohse et al., *HERA−B – An experiment to study CP violation in the B system using an internal target at the HERA proton ring*, Proposal, DESY-PRC 94/02 (May 1994)

[Loh95] T. Lohse, *Vertex reconstruction and fitting*, HERA−B Note 95-013, DESY, Hamburg (1995)

[Lyn91] G.R. Lynch and O.I. Dahl, *Approximations to multiple Coulomb scattering*, Nucl. Instrum. Meth. **B58** (1991) 6

[Man97a] R. Mankel, *A concurrent track evolution algorithm for pattern recognition in the HERA−B main tracking system*, Nucl. Instrum. Meth. **A395** (1997) 169

R. Mankel and A. Spiridonov, *The concurrent track evolution algorithm: extension for track finding in the inhomogeneous magnetic field of the HERA−B spectrometer*, Nucl. Instrum. Meth. **A426** (1999) 268

[Man97b] R. Mankel, *ranger – a pattern recognition algorithm for the HERA−B main tracking system: I, IV*, HERA−B Note 97-082, DESY, Hamburg (1997), HERA−B Note 98-079, DESY, Hamburg (1998)

R. Mankel and A. Spiridonov, *ranger – a pattern recognition algorithm for the HERA−B main tracking system: II, III, V*, HERA−B Note 98-154, DESY, Hamburg (1998), HERA−B Note 98-206, DESY, Hamburg (1998), HERA−B Note 99-101, DESY, Hamburg (1999)

[Man00] T. Mannel, *Fermion masses and mixings in the Standard Model*, talk given at the DESY Theory Workshop 2000 *CP Violation and Rare Processes: Standard Model and Beyond*, September 26-29, 2000, Hamburg

[Mas01] S. Masciocchi, *Tracking/Reco*, plenary talk given at the HERA–B collaboration meeting, February 19-23, 2001, HERA–B Note 01-031, DESY, Hamburg (2001)

[McG94] P.L. McGaughey et al., *Cross sections for the production of high-mass muon pairs from 800 GeV proton bombardment of* ^2H, Phys. Rev. **D50** (1994) 3038, Erratum: Phys. Rev. **D60** (1999) 119903

[McG96] P.L. McGaughey, *Recent measurement of quarkonia and Drell-Yan production in proton-nucleus collisions*, Nucl. Phys. **A610** (1996) 394c

[McG99] P.L. McGaughey, J.M. Moss, and J.C. Peng, *High-energy hadron-induced dilepton production from nucleons and nuclei*, Ann. Rev. Nucl. Part. Sci. **49** (1999) 217

[Mor91] G. Moreno et al., *Dimuon production in proton-copper collisions at* $\sqrt{s} = 38.8$ *GeV*, Phys. Rev. **D43** (1991) 2815

[Mos01] J.M. Moss, Los Alamos National Laboratory, private communication (February 2001)

[Nac84] O. Nachtmann and A. Reiter, *The vacuum structure in QCD and hadron-hadron scattering*, Z. Phys. **C24** (1984) 283

[Nac86] O. Nachtmann, *Phänomene und Konzepte der Elementarteilchenphysik*, Vieweg, Braunschweig (1986)

[Now94] S. Nowak, *A description of HBGEAN*, HERA–B Note 94-123, DESY, Hamburg (1994)

[Per00] T. Perschke, *Inklusive Multiplizität geladener Teilchen beim HERA–B Fixed-Target-Experiment*, Dissertation, Ludwig-Maximilians-Universität München (November 2000), in German

[Pes01] R. Pestotnik, *Identification of pions, kaons and protons in the HERA–B spectrometer*, Dissertation, Univerza v Ljubljani (2001)

[Pet01a] B. Petersen, Niels Bohr Institutet, Cøbenhavn Ø, private communication (February 2001)

[Pet01b] B. Petersen, talk given at the $J/\psi(\psi') \to \mu^+\mu^-$ Working Group meeting, February 7, 2001, DESY, Hamburg

[Pi92] H. Pi, *An event generator for interactions between hadrons ad nuclei* – FRITIOF *version 7.0*, Computer Physics Comm. **71** (1992) 173

[Pla00] M. Planck, Verhandlungen der Deutschen Physikalischen Gesellschaft **2** (1900) 237

[Pol73] H.D. Politzer, *Reliable perturbative results for strong interactions?*, Phys. Rev. Lett. **30** (1973) 1346

[Pyr98] J. Pyrlik,
`http://www-hera-b.desy.de/subgroup/pictures/detector_schematic.eps` (status 26 March 2001)

[Rey81] E. Reya, *Perturbative quantum chromodynamics*, Phys. Rep. **69C** (1981) 195

[Sak67] A.D. Sakharov, *Violation of CP invariance, C asymmetry, and baryon asymmetry of the universe*, Sov. Phys. JETP Lett. **5** (1967) 24

[Sal68] A. Salam, Proc. 8th Nobel Symposium, Stockholm 1968, ed. N. Svartholm (Almqvist and Wiksells, Stockholm 1968) 367

[Sam01] D. Samtleben, *Analysis of* $J/\psi \to e^+e^-$, in: A. Zoccoli, *Status of the analysis*, plenary talk given at the HERA−B collaboration meeting, February 19-23, 2001, HERA−B Note 01-045, DESY, Hamburg (2001)

[San00] M. Sang, *Grover manual*
for a recent version see (status Jan 28, 2001)
`http://wwwhera-b.mppmu.mpg.de/analysis/grover.html`

[Sav98] V. Saveliev et al. (HERA−B Transition Radiation Detector Group), *The HERA−B Transition Radiation Detector*, Nucl. Instrum. Meth. **A408** (1998) 289

[Sch26] E. Schrödinger, *Quantisierung als Eigenwertproblem*, Annalen der Physik **79** (1926) 361

[Sch48] J. Schwinger, *Quantum electrodynamics I–III*, Phys. Rev. **75** (1948) 1439, Phys. Rev. **75** (1948) 651, Phys. Rev. **76** (1949) 790

[Sch95] M.H. Schub et al., *Measurement of* J/ψ *and* ψ' *production in 800 GeV/c proton-gold collisions*, Phys. Rev. **D52** (1995) 1307

[Sch98a] M. Schmelling, *Numerische Methoden der Datenanalyse*, Blockseminar im Graduiertenkolleg „Erzeugung und Zerfälle von Elementarteilchen“, Universität Dortmund (1998)

[Sch98b] B. Schwenninger, *Definition of data formats for the muon pretrigger system*, Version 0.1 (December 1998)

[Sch99] M. Schmelling, *Evidence for heavy flavours in the '99 magnet-off data*, HERA−B Note 99-176, DESY, Hamburg (1999)

[Sch01a] M. Schmelling, private communication (January 2001)

[Sch01b] B. Schwenninger, Dissertation, Universität Dortmund (in preparation)

[Sjö94] T. Sjöstrand, PYTHIA *5.7 and* JETSET *7.4 – Physics and Manual*, Computer Physics Comm. **82** (1994) 74

[Soe00] L. Soezueer, DESY Hamburg, private communication (August 2000)

[Sok64] A.A. Sokolov and I.M. Ternov, *On polarization and spin effects in the theory of synchrotron radiation*, Phys. Dokl. **8** (1964) 1203

[Spi98] A. Spiridonov, *Optimized integration of the equations of motion of a particle in the HERA–B magnet*, HERA–B Note 98-133, DESY, Hamburg (1998)

[Spr00] S. Spratte, *Bestimmung der Wechselwirkungsrate des HERA–B Targets und Untersuchung des Coasting Beam am HERA Protonen-Ring*, Dissertation, Universität Dortmund (June 2000), in German

[Ste00] C. Stegmann et al. (HERA–B Outer Tracker Group), *The outer tracker for HERA–B*, Nucl. Instrum. Meth. **A453** (2000) 153

[Sti93] W.J. Stirling and M.R. Whalley, *A compilation of Drell-Yan cross sections*, J. Phys. G: Nucl. Part. Phys. **19** (1993) D1

[tHo72] G. 't Hooft, M. Veltman, *Regularization and renormalization of gauge fields*, Nucl. Phys. **B44** (1972) 189

[Tit96] M. Titov, *Study of background for muon identification at the HERA–B experiment* HERA–B Note 96-137, DESY, Hamburg (1996)

[Tit00] M. Titov, *The muon system in the HERA–B experiment*, Nucl. Instrum. Meth. **A446** (2000) 355

[Tom46] S.-I. Tomonaga, *On a relativistically invariant formulation of the quantum theory of wave fields I–V*, Prog. Theor. Phys. **1** (1946) 27, Prog. Theor. Phys. **2** (1947) 101, 198, Prog. Theor. Phys. **1** (1948) 1, 101

[Vil97] M. Villa, *Progress report on the ECAL reconstruction software*, HERA–B Note 97-005, DESY, Hamburg (1997)

[Wei67] S. Weinberg, *A model of leptons*, Phys. Rev. Lett. **19** (1967) 1264

[Wol83] L. Wolfenstein, *Parametrization of the Kobayashi-Maskawa matrix*, Phys. Rev. Lett. **51** (1983) 1945

[Zai00] Y. Zaitsev, *Muon system status and plans*, plenary talk given at the HERA–B collaboration meeting, October 2-6, 2000, HERA–B Note 00-155, DESY, Hamburg (2000)

[Zeu00] T. Zeuner, *The MSGC-GEM inner tracker for HERA–B*, Nucl. Instrum. Meth. **A446** (2000) 324

[Zoc00] A. Zoccoli, *The electromagnetic calorimeter of the HERA–B experiment*, Nucl. Instrum. Meth. **A446** (2000) 246

[Zoc01] A. Zoccoli, *HERA–B physics program in 2001/2002*, plenary talk given at the HERA–B collaboration meeting, February 19-23, 2001, HERA–B Note 01-043, DESY, Hamburg (2001)

Danksagung

Zunächst möchte ich mich bei Herrn Prof. Dr. Peter Buchholz bedanken, der im Laufe meiner Diplomarbeit immer wieder den richtigen „Riecher“ bewiesen und mich ein um das andere Mal ermutigt hat, interessante und aktuelle Themen der Datenanalyse in HERA–B zu bearbeiten.

Herrn Prof. Dr. Dietrich Wegener möchte ich dafür danken, dass er sich bereit erklärt hat, als Zweitkorrektor für meine Diplomarbeit zu fungieren. Auch möchte ich ihm für seine unnachahmlichen Kaffeerunden danken. Meiner Allgemeinbildung und besten Unterhaltung haben sie jedenfalls gedient.

Den Herren Prof. Dr. Peter Buchholz und Prof. Dr. Claus Gößling danke ich dafür, dass sie mir während meines Studiums einen unvergesslichen Sommer am CERN ermöglicht haben, durch den meine Entscheidung, meine Diplomarbeit in der experimentellen Teilchenphysik anzufertigen, nachdrücklich bestärkt wurde.

Für die hervorragende Zusammenarbeit in unserer Arbeitsgruppe möchte ich meinen Kollegen Markus Adams, Philip Bechtle, Matthias Böcker, Carsten Cruse, Elmar Klaus, Markus Kolander, Iouri Kolotaev und Björn Schwenninger danken. Mein besonderer Dank gilt meinem „direkten Betreuer“ Markus Adams, für die vielen fruchtbaren Diskussionen über unsere Arbeit und die Verwaltung unserer Computerei („Kannste nicht mal die neueste ARTE-Version installieren ... ?!“).

Aber auch außerhalb unserer Arbeitsgruppe gab es Menschen, die immer wieder ein offenes Ohr für meine Fragen hatten. Stellvertretend seien hier Brian Petersen, Dr. Michael Schmelling, Prof. Dr. Thomas Lohse, Dr. Boris Fominykh, Dr. Werner Vogelsang und Dr. Klaus Wacker genannt.

Für die gute Zusammenarbeit bei der Erschließung des Themas „Drell-Yan“ für HERA–B möchte ich mich insbesondere bei Wolfgang Gradl bedanken. Mein herzlicher Dank gilt außerdem Prof. Dr. Gerhard Bohm und Dr. Ullrich Schwanke.

Für das Korrekturlesen meines Manuskripts und die kritischen Kommentare zu meinen Entwürfen bedanke ich mich besonders bei Markus Adams, Philip Bechtle, Carsten Cruse, Wolfgang Gradl und Björn Schwenninger. Meiner CERN-Summer-Music-School-Kollegin Christine Aidala danke ich ganz herzlich für ihre Hilfe dabei, der Arbeit ein bißchen sprachlichen Schliff zu verleihen. Many many thanks! Oder, um es mit Giovanni Trapattoni zu sagen: Non dire gatto se non ce l'hai nel sacco!

Auch wenn er nun schon zum dritten Mal auftaucht, ich danke ganz besonders meinem „kongenialen Partner“ Philip Bechtle, mit dem ich buchstäblich seit dem ersten Tag des Mathevorkurses mein Studium und auch die ein oder andere Aktion außerhalb der Uni bestritten habe.

Mein letzter und tiefster Dank gilt allerdings meinen Eltern Josef und Maritheres Husemann, denen ich unendlich viel zu verdanken habe und die mich auf meinem Lebensweg stets bedingungslos unterstützt haben. Ich möchte diese Arbeit meiner Mutter widmen in der Gewissheit, dass sie dort, wo sie jetzt sein mag, sich mit mir über diese Arbeit freut.

Diese Arbeit wurde mit Mitteln des Bundesministeriums für Bildung und Forschung unter dem Förderkennzeichen 05 7DO55P gefördert.